

**STUDY OF LOW-LYING MAGNETIC EXCITATIONS, THERMAL
AND PERCOLATION CRITICAL BEHAVIOUR AND ELECTRICAL
TRANSPORT IN QUENCH-DISORDERED FERROMAGNETS**

**A THESIS SUBMITTED FOR THE DEGREE OF
DOCTOR OF PHILOSOPHY**

**BY
P. D. BABU**



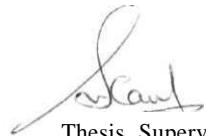
**SCHOOL OF PHYSICS
UNIVERSITY OF HYDERABAD
HYDERABAD - 500 046 INDIA
OCTOBER 1995**

CERTIFICATE

This is to certify that the work contained in this **thesis** entitled, "**Study of low-lying magnetic excitations, thermal and percolation critical behaviour, and electrical transport in quench-disordered ferromagnets**", has been carried out by Mr. P.D. Babu under my direct supervision and the same has not been submitted for the award of research degree of any University.

Place: Hyderabad

Date: 26-10-1995



Thesis Supervisor



Dean

School of Physics

26/10/95

DECLARATION

I hereby declare that the matter embodied in this thesis is the result of investigations carried out by me in the school of physics, University of Hyderabad. Hyderabad - 500 046. under the supervision of Prof.S.N.Kaul.

Place: Hyderabad

Date : 26-10-1995


(P.D.Babu)

ACKNOWLEDGEMENTS

I take this opportunity to express my profound gratitude to Prof. S.N. Kaul for his inspiring guidance, constant encouragement and cooperation through-out my work.

I thank Dean, School of Physics, for providing all the necessary facilities and all the other faculty members of the School especially those who taught in the M.Sc.

I am extremely grateful to Prof. M. Rosenberg, Institute for Experimental Physics VI, Ruhr University, Bochum. Germany and Prof. M. Fahnle, Max-Planck Institute for Metal Research, Stuttgart, Germany for providing the samples used in this work.

I am also grateful to Dr. M. Seeger and Prof. H. Kronmüller, Max-Planck Institute for Metal Research, Stuttgart, Germany for allowing the use of the SQUID magnetometer.

I am grateful to Prof. Gomez Sal and Dr. L. Fernandez Barquin for performing low temperature electrical resistivity measurements on Fe-Zr alloys.

I am thankful to the Principal Scientific Officer, Dr. K.V. Reddy and the other staff members in particular Mr. Manjunath of Central Instrumentation Laboratory for their cooperation and help.

I express my sincere thanks the Foreman and the staff of Central Workshop for their help and cooperation.

I thank my colleagues, Vasu, Sambasiva Rao, Veera Mohan, Srinath, Senthil and Manjusri and friends Mohan Babu, Goutam, Y.S. Rao, S. Srinivas, Harrish Kumar and many others who shared with me the good times as well the bad.

I must express my deep gratitude to my uncle and aunt to whom I dedicate this thesis for their support and encouragement without which I could not have reached this stage. I am grateful to my parents and other family members for their continuous support and encouragement.

Financial assistance from the University Grants Commission (UGC), New Delhi, for the fellowship, and the Department of Science and Technology (DST), New Delhi, for the experimental facilities under the project No. SP/S2/M21/86, is gratefully acknowledged.

To

Vasantha Devi and Govindarajulu

Table of Contents

1.	INTRODUCTION.....	<i>1</i>
1.1	Preparation and characterization.	<i>1</i>
1.2	Short-range order.	<i>3</i>
1.3	Types of disorder.	<i>3</i>
1.4	Effect of disorder on magnetic properties.	<i>4</i>
1.5	Magnetic order in amorphous solids.	<i>8</i>
1.6	Low-lying magnetic excitations.	<i>9</i>
1.6.1	Localized electron model.	<i>10</i>
1.6.2	Itinerant-electron model.	<i>14</i>
1.6.2A	Spin waves in itinerant-electron model.	<i>17</i>
1.6.2D	Spin fluctuatuations in itinerant-electron model.	<i>17</i>
1.7	Thermal critical phenomena.	<i>19</i>
1.8	Percolation critical behaviour.	<i>23</i>
1.9	Electrical resistivity in amorphous alloys.	<i>29</i>
1.9.1	Mott $s - d$ scattering model.	<i>30</i>
1.9.2	Diffraction model.	<i>31</i>
1.9.3	Kondo spin-flip model.	<i>33</i>
1.9.4	Two-level-tunneling model.	<i>33</i>
1.9.5	Coherent exchange scattering model.	<i>34</i>
1.9.6	Spin-disorder model.	<i>35</i>
1.9.7	Quantum corrections to the resistivity.	<i>36</i>
1.10	Aim and scope of the thesis.	<i>37</i>
	References.	<i>41</i>
2.	EXPERIMENTAL DETAILS.	<i>48</i>
2.1	Sample preparation and characterization.	<i>48</i>
2.2	Bulk magnetization measurements.	<i>48</i>
2.2.1	Vibrating Sample Magnetometer.	<i>48</i>

2.2.2	Measurements using Vibrating Sample Magnetometer.	53
2.2.3	SQUID Magnetometer.	55
2.2.4	Faraday Balance.	57
2.3	Ferromagnetic Resonance technique.	58
2.4	FMR data analysis and lineshape calculations.	61
2.5	Electrical resistivity.	64
	References.	70
3.	LOW-LYING MAGNETIC EXCITATIONS.	71
A.	a-Fe_{90+y}Zr_{10-y} and a-Fe_{90-x}Co_xZr₁₀ alloys.	71
3.1	Results and analysis.	71
3.1.1	Infield Magnetization.	71
3.1.2	Spontaneous Magnetization.	81
3.2	Discussion.	91
3.2.1	Spin fluctuation model : A unified approach.	91
3.2.2	Low-temperature or spin-wave region.	100
3.2.3	Intermediate temperature region.	108
3.2.4	Temperatures close to T_C	113
3.3	Conclusions.	118
B.	a-(Fe_pNi_{1-p})₈₀(B,Si)₂₀ and (Fe_pNi_{1-p})₈₀P₁₄B₆ alloys.	120
3.4	Results and analysis.	120
3.5	Discussion.	128
3.6	Conclusions.	134
	References.	137
4.	THERMAL AND PERCOLATION CRITICAL BEHAVIOUR . . .	143
A.	Thermal Critical Behaviour.	143
4.1	Results and analysis.	143
4.1.1	Arrottequation of state.	143
4.1.2	Single-power-law analysis.	144
4.1.3	Kouvel-Fisher method.	150
4.1.4	Scaling equation-of-state analysis.	150
4.1.5	FMR linewidth.	159
4.1.6	Analysis with 'Correction-to-scaling' (CTS) terms.	161

4.1.7	Critical isotherm.	764
4.1.8	Analysis using nonlinear variables.	767
4.2	Discussion.	776
4.2.1	Asymptotic and effective critical exponents and amplitudes.	776
4.2.2	Nonlinear scaling behaviour.	784
4.3	Conclusions.	788
B.	Percolation Critical Behaviour.	789
4.4	Results and analysis.	789
4.4.1	Magnetic phase diagram.	789
4.4.2	Thermal-to-percolation crossover exponent (ϕ).	791
4.4.3	Percolation exponent for spin-wave stiffness at 0 K.	794
4.4.4	Percolation exponent for spontaneous magnetization at 0 K.	794
4.5	Discussion.	797
4.6	Conclusions.	802
	References.	804
5.	ELECTRICAL RESISTIVITY OF (Fe,Co)-Zr AMORPHOUS ALLOYS	808
5.1	Results and data analysis.	808
5.2	Discussion.	822
5.3	Conclusions.	837
	References.	833
	Summary.	835
	Future Scope.	840
	List of Publications	847

CHAPTER 1

INTRODUCTION

Magnetic properties of amorphous alloys have received considerable attention during the recent years because of their technological applications and due to a wide variety of rich physical phenomena they offer from the fundamental point of view. Amorphous alloys are characterized by structurally disordered networks in which each atom constitutes a structural unit. Structural disorder in amorphous alloys, in turn, leads to changes in their electronic and magnetic properties as compared to those of their crystalline counterparts in which lattice periodicity and crystal structure play a decisive role in determining the basic properties. The bond and chemical disorder results in a distribution of magnetic moments and exchange interaction thereby affecting the magnetic properties of metallic glasses. The random electrostatic fields due to random atomic arrangements create local anisotropies via spin-orbit coupling giving rise to a variation in the orientation of magnetic moments. In addition, structural disorder is found to introduce new magnetic structures like speromagnetism, asperomagnetism and sperimagnetism which possess a non-collinear spin structure. The existence of positive and negative exchange interactions leads to spin-glass behaviour in many amorphous alloys. Transport properties of metallic glasses also differ considerably from those of the corresponding crystalline alloys.

Historically, it was Gubanov [1], who in 1960 first predicted theoretically the existence of amorphous ferromagnetism, based on the argument that the band structure of crystalline solids does not change in any fundamental way upon transition from crystalline to liquid or amorphous state. This implies that the band structure is essentially controlled by short range order. Ferromagnetism, which comes into existence because of the direct positive exchange interactions between the neighbouring spins, therefore, should not be destroyed. The predictions of Gubanov were experimentally verified only after first amorphous ferromagnetic *Fe - P - C* alloy was prepared by Duwez and Lin [2,3] by rapid quenching of the melt. Since then a large number of amorphous alloys have been prepared and studied in detail. The new effects and phenomena associated with amorphous alloys have led to new theoretical concepts and huge amount of experimental work resulted in the deeper understanding of disordered systems. Properties and the associated phenomena exhibited by these alloys have formed the subject of several books and review articles [4-17].

1.1. Preparation and Characterization

Amorphous alloys can be prepared by a number of techniques [4,6,11]. These techniques are broadly classified into two categories: (i) melt-quenching and (ii) deposition.

Splat quenching is the simplest form of melt-quenching. In this method, a liquid alloy droplet is squeezed between a rapidly moving piston and a fixed anvil. Alloys obtained by this method are in the form of thin discs of 1-3 cm in diameter and 20-60 μm in thickness. Another simple and the most popular technique is melt-spinning. This method employs a jet from which alloy melt is dropped onto a rapidly moving wheel made of a material with high thermal conductivity such as copper. Continuous ribbons of amorphous alloys are obtained by this method and higher cooling rates (10^6 K/sec) are achieved compared to splat-quenching. Laser quenching [18] is another form of melt-quenching technique. In this method, a short and highly intense laser beam is used to melt a portion of a thin metallic surface, which is then cooled rapidly by the surrounding crystal. The cooling rates achieved in this way are in the range of 10^{10} to 10^{12} K/sec.

The above-mentioned melt-quenching techniques are useful to prepare amorphous alloys in a narrow concentration range around the eutectic point. Preparation of amorphous alloys in the concentration range away from the eutectic point requires different techniques such as (a) thermal evaporation [19], in which metals constituting the alloy are evaporated in vacuum and condensed onto a cooled substrate, (b) sputter deposition [20], where atoms are deposited on a substrate by removing them from the source under bombardment with energetic inert gas atoms. When very high cooling rates of the order of 10^{14} K/sec are required, ion-implantation technique [21] is used. In addition, electro-deposition [22] and solid state reaction [23] are some of the occasionally used techniques.

Techniques such as x-ray, electron and neutron diffraction are mostly used to characterize amorphous alloys. A typical diffraction pattern of an amorphous alloy consists of diffuse rings or broad peak at low scattering angles. However, it is extremely difficult to distinguish purely amorphous materials from micro-crystalline materials with crystallites of size less than 20 Å using diffraction methods. A more refined x-ray technique, known as extended x-ray absorption fine structure (EXAFS), is particularly useful in probing the local atomic structure of amorphous alloys [24]. Neutron scattering is a powerful technique in probing short-range atomic order. Since neutron scattering amplitude of an individual nucleus varies with different isotopes and their spin states, coherent and incoherent scattering takes place depending upon whether or not the neutron waves scattered by different nuclei interfere with one another. While the coherent **neutron** scattering provides useful information about the collective structure and atomic pair correlation function, the incoherent neutron scattering gives important clues about localized vibration and atomic diffusion. Techniques such as nuclear magnetic resonance (NMR) and Mossbauer spectroscopy are useful in probing nearest-neighbour environments and magnetic hyperfine fields.

Various techniques are available for analyzing the chemical composition of disordered alloys.

Some of these techniques are atomic absorption spectroscopy, x-ray fluorescence, electron micro-probe analysis, Auger spectroscopy and secondary-ion mass spectroscopy.

1.2. Short-range order

In amorphous solids, atomic positions are strongly correlated in the nearest-neighbour shell but uncorrelated beyond a few interatomic spacings. In other words, glassy alloys possess short-range atomic order but no long-range atomic order and the structure of these solids resembles that of the liquids from which they have been obtained by quenching. Short-range atomic order or simply short-range order (SRO) varies from one amorphous material to the other and is of two types: compositional or chemical short-range order (CSRO) and geometrical short-range order (GSRO). In many glassy alloys, the chemical composition on a local scale is different from the macroscopic average and this deviation is called CSRO. The CSRO is confined to the first nearest-neighbours and hence can be described in terms of the deviation of the nearest-neighbour composition from the average. The topological short-range order (TSRO) describes the short-range order in the atomic positions regardless of the chemical identity of individual atoms. This type of SRO is present in all the glassy alloys including the single-component glasses made up of one kind of atoms only. In addition, geometrical distortions, which are independent of topology, can also occur in such elementary glasses and the corresponding short-range order is known as distortional short range order (DSRO). Therefore, the geometrical short-range order (GSRO), which characterizes local atomic structure includes both TSRO and DSRO.

1.3. Types of disorder

All glassy or amorphous materials are characterized by a complete lack of translational symmetry but the degree and type of short-range atomic order or local order varies from glass to glass. Different types of short-range order give rise to various kinds of disorder that have a direct bearing on the magnetic properties of these alloys [11,25].

(a) Topological disorder :

Topological disorder results when translational symmetry in the positions of atoms is completely absent and the nearest, next-nearest neighbour coordination number varies from site to site. A topologically disordered structure cannot be distorted back into a crystal. Topological disorder is intrinsic to the amorphous structure.

(b) Chemical disorder :

When different types of atoms or molecules irregularly occupy the lattice sites without disturbing the periodicity of an ordered structure, the chemical disorder results. In such cases, the translational symmetry of the atoms or molecules is broken by the chemical identity of the objects that occupy the lattice sites. Further complication can arise if in a binary or quasi-binary alloy, the concentration of one species of atoms is increased at the expense of the other. The disorder that results by changing the composition is known as compositional disorder. Compositional disorder includes substitutional disorder. A similar situation can also occur in a structurally disordered lattice. Thus, chemical and compositional disorder can occur in both crystalline and amorphous solids.

(c) Site-disorder :

The fluctuation in the coordination number arising from the random occupation of sites on a regular crystalline lattice or an aperiodic amorphous network constitutes site disorder.

(d) Bond disorder :

Bond disorder results when wild variation in the bond lengths and bond angles destroy the periodicity of the lattice or long-range atomic order. The bond-disordered network remains topologically equivalent to the crystal.

From the above description, it is clear that the site- and bond-disorder are included in topological and chemical/compositional disorder, and the terms "amorphous" and "disordered" cannot be used interchangeably. All amorphous solids are disordered but all disordered systems need not be amorphous. While the topological disorder alone is specific to amorphous solids, the other types, i.e., site-, bond-, chemical- and compositional disorder are found in both crystalline and amorphous materials.

1.4. Effect of disorder on magnetic properties

The basic **requirements for magnetic order** in a solid are (i) **the** existence of magnetic moments **associated with unpaired** electrons on atoms or ions in a solid and (ii) an interaction which couples these microscopic moments. These requirements are sufficient for a vast majority of

metallic and insulating magnetic materials whose magnetic moments are localized on the atomic sites. However, these concepts do not hold for certain class of materials known as itinerant magnetic systems in which magnetic electrons are itinerant and magnetic moments arise from the exchange splitting of spin-polarized d -band. In the latter case, the density of states (DOS) at the Fermi level, E_F , plays a crucial role in deciding the type of magnetic order. The effect of various types of disorder on these magnetic properties are discussed below.

(a) Density of states (DOS) :

Fig. 1.1 shows a schematic representation of the density of states, $N(E)$, for transition metals with fcc or bcc structure [13]. The DOS curve (ignoring the fine structure present in many crystalline solids) consists of two peaks resulting from the covalent splitting of the quasi atomic-like electronic energy levels into bonding and anti-bonding states. The shape and width of electronic bands from which DOS curves are computed, are basically controlled by the overlap of electronic wave functions on the neighbouring sites (which, in turn, depends on the nearest-neighbour distance or interatomic spacing) and by the crystalline symmetry. Since the nearest-neighbour (NN) atomic configurations in amorphous solids resembles that in their crystalline counterparts and the average NN distance is close to that of the corresponding crystalline solid, the effect of disorder is to smear out the sharp features of DOS curve and leave the value of DOS at E_F more or less unaltered.

(b) Magnetic moments :

A magnetic moment exists on an atom whenever there are unpaired electrons. Whether such a moment can persist or not when an atom becomes an ion in a solid, even a metal, depends on the extent of overlap of the wave functions of electrons in different shells on neighbouring ions. For example, considerable overlap of outer or valence electron wave functions on neighbouring ions, particularly in a metal, leads to a spread of atomic levels into energy bands of delocalized states. By comparison, the overlap of the d -shell electron wave functions for neighbouring ions in a metal is weak and hence d -band is much narrower than s -band in transition metal-based alloys. However, in rare earth based alloys, the f -electron wave functions for the neighbouring ions do not overlap because $4f$ shell is surrounded by $5s$ and $5p$ shells. As a consequence, the electrons in f -shell are localized. This picture is particularly appropriate to a magnetic ion in an insulator because electron-electron interactions in them are so strong as to open up a correlation gap in the effective density of states and make f -band narrower enough to localize the magnetic electrons. In metals, (particularly in transition metals) the delocalized s electrons complicate the situation since they are not only an extra source of itinerant magnetic moments

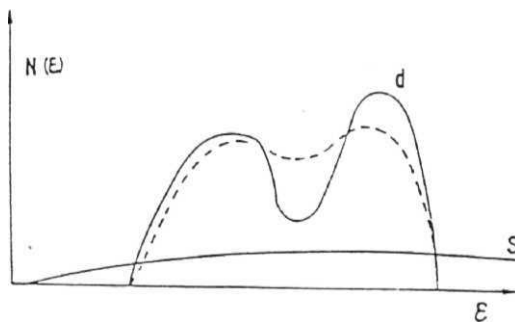


Fig. 1.1 Schematic representation of the electronic density of states (DOS) curve for amorphous (dashed curve) and crystalline (solid curve) 3d transition metals.

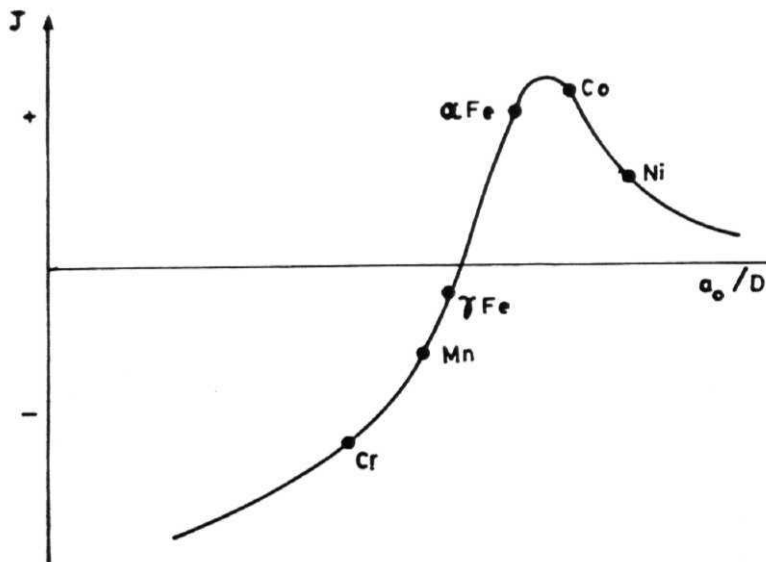


Fig. 1.2 Variation of exchange coupling with the distance between spins of 3d transition metals.

(leading to **Pauli paramagnetism**) but also their interaction with the magnetic electrons ($s - d$ interaction) renders the atomic concept of local moment of fixed magnitude meaningless. In the case of transition metals, the appropriate theoretical framework is provided by the **Stoner band model** in which the energy states of the itinerant magnetic electrons on a given ion are split into spin-up and spin-down bands and the splitting is caused by exchange interaction. In this model, the magnetic moment is proportional to the population difference in the spin-up and spin-down d sub-bands. In **metallic glasses**, the fluctuation in nearest neighbour (NN) distance and NN coordination number, the extent of overlap of electronic wave functions on neighbouring sites as well as exchange splitting change from site to site giving rise to variation in local moment from site to site and hence the moment has a distribution instead of a fixed value (as in crystalline systems).

(c) Interaction between moments :

The appearance of a magnetically ordered structure like ferromagnetism requires an interaction to couple the magnetic moments. The classical dipolar interaction of the form [11,25]

$$\mathcal{H}_{ij}^d = \frac{\vec{\mu}_i \cdot \vec{\mu}_j}{r_{ij}^3} - \frac{3(\vec{\mu}_i \cdot \vec{r}_{ij})(\vec{\mu}_j \cdot \vec{r}_{ij})}{r_{ij}^5} \quad (1.1)$$

tends to align the moments $\vec{\mu}_i$ and $\vec{\mu}_j$ parallel to the line joining the sites i and j . Dipolar interactions are weak, long-ranged and anisotropic since they depend on the orientation of the moments relative to \vec{r}_{ij} . The net dipolar field is identically zero at sites in a lattice of cubic symmetry. In amorphous systems, however, it is distributed both in magnitude and direction. A much stronger interaction is the quantum mechanical exchange interaction. Exchange interaction is an effective electrostatic interaction between two electrons which depends on the relative orientation of their spins. This isotropic Heisenberg interaction is given by [11,25]

$$\mathcal{H}_{ij}^{ex} = -2 J_{ij} \vec{S}_i \cdot \vec{S}_j \quad (1.2)$$

where J_{ij} is the exchange coupling constant between spins at sites i and j . J_{ij} is positive for ferromagnetic coupling and negative for antiferromagnetic coupling. The **Bethe-Slater** curve [11] shown in Fig. 1.2 indicates roughly how the exchange constant varies with distance between magnetic shells in 3d transition metals. It is seen from Fig. 1.2 that the distribution of interatomic separations in amorphous solids leads to a distribution of exchange interaction which may sometimes include interactions of either sign. Apart from direct exchange, there are other exchange mechanisms like superexchange via ligands and indirect exchange via conduction electrons also known as the **Ruderman-Kittel-Kasuya-Yosida** (RKKY) interaction. A distribution in the interatomic separations gives rise to a distribution of indirect exchange also. For

instance, **superexchange** is negative for 180° metal-ligand-metal bonds and weakly positive for 90° bond angles [11,25]. The **RKKY** interaction arises when the magnetic electrons of one atom induce a spin polarization in the conduction electrons which overlaps another atom and affects its magnetic electrons. RKKY interaction oscillates as a function of distance r and couples 4f shell spins/moments in rare earths. The long-range and oscillatory nature of RKKY interaction is not only responsible for spin glass behaviour in many dilute magnetic alloys but also leads to helical spin structure in many crystalline rare earth metals and compounds. In amorphous systems, RKKY interaction gives rise to positive or negative exchange coupling between moments depending on their separation but its range is severely restricted compared to that in their crystalline counterparts due to rapid decay of spin polarization amplitude with distance.

(d) Magnetic anisotropy :

Amorphous materials are generally assumed to be isotropic since there is no long-range atomic order. However, magnetic anisotropy in such systems has been observed and it reflects the existence of short-range-order in amorphous alloys. The local magnetic anisotropy that results from spin-orbit interaction or the anisotropy of local crystal field has strong influence on the nature of magnetic order in the ground state and coercivity of amorphous magnetic materials [26]. From a simple model calculation, Chi and Alben [27] have shown that when the local random anisotropy is small, the coercivity is small and high coercivities are obtained as the local anisotropy is increased. In addition, the magnetic field cooling, cold rolling and stress annealing of amorphous materials induce different forms of magnetic anisotropies. Various mechanisms [28] have been proposed to explain these anisotropies.

1.5. **Magnetic order in amorphous solids**

A wide variety of magnetic order [11,15,25,29] exists in amorphous solids even in the presence of various kinds of disorder. Chemical and structural disorder in amorphous materials produces an inequivalency of sites that leads to a distribution (i) in the magnitude of moments, (ii) in exchange interactions and (iii) induces large randomly varying electrostatic fields giving rise to locally varying single-site anisotropy [11,15,25]. Although magnetic order depends sensitively on distance and local environments, the structural disorder does not affect the collective magnetic order such as **ferromagnetism** in any fundamental way. The basic features of ferromagnetism observed in crystalline solids are retained in amorphous systems. However, in practice, it is rare to find antiferromagnetism in amorphous **materials** since antiferromagnetism demands that identical moments occupy neighbouring sites with antiparallel coupling throughout the amorphous structure. Moreover, it is difficult to conceive a random structure which can

be subdivided into two (or more) interpenetrating ferromagnetic sub-lattices with neighbouring inter-sublattice moments aligned **antiparallel** to one another, as is usually done in crystalline systems [11,15,25]. Another collinear magnetic order commonly found in many amorphous alloys is **ferrimagnetism**. Ferrimagnetism arises when two different types of magnetic ions occupy sites of two amorphous subnetworks such that intra-subnetwork moments are aligned parallel while inter-subnetwork moments are aligned antiparallel and the average magnitude of moments on each subnetwork is distinctly different from the other. Since the magnitude of moments on two subnetworks is not the same, a finite spontaneous magnetization exists. In addition to these familiar types of collinear magnetic order, **non-collinear** magnetic structures like **speromagnetism**, **asperomagnetism** and **sperimagnetism** occur in amorphous alloys. These non-collinear magnetic structures involve a competing random anisotropy and exchange interaction; the local anisotropy tries to align the magnetic moments along the locally varying crystal field axis while the exchange interaction tries to align the moments parallel or antiparallel to one another depending on whether the exchange is positive or negative [11,15,25]. Speromagnetic state is the one in which localized moments are cooperatively frozen in random directions below a certain ordering temperature T_o such that there is no net magnetization. Speromagnetism is exhibited by systems in which random anisotropy is comparable to exchange coupling and exchange coupling between the spins fluctuates in sign. Asperomagnetism arises when randomly placed localized moments of a given species are frozen in different orientations below an ordering temperature T_o but with some orientations more likely than others. Therefore, an **asperomagnet** has a net spontaneous magnetization. Asperomagnetism appears in those systems in which exchange is positive and the exchange coupling and random anisotropy are of comparable strengths. **Sperimagnetic** order comprises two or more magnetic species with moments of at least one species frozen in random orientations within a hemisphere on one subnetwork and antiferromagnetically coupled to the moments (that have ferromagnetic coupling between them) occupying sites of the other amorphous subnetwork. Sperimagnetism is to ferrimagnetism what speromagnetism is to ferromagnetism except that sperimagnet has a net spontaneous magnetization.

1.6. Low-lying Magnetic Excitations

Having briefly described the types of ground state (i.e., at $T = 0$ K) magnetic order prevalent in spin systems with quenched disorder in the previous section, this section is devoted to the changes in the magnetic order (i.e., **magnetic excitations**) brought about by increasing temperature in crystalline and amorphous **ferromagnets**.

In a crystalline **ferromagnet**, the local deviation from the perfect alignment does not remain confined to a microscopic region of space but propagates like a wave due to exchange coupling between the spins. These low-lying magnetic excitations are called spin-waves. A spin wave can

be thought of as one spin reversal coherently spread over the entire crystal. All the conventional spin-wave theories are based on **localized-electron** picture, in **which** the magnetic electrons are localized on atomic orbitals. However, in metallic systems, the magnetic electrons have itinerant character. Thus, localized-electron and itinerant-electron models form two exactly opposite descriptions of the low-lying magnetic excitations.

1.6.1. Localized-electron Model

Within the framework of the localized-electron model, Felix Bloch [30] was first to introduce the concept of spin waves in a ferromagnet. The spin waves are thermally excited and their energy is quantized. In analogy with a phonon, which represents the particle associated with a quantized lattice wave, the corresponding particle for a quantized spin wave is called a **magnon**. The Hamiltonian that describes the Heisenberg interaction between spins localized at the neighbouring sites i and j . is given by [31,32]

$$\mathcal{H} = -\frac{1}{2} \sum_{ij} J_{ij} \vec{S}_i \cdot \vec{S}_j \quad (1.3)$$

where J_{ij} is the exchange integral. At low temperatures, the spin deviations as well as the fraction of spin reversals are small and spin waves are independent of one another. Thus, in the linear approximation, the magnon dispersion relation for crystalline ferromagnets, in which the direct Heisenberg exchange interaction is confined to the nearest neighbours only, is expressed as [31,32]

$$E(k) = \hbar \omega_k = 2JSz(1 - \gamma_k) \quad (1.4)$$

with

$$\gamma_k = \frac{1}{z} \sum_{\delta} \exp(i\vec{k} \cdot \vec{\delta})$$

where the summation is carried out over z nearest neighbours. In the long wavelength limit, i.e., $|\vec{k} \cdot \vec{b}| \ll 1$, the dispersion relation for simple cubic, fcc, and bcc lattices with lattice constant 'a' takes the form

$$\hbar\omega_k = D k^2 + E k^4 + \dots \quad (1.5)$$

where the spin wave stiffness coefficient $D = 2JSa^2$ is a measure of the exchange interaction and the coefficient E is related to average mean square range of exchange interaction $\langle r^2 \rangle$ through the relation $E = -\langle r^2 \rangle D/20$. The spontaneous magnetization, $M(T, 0)$, at any temperature is given by

$$M(T, 0) = g\mu_B \langle S^z \rangle = g\mu_B (NS - \sum_k n_k) = M(0, 0) - g\mu_B \sum_k n_k$$

where $M(0, 0) = g\mu_B NS$ and n_k is the number of spin waves in thermal equilibrium at temperature T given by the Bose-Einstein distribution function. The final expression for $M(T, 0)$ has the form [31]

$$\Delta m(T, 0) \equiv \frac{[M(0, 0) - M(T, 0)]}{M(0, 0)} = \frac{g\mu_B}{M(0, 0)} \left[\xi\left(\frac{3}{2}\right) \left(\frac{k_B T}{4\pi D}\right)^{3/2} + 15\pi\beta\xi\left(\frac{5}{2}\right) \left(\frac{k_B T}{4\pi D}\right)^{5/2} \right] \quad (1.6)$$

where $\xi(3/2) = 2.612$ and $\xi(5/2) = 1.341$ are the Reimann ξ functions and $\beta = 1/k_B T$. The $T^{3/2}$ and $T^{5/2}$ terms in Eq.(1.6) arise from the k^2 and k^4 terms in the dispersion relation Eq.(1.5), respectively. The higher order terms of the form k^6 , k^8 , etc. in Eq.(1.5), if retained, give rise to additional correction terms [33] to $\Delta m(T, 0)$ that are proportional to $T^{7/2}$, $T^{9/2}$ etc. Application of an external magnetic field (or in the presence of any other fields such as dipolar fields, and so **ropy** fields, etc.) gives rise to an energy gap in the spin-wave spectrum and the dispersion relation gets modified to

$$\hbar\omega_k = g\mu_B H_{eff} + Dk^2 + Ek^4 + \dots \quad (1.7)$$

with $H_{eff} = H - 4\pi N M(0H) + H_A$, where N is the demagnetizing factor, H_A is the anisotropy field and $g\mu_B H_{eff} (= k_B T_g)$ is the energy gap. Consequently, in the presence of magnetic field, the expression for magnetization also gets modified and takes the form [31]

$$\begin{aligned} \Delta m(T, H) &\equiv [M(0, H) - M(T, H)]/M(0, H) \\ &= \frac{g\mu_B}{M(0, H)} \left[Z\left(\frac{3}{2}, t_H\right) \left(\frac{k_B T}{4\pi D}\right)^{3/2} + 15\pi\beta Z\left(\frac{5}{2}, t_H\right) \left(\frac{k_B T}{4\pi D}\right)^{5/2} \right] \end{aligned} \quad (1.8)$$

where the Bose-Einstein integral functions

$$Z(s, t_H) = \xi(s) F(s, t_H) = \sum_{n=1}^{\infty} n^{-s} \exp(-nt_H) \quad (1.9)$$

with

$$t_H = T_g/T = g\mu_B H_{eff}/k_B T \quad (1.10)$$

allow for the energy gap in the spin-wave spectrum.

The spin wave theory discussed so far assumes that the spin waves, when thermally excited, propagate independent of one another so that the superposition of spin waves is a valid approximation. However, as the temperature is increased from low temperatures, the interaction

between spin waves becomes important and these interactions have to be taken into account. Spin-wave interactions are mainly of two types: kinematic interaction and dynamic interaction [31,33]. The kinematic interaction arises due to the fact that the maximum number of spin deviations that can occur at any site carrying a spin S is $2S$. For instance, if $S = 1/2$, two spin deviations cannot reside at the same site and the kinematic interaction, which prevents this situation, is a repulsive one. The dynamic interaction arises because it costs less energy for a spin to suffer a deviation if the neighbouring spins have also undergone deviations. This dynamic interaction is of the attractive type. An analysis of the magnon-magnon interactions in the Heisenberg ferromagnets, due to Dyson [33], has demonstrated that at low temperatures, the kinematic interactions are negligibly small and the dynamic magnon-magnon interactions lead to a thermal renormalization of spin-wave energies [31,33], i.e.,

$$\hbar \omega_k = g \mu_B H_{eff} - D(T) k^2 + \dots \quad (1.11)$$

with

$$D(T) = D(0) (1 - D_{5/2} T^{5/2}) \quad (1.12a)$$

and

$$D_{5/2} = \pi < r^2 > (g \mu_B / M(0,0)) (k_B / 4\pi D(0))^{5/2} \xi(5/2) \quad (1.12b)$$

Moreover, the dynamic interaction gives rise to a T^d correction [33] to $M(T,0)$. In addition to the direct Heisenberg exchange interactions between the spins on the neighbouring d shells, the d spins in the localized model interact indirectly with one another via the conduction electron s spins. This **magnon-electron** interaction also renormalizes the spin wave stiffness coefficient $D(T)$ according to the expression [34]

$$D(T) = D(0) (1 - D_2 T^2) \quad (1.12c)$$

However, the contribution to $D(T)$ arising from the T^2 term in Eq.(1.12c) is several orders of magnitude smaller than that due to the $T^{5/2}$ term in Eq.(1.12a) since the s - d interaction is very weak compared to the direct d - d interaction. Hence, for all practical purposes the spin wave stiffness renormalizes according to Eq.(1.12a) in the localized-electron model.

Spin waves in amorphous ferromagnets :

Ample experimental evidence [35,36] exists in the literature to indicate that amorphous ferromagnets, like their crystalline counterparts, exhibit well-defined long-wavelength **spin-wave** excitations which follow the normal ferromagnetic dispersion relation given by Eq.(1.5) or Eq.(1.7) and the magnetization varies with temperature according to the expression Eq.(1.6) or Eq.(1.8).

However, the magnetization curve for amorphous ferromagnets falls below that of the corresponding crystalline **ferromagnet** and is much steeper. This implies **that** the value of spin wave stiffness for amorphous ferromagnets is *lower* with the result that the spin waves can be easily excited in them. Starting from the **Heisenberg** Hamiltonian and using the quasi-crystalline **ap** proximation, **Kaneyoshi** [13,37] arrived at the following expression for the spin wave energy of an amorphous ferromagnet:

$$E(k) = 2S\rho_o \int J(r_{ij})g(r_{ij})[1 - \exp(-i\vec{k} \cdot \vec{r}_{ij})]d^3r_{ij} \quad (1.13)$$

where $\rho_o = NV$ is the average density, $r_{ij} = |\vec{r}_{ij}| = |\vec{r}_i - \vec{r}_j|$ and $g(r_{ij})$ is the normalized pair correlation function which denotes the probability of finding atoms at the site j when an atom occupies the site i . In the long-wavelength limit, Eq.(1.13) reduces to [13,36,37]

$$E(k) = D k^2 \quad (1.14a)$$

with

$$D = \frac{1}{3} S \int r^2 J(r) F(r) dr \quad (1.146)$$

where $F(T) = 4\pi r^2 \rho_o g(r)$ is the radial distribution function. In amorphous systems, the exchange integral is not constant but fluctuates around a certain average value. $J(r_o)$ such that $J(r) = J(r_o) + \Delta J(r)$. $\Delta J(r)$ the root mean square fluctuation in the exchange integral due to structural disorder. Exchange fluctuations reduce the spin wave stiffness as [36]

$$D = D_o (1 - \delta) \quad (1.15a)$$

with

$$D_o = (1/3) z S J(r_o) \text{ and } S = 2z (\Delta r / r_o) [\Delta J / J(r_o)] \quad (1.156)$$

Similarly, the structural disorder in amorphous **ferromagnets** gives rise to fluctuations in the magnetic moment around a certain average value. Hence, the spin at the site i can be taken as $S_i = S_o + \Delta x_i$. Such fluctuations Δx_i also lead to the diminished value of D and Eq.(1.15a) retains its form with S given by [13,37]

$$\delta = \langle \Delta x_i^2 \rangle_r / S_o^2 \quad (1.15c)$$

Thus, the effect of the fluctuations in the exchange interaction and magnetic moment on the spin wave stiffness constant is to reduce the mean value by a factor $(1 - \delta)$. The factor δ in Eq.(1.15a) has a weak dependence on external field as well as temperature due to a slight variation [13,37] of the second moment $\langle \Delta x_i^2 \rangle_r$ with field and temperature whereas δ arising from $\Delta J(r)$ is independent of field but depends weakly on temperature through the temperature dependence of Ar [36].

1.6.2. Itinerant-electron Model

The itinerant-electron model for magnetism, first proposed by Bloch [38] in connection with the ferromagnetism of an electron gas, was later developed by Slater [39] and Stoner [40] to explain the magnetic properties such as non-integral values of saturation magnetization per atom at 0 K, large coefficients of T term in low temperature specific heat etc., which could not be explained in terms of the localized-electron model. The itinerant-electron model is based on the band theory of electrons in solids and regards magnetic carriers as itinerant or Bloch electrons. The interaction between Bloch electrons splits d —(d) band into spin-up (\uparrow) and spin-down (\downarrow) sub-bands and hence gives rise to ferromagnetism. Wohlfarth, Edwards and coworkers [41-43], while applying the Stoner theory to many ferromagnetic metals, made suitable refinements so as to make it more realistic. However, the basic ideas of Stoner theory remained the same. In the Stoner theory [13,40-43], the exchange interaction between the magnetic electrons is represented by a molecular field, H_m , proportional to the magnetization, i.e.,

$$H_m = \frac{1}{2} n I \zeta \quad (1.16)$$

where n is the number of electrons per atom and $\zeta = M/n\mu_B$ is the relative magnetization so that $n^+ - n^- = n\zeta$ and $n^+ + n^- = n$. Here n^+ and n^- are the number of \uparrow and \downarrow spins per atom, respectively, and I is the Stoner parameter representing the effective interaction between the magnetic electrons. According to this theory, for ferromagnetism to occur, i.e., for $\zeta > 0$, the Stoner criterion

$$I = I N(E_F) > 1 \quad (1.17)$$

must be satisfied, where $N(E_F)$ is the density of states at the Fermi level E_F . When Eq.(1.17) is satisfied, a range of values of I exists such that the relative magnetization at 0 K, Co, can take values of either $\zeta_0 = 1$ or $0 < \zeta_0 < 1$. The cases $\zeta_0 = 1$ and $0 < \zeta_0 < 1$ are realized in strong itinerant and weak itinerant ferromagnets, respectively. The former case arises when spin-up (\uparrow) sub-band is completely filled and Fermi-level lies in the spin-down (\downarrow) sub-band so that further band splitting does not increase the magnetization (Fig. 1.3(a)). The latter one arises when the band splitting is small with the result that none of the spin sub-bands is completely filled and the Fermi level lies in both the sub-bands (Fig. 1.3(b)). The temperature and field dependence of magnetization, $\zeta(T, H)$ obtained from the Stoner equations, is given by the expression [40-43]

$$n^\pm = \frac{1}{2} [n \pm \zeta(T, H)] = \int_0^\infty \frac{N(E) dE}{\exp\{[E - \mu_c \mp (1/2)nI\zeta \mp \mu_B H]/k_B T\}} \quad (1.18)$$

where μ_c is the chemical potential and $\mu_B H$ is the additional term due to the external magnetic field. Eq.(1.18) can be solved for $\zeta(T, H)$ numerically or analytically by eliminating μ_c .

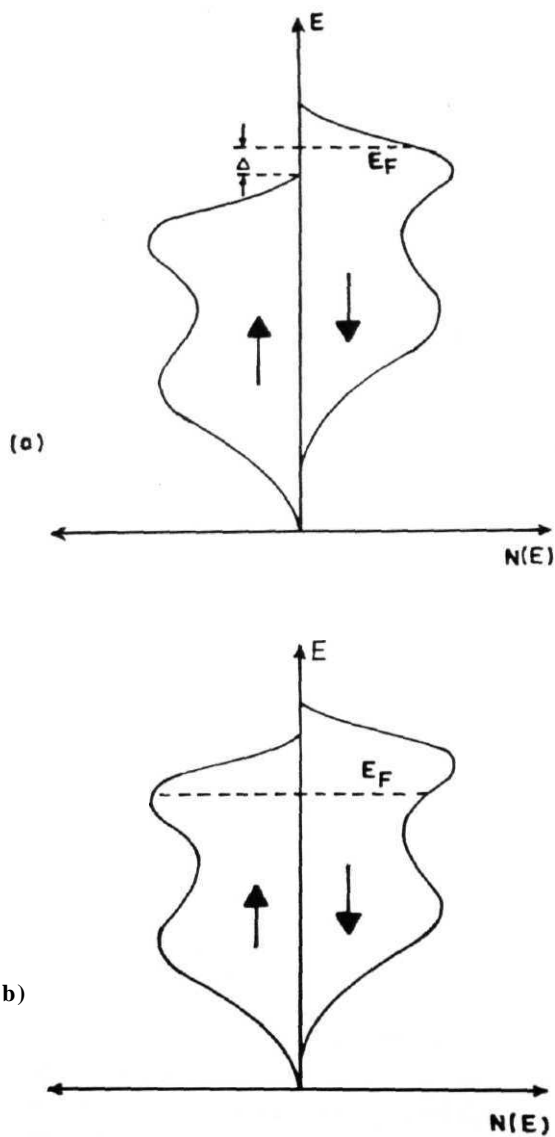


Fig. 1.3 Exchange splitting of energy bands in a (a) strong itinerant ferromagnet and (b) weak itinerant ferromagnet according to the band model.

(a) *Strong itinerant ferromagnetism* ($\zeta_o = 1$) •

In this case, the spontaneous magnetization, $M(T, 0)$, decreases slowly due to excitations of particles from filled spin-up sub-band to partially filled spin-down sub-band (generally known as Stoner single particle excitations). For such excitations, there exists an energy gap A , which is the energy difference between the Fermi level (located in the spin-down sub-band) and the top of the filled spin-up sub-band (Fig. 1.3(a)). At low temperatures, the spontaneous magnetization for strong-itinerant ferromagnets varies with temperature as [41-43]

$$M(T, 0)/M(0, 0) = 1 - A T^{3/2} \exp(-\Delta/k_B T) \quad (1.19)$$

where $M(T, 0) = n\mu_B \zeta(T, 0)$. The effect of external magnetic field is to increase the energy gap further and Eq.(1.19) remains the same except that A has to be replaced by $A + 2\mu_B H$.

(b) *Weak itinerant ferromagnetism* ($\zeta_o < 1$) :

The band splitting in weak itinerant ferromagnets is small and the Fermi level lies in both the sub-bands. This implies that both spin \uparrow and spin \downarrow sub-bands are partially filled (Fig. 1.3(b)) and there is *no energy gap* for single particle excitations from spin \uparrow to spin \downarrow sub-band concomitant with spin reversals. The contribution to thermal demagnetization of spontaneous magnetization due to single particle excitations in weak itinerant ferromagnets has the form [41-43]

$$M(T, 0)/M(0, 0) = [1 - (T/T_C)^2]^{1/2} \quad (1.20)$$

The existence of a significant contribution of Stoner single particle excitations of either strong itinerant type, Eq.(1.19), or weak itinerant type, Eq.(1.20), to the temperature dependence of magnetization in certain temperature ranges has been established experimentally in a large number of ferromagnetic transition metals and alloys. However, at very low temperatures, the magnetization follows the usual $T^{3/2}$ law which cannot be accounted for in the Stoner theory. In addition, Stoner theory fails to predict the proper value of T_C and the Curie-Weiss behaviour of magnetic susceptibility above T_C . Such a failure of the Stoner theory is primarily due to the underlying assumption that the thermally excited electrons and holes move independently in a common mean field. Number of attempts have been made to improve upon the Stoner theory by taking into account the collective nature of the electron-hole excitations with the result that the existence of spin waves as collective excitations and exchange enhanced spin fluctuations [44-48] can now be explained satisfactorily. Essential details of these aspects are given below.

1.6.2A. Spin waves in itinerant-electron model

Spin waves, whose existence could not be envisaged in the band model originally, have subsequently found a natural place in the itinerant electron model, as was first shown by Herring and Kittel [44] in their phenomenological theory of spin waves. In the band model, the collective excitations of particles with a spin reversal, but without a change in wavevector k , are spin waves of wavevector k whereas the individual spin-flip excitations with or without change in wavevector are the single-particle excitations. The spin wave dispersion relation in the long wavelength limit, calculated within the framework of the itinerant-electron model [34,44,45], has the same form as that in the localized-electron model, i.e., Eq.(1.7). However, at finite temperatures, the magnon-magnon interactions and magnon-single particle interactions become important. The effect of these interactions within the itinerant-electron model is to renormalize the spin wave energy through the renormalization of spin wave stiffness coefficient according to the relation [34,44,45]

$$D(T) = D(0) (1 - D_2 T^2 - D_{5/2} T^{5/2}) \quad (1.21)$$

where the parameter $D(0)$ is the value of $D(T)$ at 0 K, and depends on the exchange splitting of spin \uparrow and spin \downarrow sub-bands and on the dispersion relation of the single-particle energies. The dominant T^2 term in Eq.(1.21) arises from magnon-single-particle interactions whereas the $T^{5/2}$ term originates from the magnon-magnon interactions and is much smaller compared to the T^2 term. Hence the $T^{5/2}$ term in Eq.(1.21) is generally neglected and the $D(T)$ varies as T^2 in the itinerant-electron model in contrast with the $T^{5/2}$ variation of $D(T)$ (Eq.(1.21a)) in the localized-electron model.

1.6.2B. Spin fluctuations in itinerant-electron model

Considerable improvement of the Stoner model has been achieved by the inclusion of the spin fluctuation effects [46-48]. Significant advancement in this direction has been made by Moriya and his coworkers [46,47], who treated spin fluctuations within the framework of self-consistent renormalization theory. The major success of Moriya's theory is the prediction of Curie-Weiss behaviour of susceptibility above T_C and a reasonably accurate value for T_C . According to this theory, the spin-wave contribution in weak itinerant ferromagnets, though present at low temperatures, is not as significant as the exchange-enhanced T^2 contribution to magnetization and for temperatures close to T_C , the spin fluctuation contribution dominates and is given by [46,47]

$$[M(T, 0)/M(0, 0)]^2 = [1 - (T/T_C)^{4/3}] \quad (1.22)$$

A refined version of Moriya's theory, due to Lonzarich and Taillefer [48], provides a better quantitative description of the experimental results because it (i) includes the transverse as well as longitudinal local spin-density fluctuations, (ii) incorporates a natural temperature dependent cut-off wavevector for the thermally excited modes and (iii) uses band structure and other parameters appropriate to known weak itinerant ferromagnets like Ni_3Al and MnSi rather than to the special electron gas model, employed earlier by Moriya and Kawabata [47]. This theory predicts that the contributions to magnetization arising from spin wave (SW) excitations and single-particle (SP) excitations plus local spin-density fluctuations (LSF) depend on temperature in accordance with the expressions [48]

$$[M(T,0)/M(0,0)]_{\text{SW}} = 1 - BT^{3/2} \quad (1.23a)$$

at low temperatures and

$$[M(T,0)/M(0,0)]_{\text{SP+LSF}}^2 = 1 - (T/T_C) \quad (1.23b)$$

for a wide range of intermediate temperatures. Furthermore, according to this theory [48], for temperatures close to T_C , the local spin-density fluctuations alone should contribute to $M(T)$ and that this contribution varies with temperature as

$$[M(T,0)/M(0,0)]_{\text{LSF}}^2 = [1 - (T/T_C)^{4/3}] \quad (1.23c)$$

The temperature dependence of magnetization in different temperature ranges predicted by Eqs.(1.23a)-(1.23c) has indeed been observed in a number of weak itinerant ferromagnets [49,50]. Despite the success that the above-mentioned theory [46-50] has enjoyed in accounting quantitatively for essentially all the measured properties of weak itinerant ferromagnets, including magnetization, the spin-fluctuation theory as developed by Moriya and co-workers [46,47] has recently been criticized [51] on the grounds that this theory has too many adjustable parameters and wrongly predicts that the averaged square local moment is an increasing function of temperature above T_C . However, even the theory, due to Hirsch [51], which dispenses with the spin fluctuations and gets rid of the above flaw in Moriya's theory, fails to predict the $T^{4/3}$ dependence of $M^2(T,0)$ observed in many weak itinerant ferromagnets (primarily because the local spin-density fluctuations are completely ignored in this theory).

The theoretical models described so far breakdown completely in the critical region (i.e., for temperatures in the immediate vicinity of the Curie temperature) where critical fluctuations of the order parameter (spontaneous magnetization in the present case) play a crucial role. In the following section, a brief account of the theoretical predictions concerning the behaviour of magnetization, susceptibility and other thermodynamic quantities in this temperature region and for temperatures well above T_C is given.

1.7. Thermal Critical Phenomena

In zero external magnetic field, the **ferromagnetic (FM)-to-paramagnetic (PM)** phase transition at the critical point, T_C , is a second-order phase transition. The spontaneous magnetization, which is the order parameter in this case, goes continuously to zero at T_C with a critical exponent β . The zero-field susceptibility, magnetic part of specific heat and the spin-spin correlation length diverge at T_C with the critical exponents γ, α and $1/\nu$, respectively. These critical exponents are *universal* in the sense that they depend only on the lattice dimensionality, d , and order parameter dimensionality, n , and possess exactly the same values for widely different systems if all of them are described by the same values of d and n [52,53]. From the scaling arguments and using renormalization group (RG) ideas, the total free energy density, $g(T, H)$, consisting of the singular, $g_{sing}(T, H)$ and non-singular, g_o , parts, can be written as [54-56]

$$g(T, H) = g_o(T) + g_{sing}(\epsilon, h) = g_o(T) + |\epsilon|^{2-\alpha} Y_{\pm}(h/|\epsilon|^{\Delta}) \quad (1.24)$$

where the prefactor $|\epsilon|^{2-\alpha}$ in Eq.(1.24) accounts for the shrinkage in volume under the scale transformation which leaves the total free energy invariant, α is the specific heat critical exponent, $\epsilon = (T - T_C)/T_C$, $h = H$ (the ordering field), Δ is the gap exponent and the plus and minus signs refer to temperatures above and below T_C . If the macroscopic volume is set equal to unity, i.e., $V = 1$, the physical quantities such as magnetization, susceptibility and specific heat are straightforwardly obtained from the field and temperature derivatives of $g(T, H)$. Thus, the zero-field specific heat, $C(T, 0)$, magnetization, $M(T, H)$, and the 'in-field' susceptibility, $\chi(T, H)$, are given by the expression [52-56]

$$C(T, 0) = -T (\partial^2 g / \partial T^2)_{H=0} = (1 - \alpha)(2 - \alpha) T_C^{-1} Y_{\pm}(0) |\epsilon|^{-\alpha} (1 + g) \quad (1.25)$$

$$M(T, H) = -(\partial g / \partial H)_T = |\epsilon|^{\beta} f_{\pm}(h/|\epsilon|^{\Delta}) \quad (1.26)$$

and

$$\chi(T, H) = \partial M(T, H) / \partial H = |\epsilon|^{-\gamma} \partial [f_{\pm}(h/|\epsilon|^{\Delta})] / \partial h \quad (1.27)$$

where $\beta = 2 - \alpha - \Delta$, $\gamma = 2 - \alpha - 2\Delta$ and $f_{\pm} = (\partial Y_{\pm} / \partial h)_T$. The 'zero-field' quantities such as spontaneous magnetization, $M(T, 0)$ and 'zero-field' susceptibility, $\chi(T, 0)$, are then obtained by taking the limit $h = H \rightarrow 0$ and expanding $f_{\pm}(h/|\epsilon|^{\Delta})$ in Taylor series around $h = 0$ as

$$f_{\pm}(h/|\epsilon|^{\Delta}) \simeq f_{\pm}(0) + (h/|\epsilon|^{\Delta}) f'_{\pm}(0) + \dots \quad (1.28)$$

Hence one obtains

$$M(T, 0) = m_o |\epsilon|^\gamma \quad \epsilon < 0 \quad (1.29a)$$

$$\chi(T, 0) = (m_o/h_o) |\epsilon|^{-\gamma} \quad \epsilon > 0 \quad (1.29b)$$

where $m_o = f_o(0)$ and $m_o/h_o = f'_o(0)$ are the asymptotic amplitudes for spontaneous magnetization and initial susceptibility, respectively. As $\epsilon \rightarrow 0$, $|\epsilon|^\Delta/h \rightarrow 0$ the scaling-equation-of-state (SES) represented by Eq.(1.26) can be rewritten in a more convenient form [56], i.e.,

$$M(\epsilon, h) = h^{\beta/\Delta} f_o(|\epsilon|/h^{1/\Delta})$$

where f_o is analytic at $|\epsilon| = 0$ and can be directly related to f_- and f_+ . In the limit $|\epsilon|/h^{1/\Delta} \rightarrow 0$, the function $f_o(z)$ can be expanded in a Taylor series around $z = 0$ with the result

$$M(\epsilon, h) = h^{\beta/\Delta} [f_o(0) + (|\epsilon|/h^{1/\Delta})f'_o(0) + \dots]$$

Thus, the critical M versus H isotherm at $|\epsilon| = 0$ is described by the expression

$$M(0, H) = f_o(0) H^{1/\delta} \quad (1.30a)$$

or

$$H = DM^\delta \quad (1.30b)$$

with $A = \beta\delta$ and $D = f_o^{-\delta}$. Furthermore, at $|\epsilon| = 0$ and in the absence of the external magnetic field ($H = 0$), the spin-spin correlation function, defined as $G(r) = \langle S(r) \cdot S \rangle - \langle S \rangle^2$, varies with distance r as [52,53,55,57]

$$G(r) = N |T|^{-(d-2+\eta)} \quad \text{large } |r|; \quad \epsilon = H = 0 \quad (1.31a)$$

where d is the lattice dimensionality and η is the correlation function critical exponent, while the spin-spin correlation length, related to $G(r)$ through the expression $G(r) = \exp(-|r|/\xi(T))/|r|$ as $|r| \rightarrow \infty$, varies in the critical region as [52,53,55,57]

$$\xi(T) = \xi_o^\mp |\epsilon|^{-\nu^\mp}, \quad H = 0. \quad (1.31b)$$

Note that in all the foregoing equations H denotes the field that is obtained by correcting the external magnetic field for the demagnetizing field.

It is customary to determine the critical exponents β and γ from bulk magnetization data taken in external magnetic fields by using a specialized form of the general scaling-equation-of-state (SES), Eq.(1.26), proposed by Arrott and Noakes [58], i.e.,

$$(H/M)^{1/\gamma} = a' \epsilon + b' M^{1/\beta} \quad (1.32)$$

where the coefficients a' and b' are *temperature-independent*. According to the **Arrott-Noakes** SES (Eq.(1.32)), the $M(T, H)$ data taken in the critical region, when plotted in the form of $M^{1/\beta}$ vs. $(H/M)^{1/\gamma}$ (known as the modified Arrott plot) isotherms with the proper choice [57] of β and γ , fall on a set of parallel straight-line isotherms (especially in the high-field region) with the critical isotherm at T_c passing through the origin. The high-field linear portions of these isotherms when extrapolated to $H = 0$ yield intercepts on the ordinate and abscissa from which $M(T, 0)$ and $\chi(T, 0)$ are computed. The $M(T, 0)$ and $\chi(T, 0)$ data so obtained are analyzed in terms of the Eqs.(1.29a) and (1.29b). The 'zero-field' quantities such as $C(T, 0)$, $M(T, 0)$ and $\chi(T, 0)$, when analyzed in terms of single power law expressions (1.25), (1.29a) and (1.29b), yield only the *average* values for the exponents since these expressions are strictly valid for temperatures in the close proximity to T_c whereas the experimental data for such quantities are generally taken over a wide temperature range in the critical region. The exponents obtained in this way not only depend on the temperature range used but also could significantly differ from the true asymptotic values [56,57,59]. The expressions for the quantities $C(T, 0)$, $M(T, 0)$ and $\chi(T, 0)$ must, therefore, include both analytic and non-analytic 'correction-to-scaling' (CTS) terms [53-56,59,60] arising from the nonlinear relevant and irrelevant scaling fields, respectively.

From the generalized magnetic equation of state that takes into account the effect of nonlinear relevant and irrelevant scaling fields, the 'zero-field' quantities $C(T, 0)$, $M(T, 0)$ and $\chi(T, 0)$ are calculated with the result [56,60]

$$C(T, 0) = [(1-\alpha)(2-\alpha)T_c^{-1}Y_{\pm}(0)|\epsilon|^{-\alpha}(1+\epsilon)] [1 + a_{C1}|\epsilon|^{\Delta_1} + a_{C2}|\epsilon|^{\Delta_2} + a_C\epsilon + b_C\epsilon^2 + \dots] \quad (1.33a)$$

$$M(T, 0) = B|\epsilon|^{\beta} [1 + a_{M1}|\epsilon|^{\Delta_1} + a_{M2}|\epsilon|^{\Delta_2} + a_M\epsilon + b_M\epsilon^2 + \dots] \quad (1.33b)$$

and

$$\chi(T, 0) = A_{\chi}|\epsilon|^{-\gamma} [1 + a_{\chi 1}|\epsilon|^{\Delta_1} + a_{\chi 2}|\epsilon|^{\Delta_2} + a_{\chi} \epsilon + b_{\chi}\epsilon^2 + \dots] \quad (1.33c)$$

where the leading non-analytic (analytic) terms $|\epsilon|^{\Delta_1}$ and $|\epsilon|^{\Delta_2}$ (ϵ and ϵ^2) originate from the nonlinear irrelevant (relevant) scaling fields. The **renormalization group (RG)** theories [53-55,60-66] predict that the confluent corrections to the dominant singular behaviour involve only a *single leading* exponent $A = 0.550 \pm 0.016$ (i.e., $A = \Delta_2$ and $\Delta_1 = 0$) for an ordered (crystalline) isotropic 3D Heisenberg ferromagnet whereas such corrections include [63-66] the leading exponent $\Delta_1 = 0.115 \pm 0.009$ in addition to $\Delta_2 = 0.550 \pm 0.016$ for quench-disordered 3D Heisenberg systems. In keeping with the general practice, we discussed the critical behaviour in terms of the linear variables ϵ and h so far. However, as we shall see later, the behaviour of a magnetic system (that undergoes a second-order phase transition) over a wide range of temperatures, which embraces the critical region, is better described in terms of nonlinear variables $\epsilon = (T - T_c)/T = \epsilon/t$ and $h = H/t$ where $t \propto T/T_c$. In analogy with the linear case, free energy density in nonlinear variables is given by [56]

$$g(T, H) = g_o(T) \cdot \tilde{g}_{sing}(\tilde{\epsilon}, \tilde{h}) = g_o(T) \cdot |t| \in |^{2-\alpha} Y_{\pm}(h/| \in |\Delta) \quad (1.34)$$

While the scaling-equation-of-state (SES) assumes a form [56]

$$M(T, H) = M(\tilde{\epsilon}, \tilde{h}) = |\tilde{\epsilon}|^{\beta} \tilde{f}_{\pm}(\tilde{h}/|\tilde{\epsilon}|\Delta) \quad (1.35)$$

similar to its linear counterpart, Eq.(1.25), the Arrott-Noakes (AN) SES gets modified to [56]

$$M^{1/\beta} = a(-\tilde{\epsilon}) + b t^{-1/\gamma} (H/M)^{1/\gamma} \quad (1.36)$$

Unlike the original AN SES (Eq.(1.32)), the modified AN SES, Eq.(1.36). has an additional factor of $t^{-1/\gamma}$ and the coefficients a and b are *temperature-dependent*. The 'zero-field' quantities $C(T, 0)$, $M(T, 0)$ and $\chi(T, 0)$ are obtained from $g(T, H)$ Eq.(1.34), in the same way as in the case of linear variables and the final expressions [56] for these quantities are given below.

Single Power Laws :

$$C(T, 0) = (1 - \alpha)(2 - \alpha) T_C^{-1} \tilde{Y}_{\pm}(0) |\tilde{\epsilon}|^{-\alpha} (1 - \tilde{\epsilon})^2 \quad (1.37a)$$

$$M(T, 0) = m_o |\epsilon|^{\beta} \quad \epsilon < 0 \quad (1.37b)$$

and

$$\chi(T, 0) = (m_o/h_o) |\tilde{\epsilon}|^{-\gamma} \quad \epsilon > 0 \quad (1.37c)$$

With the inclusion of CTS terms :

$$C(T, 0) = A_C |\epsilon|^{-\alpha} [1 + a_{C1} |\tilde{\epsilon}|^{\Delta_1} + a_{C2} |\epsilon|^{\Delta_2} + a_{C\epsilon} + \dots] \quad (1.38a)$$

$$M(T, 0) = B_M |\epsilon|^{\beta} [1 + a_{M1} |\epsilon|^{\Delta_1} + \tilde{a}_{M2} |\epsilon|^{\Delta_2} + a_{M\epsilon} + \dots] \quad (1.38b)$$

and

$$\chi(T, 0) = \tilde{A}_{\chi} |\epsilon|^{-\gamma} [1 + \tilde{a}_{\chi 1} |\epsilon|^{\Delta_1} + \tilde{a}_{\chi 2} |\epsilon|^{\Delta_2} + \tilde{a}_{\chi \epsilon} \dots] \quad (1.38c)$$

The above expressions (Eq.(1.38)), include (only the leading terms) the analytic ($\tilde{\epsilon}$) and non-analytic ($|\epsilon|^{\Delta_i}$) corrections in non-linear variables arising from *nonlinear* relevant and irrelevant scaling fields, respectively. As already mentioned above, in the presence of nonlinear relevant and irrelevant scaling fields, the Arrott-Noakes SES in nonlinear variables has the form [56]

$$M^{1/\beta} = B(-\tilde{\epsilon}) + (B/A) t^{-1/\gamma} (H/M)^{1/\gamma} \quad (1.39)$$

with

$$B \propto [B_M(1 + \tilde{a}_M \tilde{\epsilon})]^{1/\beta} \simeq A_M(1 + \tilde{a}_M \tilde{\epsilon}) \quad (1.40a)$$

and

$$B/A = [B_M(1 + \tilde{a}_M \tilde{\epsilon})]^{1/\beta} [\tilde{A}_\chi(1 + \tilde{a}_\chi \tilde{\epsilon})]^{1/\gamma} \simeq A'(1 + \tilde{a}_\chi \tilde{\epsilon}) \quad (1.40*)$$

$$B \propto [B_M(1 + \tilde{a}_{M1} |\tilde{\epsilon}|^{\Delta_1} + \tilde{a}_{M2} |\tilde{\epsilon}|^{\Delta_2})]^{1/\beta} \simeq \tilde{A}_M(1 + \tilde{a}_{M1} |\tilde{\epsilon}|^{\Delta_1} + \tilde{a}_{M2} |\tilde{\epsilon}|^{\Delta_2}) \quad (1.41a)$$

and

$$\begin{aligned} B/A &= [\tilde{B}_M(1 + \tilde{a}_{M1} |\tilde{\epsilon}|^{\Delta_1} + \tilde{a}_{M2} |\tilde{\epsilon}|^{\Delta_2})]^{1/\beta} [\tilde{A}_\chi(1 + \tilde{a}_{\chi1} |\tilde{\epsilon}|^{\Delta_1} + \tilde{a}_{\chi2} |\tilde{\epsilon}|^{\Delta_2})]^{1/\gamma} \\ &\simeq \tilde{A}'(1 + \tilde{a}_{\chi1} |\tilde{\epsilon}|^{\Delta_1} + \tilde{a}_{\chi2} |\tilde{\epsilon}|^{\Delta_2}) \end{aligned} \quad (1.41b)$$

where the expressions for B ($= a$ in Eq.(1.36)) and B/A ($\equiv b$ in Eq.(1.36)) given by Eq.(1.40) or Eq.(1.41) correspond to the cases when only the relevant scaling fields or the irrelevant scaling fields are present. The important features of the modified Arrott-Noakes SES in nonlinear variables (Eq.(1.39)) are that apart from yielding the true asymptotic critical exponents, it accounts for the temperature variation of the slope of the Arrott plot isotherms commonly observed for a large number of crystalline and amorphous ferromagnets [56,57]; a feature that does not find any explanation in terms of the original AN SES because the coefficients a' and δ' in Eq.(1.32) do not depend on temperature.

Sections 1.6 and 1.7 have mainly dealt with the effect of temperature on magnetization in amorphous ferromagnets. The following section addresses itself to the theoretical developments that have taken place upto now in understanding the magnetic and thermodynamic behaviour of dilute magnets.

1.8. Percolation Critical Behaviour

Percolation concepts were introduced by Broadbent and Hammersley [67] as early as in 1957 and considerable progress has been made since then towards the understanding of percolation phenomena [68-73]. In order to bring out clearly the underlying concept, consider a crystal lattice in which some sites are occupied by particles and the remaining sites are vacant. The nearest neighbour particles, connected by bonds, form finite clusters. As the concentration of particles, p , is gradually increased, the cluster size increases and a concentration, known as the percolation threshold, p_c , is reached at which an infinite cluster (for an infinite lattice)

appears; the infinite cluster extends from one end of the lattice to the other. If the bonds are of conducting type, at p_c the solid is said to be conducting or **percolating**; that the current can now percolate from one side to the other of the lattice. Thus, the percolation threshold p_c marks the transition from finite clusters to an infinite cluster. The transition occurring at the percolation critical point is a second-order phase transition and in antilogy with the thermal critical behaviour, is characterized by *percolation* critical exponents. The order parameter in this case is the percolation probability, $P(p)$, defined as the fraction of occupied sites belonging to the infinite cluster. $P(p)$ is zero for $p < p_c$ and finite for $p > p_c$. The percolation exponents associated with various quantities are defined as follows [68-73].

The mean number of clusters

$$N(p) \sim (p - p_c)^{2-\alpha_p}, \quad (1.42a)$$

percolation probability (order parameter)

$$P(p) \sim (p - p_c)^{\beta_p} \quad p > p_c, \quad (1.42b)$$

mean size of finite clusters

$$S(p) \sim (p - p_c)^{-\gamma_p}, \quad (1.42c)$$

and order parameter at $p = p_c$

$$P(p_c) \sim h^{1/\delta_p} \quad (1.42d)$$

where $\alpha_p, \beta_p, \gamma_p$ and δ_p are the percolation critical exponents and the parameter h , generally known as the ghost field, performs a function similar to that of the magnetic field [70,71]. If $C(r, p)$ is the probability that a site at r is occupied and connected to the site at origin, the connectedness length is given by

$$\xi(p) \sim (p - p_c)^{-\nu_p} \quad (1.42e)$$

A number of physical systems, including the dilute magnetic systems, which are of interest to this thesis, exhibit a percolation behaviour of this type. Magnetic dilution can be achieved in different ways. One way of achieving dilution in magnetic systems is by randomly replacing magnetic atoms on a lattice by non-magnetic ones. This type of magnetic dilution is called the random site-dilution. The Hamiltonian for the random site-diluted magnetic systems can be written as [74]

$$\mathcal{H}_s = -\sum_i \vec{S}_i \cdot \vec{S}_j \eta_i \eta_j \quad (1.43a)$$

where \vec{S}_i is the spin vector at site i , J is the exchange constant and η_i is the uncorrelated site disorder variable which takes values 0 or 1 such that $\langle \eta_i \rangle = p$, where $\langle \rangle$ denotes the configurational average and p is the concentration of magnetic atoms. At this stage, it is necessary to distinguish between two types of disorder; quenched disorder and annealed disorder [74]. In

systems with quenched disorder, the **configurational** averages over spin variables are independent of thermal averages whereas in the case of annealed disorder, the disorder variables are in thermal equilibrium with the system and hence the **configurational** and thermal averages are not independent. The site probability distribution for quenched site-disorder is given by [71]

$$P(\eta_i) = (1 - p) \delta(\eta_i) + p \delta(\eta_i - 1) \quad (1.436)$$

The other way in which a magnetic system can be magnetically diluted is by randomly removing exchange bonds and this type of dilution is known as the random bond-dilution. The Hamiltonian for bond-diluted system is of the form [71]

$$\mathcal{H}_b = -\sum_i \vec{S}_i \cdot \vec{J} \cdot \vec{S}_j \eta_{ij} \quad (1.44a)$$

where the uncorrelated disorder variables η_{ij} are associated with the exchange bonds. The probability distribution for quenched bond-dilution is given by

$$P(\eta_{ij}) = (1 - p) \delta(\eta_{ij}) + p \delta(\eta_{ij} - 1) \quad (1.446)$$

where p is the bond concentration. Quenched dilute magnetic systems exhibit percolation critical phenomena in the vicinity of percolation threshold, p_c , which is the critical magnetic concentration below which only the finite spin clusters are present and no long-range magnetic order exists even for temperatures as low as $T \rightarrow 0$ K. However, for $p > p_c$ an infinite spin cluster (and hence long-range magnetic order) appears. The point $Q(p = p_c, T = 0)$ denoting the percolation critical point for dilute magnets is characterized by percolation critical exponents as defined for pure geometrical percolation earlier. A correspondence or analogy between the quantities associated with critical exponents in pure geometrical percolation and magnetic percolation can be drawn and the same is given below [71].

Geometrical percolation		Magnetic percolation
mean number of clusters	\Longleftrightarrow	zero field free energy
percolation probability (order parameter)	\Longleftrightarrow	spontaneous magnetization (order parameter)
mean size of cluster	\Longleftrightarrow	initial susceptibility
pair connectedness function	\Longleftrightarrow	correlation function
connectedness length	\Longleftrightarrow	spin-spin correlation length

The above correspondence also brings out the similarity between percolation and thermal critical phenomena. Using scaling arguments, the singular part of free energy $f_{\text{sing}}(p, h)$ for the dilute magnetic systems described above with p close to the percolation critical point can be written as [70-75]

$$f_{\text{st},g}(p, h) = q_o |\epsilon_p|^{2-\alpha_p} F_{\pm}(h/|\epsilon_p|^{\Delta_p}) \quad (1.45)$$

where $\epsilon_p = q_1 (p - p_c)/p_c$; $h = H$. The + and - signs refer to $p > p_c$ and $p < p_c$, respectively, and the parameters q_o and q_1 are model-dependent parameters introduced to make $f(p, h)$ a *universal* function. Eq.(1.45) yields the following expressions for the order parameter (i.e., the spontaneous magnetization at 0 K, in the present case) and initial susceptibility:

$$M(p, 0) = \partial f / \partial h = m_p (p - p_c)^{\beta_p} \quad p > p_c \quad (1.46a)$$

and

$$\chi(p, 0) = \partial^2 f / \partial h^2 = \chi_p (p - p_c)^{-\gamma_p} \quad p > p_c \quad (1.46b)$$

where $\beta_p = 2 - \alpha_p - \Delta_p$, $m_p = q_o (q_1/p_c)^{\beta_p} \partial F_{\pm} / \partial h$, $\gamma_p = 2\Delta_p - 2 + \alpha_p$ and $\chi_p = q_o (q_1/p_c)^{-\gamma_p} \partial^2 F_{\pm} / \partial h^2$. The percolation correlation function varies with distance r as

$$C(r, p) \sim r^{-(2-d+\eta_p)} \quad (1.46c)$$

while the associated percolation correlation length, ξ_p , diverges at p_c with an exponent ν_p according to the power law

$$\xi_p(p, 0) \sim (p - p_c)^{-\nu_p} \quad p > p_c \quad (1.46d)$$

Moreover, for $p > p_c$, long-range ferromagnetic order is present in a dilute magnetic system with $J > 0$. For such a system, the spin wave stiffness coefficient, $D(p)$, and the Curie temperature, $T_c(p)$, go to zero as $p \rightarrow p_c$ with the exponents θ_p and ϕ_p , defined as [70-74]

$$D(p) = d_p (p - p_c)^{\theta_p} \quad p > p_c \quad (1.47a)$$

and

$$T_c(p) = t_p (p - p_c)^{\phi_p} \quad p > p_c \quad (1.47b)$$

where the thermal-to-percolation crossover exponent ϕ_p is related to ν_p as $\phi_p = \nu_p/\nu_T$; ν_T is the critical exponent for the thermal correlation length. Another quantity of interest in the percolation phenomena is the macroscopic conductivity, E , in randomly diluted resistor network. In such a network $\Sigma = 0$ for $p < p_c$ and for $p > p_c$, the functional behaviour of E is characterized [70-74] by the exponent σ_p , such that

$$\Sigma(p) = \Sigma_p (p - p_c)^{\sigma_p} \quad (1.48)$$

The conductivity, $E(p)$, of the resistor network is related to the spin-wave stiffness coefficient, $D(p)$, in dilute isotropic ferromagnets through the expression [74]

$$\Sigma(p) = D(p) P(p) \quad (1.49)$$

where $P(p)$ is the percolation probability and using the definitions of $D(p)$, $P(p)$ and $E(p)$ in Eq.(1.49), one obtains the scaling relation

$$\theta_p = \sigma_p - \beta_p. \quad (1.50)$$

The percolation exponents defined above are similar to thermal critical exponents **and** are *universal* in that they do not depend on the details and type of lattice but depend only on the lattice and order parameter dimensionalities.

A complete knowledge of the structure of percolating cluster at threshold is necessary to understand the properties of random systems such as dilute **magnets**, **random** resistor networks etc. In order to study the percolation **behaviour**, three distinctly different models have been proposed for the structure of the percolating cluster at p_c .

(a) Node-link model :

This model was proposed by Skal and Shklovskii [76] and independently by De Gennes [76]. In the node-link picture (Fig. 1.4(a)), the backbone of infinite cluster is considered as a superlattice of small clusters set on nodes which are connected by one-dimensional random paths or links. The average distance between the nodes is the correlation or connectedness length, ξ_p , while the length, L , along the random one-dimensional path between nodes diverges at p_c with an exponent ζ [72,74,77], i.e.,

$$L \sim (p - p_c)^{-\zeta} \quad (1.51)$$

This model predicts that the thermal behaviour of the percolating lattice for $T > 0$ should be that of a collection of one-dimensional chains if $L > \xi_l(T)$ or that of a true d -dimensional system if $L < \xi_l(T)$, where $\xi_l(T)$ is the linear chain thermal correlation length. The node-link model also makes specific predictions about the scaling relations between different exponents [72,74,77], i.e.,

$$\phi_p = \zeta = \nu_p/\nu_T, \quad \theta_p = 2(\zeta - \nu_p) \quad \text{and} \quad \sigma_p = (d - 2)\nu_p + \zeta \quad (1.52)$$

The Skal-Shklovskii-de Gennes model describes the system properly only in dimensions $d > 3$ whereas for $d < 3$, it yields results that are inconsistent with **experimental** findings.

(b) Node-link-blob picture :

The node-link-blob picture for the percolating cluster due to Stanley and Coniglio [78] is an

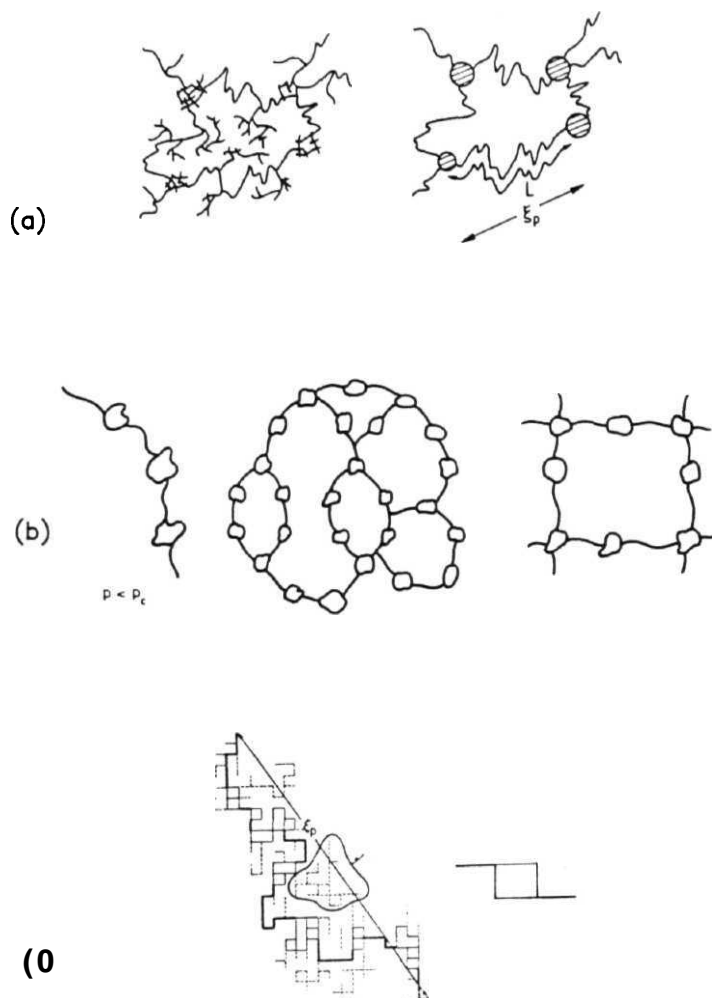


Fig. 1.4 Models for the structure of percolating cluster at threshold: (a) node-link model, (b) node-link-blob model and (c) self-similar fractal model.

improvised version of the node-link picture. In this model, two types of bonds in the backbone of the incipient infinite cluster are distinguished : the links or single bonds, also known as the cutting bonds such that if the link is cut, the cluster breaks into parts, and the multiply connected bonds, which lump together in 'blobs'. The infinite cluster at and above p_c is made up of nodes connected by links and blobs. The blobs are assumed to have self-similar structure. Based on the hierarchical node-link-blob picture (Fig. 1.4(b)) for the infinite cluster, Golden [79] predicts that the conductivity exponent σ_p should obey the inequality, known as the Golden inequality, $\sigma_p < 2$ for $d = 3$. This prediction is consistent with the simulation results.

(c) Self-similar fractal structure :

The word fractal was introduced by Mandelbrot [80] to describe objects with fractal dimension d smaller than the euclidean dimensionality of the underlying lattice [80]. Roughly speaking, if the mass or size 's' of a system varies as (length) ^{d} , then d is called the fractal dimensionality. The infinite cluster is assumed to have a self-similar fractal structure (Fig. 1.4(c)) and using the scaling arguments, the fractal dimensionality d and the spectral or fracton dimensionality \bar{d} are expressed in terms of the percolation exponents [81] as

$$\bar{d} = d - (\beta_p/\nu_p)$$

and

$$\bar{d} = 2(d\nu_p - \beta_p)/(\sigma_p - \beta_p - 2\nu_p) \quad (1.536)$$

Within the framework of the self-similar fractal picture, Alexander and Orbach [81] conjectured that for the infinite percolating cluster at threshold

$$3 = 4/3 \quad (1.53c)$$

independent of the euclidean dimensionality d .

In this and the preceeding sections, a brief resume of the theories existing in the literature about the magnetic behaviour of amorphous ferromagnets was provided. In the next section, a similar survey of the theoretical models proposed so far to understand the transport properties of amorphous metallic alloys is presented.

1.9. Electrical Resistivity in Amorphous Alloys

The behaviour of electrical resistivity of amorphous alloys in general is quite different from that of the corresponding crystalline systems. The salient features of the electrical resistivity

data taken on a large number of metallic glasses are [82-85]:

- (a) The residual resistivities ρ_o of amorphous alloys are considerably larger than those of their crystalline counterparts but similar in magnitude to that of the corresponding liquids.
- (b) The temperature coefficient of resistivity (TCR) is small and usually *positive* for alloys with $\rho_o < 150 \mu\Omega \text{ cm}$ and *negative* for alloys with $\rho_o > 150 \mu\Omega \text{ cm}$. Such a relation between the magnitude of ρ_o and TCR has come to be known as the Mooij correlation [86].
- (c) In a number of alloys, resistivity as function of temperature goes through a minimum at a temperature T_{\min} and resistivity saturates at high temperatures at a value $\sim 150 \mu\Omega \text{ cm}$.

The resistivity minimum in most of the *3d* transition metal-metalloid alloys occurs at temperatures as low as 20 K [82-85, 87,88], but in some transition metal based alloys containing Cr, Mn, Mo, V, W etc., the resistivity minimum is found to occur at temperatures $T \sim 250 \text{ K}$ [82-85,89]. The origin of resistivity minimum is not yet clearly understood. A number of theoretical models have been proposed to explain the resistivity minimum and other characteristic features of resistivity behaviour in amorphous materials. None of these models on its own can describe the variation of resistivity in the entire temperature range. Therefore, assuming the validity of Mathiessen's rule, the contributions to total resistivity arising from different scattering mechanisms are considered to be additive. A brief description of some relevant theoretical models is given below.

1.9.1. Mott s-d scattering model

This model, originally proposed by Mott [90] for transition metals and alloys, assumes that the current is carried by nearly free *s* electrons which are scattered from fluctuations in the local environment (arising from structural disorder) into the vacant states above the Fermi level in the *d*-band. The electrical resistivity is, thus, proportional to $N(E_F)$ the density of *d* states (DOS) at the Fermi level. The temperature dependence of resistivity arises because of the shift in E_F with increasing temperature. The expression for resistivity given by this model is [84,85,90]

$$\rho_{Mott}(T) = \rho(0) \left\{ 1 - \frac{\pi^2}{6} (k_B T)^2 \left[3 \left(\frac{N'(E_F)}{N(E_F)} \right)^2 - \frac{N''(E_F)}{N(E_F)} \right] \right\}$$

where $N'(E_F)$ and $N''(E_F)$ are the first and second energy derivatives of DOS at $E = E_F$, respectively. For the nearly filled *d* - band, the TCR is negative. The energy derivatives of $N(E)$ at E_F for amorphous metals are expected to be extremely small, hence the Mott model when applied to amorphous materials gives a weak temperature dependence of resistivity [85].

1.9.2. Diffraction Model

This model, originally proposed by Ziman [91] for simple liquid metals, is based on the following assumptions [84,85,91]. (a) The electronic transport properties can be described by the **Boltzmann** transport equation, (b) the interaction between the conduction electrons and ions can be described by a pseudo potential and (c) the conduction electrons are assumed to be nearly free and the scattering potential is weak enough to be treated by first-order perturbation theory. Evans et al. [92] extended the Ziman theory to include liquid transition metals by using the muffin-tin potential and arrived at the following expression for resistivity [82,84,85,92,93]

$$\rho \simeq \frac{30\pi^3\hbar^3}{m\epsilon^2k_F^2E_F\Omega} \sin^2[\eta_2(E_F)] S_T(2k_F) \quad (1.55a)$$

where k_F and E_F are the Fermi wavevector and Fermi energy, respectively, Ω is the volume, $\eta_2(E_F)$ is the d partial-wave phase shift describing the scattering of the conduction electrons by the ion-cores which carry a muffin-tin potential centered around each ion position and $S_T(2k_F)$ is the structure factor. The temperature dependence of ρ comes from the temperature dependence of $S_T(2k_F)$. Within the framework of the diffraction model, there are several ways [93] of calculating the $S_T(k)$ however, the one using a Debye spectrum due to Nagel [93] yields the expression

$$S_T(k) \sim 1 + [S_o(k) - 1] e^{-2W_k(T)} \quad (1.55b)$$

where $S_o(k)$ is the static structure factor and $e^{-2W_k(T)}$ is the Debye-Waller factor, with $W_k(T)$ in the Debye approximation given by [87,94]

$$W_k(T) = W_k(0) + 4 W_k(0) \left(\frac{T}{\Theta_D} \right)^2 \int_0^{\Theta_D/T} \frac{z dz}{e^z - 1} \quad (1.56a)$$

with

$$W_k(0) = 3\hbar^2k^2/8Mk_B\Theta_D \quad (1.56b)$$

where M is the atomic mass and Θ_D is the Debye temperature. Substituting Eq.(1.56) in Eq.(1.55), one obtains [87]

$$\rho(T) \simeq \frac{30\pi^3\hbar^3}{m\epsilon^2k_F^2E_F\Omega} \sin^2[\eta_2(E_F)] S_T(2k_F) \left[1 + [S_o(2k_F) - 1] e^{-2[W(T)-W(0)]} \right] \quad (1.57)$$

where $W(T) = W_{2k_F}(T)$ and $W(0) = W_{2k_F}(0)$ are the values of $W_k(T)$ and $W_k(0)$ at $k = 2k_F$ respectively, i.e.,

$$W(0) = 3\hbar^2k_F^2/2Mk_B\Theta_D \quad (1.58)$$

The temperature coefficient of resistivity (TCR), α , can be calculated from Eq.(1.57) as [87]

$$\begin{aligned}\alpha = \frac{1}{\rho} \frac{\partial \rho}{\partial T} &= 2 \left[\frac{1 - S_T(2k_F)}{S_T(2k_F)} \right] \frac{\partial W(T)}{\partial T} \\ &= 8 \left[\frac{1 - S_T(2k_F)}{S_T(2k_F)} \right] \frac{W(0)}{T} \times \left\{ 2 \left(\frac{T}{\Theta_D} \right)^2 \int_0^{\frac{\Theta_D}{T}} \frac{z dz}{e^z - 1} - \frac{1}{e^{\Theta_D/T} - 1} \right\} \quad (1.59)\end{aligned}$$

Eq.(1.59) clearly shows that $\partial W(T)/\partial T > 0$ for all temperatures and hence α is negative if $S_T(2k_F) > 1$ and positive if $S_T(2k_F) < 1$. In other words, negative TCR is expected only when $2k_F$ lies close to k_p , the position of first peak in $S(k)$, whereas a positive TCR is expected when $2k_F$ is far away from k_p . In the low- and high-temperature asymptotic limits, Eq.(1.57) simplifies to

$$\rho(T) \sim C + BT^2 \quad \text{for} \quad T \ll \Theta_D \quad (1.60a)$$

$$\sim C' + B'T \quad \text{for} \quad T \gtrsim \Theta_D \quad (1.60b)$$

where the constants C , B , C' and B' are related to various parameters of Eq.(1.57). Thus, according to the diffraction model, resistivity varies as T^2 at low temperatures and linearly at high temperatures. In order to facilitate a direct comparison with experiments, Eq.(1.57) is written in a different form [87] as

$$\begin{aligned}r(T) = \frac{\rho(T)}{\rho(0)} &= a_1 + a_2 e^{-2[W(T) - W(0)]} \\ &= a_1 + a_2 \exp \left\{ -8W(0) \left(\frac{T}{\Theta_D} \right)^2 \int_0^{\Theta_D/T} \frac{z dz}{e^z - 1} \right\} \quad (1.61a)\end{aligned}$$

with

$$a_1 = \{l + [S_o(2k_F) - 1] e^{-2[W(T) - W(0)]}\} \quad (1.61b)$$

and

$$a_2 = a_1 [S_o(2k_F) - 1] \quad (1.61c)$$

where $T_o = 273.15$ K is the ice temperature.

The diffraction model has been successfully used to describe the electrical resistivity behaviour of a large number of low resistivity ($\rho_o < 150 \mu\Omega$ cm) amorphous alloys. However, the model does not provide an adequate description in the case of high resistivity materials.

1.9.3. Kondo spin-flip model

The model was originally conceived by Kondo [95] to explain the resistivity minimum in dilute crystalline alloys consisting of a non-magnetic host containing a few ppm of magnetic impurities. The scattering of conduction electrons of the host from the localized spin of local magnetic impurities gives rise to spin-dependent increase in the resistivity at low temperatures, which in combination with the contribution to resistivity arising from the usual electron-phonon scattering at high temperatures produces a minimum in the total resistivity of these alloys [84,95]. Using the perturbation theory in the second Born-approximation, Kondo calculated the spin-dependent part of resistivity with the result [84,95]

$$\rho_K(T) = \rho_M [1 + J c \ln(T/T_K)] \quad (1.62)$$

where c is the magnetic impurity concentration, J is the local exchange and T_K is the Kondo temperature defined as $k_B T_K = D$, the conduction band width. When J is negative, the resistivity increases at low temperatures giving rise to negative TCR. The unphysical logarithmic divergence in the original expression for $\rho_K(T)$ Eq.(1.62), was later removed by introducing the concept of spin compensation which asserts that effective local moment decreases with decreasing temperature and finally vanishes at $T = 0$ K. Taking this aspect into account, Hamann [96] obtained a modified expression for the Kondo contribution to resistivity as

$$\frac{\Delta\rho}{\rho} = 1 - \frac{\ln(T/T_K)}{[\ln^2(T/T_K) + S(S+1)\pi^2]^{1/2}} \quad (1.63)$$

The above expression ensures that the resistivity saturates at a finite value at low temperatures. Although the Kondo model is strictly applicable to dilute crystalline materials only, it has been employed to explain the resistivity minimum in a number of amorphous alloys including concentrated magnetic systems with reasonable success. However, certain inconsistencies have surfaced while applying the Kondo model to concentrated amorphous systems [83-85].

1.9.4. Two-level-tunneling model

The observation of resistivity minimum in a large number of amorphous alloys regardless of whether they are magnetic or nonmagnetic has prompted some workers to propose scattering mechanisms which are inherent to the amorphous structure itself. One such model is the two-level tunneling model [97] which is the structural analogue of the Kondo model. The amorphous state is a high energy metastable state and there exist a number of local atomic configurations which are energetically equivalent. Eventhough many of these are not favourable for tunneling,

there exist a significant number of atoms or group of atoms which can tunnel between the states of equivalent energy. In the simplest form, they constitute the two-level systems (TLS) [83-85,97]. The model due to Cochrane et al. [97] considers a potential well with two minima of equal energy and asserts that the electron scattering by such two-level states is analogous to the Kondo scattering. This approach leads to the following expression for the contribution to total resistivity arising from electron-TLS scattering [83-85,97]

$$\rho_{TLS}(T) = -c \ln(k_B^2 T^2 + A^2) \quad (1.64)$$

where A is the energy difference between the two atomic tunneling states and c is a constant whose magnitude depends only on the number of sites and the strength of the coulomb interaction. The tunneling model, thus predicts that the resistivity increases as the temperature is lowered and finally saturates at low temperatures.

1.9.5. Coherent exchange scattering model

Another model, which, like the Kondo model, is applicable to magnetic systems, is the so-called coherent exchange scattering model. This model was proposed by Asomoza et al. [98] to describe the unusual resistivity behaviour of rare earth based amorphous alloys. This model deals with a system in which magnetic ions of angular momenta J_R are coupled to the conduction electron spin S by an exchange interaction of the form

$$\mathcal{H}_{ex} = -\Gamma \sum_R \vec{S}_r \cdot \vec{J}_R \delta(r - R) \quad (1.65a)$$

Using this Hamiltonian, the magnetic contribution to resistivity is calculated within the framework of nearly free-electron model of Ziman, i.e., the diffraction model for the transport properties of liquid metals and amorphous alloys. The exchange scattering contribution to resistivity, obtained by taking into account the interference between the scattered waves from neighbouring magnetic ions, is given by [84,98]

$$\rho_{CES}(T) = c \rho_m [1 + c m(2k_F)] \quad (1.656)$$

with

$$\rho_m = [m^2 k_F^2 J(J+1)] / [4 n e^2 \hbar^3 \pi] \quad (1.65c)$$

where n is the number of conduction electrons per atom, c is the magnetic concentration and $m(2k_F)$ is magnetic structure factor calculated at $k = 2k_F$ and defined as

$$m(2k_F) \sim \sum_j \langle S_j \cdot S_k \rangle \exp[-i(2k_F)(\vec{R}_j - R_k)] \quad (1.65d)$$

The first term in Eq.(1.656), arising from independent scattering by magnetic ions, does not

depend on the magnetic ordering of the system. The second term due to coherent exchange scattering by the neighbouring ions is non-zero at **low** temperatures where the spins are correlated and vanishes **at** high temperatures. The change in resistivity due to magnetic ordering is either positive or negative depending on whether the interference between the scattered waves is constructive, i.e., when $m(2k_F) > 1$ or destructive, i.e., when $m(2k_F) < 1$.

1.9.6. Spin-disorder model

The spin-disorder model, applicable to ferromagnetic materials, deals with the scattering of conduction electrons by spin-waves. The spin-disorder model for amorphous ferromagnets developed by Richter et al. [99], considers a Heisenberg spin system in which spins are localized at the sites of an amorphous network and conduction electrons get scattered from these localized spins (moments) through the $s-d$ exchange interaction. Using the nearly free-electron concept, the magnetic part of resistivity in the spin-wave approximation is given by [87,99]

$$\rho_{SD}(T) = \rho_{SD}(0) \left\{ 1 + \frac{\Omega_C}{(2\pi)^2 S} \Gamma\left(\frac{3}{2}\right) \xi\left(\frac{3}{2}\right) \left(\frac{k_B T}{D_{SW}}\right)^{3/2} + \frac{1}{J_S(2k_F)} \left[\frac{\pi^2}{3S} \left(\frac{k_B T}{D_{SW}}\right)^2 - F(T) \right] \right\} \quad (1.66a)$$

with

$$\rho_{SD}(0) = (2\Omega_C/3 h^3) [(\Omega/N_e e) m S J_{sd}]^2 J_S(2k_F) \quad (1.66b)$$

where N_e is the number of electrons, f_c and Ω are the atomic and sample volumes, respectively, S is the spin of local atomic magnetic moment, D_{sw} is the spin wave stiffness coefficient, T and ξ are the gamma and Riemann zeta functions, respectively, J_{sd} is the exchange coupling constant and $J_S(2k_F) = \int_0^{2k_F} k^3 S_m(k) dk$; $S_m(k)$ is the static magnetic structure factor. The $T^{3/2}$ term in Eq.(1.66a) is the net result of a partial cancellation of two competing $T^{3/2}$ terms; one arising from *incoherent* (momentum non-conserving) electron-magnon scattering and increasing with increasing temperature, and the other originating from the *elastic* scattering of conduction electrons from randomly oriented temperature-dependent local moments and decreasing with increasing temperature, whereas the T^2 term in Eq.(1.66a) is the *coherent* electron-magnon scattering term. The function $F(T)$, arising because of structural disorder, constitutes only a minute correction to the T^2 term indicating thereby that the coherent electron-magnon scattering is not significantly altered by the presence of quenched disorder. $\rho_{SD}(0)$ and the $T^{3/2}$ term both go to zero for crystalline ferromagnets but possess finite values in the case of amorphous ferromagnets. In addition, the coefficient of the $T^{3/2}$ term in amorphous magnets is expected to be roughly two orders of magnitude [99] larger than that of T^2 term. Thus, the spin-disorder model predicts that at low temperatures, $\rho_{SD}(T)$ should vary as $T^{3/2}$ in amorphous ferromagnets in contrast with the T^2 variation in crystalline systems [87,99].

1.9.7. Quantum corrections to the resistivity

In highly disordered systems, the motion of electrons at low temperatures is *diffusive* rather than *ballistic* [85] and this realization has prompted many workers [100-103] to propose quantum corrections to the normal Boltzmann conductivity arising from enhanced electron-electron interaction (EEI) effects and Quantum interference (QI) or weak localization (WL) effects. The conduction electrons in disordered systems with high values of resistivity undergo more frequent collisions than in crystalline systems. Such an increased scattering reduces the effective electronic screening and hence enhances the electron-electron interactions. The enhanced electron-electron interaction gives rise to an additional contribution to conductivity, which can be expressed as [101]

$$\Delta\sigma_{EEI}(T) = [\sigma(T) - \sigma(0)]_{EEI} = \left(\frac{e^2}{4\pi^2\hbar} \right) \frac{1.294}{\sqrt{2}} \left(\frac{4}{3} - \frac{3}{2}\bar{F}_\sigma \right) \left(\frac{k_B T}{\hbar D} \right)^{1/2} \quad (1.67a)$$

with

$$\bar{F}_\sigma = (32/3F) \left[\left(1 + \frac{1}{2}F \right)^{3/2} - \frac{3}{4}F - 1 \right] \quad (1.67b)$$

where F is the average static screened coulomb interaction potential over the Fermi surface and D is the diffusion constant. Eq.(1.67a) rewritten in the following form represents the EEI contribution to resistivity

$$\frac{\rho_{EEI}(T)}{\rho_{EEI}(0)} = 1 - \rho_{EEI}(0) \left(\frac{1.294}{\sqrt{2}} \right) \left(\frac{4}{3} - \frac{3}{2}\bar{F}_\sigma \right) \left(\frac{k_B T}{\hbar D} \right)^{1/2} \quad (1.68)$$

The contribution to total resistivity due to the electron-electron interaction is thus proportional to \sqrt{T} .

In addition, the electrons in disordered systems undergo multiple scattering and the electron mean free path is of the order of the interatomic spacing. At low temperatures, these collisions are elastic, and hence the electron wave functions retain their phase over large distances. Therefore, there exists a finite probability for two partial waves of the electron, originating from a point (origin) and propagating in opposite directions on a given path, to return to the origin in phase and interfere constructively. In other words, the multiple elastic scattering leads to a phase coherence between partial waves scattered from nearby ions and hence enhances the probability for an electron to return to its origin. The electron localization gives rise to high resistivity in disordered materials. If the disorder is strong enough, the electrons get completely localized leading to a **transition from** metallic to the insulating state. However, if the disorder is not sufficiently strong, the above-mentioned weak localization or quantum interference effects become important. As the temperature is increased from absolute zero, the inelastic electron-phonon scattering tends to destroy the phase coherence and thereby leads to an increase in **conductivity**.

In addition, a number of other scattering processes such as inelastic **electron-magnon scatter** **ing**, external magnetic field and **Zeeman** splitting of spin sub-bands can also **destruc** the phase coherence and delocalize electrons. The final expression for the contribution to total resistivity arising from weak localization in the presence of spin-orbit and inelastic scattering and including the splitting of spin sub-bands, is given by [102-104]

$$\rho_{WL}(T) = \rho_{WL}(0) \left[1 - \rho_{WL}(0) \left(\frac{e^2}{2\pi^2\hbar} \right) \left(\frac{e}{c\hbar} \right)^{\frac{1}{2}} (3\sqrt{B_2} - \sqrt{B_\phi}) \right] \quad (1.69a)$$

with

$$B_2 = B_{ie} + \frac{2}{3}B_{so} + \frac{4}{3}B_s \quad (1.69b)$$

$$B_\phi = B_{ie} + 2B_s \quad (1.69c)$$

where $B_j = (e\hbar/4\pi D\tau_j)$; $j = ie, so, s, \phi$ and $\tau_\phi, \tau_{ie}, \tau_{so}$ and τ_s are the phase coherence, inelastic scattering, spin-orbit scattering and spin scattering times, respectively. If $B_{so} < B \ll B_{ie}$, Eq.(1.69) reduces to

$$\rho_{WL}(T) = \rho_{WL}(0) \left[1 - \rho_{WL}(0) \left(\frac{e^2}{2\pi^2\hbar} \right) (D\tau_{ie})^{-1/2} \right] \quad (1.70)$$

In the case of inelastic electron-phonon interaction, the relaxation time τ_{ep} varies as $\tau_{ep}^{-1} \propto T^p$ (where p ranges between 2 and 4) for $T < \Theta_D$ and $\tau_{ep}^{-1} \propto T$ for $T > \Theta_D$. Thus, the variation of resistivity due to weak localization effects is of the form

$$\rho_{WL}(T) \propto -T^{p/2} \quad \text{for } T < \Theta_D \quad (1.71a)$$

$$\rho_{WL}(T) \propto -\sqrt{T} \quad \text{for } T > \Theta_D \quad (1.71b)$$

The temperature dependences of $\rho_{WL}(T)$ and $PEEI(T)$ due to weak localization and electron-electron interaction effects predicted by Eqs.(1.71) and (1.68), respectively, have been found in a number of metallic glasses [85,105].

1.10. Aim and Scope of the Thesis

Amorphous (a-) $Fe_{90+y}Zr_{10-y}$ and $Fe_{90-x}Co_xZr_{10}$ alloys have attracted considerable attention during recent years because they exhibit widely different but interesting physical phenomena [106]. The novel physical phenomena that these alloys exhibit are: weak itinerant-electron **ferromagnetism** [106], invar effect [107], broad distribution of magnetic hyperfine fields with finite probability even at zero fields [108-112] and electrical resistivity minima at temperatures close to T_C [113]. Moreover, the alloys with $y = 0, 1$ and $0 < x < 4$ present an additional feature

[106,111,114-118] in that a transition to a *spin-glass (SG)-like* state, known as reentrant (RE) state, occurs at a temperature T_{RE} , which lies well below the paramagnetic (PM) to ferromagnetic (FM) phase transition (Curie) temperature, T_C . The PM-FM, PM-SG and FM-RE phase transition lines for $a - Fe_{90 \pm y}Zr_{10 \mp y}$ alloys meet at 93 at.% Fe. The nature of the reentrant state and the transition to such a state remained controversial (due to the conflicting results reported in the literature) until recently when the direct observation of magnetic domains even in the RE state by Lorentz electron microscopy [119] and Kerr-effect method [120] as well as the neutron depolarization measurements [121] coupled with magnetic and Mossbauer results [118] unambiguously demonstrated that the reentrant state is a mixed state in which cluster spin-glass order coexists with long-range ferromagnetic order and that the transition to such a state is *not a true* thermodynamic phase transition.

Failure to detect any propagating features in the inelastic neutron scattering experiments [122] on $a - Fe_{91}Zr_9$ at any temperature $T < T_C$ within the momentum transfer range $0.05 \text{ \AA}^{-1} < q < 0.12 \text{ \AA}^{-1}$ has been interpreted as a total absence of spin waves in $a - Fe_{90+y}Zr_{10-y}$ alloys. However, detailed analysis of spontaneous magnetization data [123] on $a - Fe_{90+y}Zr_{10-y}$ alloys revealed that spin wave excitations are mainly responsible for thermal demagnetization at low temperatures, while single-particle excitations plus local spin-density fluctuations (LSF) and LSF dominantly contribute to the decrease of magnetization in the intermediate temperature range and for temperatures close to T_C , respectively. A similar type of conflicting reports have also been made for $a - Fe_{90-x}Co_xZr_{10}$ alloys. While early *BM* study [106] on the $a - Co_{90}Zr_{10}$ alloy (which does not exhibit reentrant behaviour at low temperatures and behaves like a conventional ferromagnet down to the lowest temperature [106]) provides strong evidence for weak-itinerant ferromagnetism in this alloy, the recent low-temperature specific heat measurements [124] on $a - Fe_{90-x}Co_xZr_{10}$ alloys indicate that the Co-rich alloys, including $a - Co_{90}Zr_{10}$, behave like strong-itinerant ferromagnets. These contradictions have been the main motivating factors for a detailed study of the low-lying magnetic excitations in $a - Fe_{90+y}Zr_{10-y}$ and $a - Fe_{90-x}Co_xZr_{10}$ alloys.

In addition, the FM-PM phase transition in the above mentioned amorphous alloy series has given rise to much controversy [116,125] in the recent years because the early *BM* data [126,127] taken in the critical region yielded values for the spontaneous magnetization and 'zero-field' susceptibility critical exponents β and γ that are 1.4 times larger than those theoretically predicted for an isotropic 3D Heisenberg ferromagnet. These unphysically large exponent values have been taken to reflect large fluctuations in the exchange interactions and a transition to the spin glass state directly at T_C . Subsequent analysis of new high-precision *BM* data [125,128] on $a - Fe_{90}Zr_{10}$ and reanalysis of earlier *BM* data [125] on $a - Fe_{91}Zr_9$ and $a - Fe_{92}Zr_8$ alloys as well as the *ac* susceptibility results [125,129] revealed that the values of the critical exponents β , γ and δ (exponent for the critical isotherm) are close to the theoretically predicted estimates for 3D Heisenberg ferromagnets. This raises serious doubts about the genuineness of

the unphysically large exponent values reported [127] for $a - Fe_{90-x}Co_xZr_{10}$ alloys. Moreover, the exponent values reported earlier in the literature are only the *effective* exponents and not the true *asymptotic* values that the theory predicts. This necessitated a detailed study of thermal critical behaviour in $a - Fe_{90+y}Zr_{10-y}$ and $a - Fe_{90-x}Co_xZr_{10}$ alloys.

The thermal critical behaviour associated with the FM-PM phase transition at T_C had been extensively studied experimentally in a number of amorphous as well as crystalline systems. By comparison, a similar study of percolation behaviour near the critical concentration or percolation threshold, p_c (at which PM-FM, PM-SG and FM-RE phase transition lines meet) has received little or even no attention for various reasons. While dilute magnets with quenched disorder have long been regarded as model systems [73] to study percolation critical behaviour, the sole attempt [130] to experimentally determine the percolation exponents for such systems reported in the literature is plagued with thermal-to-percolation crossover effects. All the theoretical models, proposed so far to describe percolation phenomena, treat site- or bond-percolation on a regular crystalline lattice and assume [70-75] the validity of the famous Harris criterion even in the strong disorder limit to describe the percolation critical behaviour of quenched random site- or bond-diluted ferromagnets. Furthermore, the nature of magnetism in $a - (Fe_pNi_{1-p})_{80}(B,Si)_{20}$ and $a - (Fe_pNi_{1-p})_{80}P_{14}B_{16}$ alloys is not clearly understood as conflicting results with regard to strong or weak itinerant ferromagnetism in these alloys exist in the literature (as was the case for the $a - Fe_{90-x}Co_xZr_{10}$ alloys too). In order to test the validity of the predictions of existing percolation theories and to resolve the controversy surrounding the nature of magnetism in these alloys, a detailed study of low-lying magnetic excitations and percolation critical behaviour in them was undertaken. The main reasons for the choice of these alloy systems for the intended type of study are : (i) unlike amorphous $Fe - Zr$ alloys, these alloys exhibit the critical concentration p_c on the Fe -poor side, (ii) Ni atoms in them carry negligibly small moment [131] and hence act as magnetic dilutents (i.e., essentially quenched random site-dilution occurs when Fe is progressively replaced by Ni), (iii) the thermal correlation length in $(Ni - Fe)$ -metalloid alloys diverges at T_C even for compositions close to p_c [132], (iv) the thermal critical behaviour for concentrations close to p_c in these alloy systems has already been exhaustively studied [57,59,133], and (v) inelastic neutron scattering experiments have revealed that well-defined spin wave excitations [134] exist for $p > p_c$ in such systems.

The electrical resistivity [113,135-137] in $a - Fe_{90+y}Zr_{10-y}$ and $a - Fe_{90-x}Co_xZr_{10}$ alloy systems as a function of temperature goes through a minimum at temperatures $T_{min} \approx T_C \approx 250$ K compared to that ($T_{min} \sim 12$ K) in amorphous 3d transition metal-metalloid alloys. A large temperature range below T_{min} in these alloys, therefore, facilitates a detailed study of the effect of enhanced electron-electron interaction, weak localization or quantum interference and magnetic excitations such as magnons, single particle excitations and local spin-density fluctuations (LSF) on the temperature dependence of electrical resistivity. Moreover, such an investigation enables us to ascertain whether a 'one-to-one' correspondence exists between the

results of BM and electrical resistivity measurements so far as the magnetic excitations in these alloys is concerned.

Keeping the above remarks in mind, the main objectives of this thesis are:

- (i) To make an in-depth study of low-lying magnetic excitations in a - $Fe_{90+y}Zr_{10-y}$, - $Fe_{90-x}Co_xZr_{10}$ and - $(Fe_pNi_{1-p})_{80}(B, Si)_{20}$ and a - $(Fe_pNi_{1-p})_{80}P_{14}B_{6}$ alloys.
- (ii) To investigate the thermal critical behaviour of a - $Fe_{90+y}Zr_{10-y}$ and a - $Fe_{90-x}Co_xZr_{10}$ alloys in detail.
- (iii) To test the validity of the predictions based on the percolation theories and to determine percolation exponents for three-dimensional quenched random site-diluted ferromagnets.
- (iv) To identify the various scattering mechanisms responsible for resistivity minima in a - $Fe_{90+y}Zr_{10-y}$ and a - $Fe_{90-x}Co_xZr_{10}$ alloys and to determine their relative magnitudes.

In order to achieve the above mentioned objectives, experimental probes such as bulk magnetization, ferromagnetic resonance and electrical resistivity were chosen. Apart from the introduction chapter, the thesis contains four chapters. The second chapter deals with the experimental details whereas the remaining three chapters describe the present results and discuss them under the headings Low-lying magnetic excitations, Thermal and Percolation critical behaviour, and electrical resistivity. Each of these three chapters is self-contained in the sense that following a thorough discussion of the relevant experimental results, the conclusions are summarized and the references cited are listed at end of each chapter.

References

- [1] A.I. Gubanov, Sov. Phys. Solid State 2, 468 (1960).
- [2] P. Duwez and S.C.H. Lin, J. Appl. Phys. 38, 4096 (1967).
- [3] P. Duwez, in *Glassy Metals I*, edited by H. -J. Giintherodt and H. Beck (Springer-verlag, Berlin, 1981) p.19.
- [4] F.E. Lubrosky, in *Ferromagnetic Materials*, edited by E.P. Wohlfarth (North-Holland, Amsterdam, 1980) vol. 1 p. 451.
- [5] T. Mizoguchi, A.I.P. conf. Proc. 34, 286 (1976).
- [6] *Glassy Metals I*, edited by H.-J. Giintherodt and H. Beck (Springer-Verlag, Berlin, 1981).
- [7] *Glassy Metals II*, edited by H.-J. Giintherodt and H. Beck (Springer-Verlag, Berlin, 1983).
- [8] *Amorphous Magnetic Alloys*, edited by F.E. Lubrosky (Butterworths, London 1983).
- [9] K. Handrich and S. Kobe, *Amorphous ferro- and ferri-magnetika* (Akademie Verlag, Berlin, 1980).
- [10] *Glassy Metals: Magnetic, Chemical and Structural Properties*, edited by R. Hasegawa (CRC, Boca Raton, Florida, 1983).
- [11] K. Moorjani and J.M.D. Coey, *Magnetic Glasses* (Elsevier, Amsterdam, 1984).
- [12] T. Kaneyoshi, *Amorphous magnetism* (CRC press, Boca Raton 1984).
- [13] T. Kaneyoshi, *Introduction to Amorphous magnets* (World Scientific, Singapore, 1992).
- [14] T. Egami, Rep. Prog. Phys. 47. 1601 (1984).
- [15] P. Hansen, in *Handbook of Magnetic Materials*, edited by K.H. J. Buschow (North-Holland, Amsterdam, 1991) vol.6, p.292.
- [16] A.R. Ferchmin and S. Kobe, *Amorphous Magnetism and Metallic Magnetic Materials - Digest, Selected topics in Solid State Physics*, Vol.17 (North-Holland, Amsterdam, 1983).
- [17] S. Kobe, A.R. Ferchmin and S. Sostrach, Landolt-Bornstein, New Series group III, Vol.19/h (Springer-Verlag, Berlin, 1991).
- [18] M. Von Allmen, in *Glassy Metals II*, edited by H.-J. Giintherodt and H. Beck (Springer-Verlag, 1983) p.261.

- [19] R. Glang, in *Handbook of thin film technology*, edited by L.I. Maissel and R. Clang (Mc Graw Hill, New York, 1970).
- [20] *Thin film Processes, Part II*, edited by J.L. Vossen and W. Kern, (Academic press, New York, 1978).
- [21] A. Ali, W.A. Grant and P.J. Grundy, *Phil. Mag.* **337**, 335 (1978).
- [22] A. Bernner, D.E. Cocich and E.K. Williams, *J. Res. Nat. Bur. Std.* 109 (1950).
- [23] W.L. Johnson, M. Atzmon, M. Van Renssum, B.P. Dolgin and X.L. Yeh, in *Rapidly Quenched Metals*, edited by S. Steeb and H. Warlimount (Elsevier, North-Holland, New York, 1985) p.1515.
- [24] J. Wong, in *Glassy Metals I*, edited by H.-J. Güntherodt and H. Beck (Springer-Verlag, Berlin, 1981) chapter 4.
- [25] S.N. Kaul, in *Lecture Notes*, workshop on Glassy materials held at IUC-DAEF, Indore, India (1994).
- [26] G. A. Petrakovskii, *Sov. Phys. Usp* 24, 511 (1981).
- [27] M.C. Chi and R. Alben, *A.I.P. Conf. Proc.* 34, 316 (1976).
- [28] H. Fujimori, in *Amorphous Magnetic Alloys*, edited by F.E. Lubrosky (Butterworths, London, 1983) p.300.
- [29] C.M. Hurd, *Contemp. Phys.* **23**, 469 (1982).
- [30] F. Bloch, *Z. Physik*, 61, 206 (1930).
- [31] F. Keffer, in *Encyclopaedia of Physics*, edited by H.P.J. Wijn (Springer, Berlin, 1966) Vol. XVIII, part 2, p.1.
- [32] C. Kittel, in *Quantum theory of Solids* (John Wiley & Sons, New York, 1963).
- [33] F.J. Dyson, *Phys. Rev.* **102**, 1217, 1230 (1956).
- [34] T. Izuyama and R. Kubo, *J. Appl. Phys.* 35, 1074 (1964).
- [35] S.N. Kaul, *Phys. Rev. B* **27**, 5761 (1983) and the references cited therein.
- [36] S.N. Kaul, *Phys. Rev. B* 24, 6550 (1981) and the references cited therein.
- [37] T. Kaneyoshi, *J. Phys. Soc. Jpn.* 45, 1835 (1978), *J. Phys. C* 5, 3504 (1972).
- [38] F. Bloch, *Z. Physik*. 57, 545 (1929).
- [39] J.C. Slater, *Phys. Rev.* 49, 537 (1936).

- [40] E.C. Stoner, *Proc. Roy. Soc. A* **165**, 372 (1938); *A* **169**, 339 (1939).
- [41] E.P. Wohlfarth, *J. Appl. Phys.* **39**, 1061 (1968); *Inst. Phys. Conf. Series* **55**, 165 (1980); *Handbook of Ferromagnetic Materials*, Vol.1. **1** (1980); *J. Magn. Magn. Mater.* **45**, 1 (1984).
- [42] D.M. Edwards and E.P. Wohlfarth, *Proc. Roy. Soc. A* **303**, 127 (1968).
- [43] E.D. Thomson, E.P. Wohlfarth and C. Bryan, *Proc. Phys. Soc.* **83**, 59 (1964).
- [44] C. Herring and C. Kittel, *Phys. Rev.* **81**, 869 (1951); C. Herring, *Phys. Rev.* **85**, 1003 (1952); *ibid* **87**, 60 (1952).
- [45] J. Mathon and E.P. Wohlfarth, *Proc. Roy. Soc. A* **302**, 409 (1968).
- [46] T. Moriya, *J. Magn. Magn. Mater* **31-34**, 10 (1983); *ibid* **14**, **1** (1979).
- [47] T. Moriya and A. Kawabata, *J. Phys. Soc. Jpn.* **34**, 639 (1973); *ibid* **35**, 669 (1973).
- [48] G. G. Lonzarich and L. Taillefer, *J. Phys. C* **13**, 4339 (1985).
- [49] T. Moriya, *Spin Fluctuations in Itinerant Electron Magnetism* (Springer-verlag, Berlin, 1985).
- [50] S.G. Mishra, *Mod. Phys. Lett. B* **4**, 83 (1990).
- [51] J.E. Hirsch, *Phys. Rev. B* **40**, 2354, 9061 (1989); S. Tang and J.E. Hirsch, *Phys. Rev. B* **42**, 771 (1990); J.E. Hirsch, *Phys. Rev. B* **43**, 705 (1991); *ibid* **44**, 675 (1991).
- [52] H.E. Stanley, *Introduction to Phase Transitions and Critical Phenomena* (Clarendon Press. Oxford. 1971).
- [53] S.K. Ma, *Modern Theory of Critical Phenomena* (W.A. Benjamin, Inc. London, 1976).
- [54] F.J. Wegner, *Phys. Rev. B* **5**, 4529 (1972); in *Phase Transitions and Critical Phenomena*, edited by C. Domb and M.S. Green (Academic Press, New York, 1976) Vol.6, p.7.
- [55] M.E. Fisher, *Rev. Mod. Phys.* **46**, 597 (1974).
- [56] S.N. Kaul, *Phase Transitions* **47**, 23 (1994) and references cited therein.
- [57] S.N. Kaul, *J. Magn. Magn. Mater.* **53**, 5 (1985).
- [58] A. Arrott and J.E. Noakes, *Phys. Rev. Lett.* **19**, 786 (1967).
- [59] S.N. Kaul, *Phys. Rev. B* **38**, 9178 (1988).
- [60] A. Aharony and M.E. Fisher, *Phys. Rev. B* **27**, 4394 (1983).

- [61] A. Aharony, in *Phase Transitions and Critical Phenomena* edited by C. Domb and M.S. Green (Academic Press, New York, 1976) Vol.6, p.357.
- [62] L.C. Le Guillou and J. Zinn-Justin, *Phys. Rev. B* **21**, 3976 (1980).
- [63] T.C. Lubensky, *Phys. Rev. B* **11**, 3573 (1975).
- [64] G. Grinstein and A. Luther, *Phys. Rev. B* **13**, 1329 (1976).
- [65] G.Jug, *Phys. Rev. B* **27**, 609 (1983).
- [66] A. Weinrib and B.I. Halperin, *Phys. Rev. B* **27**, 413 (1983).
- [67] S.R. Broadbent and J.M. Hammersley, *Proc. Camb. Phil. Soc.* **53**, 639 (1957).
- [68] V.K.S. Shante and S. Kirkpatrick, *Adv. in Phys.* **20**, 325, (1971).
- [69] S. Kirkpatrick, *Rev. Mod. Phys.* **45**, 574 (1973).
- [70] D. Stauffer, *Phys. Rep.* **54**, 1 (1979); in *Introduction to Percolation Theory* (Taylor & Francis, London, 1985); D. Stauffer and A. Aharony, *Introduction to Percolation Theory* (Taylor & Francis, Bristol, 1991).
- [71] J.W. Essam, *Rep. Prog. Phys.* **43**, 833 (1980); in *Phase Transitions and Critical Phenomena*, edited by C. Domb and M.S. Green (Academic Press, London, 1972) Vol.2, p.197.
- [72] Michael J. Stephen, *Lecture Notes in Physics: Critical Phenomena*, edited by F.J.W. Hahne (Springer-Verlag, Berlin, 1983) Vol.186, p.259.
- [73] Articles by D.J. Thouless, S. Kirkpatrick and T.C. Lubensky, in *Ill-Condensed Matter*, edited by R. Balian, R. Maynard and G. Toulouse (North-Holland, Amsterdam, 1979) p.1, 321,405.
- [74] R.B. Stinchcombe, in *Phase Transitions and Critical Phenomena*, edited by C. Domb and J.L. Lebowitz (Academic Press, London, 1983) p.151.
- [75] T.C. Lubensky, *Phys. Rev. B* **15**, 311 (1977); A. Aharony, in *Multicritical Phenomena*, edited by R. Pynn and A. Skjeltorp (Plenum Press, 1984), NATO ASI series Vol.106. p.309.
- [76] A.S. Skal and B.I. Shklovskii, *Sov. Phys. Semicond.* **8**, 1029 (1975); P.G. de Gennes, *J. Phys. (Paris) Lett.* **37**, **L1** (1976).
- [77] T.A.L. Ziman, *J. Phys. C* **12**, 2645 (1979).
- [78] H.E. Stanley, *J. Phys. A* **10**, L211 (1977); A. Coniglio, *Phys. Rev. Lett.* **46**, 250 (1981); *J. Phys. A* **15**, 3829 (1982).

- [79] K. Golden, Phys. Rev. Lett. 65, 2923 (1990).
- [80] B.B. Mandelbrot, *Fractals, Form, Chance and Dimension* (Freeman, San Francisco, 1977).
- [81] S. Alexander and R. Orbach, J. Phys. (Paris) Lett. 43, L625 (1982); R. Rammal and G. Toulouse, J. Phys. (Paris) Lett. 44, L13 (1983).
- [82] P.J. Cote and L.V. Meissel, in *Glassy Metals I*, edited by H.-J. Güntherodt and H. Beck (Springer-Verlag, Berlin, 1983), p.141.
- [83] R. Harris and J.O. Strom-Olsen. in *Glassy Metals II*, edited by H.-J. Giintherodt and H. Beck (Springer-Verlag, Berlin. 1983), p.325.
- [84] K.V. Rao, in *Amorphous Magnetic Alloys*, edited by F.E. Lubrosky (Butterworths, London, 1983) p.401.
- [85] J.S. Dugdale, Contemp. Phys. 28, 547 (1987); M.A. Howson and B.L. Gallagher, Phys. Rep. **170**, 265 (1988).
- [86] J.H. Mooij, Phys. Stat. Sol. A 17, 321 (1973).
- [87] S.N. Kaul, W.H. Kettler and M. Rosenberg, Phys. Rev. B **33**, 4987 (1986); S.N. Kaul, W.H. Kettler and M. Rosenberg. Phys. Rev. B **35**, 7153 (1987).
- [88] S.N. Kaul and M. Rosenberg. Key Engg. Mater. **13-15**, 475 (1987).
- [89] B. Sas, J. Toth, A. Lovas and G. Konczos, Key Engg. Mater. **13-15**, 493 (1987).
- [90] N.F. Mott, Phil. Mag. 26, 1249 (1972).
- [91] J.M. Ziman, Phil. Mag. 6, 1013 (1961).
- [92] R. Evans, D.A. Greenwood and P. Lloyd, Phys. Lett. A **35**, 57 (1971); A **38**, 151 (1972).
- [93] S.R. Nagel, Phys. Rev. B 16, 1694 (1977); P.J. Cote and L.V. Meissel Phys. Rev. Lett. 39, 102 (1977); K. Frobose and J. Jackie, J. Phys. F 7, 2331 (1977).
- [94] J.M. Ziman, *Principles of Theory of Solids* (Cambridge Univ., England, 1972) p.64.
- [95] J. Kondo, *Solid State Physics* Vol.23, edited by F. Seitz, D. Turnbull and H. Ehrenreich (Academic Press, New York, 1969), p.184.
- [96] D.R. Hamann, Phys. Rev. **158**, 570 (1967).
- [97] R.W. Cochrane, R. Harris, J.O. Strom-Olsen and M.J. Zuckerman, Phys. Rev. Lett. **35**, 676(1975).
- [98] R. Asomoza, LA. Campbell, A. Fert, A. Leinard and J.P. Rebouillat, J. Phys. F 9, 349 (1979).

- [99] R. Richter, **M. Wolf** and F. Goedsche, Phys. Stat. Sol. **B 95**, 475 (1979); R. Richter and F. Goedsche, Phys. Stat. Sol. **B 123**, 143 (1984).
- [100] E. Abrahams, P.W. Anderson, D.C. Licciardello and T.V. **Ramakrishnan**, Phys. Rev. Lett. **42**, 673 (1979).
- [101] B.L. Altshuler and A.G. Aronov, in *Electron-Electron Interactions in Disordered Systems*, edited by F.L. Efros and **M. Pollak** (Elsevier, New York, 1985) p.1.
- [102] P.A. Lee and T.V. Ramakrishnan, Rev. Mod. Phys. **57**, 287 (1985).
- [103] G. **Begmann**, Phys. Rep. **107**, 1 (1984).
- [104] H. **Fukuyama** and K. Hoshimo, J. Phys. Soc. Jpn. **50**, 2131 (1981).
- [105] G. **Thummes**, J. Kotzler, R. Ranganathan and R. **Krishnan**, Z. Phys. B 69, 489 (1988); A. Das and A.K. **Majumdar**, Phys. Rev. B **43**, 6042 (1991).
- [106] S.N. **Kaul**, Phys. Rev. B **27**, 6923 (1983) and references cited therein.
- [107] K. Shirakawa, S. Ohnuma, M. Nose and T. Masumoto, IEEE Trans. Magn. 16, 910 (1980); S. Ohnuma, K. Shirakawa, M. Nose and T. **Mosumoto**, IEEE Trans. Magn. 16, 1129 (1980).
- [108] H. Yamamoto, H. Onodera, K. Hosoyama, T. Masumoto and H. Yamauchi, J. Magn. Magn. Mater. **13-34**, 1579 (1983).
- [109] H. Tange, K. **Inoue** and K. Shirakawa, J. Magn. Magn. Mater. **54-57**, 303 (1986).
- [110] J.A. Heller, E.F. **Wassermann**, M.F. Brawn and R.A. Brand, J. Magn. Magn. Mater. **54-57**, 307 (1986).
- [111] D.H. Ryan, J.M.D. Coey, E. Batalla, Z. Altounian and J.O. Ström-Olsen, Phys. Rev. B **35**, 8630 (1987).
- [112] S.N. Kaul, C. Bansal, T. **Kumaran** and M. Havalgi, Phys. Rev. B 38, 9248 (1988).
- [113] Y. Obi, **L.C. Wang**, R. Motsay, D.G. Onn and M. Nose, J. Appl. Phys. **53**, 2304 (1982).
- [114] H. Hiroyoshi and K. **Fukamichi**, J. Appl. Phys. **53**, 2226 (1980).
- [115] N. Saito, H. Hiroyoshi, K. Fukamichi and Y. Nakyawa, J. Phys. F: Met. Phys. 16, 911 (1986).
- [116] S.N. Kaul, J. Appl. Phys. 61, 451 (1987).
- [117] **J.M.D. Coey**, D.H. Ryan and R. Buder, Phys. Rev. Lett. 58, 385 (1987).
- [118] S.N. Kaul, V. Siruguri and G. Chandra, Phys. Rev. B **45**, 12343 (1992).

- [119] S. Hadjoudji, S. Senoussi and I. Mirebeau, *J. Magn. Magn. Mater.* **93**, 136 (1991) and references cited therein.
- [120] A. Fork], R. Reisser and H. Kronmüller, in *Proc. of the Symposium on magnetic properties of amorphous metals*, edited by A. Hernando, V. Madurga, M.C. Sanchez-Truyillo and M. Vazquez (Norht-HoUand, Amsterdam, 1987).
- [121] I. Mirebeau, S. Itoh, S. Missuda, F. Watanabe, Y. Endoh, M. Hennion and P. Calmethes, *Phys. Rev. B* **44**, 5120 (1991).
- [122] G.E. Fish and J.J. Rhyne, *J. Appl. Phys.* **61**, 454 (1987).
- [123] S.N. Kaul, *J. Phys.:Condens. Matter* **3**, 4027 (1991).
- [124] M. Rosenberg, U. Hardebush, H. Schone-Warnefeld, R. Wernhardt and K. Fukamichi, *J. Phys. F* **18**, 259 (1988).
- [125] S.N. Kaul, *J. Phys.: F* **18**, 2089 (1988).
- [126] H. Yamamuchi, H. Onodera and H. Yamamoto, *J. Phys. Soc. Jpn.* **53**, 747 (1984).
- [127] K. Winschuh and M. Rosenberg, *J. Appl. Phys.* **61**, 4401 (1987).
- [128] R. Reisser, M. Fanhle and H. Kronmüller, *J. Magn. Magn. Mater.* **75**, 45 (1988).
- [129] S.N. Kaul, A. Hofmann and H. Kronmüller, *J. Phys.* **F16**, 365 (1986).
- [130] P. Majumdar, S.M. Bhagat and A. Manheimer, *J. Magn. Magn. Mater.* **54-57**, 271 (1986); *J. Appl. Phys.* **57**, 3479 (1985).
- [131] S.N. Kaul, *IEEE Trans. Magn.* **MAG-17**, 1208 (1981).
- [132] J.A. Tarvin, G. Shirane, R.J. Birgeneau and H.S. Chen, *Phys. Rev. B* **17**, 241 (1978); M. B. Salamon and A.P. Murani, *J. Appl. Phys.* **55**, 1688 (1984).
- [133] S.N. Kaul and M. Sambasiva Rao, *J. Phys.:Condens. Matter* **6**, 7403 (1994); M. Sambasiva Rao and S.N. Kaul, *J. Magn. Magn. Mater.* (1995) to be published; M. Sambasiva Rao, Ph.D. Thesis (unpublished, 1995).
- [134] R.J. Birgeneau, J.A. Tarvin, G. Shirane, E.M. Gyorgy, R.C. Sherwood, H.S. Chen and C.L. Chien, *Phys. Rev. B* **18**, 2192 (1978).
- [135] K. Shirakawa, K. Fukamichi, T. Kaneko and T. Masumoto, *J. Phys.* **F14**, 1491 (1984).
- [136] P. Pureur, W.H. Schreiner, J.V. Kunzler, D.H. Ryan and J.M.D. Coey, *Solid State Commun.* **65**, 163 (1988).
- [137] Ch.V. Mohan, P.D. Babu, M. Sambasiva Rao, T. Lucinski and S.N. Kaul, *Proc. Solid State Phys. Symposium (India)* **32C**, 44 (1989).

CHAPTER 2 EXPERIMENTAL DETAILS

2.1. Sample Preparation and Characterization

Amorphous (a-) $Fe_{90+y}Zr_{10-y}$ ($y = 0, 1$), $Fe_{90-x}Co_xZr_{10}$ ($x = 0, 1, 2, 4, 6, 8$, and 10), $(Fe_pNi_{1-p})_{80}B_{19}Si_1$ ($0.0625 < p < 0.20$), $(Fe_pNi_{1-p})_{80}B_{20}$ ($0.25 < p < 1.0$) and $(Fe_pNi_{1-p})_{80}P_{14}B_{6}$ ($0.1125 < p < 1.0$) alloys were prepared under inert (high purity Argon) atmosphere by single-roller melt-quenching technique in the form of long ribbons of ~ 1 - 2 mm width and 30 - 40 μm thickness. The amorphicity of these samples was verified by Mo $K\alpha$ x-ray diffraction and high-resolution electron microscopy techniques. A detailed compositional analysis, carried out using JEOL JCS four crystal (wave length dispersive) spectrometer, revealed no deviation from the nominal Fe [or (Fe, Ni)] concentration over a 10 cm long ribbon of a given alloy within the resolution (0.1 at.%) of the spectrometer. All the samples (compositions) in the alloy series $Fe_{90-x}Co_xZr_{10}$, $(Fe_pNi_{1-p})_{80}(Si)_{20}$ and $(Fe_pNi_{1-p})_{80}P_{14}B_6(Fe_{90+y}Zr_{10-y})$ were prepared and characterized at the Institute for Experimental Physics VI, Ruhr University, Bochum (Institute of Physics, Max-Planck Institute for Metal Research, Stuttgart), Germany.

2.2. Bulk Magnetization Measurements

Bulk magnetization measurements were performed using Vibrating Sample Magnetometer in the temperature range $70K$ to $450A$ in external magnetic fields up to 15 kOe. However, due to the lack of low temperature facilities at the home institution, magnetization measurements at lower temperatures were carried out **elsewhere** on experimental set-ups such as the SQUID magnetometer and Faraday Balance. The relevant details concerning the principle and operation of these **set-ups** are given below.

2.2.1. Vibrating Sample Magnetometer

Principle :

The Vibrating Sample Magnetometer (VSM) was first developed by Simon Foner [1] and independently by Van Oosterhout [2]. The underlying principle [1-4] of VSM is that a magnetic dipole placed in an external static magnetic field and undergoing sinusoidal oscillation induces

an electrical signal in suitably located pickup coils. The induced signal, which is at the frequency of dipole oscillation, is proportional to the magnetic moment, amplitude and frequency of oscillation. If the amplitude and frequency of oscillation are kept constant, the induced signal is proportional to the magnetic moment alone.

Experimental Set-up :

The block diagram of EG & G Princeton Applied Research VSM Model 4500 system used in the present work is shown in Fig. 2.1. The VSM system consists of a microprocessor based VSM controller unit, temperature controller, electromagnet capable of producing magnetic fields up to ± 20 kOe and a bipolar *dc* power supply (maximum current ± 65 A dc, at, 130 V). The *ar* drive signal from VSM controller drives the transducer located above the magnet, which, in turn, transmits vibrations to the sample through the sample holder assembly. That the amplitude and frequency of vibration remain constant is ensured by means of a feedback mechanism involving a vibrating capacitor arrangement. The vibrating capacitor located just beneath the transducer generates an *ac* signal that depends solely on the amplitude and frequency of vibration and is fed back to the VSM controller where it is compared with the drive signal so as to maintain constant drive output. This *ac* control signal is also phase-adjusted and routed to the signal demodulator in which it serves as reference drive signal. Thus, the feedback mechanism ensures that both the amplitude and frequency of vibration remain constant. The output signal due to the magnetic moment of the specimen induced in the pickup coils (located at the center of the pole pieces) is detected by means of lock-in phase detector housed in the VSM controller. The hall probe placed between the pole pieces of the electromagnet forms a part of the Gaussmeter which measures the external magnetic field strength at the sample site. The VSM controller, which has a provision to control the bipolar *dc* power supply, can either sweep the field at any constant rate or maintain it stable at any given value.

A variation in sample temperature in the ranges from 70 K to 300 K and $300 \text{ K} < T < 1100$ K is achieved by using a liquid nitrogen (N_2) cryostat and a high-temperature oven assembly, respectively.

Liquid Nitrogen Cryostat :

The cross-sectional view of the commercial liquid (L) N_2 cryostat (Model 153N, Janis Research, USA) is shown in Fig. 2.2(a). It consists of a vacuum insulated sample chamber in which the sample holder assembly vibrates. The sample is cooled by cold N_2 gas (obtained by boiling LN_2 with the help of a heater located in the reservoir) that enters the sample chamber

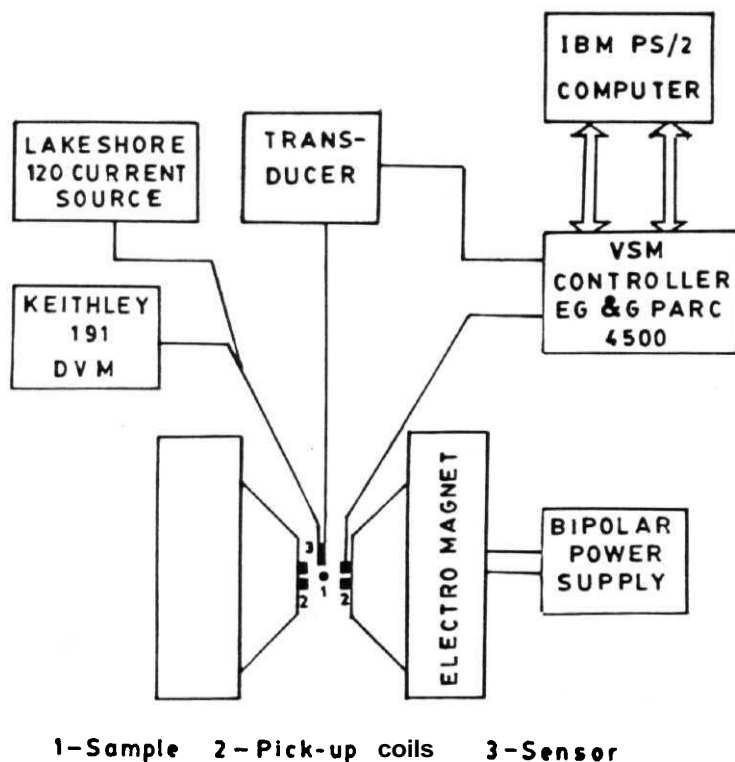


Fig. 2.1 Block diagram of the Vibrating Sample Magnetometer.

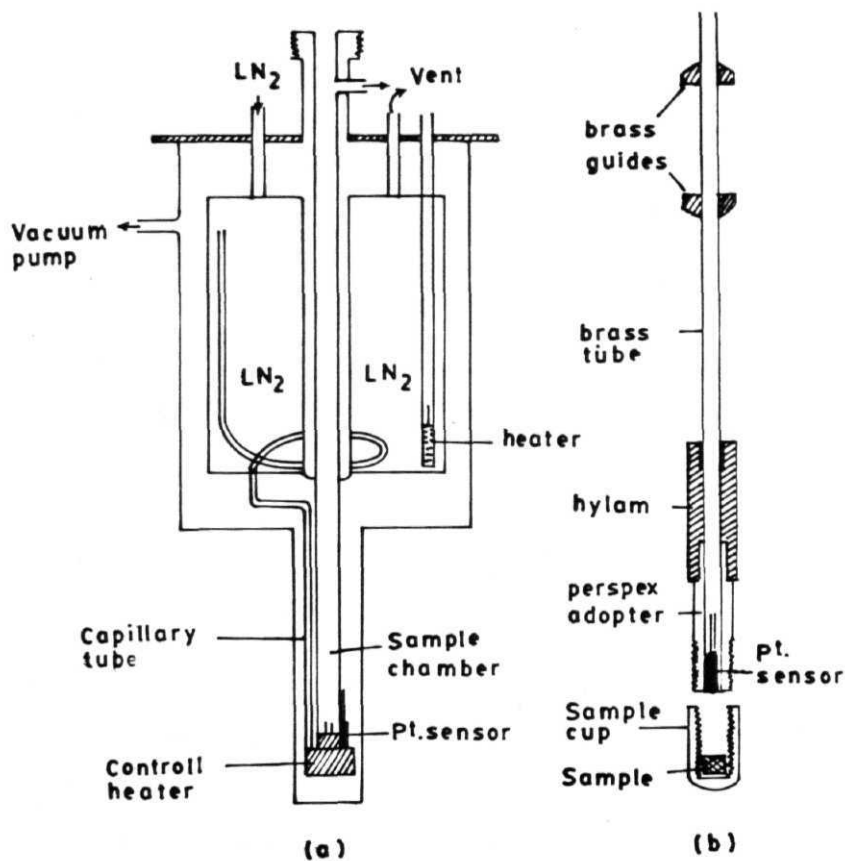


Fig. 2.2 Schematic diagrams of the (a) liquid nitrogen cryostat and (b) low-temperature sample holder assembly for VSM.

through a small connecting tube. Another heater located at the bottom of the sample tube through which cold N_2 gas enters the sample zone is used to control the sample temperature. A platinum sensor (PT 103) mounted on this heater serves as a control sensor. Since this sensor is located some distance away from the sample, the sample temperature could be considerably different from that indicated by the controlling sensor.

Sample holder assembly :

In order to monitor the sample temperature accurately, a sample holder shown in Fig. 2.2(6), whose design ensures that the platinum sensor is in very good thermal contact with the sample, has been fabricated. The sample holder designed for use at low temperatures consists of a brass tube, 75 cm in length, connected to a hylam tube of 15 cm length (4 mm outer and 2 mm inner diameter) which, in turn, is joined to a perspex adopter. This adopter houses a precalibrated platinum (PT 103) sensor whose tip is in body contact with the sample when the perspex sample cup containing the sample is screwed on to this adopter. Small holes have been drilled at the bottom of the cup as well as on its sides at different locations close to the sample site so that the sample is in direct thermal contact with the cold N_2 vapour. A proportional and integral (PI) temperature controller (Model 805, Lake Shore Cryogenics, USA) facilitates temperature control over the range $70\text{ K} < T < 300\text{ K}$. Sample temperature is monitored by sending an excitation current of 1 mA through the precalibrated platinum sensor and the sensor voltage is measured with the help of the Keithley 191 digital voltmeter.

High-temperature Oven and sample-holder assembly :

Temperatures above 300 K are obtained with the help of a high-temperature oven assembly (Model 151H, EG&G PARC, USA). Temperature of the heater, located inside the oven, is measured by means of a Chromel-Alumel thermocouple and controlled by the temperature-controller card of the VSM controller. The sample temperature is accurately measured by a precalibrated Copper-Constantan thermocouple which finds itself in the high-temperature sample holder assembly. The sample holder consists of a brass tube, a quartz rod extension and a boron nitride adapter. The sample is placed in a boron nitride sample cup, which is screwed on to the boron nitride adapter. The hot junction of the Copper-Constantan thermocouple is inserted into the sample cup through a small hole drilled at the bottom of the sample cup so that it is in physical contact with the sample. The thermo-emf developed between the hot and cold (kept fixed at the ice point) thermocouple junctions and measured with the help of a Keithley 191 digital voltmeter (DVM), then determines the sample temperature.

2.2.2. Measurements using Vibrating Sample Magnetometer

Several strips of amorphous alloy ribbons, all of 2.5 mm length and 1-2 mm width, were stacked one above the other after a thin layer of Apeizon N grease was applied in between them to ensure a good thermal contact between the ribbon strips. The sample in the form of a stacked bundle was placed in the sample holder assembly and rotated such that the field lies within the ribbon plane and is directed along the length of the ribbons. This arrangement minimizes the demagnetizing effects.

Determination of demagnetization factor :

In order to determine the demagnetization factor, magnetization as a function of field in the range -100 Oe to +100 Oe has been measured at a temperature ($T \sim 90$ K) well below the Curie temperature (T_c) for all alloy compositions under investigation. In the demagnetization-limited region, i.e., in the low field region where the external magnetic field (H) is completely balanced by the demagnetizing field ($= 4\pi NM$), the internal field, H_i , given by the expression $H_i = H - 4\pi NM$, goes to zero so that $M = (1/4\pi N)H$. Thus, at low fields the M vs. H curve is linear (Fig. 2.3) and inverse slope of this straight line yields the demagnetization factor N .

Determination of Curie temperature using the kink-point method :

In order to arrive at a reasonably accurate estimate of the Curie temperature T_c , magnetization (M) as a function of temperature (T) at a constant but low value of the applied field (typically $H \sim 10$ Oe) has been measured for $a - Fe_{90+y}Zr_{10-y}$ ($y = 0, 1$) and $a - Fe_{90-x}Co_xZr_{10}$ ($x = 0, 1, 2, 4$ and 6) alloys. Such a plot of M vs T at $H = 10$ Oe for $a - Fe_{91}Zr_9$ shown in Fig. 2.4, is representative of all the alloys in question. It is noticed from this figure that magnetization remains nearly constant for temperature below T_c and decreases abruptly beyond a certain temperature corresponding to the *kink*. The plateau in the M vs T curve for $T < T_c$ is the manifestation of the exact cancellation of the external field by the demagnetizing field, as already mentioned above, since in this case $M = H/4\pi N$. The temperature corresponding to the intersection of the tangents drawn to the $M(T)$ curve on either side of the kink determines the T_c to an accuracy of ± 1 K.

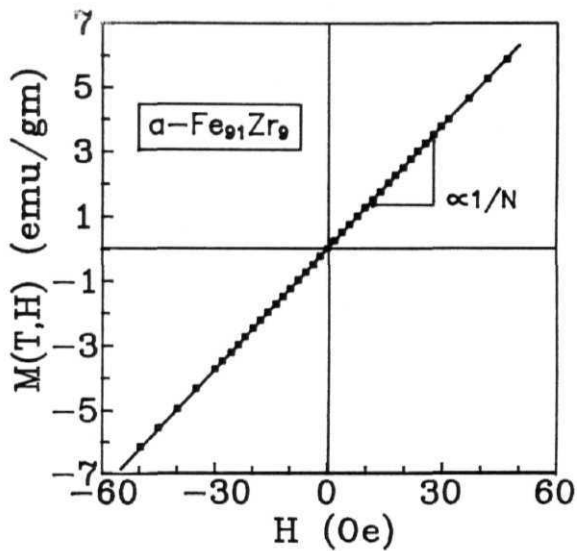


Fig. 2.3 M vs. H at low fields.

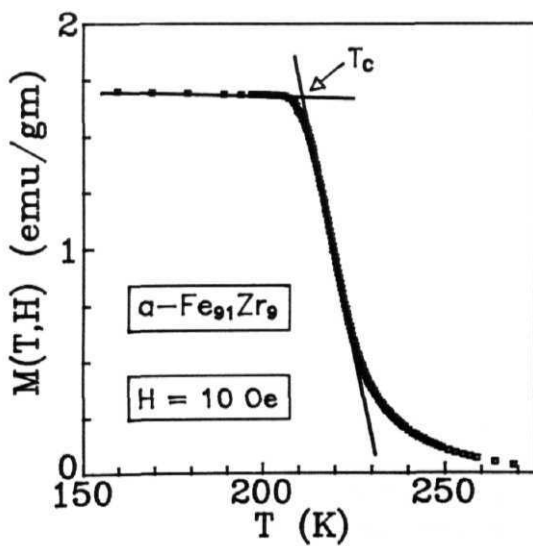


Fig. 2.4 Low-field magnetization as a function of temperature; kink-point measurement.

M vs. H isotherms :

M vs. H isotherms in fields up to 15 kOe were measured on $a - Fe_{90+y}Zr_{10-y}$ ($y = 0, 1$) and $a - Fe_{90-x}Co_xZr_{10}$ ($x = 0, 1, 2, 4 \& 6$) alloys at 1 K (2 K for $x = 2, 4 \& 6$) intervals outside the critical region and at 0.2 K intervals in the critical region ($\sim T_C \pm 15$ K). The temperature interval at which the isotherms were recorded was gradually increased to 5 K for temperatures well above T_C . The isotherms were obtained by measuring $M(T, H)$ at 55 predetermined fixed field values (stable to within ± 1 Oe) in the range $0 < H < 15$ kOe. The relative accuracy in the measurement of the magnetic moment was 5×10^{-5} emu and the temperature stability was better than ± 25 mK (± 40 mK) for $T < 300$ K ($T > 300$ K). The magnetization measurements were extended to temperatures beyond 300 K only for the alloys with $x = 4$ and 6 since their Curie temperatures exceed the room temperature. Now that for the alloy with $x = 6$, T_C possesses as high a value as 375 K and its crystallization temperature (as for other compositions in the alloy series in question) being ~ 750 K, before proceeding with the type of measurements mentioned above, the sample of this alloy was annealed at 450 K for different durations of time till no shift in T_C was observed in the 'kink-point' measurement. This procedure ensured that the specious effects due to structural relaxation did not contaminate the magnetization data taken in the critical region. The *M vs. H* isotherms were measured by controlling the VSM controller remotely by a personal computer through GPIB IEEE 488 interface.

2.2.3. SQUID Magnetometer

Principle :

Superconducting quantum interference device (SQUID) is used to determine the magnetic moment of a material in a SQUID magnetometer. The SQUID response signal is a periodic function of the magnetic flux. The period of this function equals the flux quantum. The magnetic moment due to the specimen is measured by monitoring the change in flux through the pickup coil as the specimen is moved through the pickup coil. The controlling electronics sends a dc current through another coil in the feed back loop to offset the change in field at SQUID and the voltage output is directly proportional to the feed back current. Therefore, the change in field at the main pick-up coil is read as an output voltage from the SQUID controlling electronics, i.e., $\Delta V_{SQUID} \propto \Delta \Phi$, where Φ is the magnetic flux through the pick-up coil. The pick-up coil is wound in a second order gradiometer configuration (Fig. 2.5(a)) so as to measure only $\partial^2 H / \partial z^2$ and higher gradients. This configuration rejects any response due to change in uniform field or change in its first order derivative. A typical SQUID voltage response as the specimen is moved through the SQUID coils, is shown in Fig. 2.5(b). The magnetic moment

SECOND—DERIVATIVE COIL CONFIGURATION

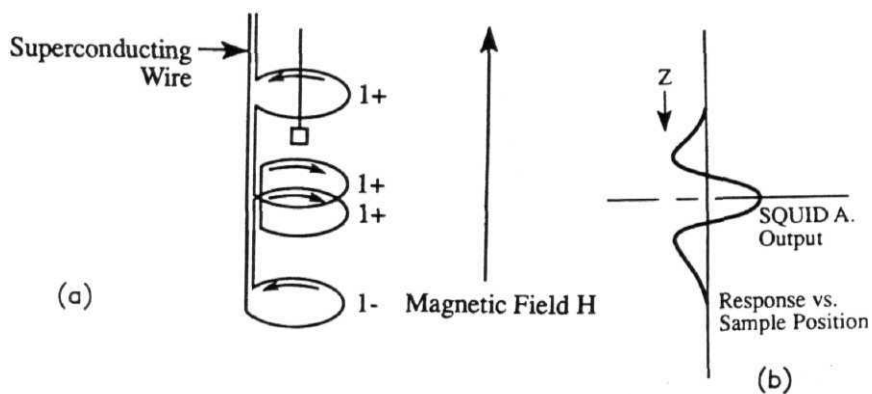


Fig. 2.5 SQUID pick-up coils the second-derivative configuration (b) SQUID response as the sample is moved through the coils.

of the specimen is then obtained from this SQUID response curve with the help of various algorithms. The SQUID magnetometer used in the present work is a completely automated, computer controlled and software driven system of Model MPMS7 from Quantum Design.

Measurements with SQUID :

Bulk magnetization as a function of temperature at a constant external magnetic field of $H = 10$ kOe was measured for $a - \text{Fe}_{90+y}\text{Zr}_{10-y}$ ($y = 0, 1$) and $a - \text{Fe}_{90-x}\text{Co}_x\text{Zr}_{10}$ ($x = 0, 1, 2, 4, 6, 8 \text{ \& } 10$) alloys at 1 K intervals in the temperature range $5 \text{ K} < T < 350 \text{ K}$ using the SQUID magnetometer. Furthermore, M vs. H isotherm at 5 K in magnetic fields up to 70 kOe (7 Tesla) was measured for all the above-mentioned compositions. Although the SQUID magnetometer has a very high sensitivity in that magnetic moment can be measured to a relative accuracy of 10^{-8} emu, the sample temperature was not as accurate as in the case of VSM since the measuring sensors (platinum and carbon-glass), unlike in the VSM sample holder, are located a few centimeters away from the sample. These measurements on **SQUID Magnetometer** (Model: MPMS7, Quantum Design) were performed at the **Max-Planck Institut für Metallforschung, Stuttgart, GERMANY**.

2.2.4. Faraday Balance

Principle :

In this method, a constant field gradient is produced by suitably graded pole pieces of an electromagnet in the vertical (say z) direction while the base (static) field is along the x -direction. The field gradient along the vertical direction can also be generated by a pair of suitably designed coils known as Lewis coils, which are mounted on the pole pieces of the electromagnet. A magnetic specimen suspended freely from an electronic balance in such a field gradient experiences a force proportional to the magnetization (M) of the specimen according to the expression [3,4]

$$F_z = VM(\partial H/\partial z) = V\chi H(\partial H/\partial z)$$

where χ is the susceptibility, V is the volume and dH/dz is the field gradient along z -direction. By precisely measuring the changes in the weight of the specimen due to this force, its magnetic moment can be accurately determined provided the values of H and (dH/dz) are already known.

Measurements with Faraday balance :

Magnetic measurements at a constant magnetic field of $H = 9$ kOe in the temperature range from 4.2 K to 300 K were performed on $a - (Fe_pNi_{1-p})_{80}B_{19.6}Co_{0.25}$ ($0.25 < p < 0.25$), $a - (Fe_pNi_{1-p})_{80}B_{19.6}Co_{0.25}$ ($0.25 < p < 1.0$), $a - (Fe_pNi_{1-p})_{80}B_{19.6}Co_{0.25}$ ($0.25 < p < 1.0$) and $a - Co_{90}Zr_{10}$ alloys using Faraday method with a relative accuracy of 10 ppm. The sample temperature was varied at a typical rate of ~ 0.5 K/min during the cooling or heating cycle. In addition, the M vs. H isotherms in the field range $0 < H < 15$ kOe were measured at 5 K intervals from 4.2 K to 300 K by means of PAR model 155 vibrating sample magnetometer. All the above-mentioned measurements were carried out at the **Ruhr Universitat, Bochum, GERMANY**.

2.3. Ferromagnetic Resonance technique

Principle :

The phenomenon of ferromagnetic resonance (FMR), first discovered by Griffiths [5], is the resonant microwave absorption in a system of strongly interacting spins. An electron spin, which acts like a magnetic dipole, when placed in a uniform static magnetic field H , precesses around the direction of the magnetic field. The frequency of precession, known as the Larmor frequency, is related to H by

$$\omega_L = \gamma H \quad (2.1)$$

where $\gamma = g\mu_B/\hbar$ is the gyromagnetic ratio of the electron. Resonant absorption of energy can occur when the precessing electron spin is exposed to an external electromagnetic radiation field of frequency $\omega = \omega_L$ applied perpendicular to H and the resonance condition is given by

$$\hbar\omega = g\mu_B H \quad (2.2)$$

This is the well-known electron spin resonance (ESR) phenomenon which occurs in materials with unpaired non-interacting electron spins. By contrast, in ferromagnetic materials, exchange interaction couples spins, and the resultant magnetization vector, instead of the individual spins, precesses around the direction of the applied field H . The resonance condition for this case is obtained from Eq.(2.2) by replacing H with an effective field, H_{eff} , that includes the demagnetizing and other anisotropic fields present in the ferromagnetic material under study.

ESR Spectrometer - principle and working :

A JEOL FE-3X commercial ESR spectrometer operating in the X-band has been used in the present work. Fig. 2.6 shows the block diagram of the experimental set-up. The sample is placed in a cavity resonator, which is located between the pole pieces of an electromagnet. The steady uniform magnetic field, produced by the electromagnet, is swept at a constant rate and is modulated at a frequency of 100 kHz. The sample is exposed to not only the steady field but also the transverse microwave field of constant frequency. At resonance, the sample absorbs a part of the microwave energy and thus changes the **Q-value** of the cavity resonator. The microwaves originating from the klystron oscillator are split into two parts with the help of a directional coupler, one part is fed into a phase shifter and the other to the cavity resonator through a circulator. The phase adjusted reference wave and the reflected wave from the cavity are then mixed and detected by the detector. The reference wave in off-resonant condition is adjusted to give a reflection equal in amplitude, but opposite in phase, to the reflection from the sample and cavity, thus sending zero power to the detector. When the resonance occurs, the balance signal is detected.

The sample temperature was varied with the aid of a variable temperature accessory. The sample was cooled by cold nitrogen (N_2) gas, obtained by boiling liquid nitrogen, circulated through the cavity. A proportional, integral and differential (PID) temperature controller adjusts the power to the heater immersed in liquid N_2 container to regulate the N_2 gas flow and thereby controls the temperature to within ± 0.5 K at a point just outside the cavity. The temperature at this point was monitored by a precalibrated Copper-Constantan thermocouple which serves as the controlling sensor. The temperature stability at the sample site was better than ± 50 mK and the sample temperature was monitored continuously with the help of another calibrated Copper-Constantan thermocouple in direct contact with the sample. Temperatures exceeding 300 K were obtained by sending hot air through the cavity by means of an air compressor. The temperature of the air is controlled by the PID temperature controller.

Measurements with ESR spectrometer :

In the present work, FMR spectra at a fixed microwave field frequency of 9.3 GHz were recorded on a - $Fe_{90-x}Co_xZr_{10}$ = 0, 1, 2, 4, 6, & 8) alloys at constant temperatures of 0.5 K apart in the critical region ($T_C \pm 20$ K). Since the amorphous alloys are extremely stress-sensitive, an elaborate sample mounting technique [6], that gets rid of stress-induced spurious effects, was used for such measurements. The sample holder consists of a quartz rod, half cut at one end. The sample strip of dimensions 2×3 mm cut from a long ribbon was placed on the half-cut portion of the quartz rod and sandwiched by another matching half-cut quartz piece.

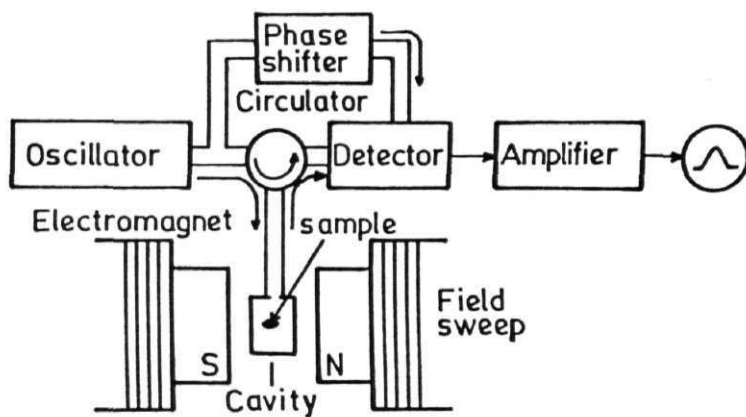


Fig. 2.6 Block diagram of the ESR spectrometer.

Two paper spacers of thickness just greater than the sample thickness were inserted between half-cut portions so as to position the sample in the middle and to ensure that there is no external stress on the sample. The quartz rod was inserted into a quartz tube which was then inserted into the cavity. Two different sample configurations were used in the present work - (i) horizontal-parallel (\parallel^h), in which the external field H lies within the ribbon plane and is directed along the length, (ii) vertical-parallel (\parallel^v), in which H lies within the ribbon plane but is directed along the breadth. The accuracy of the FMR data depends on two factors: the resolution in the external field measurements and the temperature stability. The field resolution (ΔH) depends on the sweep width used; for instance, $\Delta H = \pm 2.5$ Oe ($= \pm 12.5$ Oe) for 1000 Oe (2500 Oe) sweep width. The present measurements were carried out mostly with 1000 Oe sweep width. Different FMR runs on the same sample have revealed that the resonance field, H_{res} , (defined as the field at which $dP/dH = 0$ line cuts the power absorption derivative curve) and the 'peak-to-peak' linewidth, ΔH_{pp} , are reproduced to within $\pm 1\%$ and $\pm 10\%$, respectively.

2.4. FMR data analysis and lineshape calculations

The power absorption derivative (PAD), i.e., dP/dH vs. H , curves recorded in the \parallel^h configuration at a few selected temperatures in the critical region for a — $Fe_{90}Zr_{10}$ alloy are depicted in Fig. 2.7 (continuous lines). These curves are also representative of those recorded for a — $Fe_{90}Zr_{10}$ in the \parallel^v configuration and for other alloys in both \parallel^h and \parallel^v geometries. An examination of Fig. 2.7 reveals that as the temperature is increased through T_C , the peak in dP/dH vs. H curves at a lower field value ~ 800 Oe develops into a full-fledged resonance (secondary resonance) for $T \sim T_C \pm 10$ K whereas the main (primary) resonance shifts to higher fields and broadens out. A detailed FMR study [7,8] carried out on the glassy alloys in question over a temperature range $77\text{ K} < T < 500\text{ K}$ reveals that the secondary resonance (whose signature is first noticed at a temperature close to or above T_C in the most sensitive setting of the spectrometer) exhibits a "cluster-spin-glass-like" behaviour whereas the primary resonance possesses features characteristic of ferromagnets with ($x < 4$) [9,10] or without [10] ($x > 4$) reentrant behaviour at low temperatures. Since the present work concerns itself with the critical behaviour near the ferromagnetic (FM)-paramagnetic (PM) phase transition in a — $Fe_{90-x}Co_xZr_{10}$ alloys and the FMR data recorded in \parallel^h and \parallel^v configurations yield exactly the same results as far as the critical behaviour is concerned, hereafter we will be dealing with primary resonance recorded in the \parallel^h configuration only. Since the resonance field, H_{res} , in the critical region is nearly fourtimes ΔH_{pp} , the observed value of H_{res} could significantly differ from the 'true' resonance center. Hence, a detailed lineshape analysis for each resonance line is called for. The resonance curves recorded at different temperatures in the \parallel^h configuration have been fitted to the theoretical expression [7,8,11]

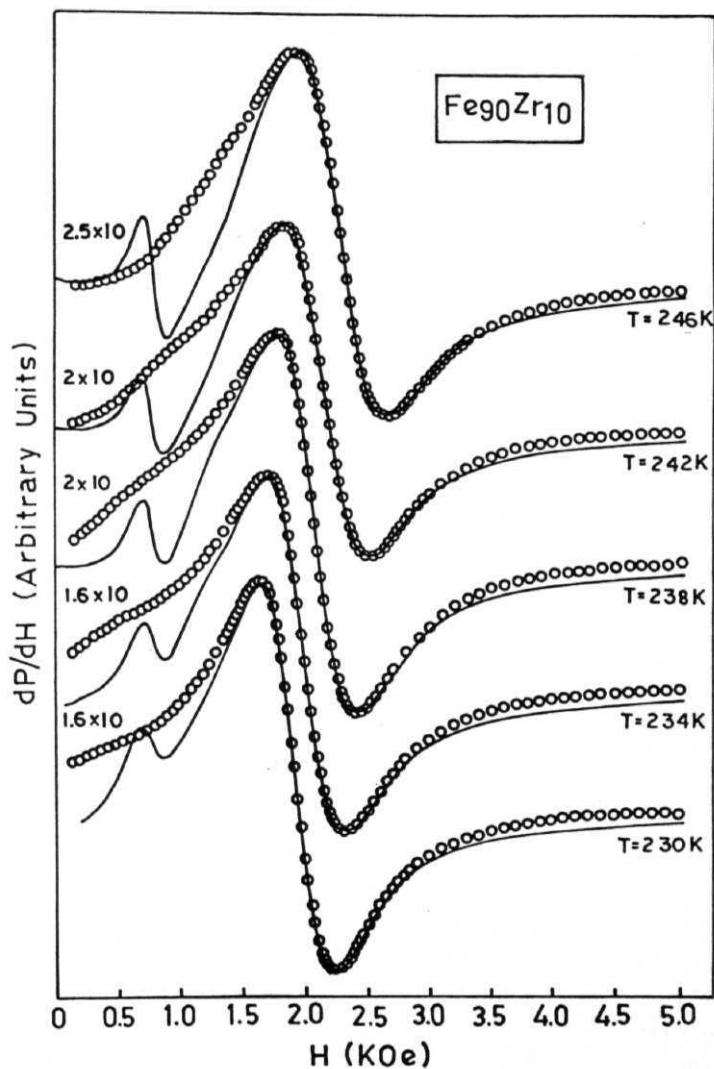


Fig. 2.7 FMR spectra (continuous curves) for $a\text{-Fe}_{90}\text{Zr}_{10}$ horizontal-parallel sample configuration at a few selected temperatures in the critical region. Open circles represent the theoretical fit to the spectra based on Eq.(2.3)

$$\frac{dP_{||}}{dH} \propto \frac{d}{dH} \left[(\mu'^2 + \mu''^2)^{1/2} + \mu'' \right]^{1/2} \quad (2.3)$$

with the real and imaginary components of the dynamic permeability given by,

$$\mu' = \frac{[(H+H_K)(B+H_K)-\Gamma^2-(\omega/\gamma)^2][(B+H_K)^2-\Gamma^2-(\omega/\gamma)^2]+2\Gamma^2(B+H_K)(B+H+2H_K)}{[(H+H_K)(B+H_K)-\Gamma^2-(\omega/\gamma)^2]^2+\Gamma^2(B+H+2H_K)^2} \quad (2.4a)$$

and

$$\mu'' = \frac{-2\Gamma(B+H_K)[(H+H_K)(B+H_K)-\Gamma^2-(\omega/\gamma)^2]+\Gamma(B+H+2H_K)[(B+H_K)^2-\Gamma^2-(\omega/\gamma)^2]}{[(H+H_K)(B+H_K)-\Gamma^2-(\omega/\gamma)^2]^2+\Gamma^2(B+H+2H_K)^2} \quad (2.4b)$$

Eqs.(2.3) and (2.4), derived for dP/dH in the parallel geometry, are obtained by solving the Landau-Lifshitz-Gilbert (LLG) phenomenological equation of motion for dynamic magnetization [7,8,11-13], i.e.,

$$d\vec{M}/dt = -\gamma (\vec{M} \times \vec{H}_{eff}) + (\lambda/\gamma M_s^2) [\vec{M} \times (d\vec{M}/dt)] \quad (2.5)$$

(H_{eff} is the effective field 'seen' by the spins) in conjunction with Maxwell's equations for the parallel geometry used in the present work. The best fits to the dP/dH vs. H data have been obtained with the help of anon-linear least-squares-fit computer program which treats the Lande splitting factor g and saturation magnetization $M_s = (B - H)/4\pi$ as free fitting parameters and uses the observed values of ΔH_{pp} a $1.45\Gamma = 1.45\lambda\omega/\gamma^2 M_s$ (where A is the Gilbert damping parameter, $\gamma = g |e|/2mc$ and $\nu = \omega/2\pi$ is the microwave field frequency) and values of the 'in-plane' uniaxial anisotropy field, H_K , deduced from the relations [7,8,11]

$$H_{res}^{||h} = H_{res}^{||} - H_K \quad \text{and} \quad H_{res}^{||v} = H_{res}^{||} + H_K. \quad (2.6)$$

The $H_{res}^{||h}$ and $H_{res}^{||v}$ in above expression are the observed resonance fields in the $||^h$ and $||^v$ configurations, respectively, and $H_{res}^{||}$ is the resonance field in the absence of H_K . The theoretical fits represented by open circles in Fig. 2.7 not only provide 'true' values for the resonance centers for the primary resonance but also indicate that the LLG equation adequately describes the resonant behaviour in the critical region. In addition, the lineshape calculations reveal that the splitting factor g has a constant value of 2.07 ± 0.02 within the investigated temperature range for the presently investigated alloys. That the **g-factor** is temperature-independent and LLG equation forms an adequate description of $H_{res}(T)$ and $\Delta H_{pp}(T)$ in the critical region for crystalline **ferromagnets** has also been claimed by **Rodbell** [14] and by Haraldson and Pettersson [15] but this claim has been refuted by Bhagat and his co workers [16]. Further, the lineshape analysis also revealed that the corrections to the observed values of H_{eff} at different temperatures due to finite linewidth are negligibly small at all temperatures and fall well within the

experimental uncertainty limits of $H_{eff}(T)$. This result is consistent with the observation that the experimental values of H_{res}^h , and H_K^h , satisfy the resonance conditions [7,8,11-13]

$$\left[(\omega/\gamma)^2 + \Gamma_{||h}^2 \right] = \left(H_{res}^h + 4\pi M_S + H_K \right) \left(H_{res}^h - H_K \right) \quad (2.7a)$$

and

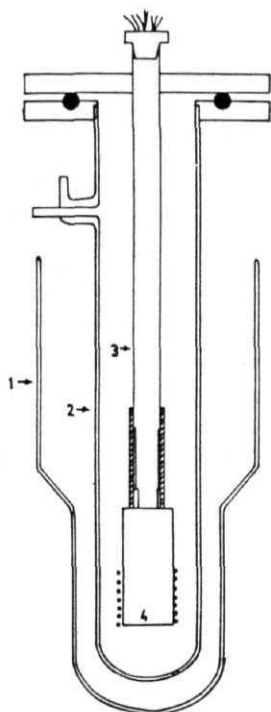
$$\left[(\omega/\gamma)^2 + \Gamma_{||v}^2 \right] = \left(H_{res}^v - 4\pi M_S - H_K \right) \left(H_{res}^v - H_K \right) \quad (2.7b)$$

for $||^h$ and $||^v$ sample geometries, obtained by solving LLG equation (Eq.(2.5)) of motion. Note that the **exchange** term $[(2A\gamma/M^2)(\dot{M} \times \nabla^2 M)]$ in Eq.(2.5) has been dropped in view of the observation [17,18] that the contributions to the linewidth and resonance field due to this term are so small as to fall well within the error limits because the macroscopic exchange stiffness parameter A and conductivity are both at least one order of magnitude lower [9,19] than their corresponding values for crystalline metals. The **present** results are consistent with the earlier observation [7] that $M_S(T)$ deduced in this way from the FMR data are in excellent agreement with $M(T,H)$ data measured on the same sample at an external magnetic field of magnitude comparable to H_{res} . The $M_S(T)$ data in the critical region are analyzed in Chapter 4 and the results **are** also discussed in the same chapter.

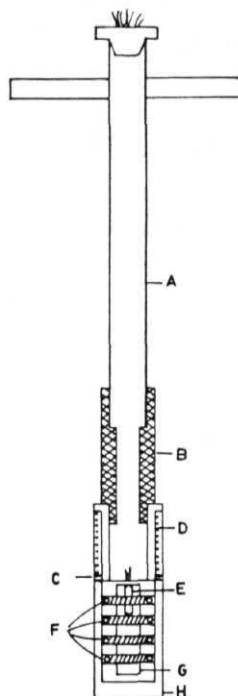
2.5. Electrical Resistivity

Design and fabrication of the experimental set-up :

The electrical resistivity measurements were performed using a home-built apparatus which employs the dc four probe technique. The cryostat arrangement, whose schematic diagram is shown in Fig. 2.8(a), consists of a liquid nitrogen glass dewar and a **double-walled glass cryostat** (the surfaces of both the walls in the annular space are silvered to minimize radiation) with a provision for evacuating the annular space as well as the sample chamber. The sample holder assembly, shown separately in Fig. 2.8(b), is made up of stainless steel tube and a copper **sample-mounting-cum-heater** assembly joined to one another by a **hylam** tube. The heater is wound **non-inductively** on a cylindrical copper bobbin and the sample is mounted in a rectangular copper plate attached to the heater as shown in Fig. 2.8(c). A calibrated platinum (**PT-103**) sensor, placed below the copper plate, measures and controls the sample temperature. Pressure contacts are used to from current and voltage probes. A rectangular stainless steel (SS) plate with a flat protruding step in the middle (Fig. 2.8(d)) and a copper foil to which the current carrying lead is soldered, are used to make the current contact. The copper foil, sandwiched between the SS plate and the sample, is pressed against the sample by tightening two SS screws threading the SS plate. This arrangement ensures a good electrical contact with the sample. A

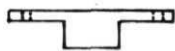
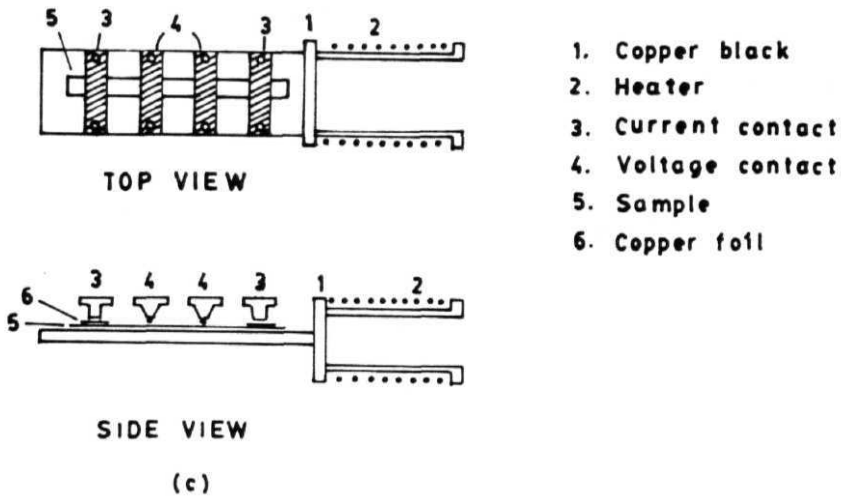


1. Liq N_2 dewar
 2. Double walled Glass Cryostat
 3. Sample holder
 4. Auxiliary heater can
- (a)



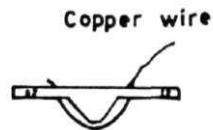
- A-SS tube
 B - phenolic tube
 C - Cu sample mount + heater asstmbly
 D- Heater
 E- Pt.sensor
 F-Electrical probes
 G-Somple
 H-Auxiliary heater
- (b)

Fig. 2.8 (a) Schematic diagrams of the low-temperature cryostat and (b) sample holder assembly for the electrical resistivity set-up.



Current contact

(d)



Voltage contact

(e)

Fig. 2.8(cont.) Schematic diagrams of the (c) heater and sample mounting assembly, (d) current contacts and (e) voltage contacts.

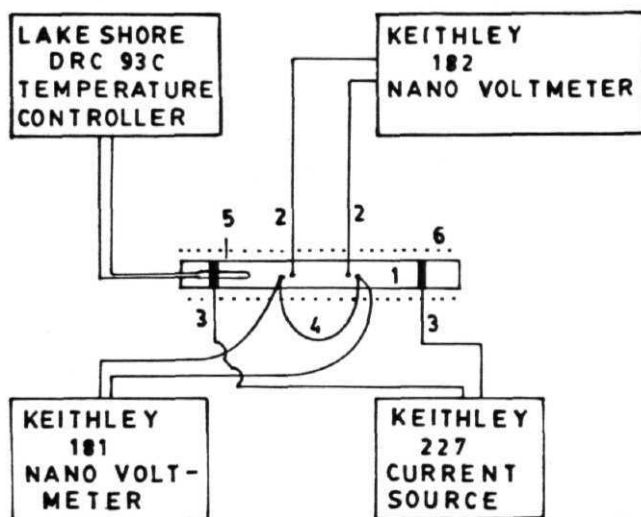


Fig. 2.9 Block diagram of the electrical resistivity set-up, numbers denote: 1 - sample, 2 voltage probes, 3 - current leads, 4 - differential thermocouple, 5 - platinum sensor and 6 heater.

thin sheet of mylar is inserted between the copper foil and the SS plate in order to insulate them from each other. Similarly, the sample is electrically isolated from the copper plate on which it is mounted by using a mylar sheet in between them. The voltage contacts are also made up of SS plates with circular conical protruding portions in the middle which press the voltage-measuring copper leads against the sample with the help of two (each) SS screws (Fig. 2.8(e)). In this way, one end of the voltage leads (wires) is in direct contact with the sample while the other end goes to the nanovoltmeter (Keithley Model 182) without any intervening joints or junctions. This avoids any spurious junction voltages or thermo emf's generated by soldering joints. The temperature gradient along the length of the sample, if any, is monitored by means of a differential thermocouple, whose junctions are placed at either ends of the sample. An auxiliary heater wound on a copper can (which fits onto the copper heater cum sample mounting assembly) produces a temperature gradient in a direction opposite to that present in the sample so that the temperature difference at the ends of the sample in no case exceeds 20 mK. The block diagram of the resistivity setup depicted in figure 2.9 shows the electrical connections and the electronic instruments involved.

Resistivity Measurements :

Electrical resistivity measurements were performed on $a - Fe_{90+y}Zr_{10-y}$ ($y = 0, 1$) and $a - Fe_{90-x}Co_xZr_{10}$ ($x = 0, 1, 2, 4, 6, 8$ & 10) alloys over a temperature range of 77 K - 350 K at 0.5 K steps outside the critical region and at fixed temperatures of 50 mK apart in the critical region ($T_C \pm 15$ K). At every setting, temperature was stabilized to within ± 10 mK using a PID temperature controller (DRC 93C, LakeShore Cryotronics, USA). A typical current of 1 mA was passed through the sample and voltages of the order of 2-3 mV were measured with a resolution of 1 nV using a Keithley 182 nanovoltmeter. The sample current at each temperature was reversed in order to correct the measured voltage for thermo emf generated due to small temperature gradient, if present, across the sample and also for the zero drift of the nanovoltmeter. The temperature gradient measured by the differential thermocouple was continuously monitored by means of another Keithley 181 nanovoltmeter.

The resistivity measurements over a wide temperature range extending from 1100 K down to 4.2 K were carried out on $a - Fe_{90+y}Zr_{10-y}$ ($y = 0$ & 1) alloys at **Facultad de Ciencias, Universidad de Cantabria, Santander, SPAIN**, using the ac four probe technique. In such measurements, a uniform heating rate of ~ 1 K/min was used from 4.2 K to 600 K and a relative accuracy of 50 ppm was achieved.

This thesis also presents the analysis (and its results) of yet another set of resistivity data on $a - Fe_{90}Zr_{10}$ alloy in the temperature region $1.6 \text{ K} < T < 300 \text{ K}$ made available to us by the research group at the **Ruhr Universitat, Bochum, GERMANY**. Though this measurement

too employs the ac four probe technique, electrical resistivity has been measured to a relative accuracy of 5 ppm in this case. The typical heating and cooling rates used in these measurements were ~ 1 K/min outside the critical region and ~ 0.15 K/min in the critical region.

An elaborate analysis of the resistivity data and the results obtained thereby are presented and discussed in the light of various existing theoretical models in Chapter 5.

References

- [1] S. Foner, **Rev.Sci.Instr.** 27, 548 (1956); *ibid* **30**, 548 (1959).
- [2] G.W. Van **Oosterhout**, **Appl.Sci.Res.** B6, 101 (1956).
- [3] H. Zijlstra, in *Experimental Methods in Magnetism* (North-Holland, Amsterdam, 1967) vol.2, **p.**116.
- [4] T.T. **Mc Guire** and P.J. Flanders, in *Magnetism and Metallurgy*, ed. by A.E. Berkowitz and E. Kneller (Academic press, New York, 1969) vol.1, **p.170**; L.F. Bates, in *Modern Magnetism* (Cambridge Univ. press, London, 1963), **p.122**.
- [5] J.H.E. Griffiths, *Nature* **158**, 670 (1946).
- [6] S.N. **Kaul** and T.V.S.M. Mohan Babu, *J.Phys.:Condens. Matter* 1, 8509 (1989).
- [7] S.N. Kaul and V. Siruguri, *J.Phys.:Condens. Matter* 4, 505 (1992); V. Siruguri and S.N. Kaul, *Phys.Rev. B* (to be published).
- [8] V. Siruguri, Ph.D. thesis (1993), University of Hyderabad, India (unpublished).
- [9] S.N. Kaul, *Phys. Rev. B* 27, 6923 (1983).
- [10] P. Deppe, K. **Fukamichi**, F.S. Li, M. Rosenberg and M. Sostarich, *IEEE Trans. Magn.* **MAG-20**, 1367 (1984).
- [11] S.N. Kaul and V. Siruguri, *J.Phys. F* 17, L255 (1987).
- [12] L. Landau and E. Lifshitz, *Phys. Z. Sowiet Union* 8, 153 (1935); T.L. Gilbert, *Phys. Rev.* **100**, 1243 (1955).
- [13] *Ferromagnetic Resonance* ed. by S. Vonskovskii (Paragamon press, London, 1966).
- [14] D.S. Rodbell, *Phys. Rev. Lett.* **13**, 471 (1964).
- [15] S. Haraldson and L. Pettersson, **J.Phys.Chem.** Solids 42, 681 (1981).
- [16] S.M. Bhagat and M.S. Rothstein, *Solid State Commun.* **11**, 1535 (1972) and references cited therein.
- [17] S.M. Bhagat, S. Haraldson and O. **Beckman**, *J. Phys. Chem.* Solids **38**, 593 (1977).
- [18] S.N. Kaul and Srinivasa Kasyapa, *J. Mater. Sci.* 24, 3337 (**1989**).
- [19] W. Beck and H. **Kronmüller**, *Phys. Stat. Solidi (b)* **132**, 449 (1985).

CHAPTER 3

LOW-LYING MAGNETIC EXCITATIONS

In this chapter, the magnetization data taken over a wide temperature range extending from 4.2 K to T_C on amorphous $Ft - Zr$, $Fe - Co - Zr$ and (Fe, Ni) -metalloid alloy systems are presented, analyzed and discussed in the light of existing theoretical models.

A. $a\text{-Fe}_{90+y}\text{Zr}_{10-y}$ and $a\text{-Fe}_{90-x}\text{Co}_x\text{Zr}_{10}$ alloys

3.1. Results and Analysis

3.1.1. 'In-field' Magnetization

The reduced 'in-field' magnetization, $M(T, H)/M(0, H)$ for $a - Fe_{90+y}Zr_{10-y}$ ($y = 0, 1$) and $a - Fe_{90-x}Co_xZr_{10}$ ($x = 0, 1, 2, 4, 6, 8$ and 10) alloys measured at different temperatures in a constant magnetic field of 10 kOe by VSM (vibrating sample magnetometer) and SQUID magnetometer is plotted as a function of temperature in Fig. 3.1. A remarkably good agreement between the SQUID and VSM data in the overlapping temperature range is noticed from this figure. An elaborate analysis of the $M(T, H)$ data, whose details are given below, is attempted based on the following expressions, predicted by the conventional spin-wave (SW) theory [1-3], Stoner model [3,4] and theoretical treatments [5] that include local spin density fluctuations (LSF) in addition to spin waves and single-particle (SP) excitations, for various contributions to the thermal demagnetization of either 'in-field' magnetization, i.e., $\Delta m(T, H) = [M(0, H) - M(T, H)]/M(0, H)$, or spontaneous magnetization, i.e., $\Delta m(T, 0) = [M(0, 0) - M(T, 0)]/M(0, 0)$ (for details see Chapter 1),

$$\Delta m_{SW}(T, H) = \frac{g\mu_B}{M(0, H)} \left\{ Z\left(\frac{3}{2}, t_H\right) \left(\frac{k_B T}{4\pi D(T)}\right)^{3/2} + 15\pi\beta Z\left(\frac{5}{2}, t_H\right) \left(\frac{k_B T}{4\pi D(T)}\right)^{5/2} \right\} \quad (3.1a)$$

with the spin wave stiffness coefficient $D(T)$ given by

$$D(T) = D(0)(1 - D_2 T^2) \quad (3.16)$$

or

$$D(T) = D(0)(1 - D_{5/2} T^{5/2}) \quad (3.1c)$$

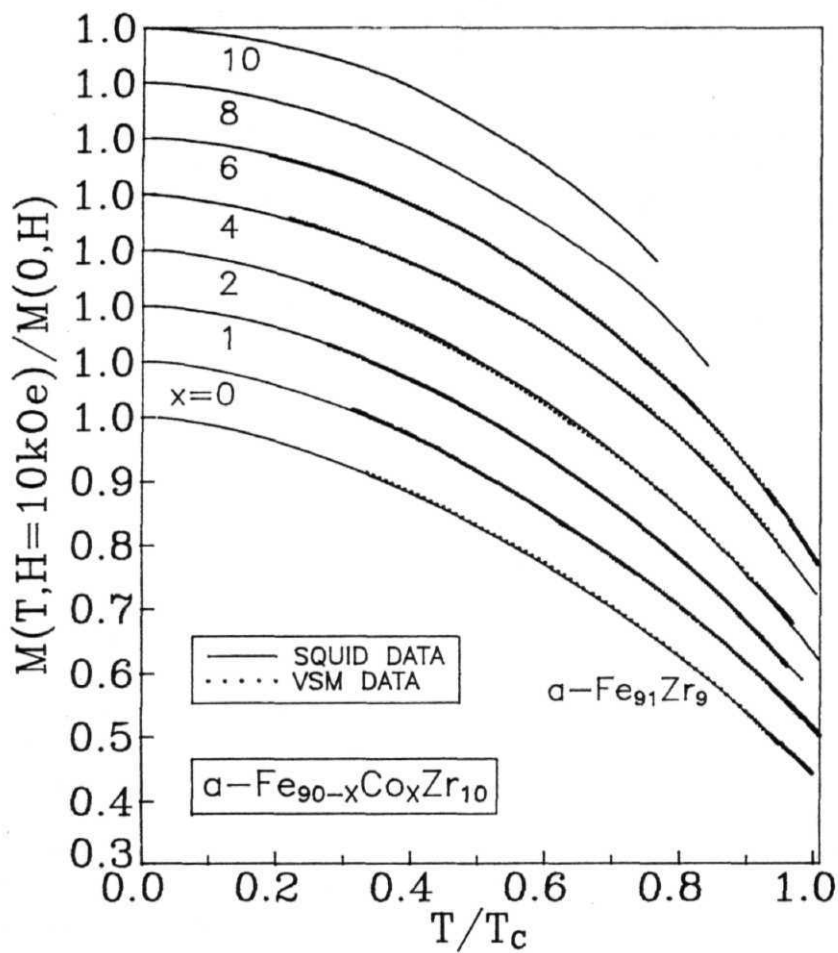


Fig. 3.1 Comparison of the SQUID and VSM magnetization data taken at $H = 10$ kOe.

$$\Delta m_{SP}(T, H) = A(H)T^{3/2} \exp(-\Delta/k_B T) \quad \text{for strong itinerant ferromagnets} \quad (3.2a)$$

$$\Delta m_{SP}(T, H) = A(H) T^2 \quad \text{for weak itinerant ferromagnets} \quad (3.26)$$

$$[M(T, 0)/M(0, 0)]_{SP+LSFS}^2 [1 - \Delta m(T, 0)]^2 = 1 - (T/T_C)^2 \quad (3.3a)$$

and

$$[M(T, 0)/M(0, 0)]_{LSF}^2 [1 - \Delta m(T, 0)]^2 = 1 - (T/T_C)^4/3. \quad (3.36)$$

Since the spin fluctuation theories [5-7], based on the itinerant-electron model, predict that both single-particle excitations and local spin density fluctuations get strongly suppressed in the presence of an external magnetic field, Eqs.(3.3a) and (3.36) can be generalized to include the effect of external field as

$$[M(T, H)/M(0, H)]^2 [1 - \Delta m(T, H)]^2 = C'' - A''(H) T^2 \quad (3.3c)$$

and

$$[M(T, H)/M(0, H)]^2 [1 - \Delta m(T, H)]^2 = C' - A'(H) T^{4/3} \quad (3.3d)$$

so that in zero-field Eqs.(3.3c) and (3.3d) reduce to Eqs.(3.3a) and (3.36), respectively. In order to test the validity of the above expressions (i.e., Eqs.(3.1), (3.26), (3.3c) and (3.3d)), the reduced magnetization $m(T, H) = M(T, H)/M(0, H)$ and its square are plotted against various powers of T , as shown in figures 3.2(a)-(d) for the $M(T, H)$ data taken on the amorphous alloys in question using SQUID magnetometer. These plots clearly indicate that the power laws $m(T, H) \sim 1 - BT^{3/2}$, $m(T, H) \sim C - AT^2$ and $m^2(T, H) \sim C - A'T^{4/3}$ describe very well the observed temperature dependence of $M(T, H)$ at low temperatures, over intermediate temperatures and for temperatures close to T_C , respectively, for the alloys with $y = 0$ and 1 and $0 < x < 10$ with the exception of $x = 8$ and 10 alloys for which the expression $m^2(T, H) \sim C'' - A''T^2$ reproduces the $M(T, H)$ data more closely than the one, $m(T, H) \sim C - AT^2$, in the intermediate temperature range. Similar plots constructed for the alloy with $x = 90$ (the $M(T, H)$ data for this alloy were taken in the temperature range from 4.2 K to 300 K at $H = 9$ kOe using Faraday balance) and shown in Figs. 3.3(a) and 3.3(b) indicate that the $T^{3/2}$ law alone seems to describe $M(T, H)$ data at low temperatures ($T < 175$ K), as is the case for other compositions in the alloy series a - $Fe_{90+y}Zr_{10-y}$ and a - $Fe_{90-x}Co_xZr_{10}$. However, for temperatures above 175 K, this alloy exhibits the same behaviour as that of the alloys with $x = 8$ and 10 in that the expression $m^2(T, H) \sim C'' - A''T^2$ fits the $M(T, H)$ data better than the relation $m(T, H) \sim C - AT^2$.

Having roughly identified the temperature ranges over which different types of excitations dominantly contribute to the thermal demagnetization of 'in-field' magnetization for all the

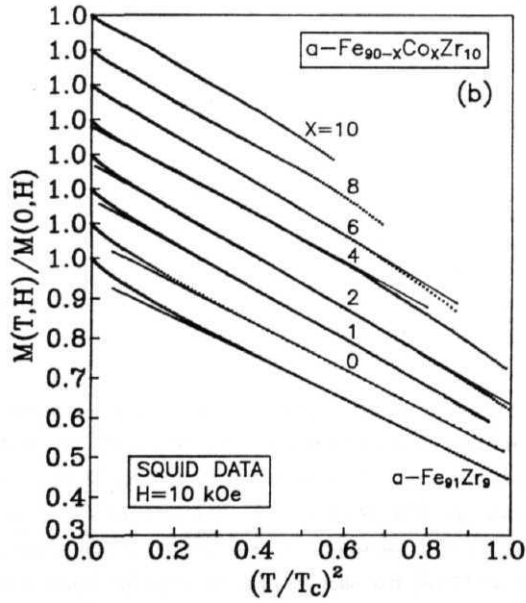
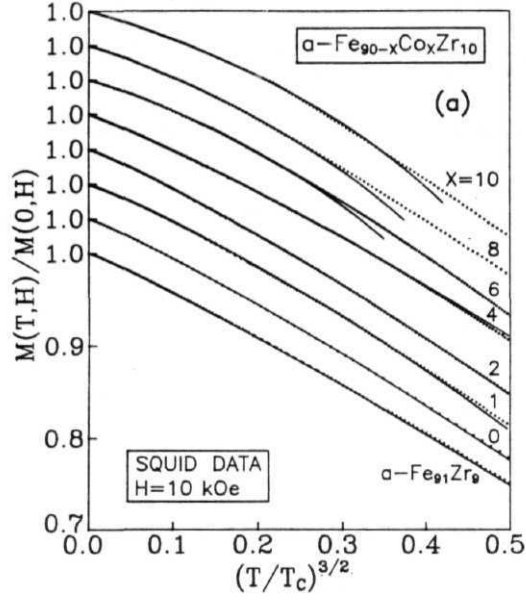


Fig. 3.2 Reduced magnetization versus (a) $(T/T_c)^{3/2}$ and (b) $(T/T_c)^2$. Solid lines denote the least-squares fits to the data.

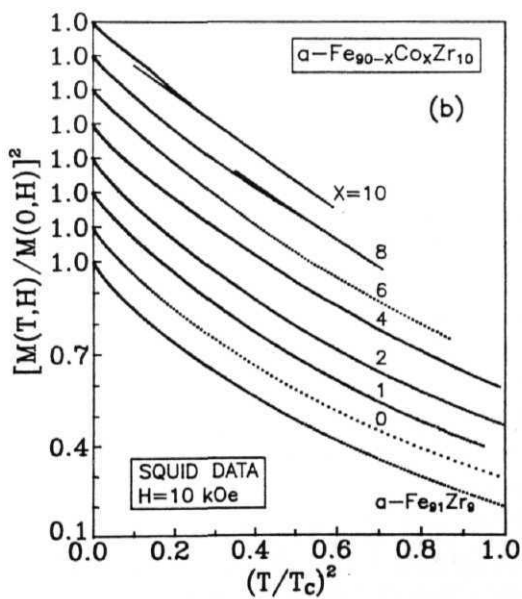
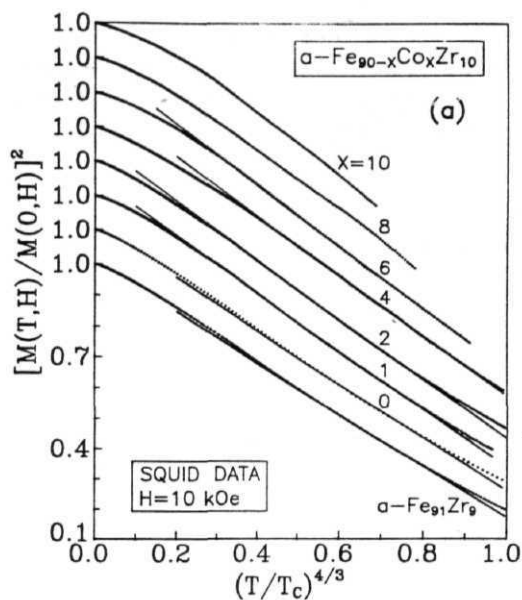


Fig. 3.2 $[M(T,H)/M(0,H)]^2$ as function of (c) T/T_c and (d) $(T/T_c)^2$. Solid lines denote the least squares fits to the data.

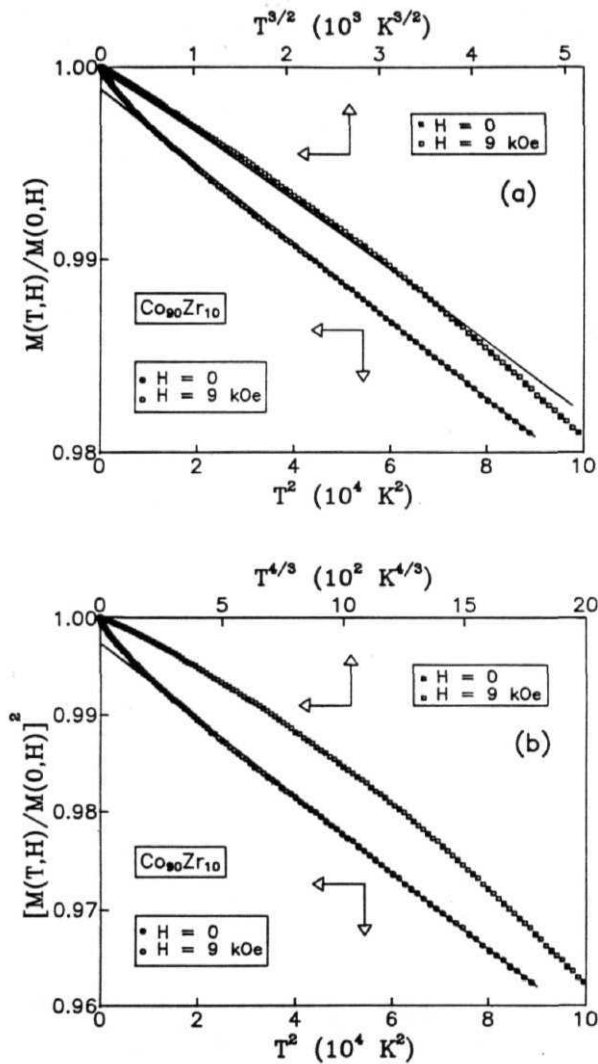


Fig. 3.3 (a) $M(T,H)/M(0,H)$ versus $T^{3/2}$ and T^2 , (b) $[M(T,H)/M(0,H)]^2$ versus $T^{4/3}$ and T^2 for a $\text{Co}_{90}\text{Zr}_{10}$ at $H = 0$ and 9 kOe. Solid lines denote theoretical fits to the data.

alloys under investigation, a detailed range-of-fit analysis of the magnetization data based on the expressions predicted by the existing theoretical models is performed to find out their relative importance in different temperature ranges. The details of this range-of-fit analysis are given below.

Using the value of demagnetizing factor N , obtained by the method described in chapter 2, and the estimates of splitting factor g ($\sim 2.07 \pm 0.02$) and anisotropy field, H_A , deduced from the FMR measurements [8-10], theoretical fits to $\Delta m(T, H)$ data have been attempted based on the expression

$$\Delta m(T, H) = \Delta m_{SW}(T, H) + \Delta m_{SP}(T, H) \quad (3.4)$$

(where $\Delta m_{SW}(T, H)$ and $\Delta m_{SP}(T, H)$ are given by Eqs.(3.1a) and (3.2)) with $D(T)$ given by either Eq.(3.1b) or Eq.(3.1e). A nonlinear least-squares (LS) fit computer program, developed for this purpose, was employed to arrive at the best LS fits. Such fits involve all the possible combinations based on Eqs.(3.1)-(3.2), i.e., the cases (i) $\beta = A = 0$ or (ii) $\beta \neq 0, A = 0$ or (iii) $\beta = A = 0, A \neq 0$ or (iv) $\beta = A = 0, A \neq 0$ or (v) $\Delta m_{SW} - A = 0, A \neq 0$ or (vi) $\Delta m_{SW} - A = 0, A \neq 0$ corresponding to the fits based on (i) the $T^{3/2}$ term alone or (ii) the $T^{3/2} + T^{5/2}$ terms or (iii) the $T^{3/2} + T^2$ terms or (iv) the $T^{3/2} + T^{3/2} \exp(-\Delta/k_B T)$ or (v) Eq.(3.2a) alone or (vi) Eq.(3.2b) alone, respectively. Moreover, in each one of the cases (i)-(iv), three possible expressions for $D(T)$, i.e., $D(T) = D(0)$ or $D(T) = D(0)(1 - D_2 T^2)$ or $D(T) = D(0)(1 - D_{5/2} T^{5/2})$, are considered. In addition to these fits, theoretical fits based on Eq.(3.3c) and Eq.(3.3d) are also attempted. In other words, sixteen different types of fits to $\Delta m(T, H)$ data have been attempted in total. In the range-of-fit analysis of the above-mentioned theoretical fits, the values of free fitting parameters and the quality of fits are monitored continuously as the temperature interval $T_{\min} < T < T_{\max}$ is progressively narrowed down either by keeping T_{\min} fixed at a given value and lowering T_{\max} in steps of 2-3 K towards T_{\min} or by keeping T_{\max} fixed at a certain value and raising T_{\min} towards T_{\max} . Typical results of this type of analysis when T_{\max} is varied are shown in Figs. 3.4(a)-(e) for the alloy with $x = 90$. These plots are representative of all other alloy compositions. Similar plots are obtained when T_{\min} is varied. In these figures, a reduced chi square, χ_r^2 is defined as the sum of deviation squares (χ^2) for the $M(T, H)$ data in a given temperature interval divided by the total number of data points (N) in that temperature interval minus the number of free fitting parameters (N_{para}), i.e., $\chi_r^2 = \chi^2 / (N - N_{\text{para}})$. Such a choice enables one to make an unambiguous assessment of the quality of not only a given type of fit as a function of T_{\max} or T_{\min} but also of different type of fits in the same temperature interval. Judging by the value of χ_r^2 and by the stability of fitting parameters against a wide variation of T_{\max} or T_{\min} (cf. Figs. 3.4(a)-(e)), the following observations can be made. (i) Out of all the fits attempted, the one, based on the theoretical expression Eq.(3.4), that combines Eq.(3.1a) and Eq.(3.1b) and sets $\Delta m_{SP} - \beta = 0$ provides the best fit to $\Delta m(T, H)$ data for temperatures below a certain temperature T^* . For temperatures $T > T^*$, even this combination does not describe

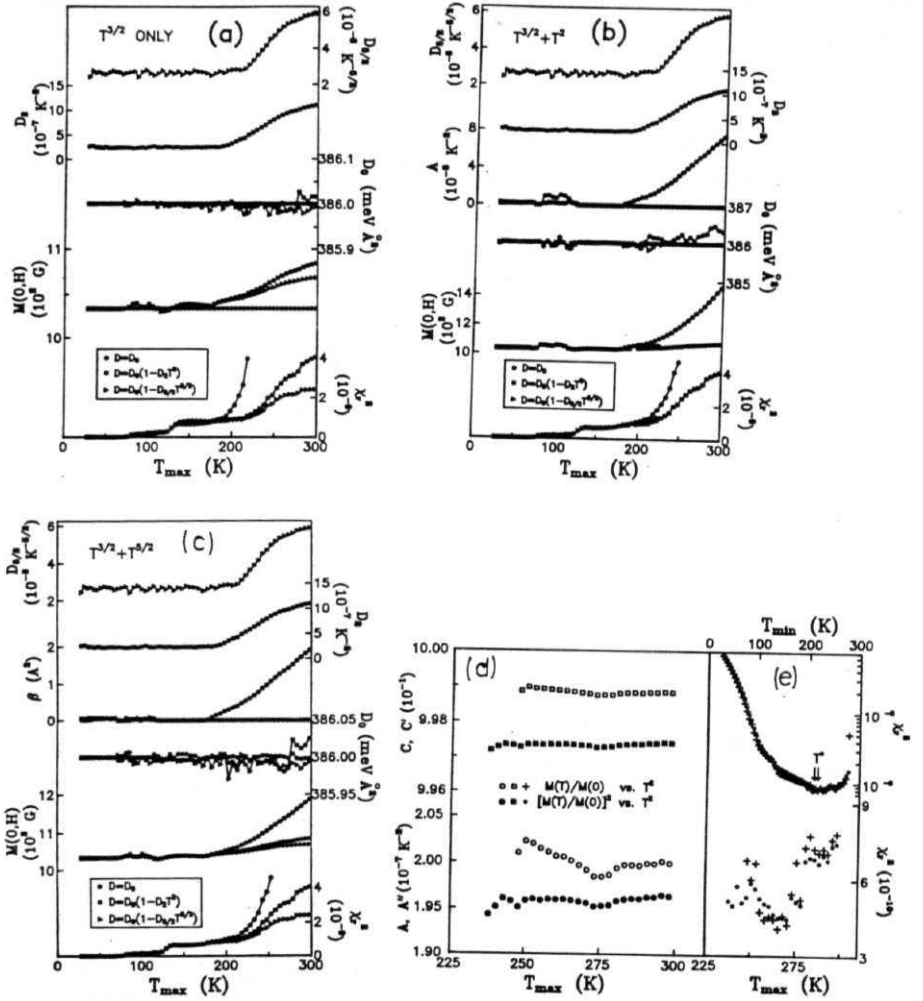


Fig. 3.4 (a)-(d) Variation of free fitting parameters for $a\text{-C}_{60}\text{Zr}_{10}$ with the upper limit (T_{\max}) of the range $T_{\min} < T < T_{\max}$ when T_{\min} is fixed at 4.2 K for the LS fits to the $M(T, H = 9\text{kOe})$ data based on Eqs.(3.1)-(3.4). (e) Variation of χ^2 with T_{\min} (T_{\max}) when T_{\max} (T_{\min}) is kept fixed.

the temperature variation of $\Delta m(T, H)$ properly as indicated by the unphysical increase in χ^2 as well as in most of the fitting parameters with increasing T_{\max} . (ii) For $T < T''$, regardless of temperature range chosen, addition of single-particle term (Δm_{SP}) or higher-order spin wave term ($T^{5/2}$) to the $T^{3/2}$ term does not improve the quality of fit and leaves the parameters of the $T^{3/2}$ fit practically unaltered. (iii) The LS fits to the $\Delta m(T, H)$ data for $T < T''$ based on theoretical expressions which set $D(T) = D(0)(1 - D_2 T^2)$ give lower χ^2 than those for which $D(T) = D(0)(1 - D_{5/2} T^{5/2})$ whereas the quality of fits based on the expressions that consider $D(T)$ to be temperature-independent, i.e., $D(T) = D(0)$, are much worse compared to the ones that allow for the temperature dependence of D. (iv) Eq.(3.26) provides an excellent fit to the data in the intermediate temperature range whereas Eq.(3.2a) does not describe the $\Delta m(T, H)$ data in any temperature range even with unphysical values for the parameters A and A'. For the alloy with $x = 90$, the situation in the intermediate temperature range is similar to that of the alloys with $x = 8$ and 10. As seen from the Figs. 3.4(d) and 3.4(e) for the alloy with $x = 90$, the expression $m^2(T, H) = C'' - A'' T^2$ yields a slightly lower χ^2 in a larger temperature range of 210 K to 300 K compared to that $m(T, H) = C - A T^2$ which fits in the range 220 K to 300 K. (v) For temperatures close to T_C , the best description to $M(T, H)$ data is provided by the expression $m^2(T, H) = C' - A' T^{4/3}$ for the alloys with $y = 0$ & 1 and $x < 6$. The analysis of the type described above has also been performed on the $M(T, H)$ data taken at $H = 10$ kOe using VSM in the temperature range from 70 K to T_C on the alloys with $y = 0$ & 1 and $x < 6$ with the same results as those yielded by the SQUID data.

With a view to study in detail the effect of external magnetic field on the single-particle excitations and local spin density fluctuations (LSF), the $M(T, H)$ data at several constant external magnetic field values in steps of 1 kOe in the interval $1.5 \text{ kOe} < H < 15 \text{ kOe}$ are obtained from the M vs. H isotherms measured using VSM in the temperature range from 70 K to T_C on the alloys with $y = 0$ & 1 and $x < 6$. A detailed range-of-fit analysis based on Eqs.(3.2b) and Eq.(3.3d), as described earlier, has been carried out to determine the field dependence of the coefficients A and A' of the T^2 and $T^{4/3}$ terms, respectively. The best LS fits for the alloy with $x = 4$ are shown in Figs. 3.5(a) and 3.5(b) as continuous straight lines through the data points at a few representative field values. Such plots for other alloy concentrations are identical to those depicted in Figs. 3.5(a) and 3.5(b). As the applied field is increased, the temperature range over which the T^2 term fits broadens slightly and shifts to higher temperatures whereas the range of the $T^{4/3}$ fit seems to shift to lower temperatures. For a given concentration, considerable overlap of temperature ranges of T^2 and $T^{4/3}$ fits occurs as the field is increased, so much so that for certain Co concentrations the overlap is nearly complete at fields $H \sim 10$ kOe. However, if the temperature range is narrowed down by lowering T_{\max} towards T_{\min} , the T^2 term (Eq.(3.2b)) provides a better fit to the data than the $T^{4/3}$ term whereas the reverse is true when the temperature range is narrowed down by raising T_{\min} towards T_C .

The final outcome of such an elaborate data analysis can be summarized as follows.

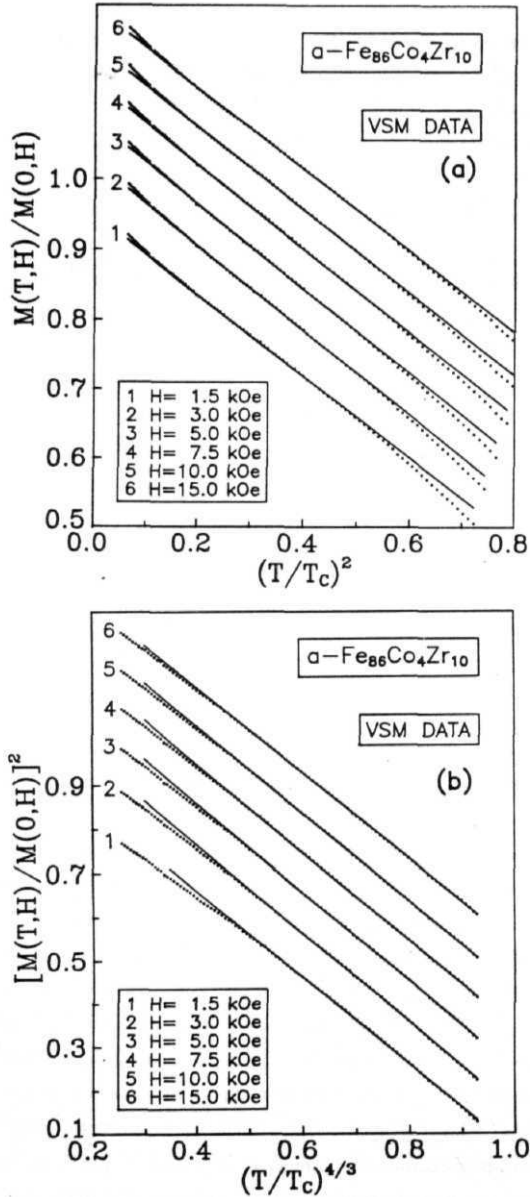


Fig. 3.5 $M(T,H)/M(0,H)$ vs. $(T/T_c)^2$ and $[M(T,H)/M(0H)]^2$ vs. $(T/T_c)^{4/3}$ plots at a few selected field values. Continuous curves denote LS fits to the data based on Eqs.(3.5b) and (3.3d), respectively. Note that the data denoted by the numbers 2,3,4,5 are shifted up by the amounts 0.05,0.10,0.15,0.20 and 0.08,0.16,0.24,0.32 with respect to data] in (a) and (b) respectively.

(i) For all the alloys including the one with $x = 90$, the best fit to $\Delta m(T, H)$ data for temperatures $T < T''$ is provided by the expression

$$\Delta m(T, H) = \frac{g\mu_B}{M(0, H)} Z\left(\frac{3}{2}, t_H\right) \left[\frac{k_B T}{4\pi D(0)(1 - D_2 T^2)} \right]^{3/2} \quad (3.5a)$$

with the parameter values and temperature ranges for different compositions given in Table 3.1, which also includes the corresponding values for the VSM data taken at $H = 10$ kOe within the square brackets. (ii) For the alloys with $y = 0$ & 1 and $x < 6$, $M(T, H)$ data are best described by Eq.(3.26) or its more general form given by

$$M(T, H)/M(0, H) = C - A(H)T^2 \quad (3.56)$$

over the intermediate temperature range $T^{**} < T < T''''$ while Eq.(3.3d) yields the best fit to the $M(T, H)$ data for temperatures close to T_C in the interval $V < T < T''$; the values of different parameters and the temperature ranges for such fits are listed in Table 3.1. These fits are represented by the continuous straight lines in Figs. 3.2(a)-(d). By contrast, for the alloys with $x = 8, 10$ & 90, Eq.(3.3c) reproduces the observed temperature variation of magnetization more closely in the range $T^\dagger < T < T^{\dagger\dagger}$ than Eq.(3.2b) (Figs. 3.2(d), 3.3(a) and 3.3(b)). (iii) The VSM and SQUID data taken at $H = 10$ kOe yield identical results (Table 3.1). In this context, it is gratifying to note that even though the VSM data for temperatures below 70 K, which are crucial to an accurate determination of the spin-wave parameters such as $D(0)$, D_2 , etc., are not presently available, the $T^{3/2}$ fits to VSM and SQUID data, based on Eq.(3.5a), give the same (within the uncertainty limits) values for these parameters. (iv) The coefficients A and A' of the T^2 and $T^{4/3}$ terms in Eq.(3.56) and Eq.(3.3d), respectively, decrease with increasing applied magnetic field for a given composition and with increasing Co concentration for a given field value (Figs. 3.6(a) and 3.6(b)). This observation implies that single-particle excitations and LSF get suppressed by both magnetic field and Co substitution. These results are discussed in section 3.2.

3.1.2. Spontaneous Magnetization

Temperature dependence :

In order to determine spontaneous magnetization at different temperatures, the M vs. H isotherms in external fields up to 15 kOe have been measured by means of VSM on a - $Fe_{90+y}Zr_{10-y}$ ($y = 0$ & 1) and a - $Fe_{90-x}Co_xZr_x$ ($x = 0, 1, 2, 4, 6$) alloys in steps of 1 K from 70 K to T_C (4.2-300 K for $x = 90$). Typical plots of M^2 versus H/M (Arrott plots) at a few specified temperatures, constructed out of these M vs. H isotherms with external field corrected for the demagnetizing field, are displayed in figures 3.7(a)-(c). The customary approach of determining spontaneous magnetization at different temperatures, $M(T, 0)$, from

Table 3.1(a): The spin-wave parameters for a - $Fe_{91}Zr_9$ and a - $Fe_{90-x}Co_xZr_{10}$ alloys deduced from the SQUID magnetization data at $H = 10$ kOe. The corresponding parameter values obtained from the VSM magnetization data at $H = 10$ kOe are displayed within the square brackets. The numbers in parentheses denote the uncertainty in the least significant figure. ^aEstimated from the value of coefficient A'' in Eq.(3.3a).

Alloy/ Conc. x	$t^* = T^*/T_C$	$M(0,H)$ (G)	$D(0)$ (meV \AA^2)	D_2 (10^{-6} K $^{-2}$)	T_C (K)	$D(0)/T_C$ (meV $\text{\AA}^2/\text{K}$)
$Fe_{91}Zr_9$	0.50	969(25) [930(30)]	29(2) [29(3)]	2.0(10) [1.9(10)]	209.66(5)	0.138(10)
0	0.50	1052(20) [1015(30)]	31(2) [32(3)]	1.5(10) [1.4(10)]	225.00(5)	0.137(10)
1	0.45	1120(25) [1100(30)]	35(2) [34(3)]	2.0(5) [2.0(5)]	256.66(5)	0.136(12)
2	0.45	1165(25) [1150(35)]	38(3) [36(3)]	2.5(5) [2.6(5)]	281.60(5)	0.135(14)
4	0.45	1305(20) [1280(25)]	45(3) [41(4)]	2.0(5) [2.2(5)]	327.95(5)	0.137(13)
6	0.40	1315(25) [1290(30)]	52(3) [48(5)]	3.5(10) [3.2(10)]	374.75(5)	0.142(14)
8	0.40	1343(25)	62(3)	3.5(10)	419.50(10)	0.148(8)
10	0.40	1360(25)	70(2)	3.0(10)	462.50(10)	0.152(5)
90	0.10	1034(20)	386(4)	0.3(1)	1600(80) ^a	

Table 3.1(b): Parameter values and temperature ranges for the fit to the SQUID [VSM] $M(T,H)$ data at $H = 10$ kOe based on Eqs.(3.26), (3.3c) and (3.3d) of the text and $t = T/T_C$.

Alloy/ Conc. x	fit range $t'' - t'''$	A (10^{-6} K^{-2})	fit range $t^\dagger - t^{\dagger\dagger}$	A'' (10^{-6} K^{-2})	fit range $t' - t''$	A' ($10^{-4} \text{ K}^{-4/3}$)
$Fe_{91}Zr_9$	0.58-0.98 [0.65-0.98]	12.0(2) [12.2(2)]			0.53-0.87 [0.66-0.83]	6.60(5) [6.65(5)]
0	0.55-0.91 [0.58-0.98]	11.0(3) [11.2(2)]			0.62-0.84 [0.62-0.84]	6.12(8) [6.22(8)]
1	0.53-0.92 [0.55-0.95]	9.2(1) [9.2(2)]			0.50-0.82 [0.50-0.85]	5.50(5) [5.46(4)]
2	0.49-0.84 [0.45-0.89]	7.8(3) [7.6(2)]			0.46-0.79 [0.50-0.80]	4.94(8) [4.85(5)]
4	0.40-0.69 [0.40-0.75]	5.4(2) [5.5(1)]			0.56-0.93 [0.56-0.93]	3.90(5) [3.98(4)]
6	0.44-0.79 [0.45-0.78]	4.5(2) [4.4(1)]			0.70-0.90 [0.55-0.87]	3.44(4) [3.41(3)]
8			0.74-0.83	5.45(5)		
10			0.53-0.75	4.72(5)		
90			0.14-0.20	0.39(1)		

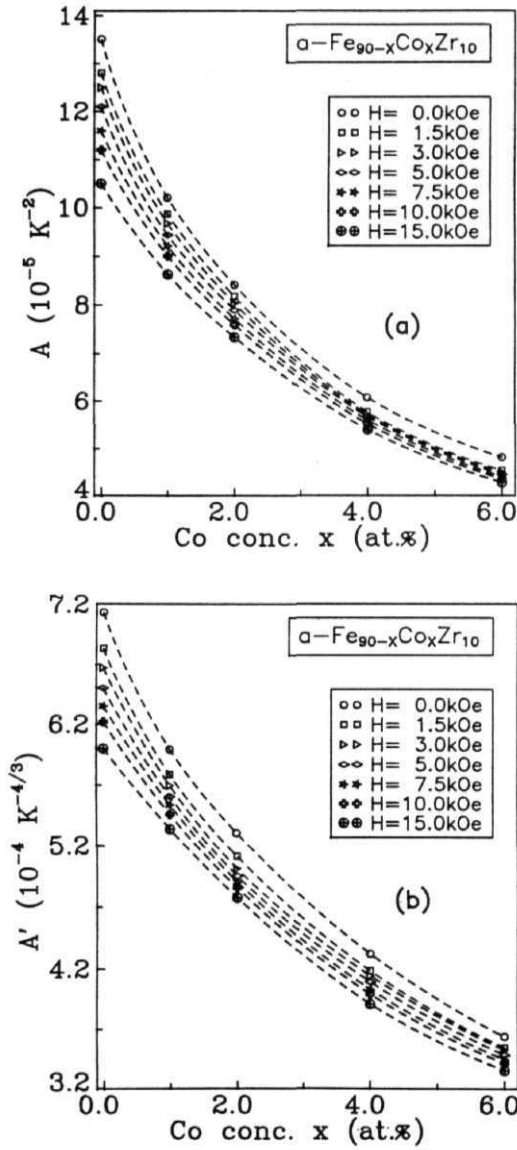


Fig. 3.6 Concentration dependence of the coefficients (a) A in Eq.(3.2b) or (3.5b) and (b) A' in Eq.(3.3d) for a few selected values of H .

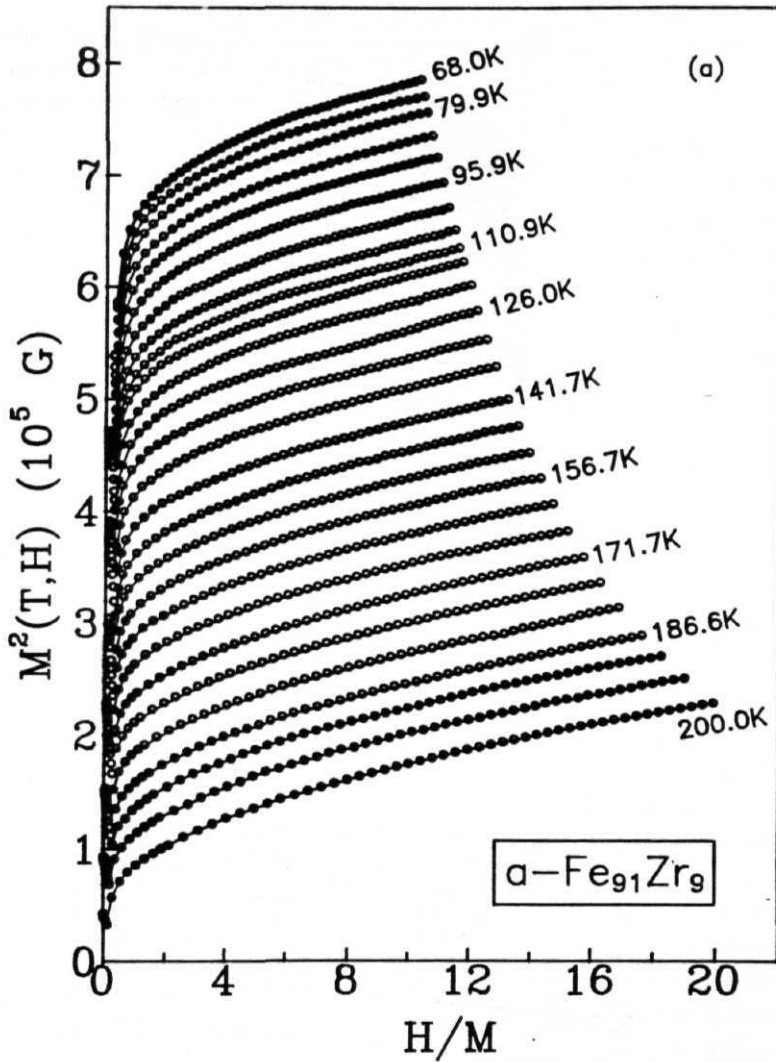


Fig. 3.7 (a) Arrott plot isotherms for $\alpha\text{-Fe}_{91}\text{Zr}_9$ at a few selected temperatures.

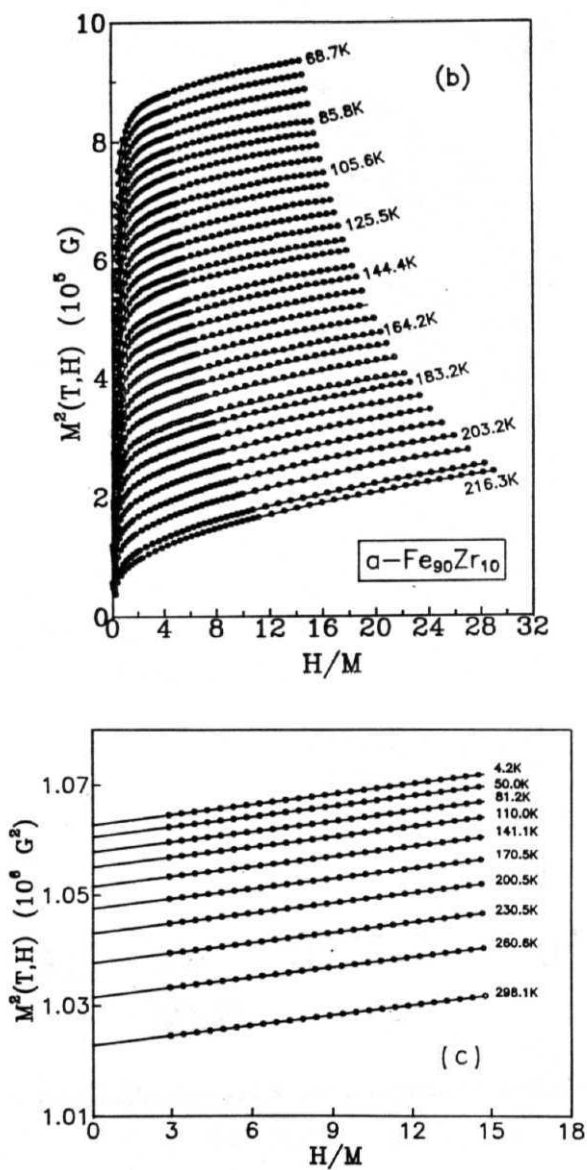


Fig. 3.7 M^2 vs. H/M isotherms at a few representative temperatures for (b) $\alpha\text{-Fe}_{90}\text{Zr}_{10}$ and (c) $\alpha\text{-Co}_{90}\text{Zr}_{10}$.

the intercepts on the ordinate that the linear extrapolation of the high-field portions of M^2 vs. H/M isotherms to $H = 0$ yields has not been adopted in the present case (except for the alloy with $x = 90$) for the following reason. Slight but finite curvature even in the high-field portion of the M^2 vs. H/M isotherms makes an accurate determination of $M(T, 0)$ impossible because such an extrapolation cannot be carried out unambiguously. Since such a problem has not been encountered in the case of $a\text{-Co}_{90}\text{Zr}_{10}$, this procedure has been followed for that alloy only. For the remaining alloys, this problem has been effectively tackled by constructing the modified Arrott plot (MAP) ($M^{1/\beta}$ vs. $(H/M)^{1/\beta}$ plot) with the choice of spontaneous magnetization and initial susceptibility critical exponents β and γ , respectively, that makes MAP isotherms a set of parallel straight lines in the critical region. This procedure is discussed in detail in Chapter 4, which deals with the thermal critical behaviour of these alloys. The modified Arrott plot for $a\text{-Fe}_{91}\text{Zr}_9$, which is representative of all the remaining alloy compositions in the above-mentioned series, is shown in Fig. 4.10 of Chapter 4. The values of spontaneous magnetization at different temperatures are then computed from the intercepts on the ordinate ($M^{1/\beta}$ axis) obtained by extrapolating high-field linear portions of the MAP isotherms to $H = 0$. The spontaneous magnetization, $M(T, 0)$, data, so obtained, for the alloys with $y = 0, 1$ and $x < 6$ are shown in Fig. 3.8. The $M(T, 0)$ data have been analyzed in exactly the same way as the 'in-field' magnetization data. The data presented in figures 3.9(a) and 3.9(b) clearly demonstrate that the functional dependence of $M(T, 0)$ on T is adequately described by Eq.(3.56) or Eq.(3.2b) with $M(T, H)/M(0, H)$ replaced by $M(T, 0)/M(0, 0)$, ($\equiv m(T, 0)$) in the intermediate temperature range and by Eq.(3.36) for temperatures close to T_C . The departure of the $m(T, 0)$ data from fits based on Eq.(3.56) on the low-temperature side is mainly caused by spin wave excitations which dominate at low temperatures. For the alloy with $x = 90$, $M(T, 0)$ data almost coincides with $M(T, H)$ data (cf. Figs. 3.3(a) and 3.3(b)) and hence the functional dependence of $M(T, 0)$ on T is exactly the same as that of $M(T, H)$. The range-of-fit analysis of $M(T, 0)$ data (for $x = 90$), based on Eqs.(3.3a) and suitably modified versions of Eqs.(3.1), (3.2) and (3.5), carried out in the same way as described for the $M(T, H)$ data, reveals that the best fits to the $M(T, 0)$ data for $T < T^*$ are provided by Eq.(3.5a) with the quantities $Z(3/2, t_H)$ and $M(0, H)$ in this equation replaced by $\xi(3/2)$ and $M(0, 0)$, and with the parameter values given in Table 3.2 while Eq.(3.3a) reproduces the observed temperature variation of $M(T, 0)$ over the intermediate temperature range ($T'' < T < T^{***}$) more closely than the modified zero-field version of Eq.(3.5b) does. The temperature ranges and values of free fitting parameters for the above-mentioned alloys are given in Table 3.2 and the best LS fits are represented by solid straight lines through data points in Figs. 3.9(a) and 3.9(b).

The values at 0 K :

The magnetization, $M(T, H)$, data taken at $T = 5$ K in applied fields up to 70 kOe on

Table 3.2: The parameter values and temperature ranges for the fits to the $M(H=0, T)$ data based on Eqs.(3.1)-(3.3) of the text for the $\alpha - Fe_{91}Zr_9$ and $\alpha - Fe_{90-x}Co_xZr_{10}$ alloys. The values within the square brackets are the $M(0,0)$ values obtained directly from M vs. H isotherm at $T = 5$ K. The numbers in parentheses denote the uncertainty in the least significant figure. ^aExtrapolated values of the coefficient $A''(0)$ in Eq.(3.3c) obtained from $A''(H)$ at $H = 10$ kOe. ^bObserved value of $A''(0)$.

Alloy/ Conc. x	t^*	$M(0,0)$ (G)	$D(0)$ (meV \AA^2)	D_2 (10^{-6} K $^{-2}$)	fit range $t^{**} - t^{***}$	A (10^{-6} K $^{-2}$)	fit range $t' - t''$	A' (10^{-4} K $^{-4/3}$)
$Fe_{91}Zr_9$	0.50	945(35) [965(30)]	28(3)	1.8(10)	0.53-0.77	15.4(2)	0.74-0.95	7.85(5)
0	0.50	1026(30) [1041(30)]	32(3)	1.7(10)	0.51-0.78	13.5(4)	0.67-0.97	7.13(8)
1	0.45	1075(35) [1100(30)]	34(3)	2.2(5)	0.44-0.71	9.7(1)	0.74-0.94	5.99(5)
2	0.45	1145(35) [1170(30)]	37(3)	2.5(5)	0.45-0.69	8.4(2)	0.67-0.95	5.30(8)
4	0.45	1275(35) [1296(30)]	44(4)	2.2(5)	0.44-0.73	6.1(1)	0.64-0.93	4.31(5)
6	0.40	1290(30) [1305(30)]	51(5)	3.0(10)	0.45-0.75	4.8(2)	0.64-0.96	3.63(4)
8		[1344(30)]				{7.6(2)} ^a		
10		[1359(30)]				{6.3(2)} ^a		
90	0.10	1031(20)	386(4)	0.3(1)		{0.20(1)} ^b		

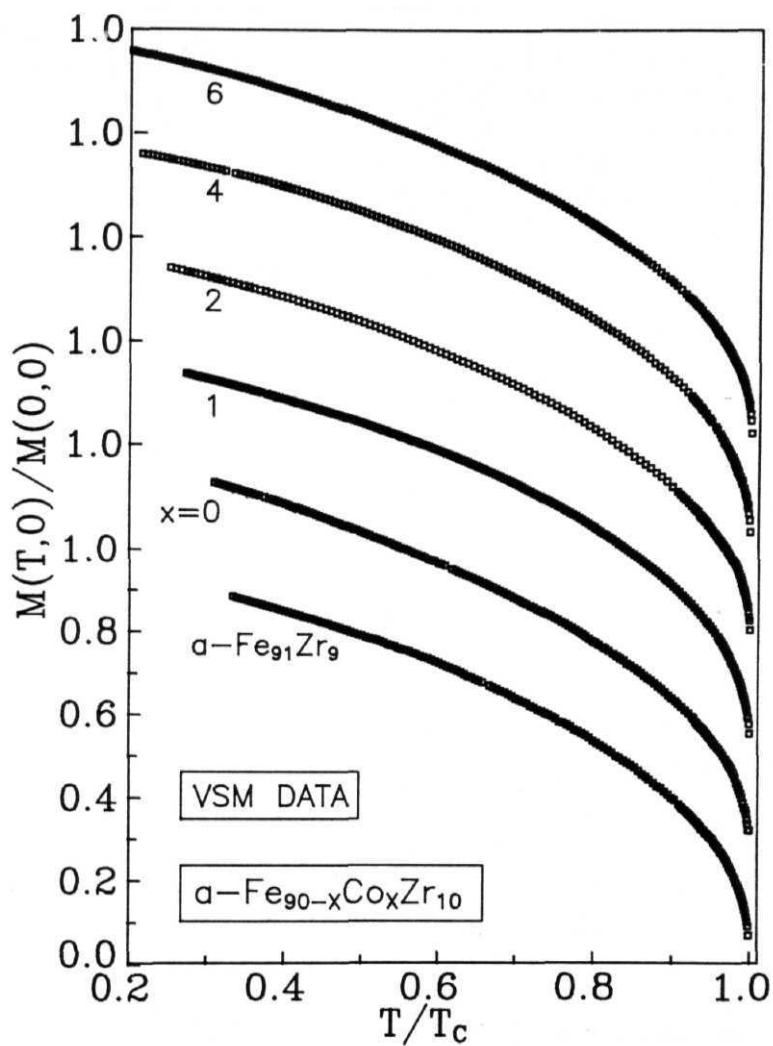


Fig. 3.8 Reduced spontaneous magnetization versus reduced temperature.

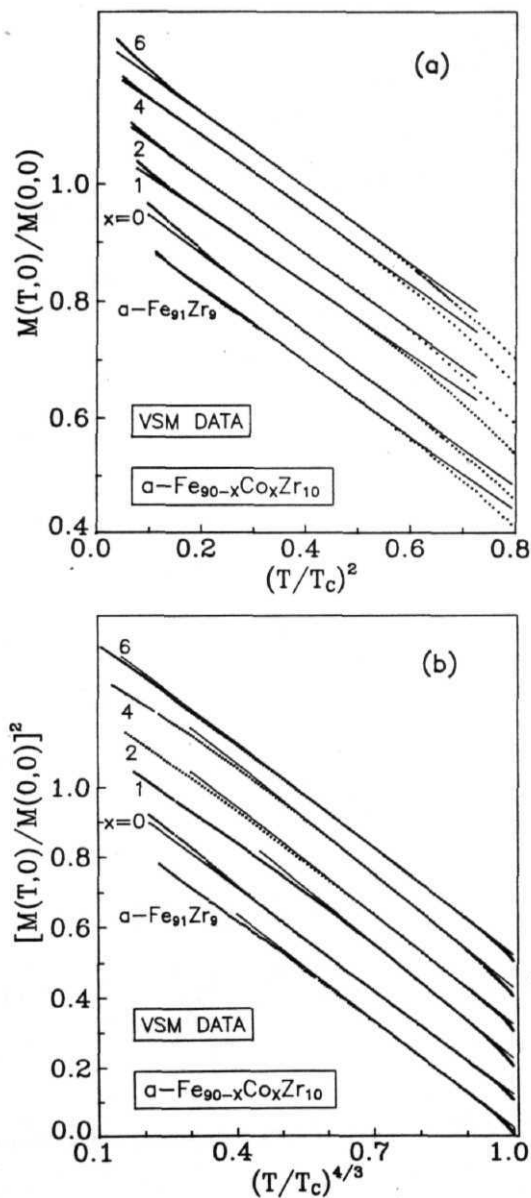


Fig. 3.9 $M(T,0)/M(0,0)$ vs. $(T/T_c)^2$ and $[M(T,0)/M(0,0)]^2$ vs. $(T/T_c)^{4/3}$ plots constructed using VSM $M(T,0)$ data. Note that the data for $x = 0, 1, 2, 4, 6$ are shifted up by the amounts 0.06, 0.12, 0.18, 0.24, 0.30 and 0.10, 0.20, 0.30, 0.40, 0.50 with respect to that of $\alpha\text{-Fe}_{90}\text{Zr}_{10}$ in (a) and (b), respectively. Solid lines denote LS fits to the data based on Eqs.(3.5b) and (3.5d), in (a) and (b), respectively.

$a - \text{Fe}_{91}\text{Zr}_9$ and $a - \text{Fe}_{90-x}\text{Co}_x\text{Zr}_{10}$ ($0 < x < 10$) alloys using SQUID magnetometer are plotted in the form of $M(0, H)/M(0, 0)$ vs. H curves in figure 3.10. Note that no distinction has been made between the value of magnetization at 5 K and 0 K in this figure and in the figures 3.9(a) and 3.9(b). The differential susceptibility, $\chi(0, H)$, as a function of field, obtained by numerical differentiation of these M vs. H curves, is shown in Fig. 3.11. A close examination of these figures reveals that for the alloys with zero or low Co concentration, magnetization does not saturate even in fields as high as 70 kOe and that $\chi(0, H)$ gradually decreases with increasing H and approaches a constant value at high fields. This limiting value is nothing but the high-field susceptibility, χ_{hf} . The inset of Fig. 3.11 shows χ_{hf} plotted against Co concentration, x . As the Co concentration is increased, a plateau in the $\chi(0, H)$ vs. H curve is reached at a lower field and correspondingly the field at which technical saturation in magnetization occurs also shifts to lower values (inset of Fig. 3.10) while χ_{hf} decreases rapidly for $x < 4$ and the decreasing trend slows down considerably for $x > 6$ (inset of Fig. 3.11). The value of spontaneous magnetization at 0 K, $M(0, 0)$, is then obtained by subtracting $\chi_{hf}H$ from $M(T, H)$ at $H = 70$ kOe. The values of $M(0, 0)$ and χ_{hf} , so obtained, are listed in Tables 3.2 and 3.3, respectively.

3.2. Discussion

Before applying the theoretical models briefly introduced in Chapter 1 to the systems under consideration, relevant details about the itinerant-electron models that bring out clearly the role of spin density fluctuations and Stoner single-particle excitations in determining the magnetic properties of weak itinerant ferromagnets are given below. The main reason for giving these details is to explore the possibility of attempting a *quantitative* comparison between experiment and theory.

3.2.1. Spin fluctuation model: A unified approach

In this model, it is assumed that following the Ginzburg-Landau formalism, the *local* free energy density can be expanded in terms of a small and slowly varying *classical* order parameter (local magnetization) $M + \vec{m}(\vec{r})$ as [5]

$$f(\vec{r}) = f_0 + \frac{a}{2} |\vec{M} + \vec{m}(\vec{r})|^2 + \frac{b}{4} |\vec{M} + \vec{m}(\vec{r})|^4 + \frac{c}{2} \sum_{\nu} |\nabla_{\nu} \vec{m}(\vec{r})|^2 + \dots$$

where

$$\vec{m}(\vec{r}) = \frac{1}{V} \sum_{\vec{q}} \vec{m}(\vec{q}) \exp(i\vec{q} \cdot \vec{r}), \quad \vec{m}(\vec{q}) = \begin{cases} \vec{m}(\vec{q}) & q < q_c \\ 0 & \text{otherwise} \end{cases}$$

Table 3.3: Band and exchange parameters. ^a Ref.[40,41].

Alloy/ Conc. x	μ_o (μ_B)	χ_{hf} (10^{-4})	$\chi(0,0)$ (10^{-4})	S	$IN(E_F)$	$N(E_F)^a$ (eV^{-1})	I (eV)	ν [TF] [(K)]
<i>Fe₉₁Zr₉</i>	1.34(2)	12.32(10)	14.00(20)	83(1)	1.012(1)	4.00	0.25(1)	
0	1.44(2)	8.86(20)	10.37(20)	66(1)	1.015(1)	3.74	0.27(1)	
1	1.52(2)	7.32(15)	7.78(10)	53(1)	1.019(1)	3.49	0.29(1)	
2	1.62(2)	4.47(15)	4.72(10)	34(2)	1.029(1)	3.30	0.31(1)	
4	1.79(2)	2.61(10)	2.97(10)	24(1)	1.042(1)	3.00	0.35(1)	
6	1.81(2)	1.38(10)	1.50(10)	13(1)	1.079(4)	2.82	0.38(1)	
8	1.82(2)	1.00(15)	1.34(10)	12(1)	1.084(5)	2.70	0.40(1)	
10	1.84(2)	0.60(20)	0.64(10)	6(1)	1.170(23)	2.61	0.45(1)	
90	1.52(2)	3.50(10)	3.07(5)	36(1)	1.028(10)	1.94	0.53(1)	0.9 [9650(350)]

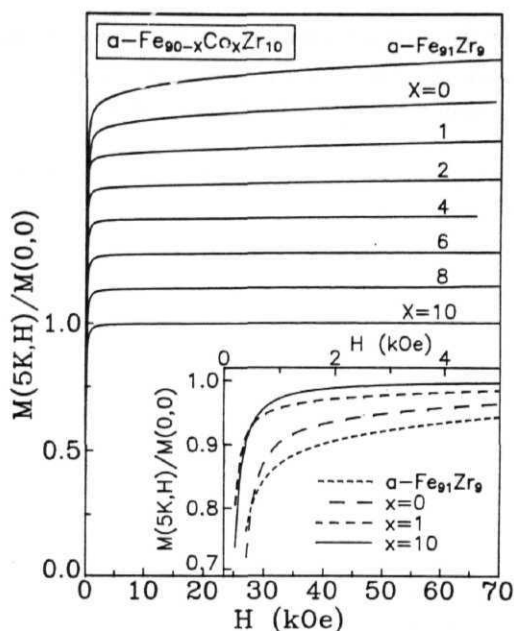


Fig. 3.10 M vs. H curves taken at $T = 5$ K; for the sake of clarity, such curves for $x = 8, 6, 4, 2, 1, 0$ and $a\text{-Fe}_{91}\text{Zr}_9$ are shifted up by the amounts 0.1375, 0.275, 0.4125, 0.552, 0.6875, 0.825 and 0.9625 with respect to the one for $x = 10$, respectively.

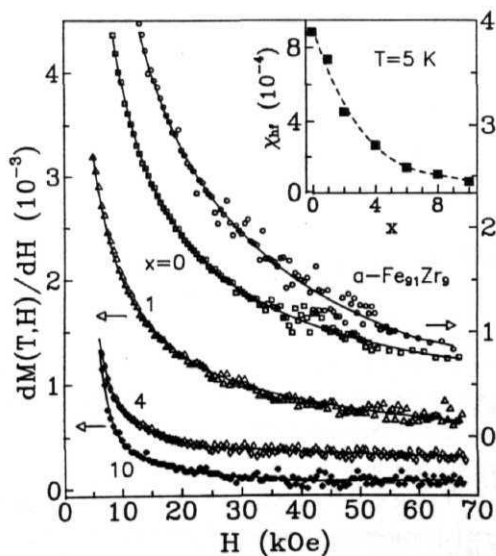


Fig. 3.11 Differential susceptibility as a function of H . Inset shows the variation of χ_{hf} with x . Note that the error bars for χ_{hf} are smaller than the size of the symbols and smooth curves (dashed curve in the inset) serve as a guide to the eye.

f_o is independent of $M + \vec{m}(\vec{r})$ and ν is the polarization index. The coefficients a , b and c , in general, depend on the cut-off wavevector q_c which is itself temperature **dependent**. The total free energy is obtained from the above expression in a straightforward manner with the result [5,11]

$$F(M) = F(0) + \frac{1}{2}[a + b(3 \langle m_{\parallel}^2 \rangle + 2 \langle m_{\perp}^2 \rangle)]M^2 + \frac{b}{4}M^4$$

with

$$F(0) = F_o + \frac{1}{2}(a + c q^2)(\langle m_{\parallel}^2 \rangle + 2 \langle m_{\perp}^2 \rangle) + \frac{b}{4}(\langle m_{\parallel}^2 \rangle^2 + 4 \langle m_{\perp}^2 \rangle^2 + 4 \langle m_{\parallel}^2 \rangle \langle m_{\perp}^2 \rangle)$$

$$\langle m_{\nu}^2 \rangle = 4\hbar \int \frac{d^3 \vec{q}}{(2\pi)^3} \int_0^{\infty} \frac{d\omega}{2\pi} n(\omega) I m \chi_{\nu}(\vec{q}, \omega)$$

$$n(\omega) = [\exp(\hbar\omega/k_B T) - 1]^{-1}$$

In Eqs. (3.6)-(3.8), $\langle m_{\parallel}^2 \rangle$ and $\langle m_{\perp}^2 \rangle$ are the thermal variances of the local magnetization parallel (\parallel) and perpendicular (\perp) to the average magnetization M , respectively, $\nu = \parallel, \perp$, $n(\omega)$ is the Bose function and $\chi_{\nu}(\vec{q}, \omega)$ is the dynamical wavevector dependent susceptibility. The magnetic equation of state, which describes the dependence of M on T and H , is obtained from Eq.(3.6) by differentiating with respect to M , i.e.,

$$\frac{1}{M} \frac{\partial F}{\partial M} = \frac{H}{M} = a + b(3 \langle m_{\parallel}^2 \rangle + 2 \langle m_{\perp}^2 \rangle) + b M^2 \quad (3.9)$$

where a and 6 , the Landau coefficients for the Stoner theory, are defined by [3,4,12]

$$a(T) = -[2\chi(0,0)]^{-1} [1 - (T/T_C^S)^2 - B S T^4] \quad (3.10)$$

$$b(T) = [2\chi(0,0) M^2(0,0)]^{-1} [1 + C T^2] \quad (3.11)$$

with

$$\chi(0,0) = N \mu_B^2 N(E_F) (T_F/T_C^S)^2 = N \mu_B^2 N(E_F) S \quad (3.12)$$

$$M^2(0,0) = (N \mu_B \mu_o)^2 = (S \gamma)^{-1} \quad (3.13)$$

$$T_F^{-2} = (\pi^2 k_B^2 / 6) \nu' \quad (3.14)$$

$$\nu' = [N'(E_F)/N(E_F)]^2 - [N''(E_F)/N(E_F)] \quad (3.15)$$

$$S = [IN(E_F) - 1]^{-1} \quad (3.16)$$

$$\gamma = \{8 N^2 \mu_B^2 N^2(E_F)\}^{-1} \{[N'(E_F)/N(E_F)]^2 - [N''(E_F)/3 N(E_F)]\} \quad (3.17)$$

$$B = (\pi^2 k_B^2/6)^2 \left\{ \frac{3}{2} \left(\frac{N'(E_F)}{N(E_F)} \right)^4 - \frac{7}{2} \left(\frac{N'(E_F)}{N(E_F)} \right)^2 \frac{N''(E_F)}{N(E_F)} + \left(\frac{N''(E_F)}{N(E_F)} \right)^2 + \frac{17}{10} \left(\frac{N'(E_F)}{N(E_F)} \right) \left(\frac{N'''(E_F)}{N(E_F)} \right) - \frac{7}{10} \left(\frac{N'''(E_F)}{N(E_F)} \right) \right\} \quad (3.18)$$

$$C = \frac{(\pi^2 k_B^2/6)}{24 N^2 \mu_B^2 N^2(E_F) \gamma} \left\{ 15 \left(\frac{N'(E_F)}{N(E_F)} \right)^4 - 25 \left(\frac{N'(E_F)}{N(E_F)} \right)^2 \frac{N''(E_F)}{N(E_F)} + 4 \left(\frac{N''(E_F)}{N(E_F)} \right)^2 + 7 \left(\frac{N'(E_F)}{N(E_F)} \right) \left(\frac{N'''(E_F)}{N(E_F)} \right) - \left(\frac{N'''(E_F)}{N(E_F)} \right) \right\} \quad (3.19)$$

In above equations, $\chi(0,0)$ and μ_o are the zero-field differential susceptibility and moment per alloy atom at 0 K, respectively, S is the Stoner enhancement factor, I is a measure of the exchange splitting of bands, N is the number of atoms per unit volume, $N(E_F)$ is the density of single-particle states at the Fermi level E_F and $N'(E_F)$, $N''(E_F)$, $N'''(E_F)$ and $N''''(E_F)$ are its first, second, third and fourth energy derivatives, and T_C^S is the Stoner Curie temperature. In the event that no external magnetic field is applied ($H = 0$), Eqs.(3.7)-(3.19) permit calculation of the temperature dependence of spontaneous magnetization for temperatures below T_C as follows. When $H = 0$, Eq.(3.9) reduces to

$$M^2(T,0) = -\frac{a(T)}{b(T)} - (3 < m_{\parallel}^2 > + 2 < m_{\perp}^2 >). \quad (3.20)$$

Generally, the coefficient C in Eq.(3.11) is negligibly small so that the term CT^2 in Eq.(3.11) can be dropped altogether at all temperatures (even for $T > T_C$) and Eqs.(3.20), (3.10) and (3.11) can be combined to yield

$$M^2(T,0) = M^2(0,0)[1 - (T/T_C^S)^2 - B S T^4] - (3 < m_{\parallel}^2 > + 2 < m_{\perp}^2 >) \quad (3.21)$$

The actual functional form of $M(T,0)$ in different temperature ranges below T_C can be derived from Eq.(3.21) with the aid of Eq.(3.7) provided due consideration is given to the fact that $< m_{\perp}^2 >$ consists of two parts: spin wave (SW) part, which is dominant at low temperatures, and spin fluctuation (SF) part which dominates at intermediate temperatures and for temperatures close to T_C . The contributions of the $< m_{\perp}^2 >_{\text{SW}}$ and $< m_{\perp}^2 >_{\text{SF}}$ parts to thermal demagnetization are obtained from Eq.(3.7) by inserting the following expressions [5] for $I \mathbf{m} \chi_{\nu}(\mathbf{q}, \omega)$ in this equation and then evaluating the integrals.

$$[I \mathbf{m} \chi_{\perp}(\vec{q}, \omega)]_{\text{SW}} = \frac{\pi}{2} \omega \chi_{\perp}(\vec{q}) [\delta(\omega - \omega(\vec{q})) + \delta(\omega + \omega(\vec{q}))] \quad (3.22)$$

and

$$[I\mathbf{m} \chi_\nu(\vec{q}, \omega)]_{SF} = \omega \chi_\nu(\vec{q}) \frac{\Gamma_\nu(\vec{q})}{\omega^2 + \Gamma_\nu^2(\vec{q})} \quad (3.23)$$

with the spin wave propagation frequency $\omega(\vec{q})$ and the *relaxation* frequency of a spontaneous spin fluctuation of wavevector \vec{q} and polarization ν (one \parallel and two \perp to \mathbf{M}) $\Gamma_\nu(\vec{q})$ given by

$$\hbar \omega(\vec{q}) = g \mu_B M(T, H) \chi_\perp^{-1}(\vec{q}) = g \mu_B M(T, H) (\chi_\perp^{-1} + c_\perp q^2 + \dots) \quad (3.24)$$

and

$$\Gamma_\nu(\vec{q}) = \gamma'_\nu q \chi_\nu^{-1}(\vec{q}) = \gamma'_\nu q (\chi_\nu^{-1} + c_\nu q^2 + \dots), \quad (3.25)$$

respectively, in the random phase approximation (RPA) at low q and for a cubic lattice. In Eqs.(3.24) and (3.25), $\chi_\nu(\vec{q}) = \chi_\nu(\vec{q}, \omega = 0)$ is a component of the static susceptibility, $\chi_\nu(\vec{q} = 0)$, g is the spectroscopic splitting factor while the parameters $\gamma' = (4/\pi) S^{-1} \chi(0, 0) v_F + \dots$ (to zeroth order in $\langle m^2 \rangle$, where v_F is the Fermi velocity) and c (the coefficient of the gradient term in the Ginzburg-Landau expansion) are *independent* of ν for small M .

At **low** temperatures ($0 \sim T \sim 0.37c$), $T < T_C^S$ and the term $B S T^d$ in Eq.(3.21) is negligibly small so that Eq.(3.21) can be approximated by

$$M(T, 0) \simeq M(0, 0) \left[1 - \frac{\langle m_\perp^2 \rangle}{M^2(0, 0)} - \frac{3}{2} \frac{\langle m_\parallel^2 \rangle}{M^2(0, 0)} \right]$$

Thermal demagnetization of $M(T, 0)$ in elemental (homogeneous) crystalline ferromagnets such as *Fe*, *Co*, *Ni* at low temperatures is mainly due to spin wave excitations (transverse spin fluctuations), i.e., the second term in Eq.(3.26) is exceedingly large compared to the third. The expression for $[I\mathbf{m} \chi_\perp(\vec{q}, \omega)]_{SW}$, Eq.(3.22), when substituted in Eq.(3.7) and the result inserted in Eq.(3.26), yields the well-known **Bloch** $T^{3/2}$ power law

$$\frac{M(T, 0)}{M(0, 0)} = 1 - \frac{g \mu_B}{M(0, 0)} \xi(3/2) \left[\frac{k_B T}{4\pi D(T)} \right]^{3/2}$$

Considering that $\chi_\perp^{-1} = \partial H_\perp / \partial M_\perp = H/M$ ($\chi_\parallel^{-1} = \partial H_\parallel / \partial M_\parallel = dH/dM$), Eq.(3.24) relates the spin wave stiffness coefficient, $D(T)$, with the spontaneous magnetization, $M(T, 0)$, through the expression $D(T) = g \mu_B c_\perp M(T, 0)$. Note that in the presence of the external magnetic field, H , the same equation yields the spin-wave energy gap equal to $g \mu_B M \chi_\perp^{-1} = g \mu_B H$. In the case of crystalline or amorphous ferromagnets with competing interactions and/or Invar systems, the contribution to $M(T, 0)$ arising from longitudinal spin fluctuations, i.e., from the third term in Eq.(3.26), cannot be ignored even at low temperatures since the orientation of a given magnetic

moment in such systems is, in general, not parallel to the direction of bulk magnetization. As a consequence, the **displacements** of the longitudinal component of magnetization from the local equilibrium value are of the same order of magnitude as the transverse displacements which give rise to spin waves. Thus, the diffusive modes ("**diffusons**") associated with the longitudinal component of magnetization (which are of hydrodynamic origin) contribute to the $T^{3/2}$ decrease of magnetization as significantly as the transverse **fluctuations** (spin waves) do. In sharp contrast with spin waves (undamped modes), diffusons represent overdamped modes that are described by Eq.(3.7) with $\mathbf{Im} \chi_{\parallel}(\vec{q}, \omega)$ given by the version of Eq.(3.23) in which $\Gamma_{\parallel}(\vec{q}) \sim D_i q^2$ [13] and D_i is the diffusion constant. The contribution due to diffusons to the decline of $M(T, 0)$ with T , computed from Eq.(3.7) and the modified version of Eq.(3.23), is given by [13]

$$\langle m_{\parallel}^2 \rangle = \frac{A}{2} \xi(3/2) \left(\frac{k_B T}{2\pi D_i} \right)^{3/2} \quad (3.28)$$

where A is a constant. According to Eqs.(3.26)-(3.28), thermal demagnetization of spontaneous magnetization is **faster** in spin systems in which diffusons do contribute, besides spin waves, to the $T^{3/2}$ dependence of $M(T, 0)$. However, unlike **magnons**, diffusons show up as a broad central (elastic) peak in the (inelastic) neutron scattering intensity versus neutron energy isotherms taken at constant values of q [13]. An immediate consequence of this prediction is that the value of spin wave stiffness coefficient deduced from the magnetization data, D_M , should be substantially *lower* [13] than that measured in the inelastic neutron scattering experiments, D_N , in such systems. Such a discrepancy between the values of D , i.e., $D_N \gg D_M$, has indeed been found in a number of Invar systems.

In the intermediate range of temperatures (typically, $0.4T_C \sim T \sim 0.8T_C$), spin-wave contribution to $M(T, 0)$ is completely swamped by the spin fluctuation contribution, which, in this temperature range, **varies** with temperature as [5]

$$\frac{\langle m_{\nu}^2 \rangle_{SF}}{M^2(0, 0)} = \frac{(3 \langle m_{\parallel}^2 \rangle + 2 \langle m_{\perp}^2 \rangle)_{SF}}{M^2(0, 0)} = \left(\frac{T}{T_0} \right)^2 \quad (3.29)$$

The T^2 dependence of $\langle m_{\nu}^2 \rangle_{SF}$ over a wide range of intermediate temperatures is basically dictated by the dominant *longitudinal* spin fluctuation contribution. Combining Eqs.(3.21) and (3.29), one obtains

$$\left[\frac{M(T, 0)}{M(0, 0)} \right]^2 = 1 - \left[\left(\frac{1}{T_C^S} \right)^2 + \left(\frac{1}{T_0} \right)^2 \right] T^2 - B S T^4 = 1 - \left(\frac{T}{T_C^S} \right)^2 + B' T^4 \quad (3.30)$$

where $(1/T_C^S)^2 = (1/T_C^S)^2 (1/T_0)^2$ and $B' = -B S$. The last term in Eq.(3.30) is normally too small to merit consideration because the coefficient B usually has a value close to zero (note that depending upon the structure of the density of states curve and hence on the relative

magnitude of various terms in Eq.(3.18), B can be either positive or negative or zero) but it can be *significant* for systems in which the Stoner enhancement factor 5 has an *extremely large* value, i.e., for very weak itinerant **ferromagnets** in which $IN(E_F) \rightarrow 1$ and hence $5 \rightarrow \infty$. From the coefficient of the T^2 term in Eq.(3.30), it is evident that local spin density fluctuations (Stoner **single-particle** excitations) **dominantly** contribute to $M(T, 0)$ if $T_0 \ll T_C^S$ ($T_C^S < T_0$). However, if $T_0 \approx T_C^S$, the contributions due to *LSF* and *SP* excitations are comparable in magnitude.

For temperature close to T_C ($0.87c \sim T \sim 0.957c$), χ_{\parallel}^{-1} is essentially approximated by χ_{\perp}^{-1} and the longitudinal and transverse fluctuations are thus treated on the same footing with the result that the temperature variation of LSF contribution in this temperature region is accurately given by [5]

$$\frac{\langle m_v^2 \rangle_{SF}}{M^2(0, 0)} = \frac{(3 \langle m_{\parallel}^2 \rangle + 2 \langle m_{\perp}^2 \rangle)_{SF}}{M^2(0, 0)} = \left(\frac{T}{T_1} \right)^{4/3} \quad (3.31)$$

where $T_1 = 2.387 D(0) \sqrt{M(0, 0)} (\hbar \gamma')^{1/4} / g \mu_B k_B$. The $T^{4/3}$ dependence of $\langle m_v^2 \rangle_{SF}$ in the above-mentioned temperature range is basically due to *transverse* spin fluctuations [7]; longitudinal fluctuations lead to a change in the magnitude of T_C but do not affect the $T^{4/3}$ dependence. Moreover, at such temperatures, the spin-splitting of bands is approaching zero, $N(E_F)$ and its derivatives are undergoing substantial changes especially for weak itinerant ferromagnets (for which the T^4 term in Eq.(3.21) is significant at intermediate temperatures) and **consequently**, the coefficient B assumes a considerably reduced value compared to that in the intermediate temperature range. Substituting the result, Eq.(3.31), for the SF term and completely dropping the T^4 term in Eq.(3.21) gives

$$\left[\frac{M(T, 0)}{M(0, 0)} \right]^2 = 1 - \left(\frac{T}{T_C^S} \right)^2 - \left(\frac{T}{T_1} \right)^{4/3}. \quad (3.32)$$

The Curie temperature T_C can be determined from Eq.(3.32) by the condition $M(T, 0) = 0$ at $T = T_C$ provided the values of T_C^S and T_1 are known. Alternatively, at $T = T_C$, Eq.(3.32) reduces to

$$1 - \left(\frac{T_C}{T_C^S} \right)^2 - \left(\frac{T_C}{T_1} \right)^{4/3} = 0. \quad (3.33)$$

From Eq.(3.33), it follows that $T_C = T_C^S$ if $T_C^S < T_1$ and $T_C = T_1$ if $T_1 < T_C^S$. In these two limits, **single-particle** excitations and enhanced local spin-density fluctuations are respectively predominant. Specifically in the latter limit, Eq.(3.32) assumes the form (cf. Eq.(3.36) and Eq.(1.22) of Chapter 1)

$$\left[\frac{M(T, 0)}{M(0, 0)} \right]^2 = 1 - \left(\frac{T}{T_C} \right)^{4/3} \quad (3.34)$$

In the paramagnetic regime ($T > T_C$), $\chi_{||}^{-1} = \chi_{\perp}^{-1} = \chi^{-1}$ and as such $\langle m_{||}^2 \rangle = \langle m_{\perp}^2 \rangle = \langle m^2 \rangle / 3$, and for reasons stated above, the terms T^4 in Eq.(3.10) and T^2 in Eq.(3.11) can be completely ignored. With this input, the magnetic equation of state, Eq.(3.9), takes the form

$$\chi^{-1}(T) = a(T) + \frac{5b}{3} \langle m^2 \rangle + b, M^2(T, H) \quad (3.35)$$

with

$$a(T) = -[2\chi(0, 0)]^{-1}[1 - (T/T_C^S)^2] \quad (3.36a)$$

and

$$b = [2\chi(0, 0)M^2(0, 0)]^{-1} \quad (3.36b)$$

Mohn and Wohlfarth [14] have calculated the temperature dependence of $\langle m^2 \rangle$ by approximating the fluctuating moment by a three-dimensional harmonic oscillator whose maximum amplitude equals the saturation moment squared. For temperatures above T_C but well below T_C^S , i.e., $T \sim T_C$, such calculations yield [14]

$$\langle m^2 \rangle = 6 k_B \chi(0, 0) T \quad (3.37)$$

Now that the inverse initial susceptibility vanishes at T_C and so does the spontaneous magnetization $M(T_C, 0)$, Eqs.(3.35)-(3.37) permit an estimation of T_C through the relation

$$1 - \left(\frac{T_C}{T_C^S} \right)^2 - \frac{T_C}{T_{SF}} = 0 \quad (3.38)$$

where

$$T_{SF} = M^2(0, 0)/1 k_B \chi(0, 0) \quad (3.39)$$

Following this approach, Mohn and Wohlfarth [14] have been able to calculate the Curie temperatures for *Fe*, *Co* and *Ni* as well as for their compounds with *Y* with a fair degree of accuracy. In the event that $T_C^S > T_{SF}$, Eq.(3.38) asserts that $T_{SF} = T_C$.

In the following text, the present findings are discussed in terms of the existing theoretical models including the one described above. Since both 'in-field' and 'zero-field' (spontaneous) magnetizations exhibit roughly the same temperature in a given temperature range but completely different temperature variations in the low-temperature region, the intermediate temperature region and the region close to T_C , it is imperative to discuss the results obtained in these regions separately.

3.2.2. Low-temperature or spin-wave region

The main observations of the present study in the low temperature region can be summarized as follows. (i) In $a - Fe_{90+y}Zr_{10-y}$ ($y = 0, 1$) and $a - Fe_{90-x}Co_xZr_{10}$ ($x = 0, 1, 2, 4, 6, 8, 10$ & 90) alloys, the spin wave excitations give dominant contribution to the thermal demagnetization of both spontaneous as well as 'in-field' magnetization for temperatures below T^* ($T^* \sim 175$ K or $0.1 T_C$) which ranges between 0.57c and 0.47b for the alloys with $y = 1, 0 < x < 10$ ($x = 90$). The values of $M(0, H)$ and $M(0, 0)$ obtained from the best *LS* fits are in good agreement (within the uncertainty limits) with those actually measured at $T = 5$ K. Such a close agreement particularly in the case of $M(T, 0)$ data is gratifying considering the fact that the spontaneous magnetization for all the alloys (except for $I = 90$) in the present study was determined for $T > 70$ K only. (ii) The present results clearly demonstrate that the temperature dependence of spin wave stiffness ' D ' cannot be ignored and $D(T)$ renormalizes with temperature in accordance with the expression, $D(T) = D(0)(1 - D^2T^2)$, predicted by the itinerant-electron model for all the alloys under investigation. (iii) The spin wave stiffness at $0K$, $D(0)$, does not depend on the external magnetic field. This finding refutes the earlier claim [15,16] that $D(0)$ is field-dependent, (iv) The $D(0)/T_C$ ratio for the alloys with $y = 0, 1, x < 6$ possesses a value close to 0.14, which is typical of amorphous alloys with competing interactions, while for the alloys with $x = 8$ and 10 , $D(0)/T_C > 0.14$. On the other hand, this ratio for $a-Co_{90}Zr_{10}$ has a value that is typical of the Co-based alloys. (v) It is evident from the concentration dependence of $T_C, D(0)$ and $M(0, 0)$ shown in Fig. 3.12 that T_C and $D(0)$ increase more or less linearly with x while the steep rise in $Af(0, 0)$ observed for $x \sim 4$ slows down considerably beyond $x = 6$ so much so that $M(0, 0)$ remains nearly unaltered for higher Co concentrations.

The existence of well-defined spin wave excitations at low temperatures (observation (i)) in amorphous alloys under investigation can be understood in terms of both localized [Eq.(3.1a)] as well as itinerant-electron [Eq.(3.27)] models. However, the observation (ii) provides evidence for itinerant behaviour in these alloys and indicates that the magnon-single-particle interactions dominate over magnon-magnon interactions. The values of spin wave stiffness coefficient at 0 K, $D(0)$, obtained from spontaneous and in-field magnetization (i.e., $M(T, 0)$ and $M(T, H)$) data agree very well with one another. However, at low temperatures, the spontaneous magnetization data yield a lower value of $D(0)$ than that obtained from the $M(T, H)$ data for the alloys with $y = 0, 1, x \sim 4$, as already reported [17] for $a - Fe_{90\pm y}Zr_{10\mp y}$ alloys. This discrepancy in the values of $D(0)$ should not be taken to imply that $D(0)$ is field-dependent but the reduced value of $D(0)$ should be viewed as signaling the softening of spin wave modes [9,17,18] in the reentrant state (in which long-range ferromagnetic order coexists with cluster spin glass order) which comes into existence at temperatures $T < T_{RE}$, well below T_C , in these alloys [19,20]. In the present work, one does not observe the softening of spin wave modes for the alloys with $y = 0, 1$ and $x < 4$ because the spontaneous magnetization data in the present case are available

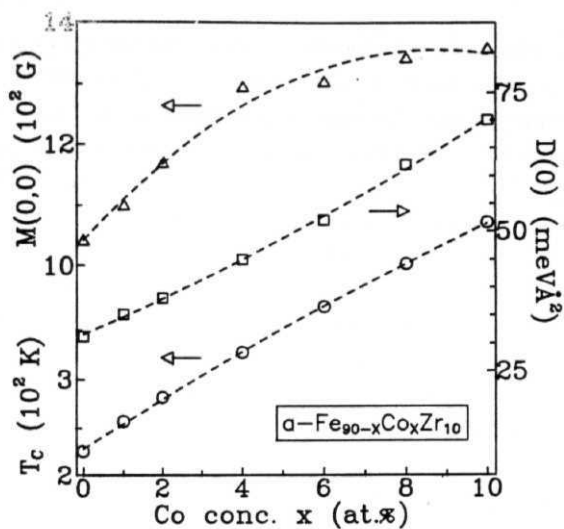


Fig. 3.12 Variation of T_c , $D(0)$ and $M(0,0)$ with Co concentration.

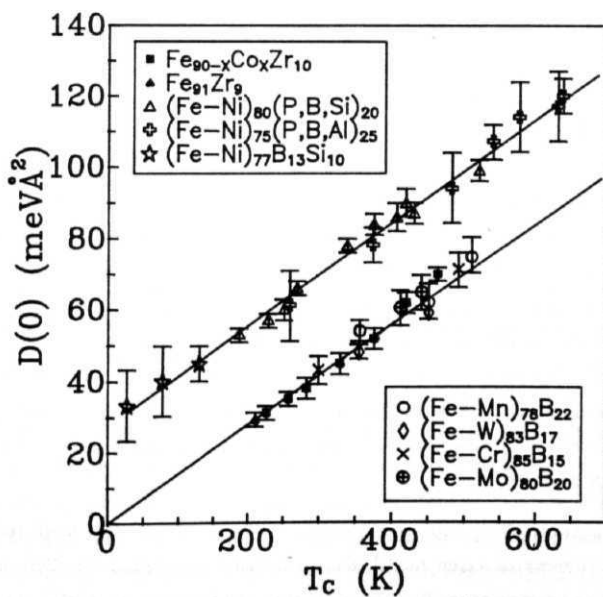


Fig. 3.13 $D(0)$ vs. T_c for a - $Fe_{91}Zr_9$ and a - $Fe_{90-x}Co_xZr_{10}$ alloys. Similar data on other systems available in the literature are also included for comparison.

only for $T > 70$ K, a temperature well above the reentrant temperature, T_{RE} . For $x \sim 6$, such a behaviour is not expected since the reentrant behaviour is completely suppressed when $x \sim 4$ [9,21]. Thus, it is not surprising that no such complication occurs in the case of $a\text{-Co}_{90}\text{Zr}_{10}$ alloy [22] which behaves like a conventional ferromagnet [19] down to the lowest temperature and for which $M(T, 0)$ data have been taken for temperatures extending from 300 K down to 4.2 K in the present work. In view of the *field-independent* value of spin wave stiffness, $D(0)$, deduced from the present study, the dependence of $D(0)$ on H reported [15,16] earlier could be an artifact of the analysis which attributes the observed thermal demagnetization to either spin-wave or **single-particle** contribution alone and neither takes into account the temperature renormalization of D nor corrects for the gap in the spin wave spectrum arising from the applied field. The plot of $D(0)$ vs. T_C for the presently investigated alloys shown in Fig. 3.13 also includes the $D(0)$ data for several 3d transition metal-metalloid amorphous alloys available in the literature. According to the theoretical prediction [23], based on the Heisenberg model, the $D(0)$ values for amorphous ferromagnetic alloys, when plotted against T_C , should fall on a straight line represented by

$$D(0) = D_o + m T_C \quad (3.40)$$

where $m = 0.144 \text{ meV}\text{\AA}^2\text{K}^{-1}$ and D_o is either finite or zero depending on whether the exchange interactions extend beyond the nearest neighbour (NN) distance or not. It is noticed from the Fig. 3.13 that the $D(0)$ values for $a - (Fe, M) - B$ alloys ($M = \text{Cr, Mn, W}$) [24-26], in which competing interactions are known to be present, fall on a straight line with slope $m = 0.144 \text{ meV}\text{\AA}^2\text{K}^{-1}$ and passing through the origin whereas the $D(0)$ values for $a - (Fe, Ni) - M(M = \text{P, B, Si, Al})$ alloys [23,27,28] fall on a different straight line parallel to the earlier one but with finite intercept $D_o = 24 \pm 3 \text{ meV}\text{\AA}^2$. This implies that the competing interactions present in the former set of amorphous alloys restrict the range of exchange interactions to the nearest neighbours only whereas the direct exchange interactions extend to the next nearest neighbours in the latter set. Following these arguments, the $D(0)$ values for the alloys with $y = 1, 0 \leq x \leq 6$ fall on the straight line with $m = 0.144 \text{ meV}\text{\AA}^2\text{K}^{-1}$ and $D_o = 0$ indicating thereby that the *competing* interactions present in these alloys confine the direct exchange interactions to nearest neighbours only. With increasing Co concentration, the competing interactions are gradually suppressed and for the alloys with $x > 6$, $D(0)$ values depart from this straight line and approach the line with finite intercept. This observation implies that exchange interactions in these alloys extend beyond the NN distance.

A linear relation between $D(0)$ and T_C of the type $D(0) = m T_C$ is also predicted by the theory, based on the itinerant-electron model, due to Katsuki and Wohlfarth [29]. With the assumption that the Curie temperature T_C is determined by the Stoner single-particle excitations alone, Katsuki and Wohlfarth [29] have derived for weak itinerant ferromagnets the following relation between $D(0)$ and T_C

$$D(0) = k_B T_C a^2 f(n) \quad (3.41)$$

where a is the nearest-neighbour (NN) distance and $f(n)$ is a function of the number of electrons per atom determined by the band structure. When the effective-mass approximation is used, Eq.(3.41) reduces to [29]

$$D(0) = (\pi k_B / 6 \sqrt{2} k_F^2) T_C \quad (3.42)$$

where k_F is the Fermi wavevector. The typical value of $k_F = 1.5 \text{ \AA}^{-1}$ when inserted into Eq.(3.42), yields the value of slope (m) as $0.014 \text{ meV \AA}^2 \text{ K}^{-1}$. This slope value is exactly one order of magnitude smaller than the observed one. Such a large discrepancy between theory and experiment is not surprising in view of the fact that the assumptions, namely, (i) T_C is determined by single-particle excitations alone and (ii) the effective-mass approximation, on which the above theory rests, are not valid in the present case. The description of different theoretical models given in Chapter 1 and section 3.2.1 asserts that even for weak itinerant **ferromagnets** the Stoner theory, which regards the single-particle excitations as the sole cause of thermal demagnetization in such systems, invariably *overestimates* T_C and that this theory has to be modified to include the effect of local spin-density fluctuations on the thermal demagnetization if a correct estimate of T_C and a proper description of **Curie-Weiss** behaviour of magnetic susceptibility for $T > T_C$ is sought. Thus, there is a dire necessity of reviewing a relation of the type Eq.(3.41) or (3.42) within the framework of a theory which includes local spin density fluctuations, besides the spin wave and Stoner single-particle excitations, i.e., in the light of the spin fluctuation model described in section 3.2.1.

The results of the present investigation that provide a strong evidence for the existence of well-defined spin wave excitations in the amorphous alloys in question are in direct contradiction with the earlier claim [30], based on inelastic neutron scattering experiments, that no propagating features, indicative of spin waves, are noticed in the constant q scans at any temperature below T_C in the wavevector transfer range $0.05 \text{ \AA}^{-1} < q < 0.12 \text{ \AA}^{-1}$ in a-**Fe_{90±y}Zr_{10∓y}** alloys. In order to resolve this apparent contradiction, recourse is taken to the *infinite* three-dimensional (3D) ferromagnetic (FM) matrix plus *finite* FM spin clusters model proposed by **Kaul** for **amorphous** ferromagnets [17,18,31-33]. In this phenomenological model, it is postulated that (a) the spin system for $T < T_C$ consists of an *infinite 3DFM* matrix and *finite* spin clusters (composed of a set of **ferromagnetically** coupled spins), which are embedded in, but '**isolated**' from, the FM matrix by zones of frustrated spins surrounding the finite clusters (Fig. 3.14(a)), (b) a wide distribution in the size of spin clusters exists, and (c) the spin clusters are not completely isolated in that the long-range **RKKY** interactions provide a *weak* coupling between the finite clusters and the FM matrix and also between the clusters themselves. The mechanism that can lead to such a spin structure can be understood as follows. In view of the fact that the cooling rate is not uniform throughout the melt during the melt-quenching process, the nearest-neighbour

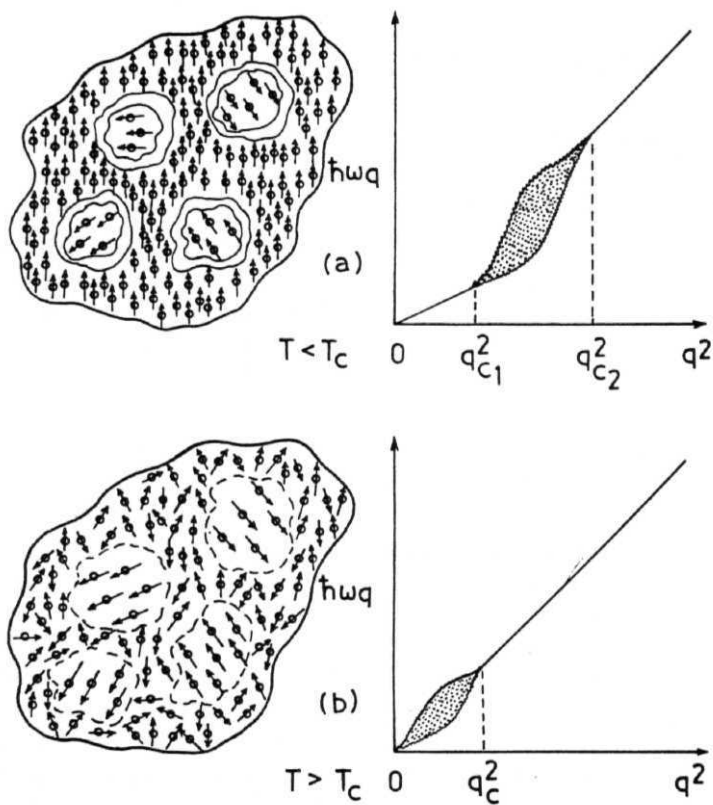


Fig. 3.14 Schematic depiction of the infinite ferromagnetic matrix plus finite spin clusters model and the spin-wave dispersion relation that it predicts for (a) $T < T_C$ and (b) $T > T_C$.

(NN) distance between the atoms varies erratically from one portion of the amorphous alloy to the other so much so that the *average* NN distance is appreciably *greater* in certain *microscopic regions* than in the remaining bulk. Considerable mismatch in the NN interatomic spacings is, therefore, expected to occur within the zones that separate these microscopic regions from the bulk. As a consequence of this mismatch, large 'quenched-in' local stresses exist in these zones. For a magnetic alloy system in which the majority of the atoms carry a magnetic moment, the microscopic regions and the bulk can be identified as the finite spin clusters and infinite matrix, respectively. If the average NN distance (r_{NN}) between the spins in the **matrix** just exceeds the critical distance, r_c , at which the exchange integral changes sign in the **Bethe-Slater** curve, ferromagnetic coupling exists not only between the spins in the infinite matrix but also between those within the finite spin clusters (ferromagnetic coupling being stronger in the finite clusters than in the bulk); whereas the spins contained in the zones surrounding the clusters get 'frustrated' due to both a sizable magnetostrictive coupling (since the amorphous alloys in question exhibit Invar behaviour [34]) between the spins and the 'quenched-in' local stresses and *competing* interactions between the spins arising due to the fluctuation in the NN distance around r_c within these zones. Within the framework of this model, the following explanation can be offered for the absence of spin-wave-like features in the inelastic neutron scattering (INS) spectra [30] taken in a certain wavevector transfer range. Though spin waves, whose stiffness is controlled by the strength of exchange interaction between spins in the **FM** matrix, are excited for **all** wavevectors in the infinite ferromagnetic matrix at temperatures $T < T_C$, **all** of them do not propagate through the matrix unhindered for the following reasons. The spin waves for which q falls within the range $q_{c1} < q < q_{c2}$ (Fig. 3.14(a)), where q_{c1} and q_{c2} are the caliper dimensions of the smallest (largest) and the largest (smallest) spin cluster in the wave vector (direct) space, get *severely damped* due to coupling to, and intense scattering from, the finite spin clusters. Therefore, if the INS measurements are performed in the wavevector range $q_{c1} < q < q_{c2}$, only a broad "diffusive-like" spectrum with no propagating features would be observed at any temperature below T_C . By contrast, **constant- q** scans recorded at the wavevector values that lie outside this q range should exhibit well-defined spin-wave peaks for all temperatures below T_C but the nature and origin of these spin waves now depend on whether $q < q_{c1}$ **or** $q > q_{c2}$. In the long-wavelength limit (i.e., when $q < q_{c1}$), well-defined spin waves can be excited in the FM matrix only and that too at temperatures well below T_C because of the low energy-cost involved, and such spin waves propagate through the matrix without any significant damping. On the other hand, in the short-wavelength limit (i.e., when $q > q_{c2}$) spin waves can be excited in the FM matrix as well as in the finite clusters; in the latter case, either at very high incident neutron energies when the temperature is low or at high temperatures for the range of incident neutron energies conventionally used. However, but in this case (i.e., when $q > q_{c2}$), the spin waves in FM matrix are expected to get damped due to strong exchange fluctuations (caused by the fluctuation in the NN distance between spins) as contrasted with the intra-cluster spin waves which should be relatively well-defined because the exchange coupling

between the spins within the clusters is much stronger and has a much narrower distribution. Thus, the INS spectra should consist of reasonably sharp spin-wave peaks signaling the existence of **intra-cluster** spin wave excitations superposed on very broad "**diffusive-like**" structure arising from the overdamped FM spin waves. The **magnon** dispersion relation for all q and $T < T_C$, schematically depicted in Fig. 3.14(a), indicates that the slope of ω , versus q^2 straight line, i.e., the spin wave stiffness coefficient, D , is larger for $q > q_{c2}$ than for $q < q_{c1}$ because the exchange coupling between the spins in the clusters is much stronger than that in the FM matrix. As the temperature is increased through T_C , exchange coupling between spins in the FM matrix weakens, the frustration zones start 'melting' away and the finite clusters grow in size by polarizing spins originally belonging to the frustration zones (as well as some spins of the FM matrix) and interact with one another through individual spins of the matrix. For $T > T_C$, the long-wavelength spin waves characteristic of the FM matrix are completely absent and well-defined intra-cluster spin waves can be excited only for $q > q_c$ (Fig. 3.14(b)) but now $q_c \ll q_{c2}$. In view of the earlier finding [33] that in $a - Fe_{90\pm y}Zr_{10\mp y}$ alloys the *average* cluster size for $T \sim T_C$ is $\sim 25 \text{ \AA}$, the range of q values ($0.05 \text{ \AA}^{-1} < q < 0.12 \text{ \AA}^{-1}$) covered in the INS experiments [30] falls well within the range $q_{c1} < q < q_{c2}$ in figure 3.14(a) and hence no resolvable spin-wave peaks are found in the INS spectra. In view of the foregoing arguments, the INS measurements for $T < T_C$ need to be extended to q values *low enough* ($q < 0.05 \text{ \AA}^{-1}$) to observe well-defined spin waves, characteristic of the 3D FM matrix.

In Co containing alloys, the **Fe-Co** and **Co-Co** exchange interactions are ferromagnetic and much stronger than the **Fe - Fe** exchange coupling with the result that a progressive replacement of **Fe** by **Co** in a $- Fe_{90-x}Co_xZr_{10}$ alloys gradually suppresses the competing interactions in the frustration zones. This, in turn, leads to breaking up of finite spin clusters into smaller ones and merging of some of them with the infinite FM matrix. Hence, as the **Co** concentration is increased, the number of spins within the FM matrix increases at the expense of those forming finite clusters, finite clusters shrink in size and decrease in number, and cluster size distribution narrows down while the average distance between the FM matrix spins increases and the spins within the FM matrix tend towards a collinear configuration. As a consequence, the exchange coupling increases in strength (hence both $D(0)$ and T_C also assume higher values; in conformity with the observation (v) mentioned above) and the spin system becomes more and more homogeneous with increasing **Co** concentration. This implies that the shaded region (Fig. 3.14(a)) in the magnon dispersion curve between q_{c1} and q_{c2} gradually shrinks and shifts to higher q values with increasing **Co** concentration so as to finally disappear at some value of x . These arguments assert that, if the inelastic neutron scattering (INS) experiments in the same range of q values (i.e., $0.05 \text{ \AA}^{-1} < q < 0.12 \text{ \AA}^{-1}$) as used earlier [30], are performed on a $- Fe_{90-x}Co_xZr_{10}$ alloys, the **constant- q** scans exhibiting broad **diffusive-like** structure at zero or even low **Co** concentrations should gradually acquire the propagating features corresponding to well-defined long wavelength spin wave excitations even in this wavevector transfer range at

higher Co concentrations. Such a behaviour has indeed been observed recently [35] in the INS spectra taken in the above-mentioned q range on the homologous alloy series $a\text{-Fe}_{90-x}\text{Zr}_{10}$. The competing interactions present in the alloys with $x \sim 6$ give rise to slight canting of the spins in the FM matrix at low temperatures, $T \sim T_{RE}$, due to large local random anisotropy fields that come into play when spin clusters freeze in random orientations [17]. The canted spin arrangement, in turn, reduces net exchange coupling between the FM matrix spins, leading to softening of FM spin wave modes, and makes the saturation in magnetization extremely **difficult** to achieve even at fields as high as 150 kOe [15,16,36] and temperatures as low as 4.2 K. As the Co concentration is increased, the competing interactions (and hence the reentrant behaviour at low temperatures) get (gets) progressively suppressed with the result that the canting angle between the spins decreases and the spin arrangement becomes increasingly collinear. This explains the sharp rise in spontaneous magnetization at 0 K, $M_S = M(0,0)$, for compositions $x \sim 4$ and slower increase or even saturation in $M_S(x)$ curve at higher Co concentrations (Fig. 3.11). The above arguments also provide a straightforward interpretation for the observation (Fig. 3.10 and inset of Fig. 3.11) that at low temperatures, saturation in magnetization is achieved at lower fields for compositions $x > 4$ than for $x \sim 4$ and that χ_{hj} decreases rapidly for $x < 6$ but remains essentially constant for $x > 6$.

Another consequence of the **non-collinear** ground state spin arrangement in amorphous $\text{Fe}_{90+y}\text{Zr}_{10-y}$ and a - $\text{Fe}_{90-x}\text{Co}_x\text{Zr}_{10}$ alloys with $y \sim 2$ and $x \sim 4$ is that the diffusive modes associated with the longitudinal component of magnetization ("diffusons") do contribute, besides magnons, to the $T^{3/2}$ decrease of magnetization, Eq.(3.28), and thereby *lower* spin wave stiffness coefficient, $D_M(0)$ in magnitude compared to the value that $D_N(0)$ possesses when such a contribution (due to diffusons) is totally absent, as happens to be the case in collinear **ferromagnets**. Considering that diffusons give rise to an elastic peak [13] in the INS spectra, the value of spin wave stiffness determined from such measurements, i.e., $D_N(0)$, should greatly exceed $D_M(0)$ in these systems. Such a disparity between $D_N(0)$ and $D_M(0)$ is expected to reduce continuously with decreasing y or increasing x as the spin orientations tend towards a collinear configuration. This process continues till a value of x is reached beyond which $D_N(0)$ equals $D_M(0)$ because by then **non-collinearity** is fully suppressed. This prediction needs to be verified by INS measurements performed at very low q ($q \ll 0.05 \text{ \AA}^{-1}$) on a - $\text{Fe}_{90-x}\text{Co}_x\text{Zr}_{10}$ alloys. It should be emphasized at this stage that a progressive suppression of Invar effect and reentrant behaviour with Co substitution is *accompanied* by an increase of $D_M(0)$ towards $D_N(0)$ and an enhancement of both $D_M(0)$ and $D_N(0)$ such that the difference $D_N(0) - D_M(0)$ diminishes in magnitude as x increases. Yet another interesting aspect of spin waves in weak itinerant ferromagnets is that in the absence of any spin-dependent (spin-orbit or magnetic) impurity scattering process, *spin diffusion* provides the sole intrinsic mechanism for relaxation of the long-wavelength, low-frequency modes of spin-density fluctuations. This diffusive relaxation causes

a damping of spin waves (proportional to the spin-diffusion constant) which is temperature-independent and varies with q as q^4 [37]. Consistent with this theoretical result, recent inelastic neutron scattering (INS) experiments [35] on the spin dynamics of amorphous $\text{Fe}_{90-x}\text{Ni}_x\text{Zr}_{10}$ alloys have revealed a temperature-independent spin-wave linewidth which exhibits a q^4 or q^5 dependence. Temperature-independent spin-wave damping proportional to q^5 is also predicted by the random Heisenberg model of localized spins [38,39] in which damping of spin waves arises from the scattering of magnons from fluctuations in the exchange interaction but this damping mechanism yields a value for magnon linewidth which is an order of magnitude *smaller* than the observed values.

3.2.3. Intermediate temperature region

In the intermediate temperature range ($T'' < T < T'''$), the main observations are as follows. (i) The temperature dependence of both 'in-field' and spontaneous magnetization is best described by the appropriate versions of Eqs.(3.56) (with $C \simeq 1$) and (3.3c) (with $C'' \sim 1$) or (3.3a) for the alloys with $y = 0, 1, x = 0, 1, 2, 4, 6$ and $x = 8, 10, 90$, respectively, (Figs. 3.2(b), 3.2(d), 3.5(a) and 3.9(a)). (ii) In the absence of the external magnetic field, the coefficient of the T^2 term in Eq.(3.56) (with $C \sim 1$ and $H = 0$) or Eq.(3.3c)(with $C'' \simeq 1, H = 0$) decreases with decreasing y or increasing x (Fig. 3.6(a)). (iii) For a given composition, the coefficient of the T^2 term, i.e., A in Eq.(3.5b) and A'' in Eq.(3.3c), decreases with increasing applied field (Figs. 3.6(a) and 3.15). Note that (a) the field dependence of A'' is not shown in figures 3.6(a) and 3.15 since the values of A'' at $H = 0$ and $H = 10$ kOe only have been determined in the present work and (b) H_{eff} in Fig. 3.15 (and those subsequent figures in which it appears) denote the effective field defined as $H_{eff} = H - 4\pi N < M >$, where N is the demagnetizing factor and $< M >$ is the *average* value of magnetization over the temperature interval ($T^{**} < T < T'''$) of the fit based on Eq.(3.5b) or Eq.(3.3c). The error bars for H_{eff} (less than or equal to the symbol size in the above-mentioned figures) are computed taking into account both the uncertainty in H and deviations of the extreme values of M from its average value, i.e., $M(T^{**}) - < M >$ and $< M > - M(T''')$.

Now that the least-squares fits to the $M(T, H)$ or $M(T, 0)$ data based on Eqs.(3.56) and (3.3c) yield values for the parameters C and C'' that are close to unity and *independent* of the field H (Tables 3.1 and 3.2), Eq.(3.5b) can be rewritten in the form

$$[M(T, H)/M(0, H)]^2 = 1 - 2A(H)T^2A^2(H)T^4 \quad (3.43)$$

where H is either *finite* or *zero*. Eq.(3.43) obviously reduces to

$$[M(T, H)/M(0, H)]^2 = 1 - 2A(H)T^2, \quad (3.44)$$

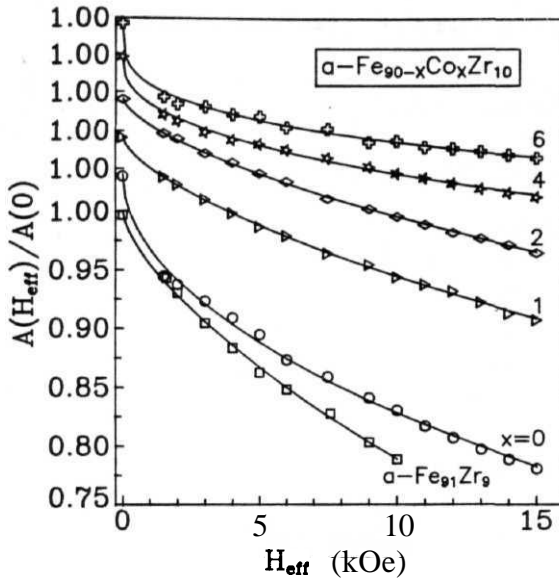


Fig. 3.15 Variation of the coefficient $A(H_{eff})$ with H_{eff} for different Co concentrations and $a\text{-Fe}_{91}\text{Zr}_9$.

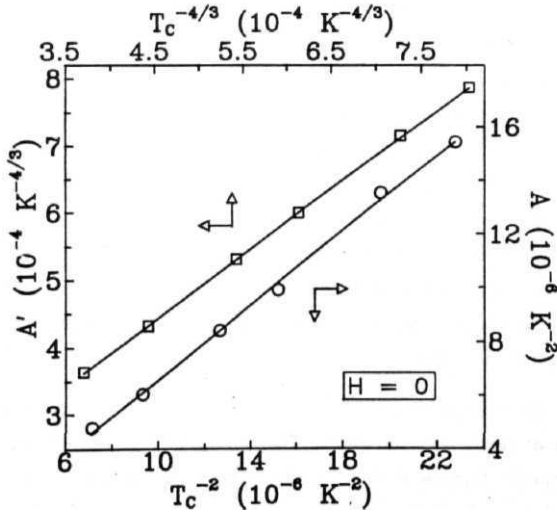


Fig. 3.16 $A(H_{eff}=0)$ vs. T_C^{-2} and $A'(H_{eff}=0)$ vs. $T_C^{-4/3}$ plots

i.e., Eq.(3.3c) with $C'' \approx 1$ and $A''(H) = 2A(H)$ or Eq.(3.3a) with

$$T_C^{-2} = 2A(0), \quad (3.45)$$

when the T^4 term in Eq.(3.43) is negligibly small compared to the T^2 term.

In view of Eq.(3.30), the finding that the expressions (3.43) and (3.44) reproduce closely the observed variation of $M(T, 0)$ and $M(T, H)$ with temperature in the alloys with $y \leq 1, 0 \leq x \leq 6$ and $x = 8, 10$ and 90 , respectively, (observation (i) mentioned above) implies that the T^4 term in Eq.(3.30) makes a significant contribution to $M(T, 0)$ and $M(T, H)$ only for the first set of alloys; presumably due to a sizable value of the Stoner enhancement factor S . To verify this, values of $\chi(0, 0)$ and $M(0, 0)$ (and hence μ_0) for each alloy are computed respectively from the slope and intercept (on the ordinate) of the Arrott (M^2 vs. H/M) plot isotherm at $T = 5$ K, constructed out the $M(T, H)$ data taken at 5 K (Fig. 3.10). From the values of these quantities so obtained and listed in Table 3.3, one can, in principle, calculate various band and exchange parameters using Eqs.(3.12) - (3.19) provided the actual shape of the density of states (DOS) curve for each composition is known. In the absence of any such information, values of S displayed in Table 3.3 are deduced from Eq.(3.12) by making use of the presently determined values of $\chi(0, 0)$ and those of $N(E_F)$ estimated from the coefficient $\gamma_E = (\nu^2 k_B^2/3)N(E_F)$ of the electronic specific heat, reported in the literature [40,41] for the glassy alloys in question, after making corrections [41] for the electron-phonon enhancement. Note that the values of $N(E_F)$ for Co concentrations other than $x = 0, 4, 10$ and 90 are the interpolated values obtained by passing a cubic spline through the data points in the $N(E_F)$ vs. x plot [40] over the concentration range $0 < x < 30$. The data presented in Table 3.3 clearly demonstrates that (a) S indeed possesses large values for $x \sim 6$ and decreases rapidly with increasing x and (b) Stoner parameter I and hence the exchange splitting of bands $AE = IM(0, 0)/N\mu_B$ increases with x while $N(E_F)$ decreases with x such that the Stoner criterion for ferromagnetism, i.e., $IN(E_F) > 1$, is satisfied for all the compositions. A direct consequence of the increase in AE with x is that the excitation of single particles and more so the formation of correlated **particle-hole** pairs (local spin-density fluctuations) becomes increasingly difficult as x is increased. This leads to a progressive suppression of spin fluctuations with Co substitution (Fig. 3.6(a)).

Considering the well-known fact that by holding the weak temperature dependence of the thermal density of states (the one-electron density of states times the Fermi function) solely responsible for the T^2 decrease of $M(T, 0)$, the Stoner model grossly overestimates $T_C, T_C^2 > T_0$ in Eq.(3.30) and as such $T_0 \leq T_C$. Alternatively, local spin-density fluctuations **dominantly** contribute to the thermal demagnetization of $M(T, 0)$ in the intermediate temperature range. This inference is vindicated by the observation that the values of T_C^* calculated from the relation $T_C^* = [2A(0)]^{-1/2}$ [cf. Eqs.(3.30) and (3.43)] using the presently determined values of $A(0)$ are consistently lower than the actual T_C values (Table 3.4), i.e., T_C^*/T_C ratio ranges between 0.85

Table 3.4: Comparison of the spin fluctuation temperatures with the Curie temperature. ^aValues obtained from the estimates of $A''(0)$ given in Table 3.2.

conc. y/x	T_C (K)	T_C^* (K)	T'_c/T_c	$\mathbf{r},$ (K)	
$V=l$	209.66(5)	180(1)	0.86(1)	213(1)	1.016(5)
$x = y=0$	225.00(5)	193(3)	0.86(1)	229(2)	1.018(9)
$x=1$	256.66(5)	227(1)	0.88(1)	261(2)	1.017(9)
$x=2$	281.60(5)	244(3)	0.87(1)	286(3)	1.016(10)
$x=4$	327.95(5)	286(2)	0.87(1)	334(3)	1.018(10)
$x=6$	374.75(5)	323(6)	0.86(2)	380(3)	1.014(9)
$x=8$	419.50(10)	[362(5)] ^a	[0.86(1)] ^a		
$x=10$	462.50(10)	[398(6)] ^a	[0.86(1)] ["]		
$x=90$		[1600(80)]			

and 0.87 for the alloys with $y = 0, 1$ and $x < 6$. If T_C^* for the alloys with $x = 8$ and 10 is computed from the relation $T_C^* = [A(0)]^{-1/2}$ (i.e., ignoring the T^4 term in Eq.(3.30) and comparing Eq.(3.30) with the zero-field ($H = 0$) version of Eq.(3.44)), T_C^*/T_C ratio for these samples too comes out to be $0.86T_C$. Since this ratio is nearly constant (~ 0.86) over this composition range, it is not surprising that the coefficient $A(0)$ scales with T_C^* (Fig. 3.16) in accordance with Eq.(3.45). The result $A(0) \propto T_C^{*-2}$ together with the finding that T_C increases with x (Fig. 3.12) is the manifestation of the fact that the spin fluctuations get progressively suppressed as the Co concentration increases. When Co concentration is increased beyond $x = 6$, the contribution to $M(T, 0)$ arising from spin fluctuations diminishes at a rapid rate with the result that it is reduced to an insignificant level for compositions in the vicinity of $x = 90$. In other words, the decline of $M(T, 0)$ with T in the intermediate temperature range in $a - \text{Co}_{90}\text{Zr}_{10}$ is mainly due to Stoner single-particle excitations. This deduction is further supported by the 'in-field' magnetization data, as shown below. Thus, $a - \text{Co}_{90}\text{Zr}_{10}$ represents the extreme situation in which the particle-hole pair excitations are *weakly* correlated and $T_C^* \simeq T_C$. In such a case, Eq.(3.30) reduces to the expression $[M(T, 0)/M(0, 0)]^2 = 1 - (T/T_C)^2$, which forms an adequate description of the observed variation of $M(T, 0)$ with T in this alloy (Fig. 3.3(b)).

A close scrutiny of the Co concentration dependence of $A(H)$ for a few representative values of H depicted in Fig. 3.6(a) reveals that the $A(H)$ vs. x curves for finite fields are similar in shape to the one for $H = 0$ but are shifted down by an increasing amount with respect to it for higher field values. For a given concentration, the field dependence of $A(H_{eff})$ is clearly brought out by the data presented in figure 3.15. A rapid decline in the magnitude of $A(H_{eff})$ with increasing H_{eff} is a clear indication of the suppression of spin fluctuations with field. The effect of increasing magnetic field in the itinerant-electron picture is to increase the splitting between spin-up and spin-down sub-bands and hence, in analogy with the influence of increasing AE by Co substitution on spin fluctuations discussed above, field, like x , strongly suppresses local spin-density fluctuations. The theoretical attempts [7,42] made so far to quantify suppression of spin fluctuations by external magnetic field within the framework of the spin fluctuation model cannot be regarded as satisfactory because a *large number* of adjustable parameters and the *unrealistic* electron-gas model have been used to achieve quantitative agreement with the experimental $M(T, H)$ data. Moreover, the same $M(T, H)$ data on Sc_3In have found qualitative explanation in terms of a band model [43] which does not take into account the local spin-density fluctuations and differs from the Stoner model in that, in addition to the Stoner exchange interaction parameter I , it has another interaction parameter (a nearest-neighbour ferromagnetic exchange interaction J) that gives rise to a temperature- and magnetization-dependent band narrowing. However, even this qualitative agreement between the experimental data and the variation predicted by the latter theoretical treatment [43] cannot be taken seriously because this model fails to produce the experimental variations, e.g., the $T^{4/3}$ dependence of $M(T, 0)$ and $T^{5/3}$ dependence of resistivity in certain temperature ranges, which the spin fluctuation model

successfully docs. The limitation of the spin fluctuation model to make specific predictions about the effect of field on spin fluctuations stems from the fact that spin fluctuations do not explicitly depend on the external magnetic field H but, by virtue of their dependence on M , indirectly couple to H via magnetization. Another point that merits attention at this stage is that while attempting a quantitative comparison between theory and experiment [7,42] due consideration has not been given to the observation that different types of excitations are primarily responsible for the decay of magnetization in different temperature ranges. In order to arrive at the exact functional dependence of the coefficient A in Eq.(3.5b) or Eq.(3.43) on H , a number of functional forms that could reproduce the observed variation of A with H were tried with the result that the empirical relation

$$A(H_{eff}) = A(0)[1 - B H_{eff}^n] \quad (3.46)$$

with the choice of the parameters B and n given in Fig. 3.17 describes the $A(H)$ data the best, as is evidenced from the quality of fits (continuous curves), based on Eq.(3.46), in figure 3.15. It is also noticed from Fig. 3.15 that the rate at which the coefficient A decreases with H_{eff} slows down considerably as x increases, e.g., $\langle dA/dH_{eff} \rangle_{x=6} \simeq (1/7) \langle dA/dH_{eff} \rangle_{x=0}$, where $\langle \rangle$ denotes the average value in the range $1.5 \text{ kOe} < H_{eff} < 15 \text{ kOe}$. Considering that in the absence of H , progressive substitution of Fe by Co leads to a strong suppression of fluctuations, it is not surprising that the coefficient A is far less sensitive to H for higher Co concentrations than it is for lower Co concentrations. An extreme situation arises when Co concentration approaches $x = 90$ in that the 'zero-field' and 'in-field' magnetization data even for fields as high as 15 kOe coincide with one another at all temperatures below 300 K (Fig. 3.3). This observation implies that spin fluctuations are completely suppressed as this concentration ($Co_{90}Zr_{10}$) is reached and no further suppression is possible with the external field. Thus the Stoner single-particle excitations are solely responsible for thermal demagnetization in this temperature range in $a - Co_{90}Zr_{10}$. Note that the exchange field (proportional to spontaneous magnetization) when $H = 0$ plays the same role as the external field so far as their influence on the spin fluctuations is concerned.

3.2.4. Temperatures close to T_c

In this temperature range ($T' < T < T''$), the main observations can be summarized as follows. (i) Appropriate versions of Eqs.(3.3d) (with $C' \simeq 1$) and (3.36) yield the best description for the temperature dependence of both 'in-field' and 'zero-field' magnetization in the temperature interval $V < T < T''$ for the alloys with $y = 0, 1$ and $x < 6$ (Figs. 3.2(c), 3.5(b) and 3.9(b)). (ii) When $H = 0$, the coefficient of the $T^{4/3}$ term in Eq.(3.3d) (with $C \sim 1$ and $H = 0$) or Eq.(3.36) decreases rapidly with decreasing y or increasing x (Fig. 3.6(b)). (iii) For

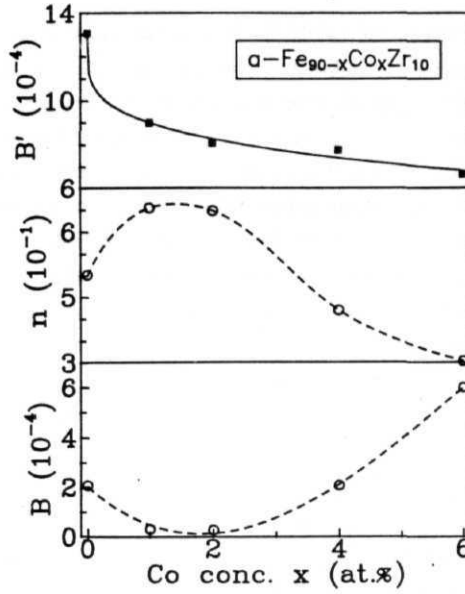


Fig. 3.17 Fit parameters for the LS fits to the $A(H_{eff})$ and $A'(H_{eff})$ data based on Eqs.(3.46) and (3.47), respectively.

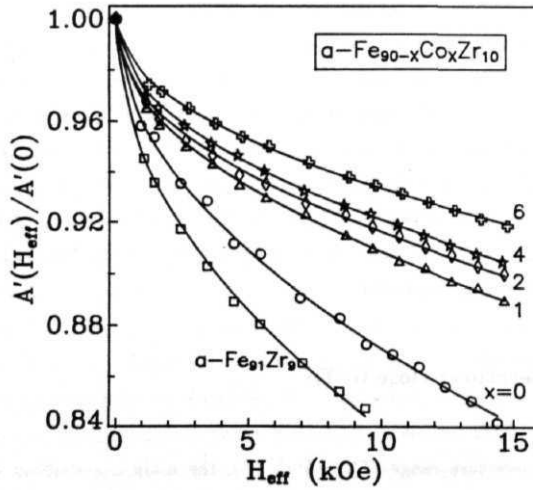


Fig. 3.18 Variation of $A'(H_{eff})$ with H_{eff} for different Co concentrations and $a - Fe_{91}Zr_9$.

a given composition, the coefficient $A'(H)$ of the $T^{4/3}$ term in Eq.(3.3d) (with $C' \sim 1$) decreases with increasing applied field (Fig. 3.6(b) and 3.18). In view of Eq.(3.32), the observation that Eq.(3.36) closely reproduces the temperature variation of $M(T, 0)$ implies that for the alloys in question, $T_C^S > T_1$ and hence $T_1 \sim T_C$, i.e., Eq.(3.34) is satisfied in the present case. This deduction is not only consistent with the assertion made in the preceding subsection that $T_C^S \gg 0.86 T_C$ but also permits determination of T_C from the observed values of $A'(0)$ when the relation $T_C = [A'(0)]^{-3/4}$ is used. The values of T_C so computed are very close to the actual T_C values (Table 3.4) but lie consistently higher. The deviation from actual values, however, does not exceed 5 K in any case. Such a close agreement, besides testifying to the correctness of the above inference that $T_1 \sim T_C$, indicates that $A'(0)$ should scale with $T_C^{-4/3}$. That this is indeed the case is demonstrated by the data displayed in Fig. 3.16. Since T_C increases roughly linearly with x (Fig. 3.12), the finding that $A'(0) \propto T_C^{-4/3}$ (Fig. 3.16) offers a simple explanation for the decline of $A'(0)$ with x (Fig. 3.6(b)) along the lines already mentioned in the subsection 3.2.3.

In an attempt to find out the exact functional dependence of the coefficient A' of the $T^{4/3}$ term in Eq.(3.3d) on H , several expressions representing different functional forms were fitted to the $A'(H)$ data. Out of these expressions, the one that yielded the best least-squares (LS) fit to the $A'(H)$ data has the form

$$A'(H_{eff}) = A'(0)[1 - B'H_{eff}^{n'}] \quad (3.47)$$

Such LS fits with the choice of parameter B' given in Fig. 3.17 and $n' = 0.50 \pm 0.02$ are represented by continuous curves in Fig. 3.18. An excellent agreement between the best LS fits based on Eq. (3.47) and $A'(H_{eff})$ data is evident from this figure. The $H^{1/2}$ power law dependence of A' on H_{eff} for the compositions $y = 0, 1$ and $x < 6$ is clearly brought out by the $A'(H_{eff})/A'(0)$ versus $H_{eff}^{1/2}$ plot shown in Fig. 3.19. Note that a similar study on the alloys with $x = 8, 10$ and 90 for temperatures close to T_C was not undertaken for the following reason. These alloys have high Curie temperatures ($T_C \gg 300$ K) so that an appreciable interference of the data from structural relaxation-induced spurious effects is expected at such temperatures. Since the data cannot be unambiguously corrected for such effects, the studies of this type are bound to be inconclusive. While the exponent n' is independent of composition in the range $0 < x < 6$, the slope B' of the $A'(H_{eff})/A'(0)$ vs. $H_{eff}^{1/2}$ straight lines (the IS fits) in Fig. 3.19 decreases with x in accordance with the empirical relation $B'(x) = B'(0)[1 - \alpha x^\beta]$ in which $B'(0) = 1.30 \pm 0.02$, $\alpha = (4.15 \pm 0.05) \times 10^{-4}$ and $\beta = 0.25 \pm 0.02$. The continuous curve through the $B'(x)$ data in Fig. 3.17 denotes the LS fit based on the above expression with the choice of parameters just stated. The spin fluctuation model, described in section 3.2.1, provides an adequate theoretical justification for the observed $H_{eff}^{1/2}$ dependence of $A'(H_{eff})$ as is evidenced below. In the temperature range under consideration, the Bose function $n(\omega)$ and χ_{11}^{-1} can be approximated by $k_B T / \hbar \omega$ and χ_{11}^{-1} , respectively. Eqs.(3.7), (3.8), (3.23) and (3.25), when

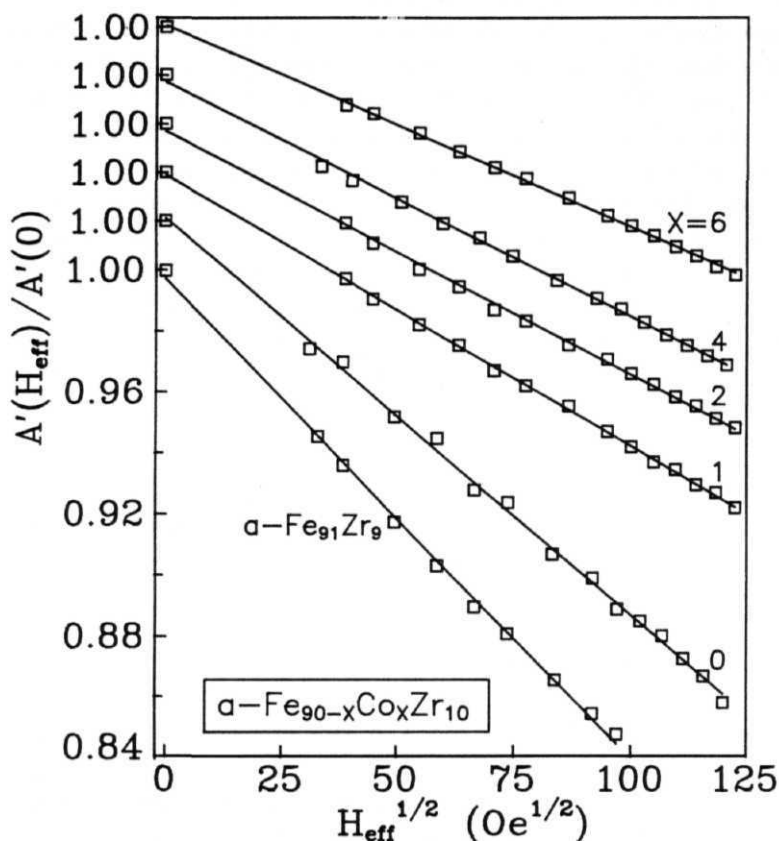


Fig. 3.19 $A'(H_{\text{eff}})/A'(0)$ vs. $H_{\text{eff}}^{1/2}$ plots for different compositions.

combined and solved for $\langle m^2 \rangle$ with these assumptions, yield [15]

$$\langle m^2 \rangle = \frac{1}{2\pi^2} g \mu_B M(T, H) \left(\frac{k_B T}{D} \right) q_c \left[1 - \frac{\pi}{2q_c} \left(\frac{g \mu_B}{D} \right)^{1/2} \sqrt{H} \right] \quad (3.48)$$

where the temperature-dependent cut-off wavevector q_c is given by [5]

$$q_c \simeq (k_B T / \hbar \gamma'_\nu c_\nu)^{1/3}. \quad (3.49)$$

Substituting for D and q_c in the prefactor, Eq.(3.48) can be cast into the form

$$\langle m^2 \rangle = \frac{1}{2\pi^2 \hbar^{1/3} \gamma'^{1/3}_\nu} \left(\frac{k_B}{c_\nu} \right)^{4/3} T^{4/3} \left[1 - \frac{\pi}{2q_c} \left(\frac{g \mu_B}{D} \right)^{1/2} \sqrt{H} \right] \quad (3.50)$$

Use of Eq.(3.50) in the following version [45] of the magnetic equation of state, Eq.(3.9),

$$\left[\frac{M(T, H)}{M(0, H)} \right]^2 = \left[\frac{M(0, 0)}{M(0, H)} \right]^2 \left[1 - \frac{3 \langle m^2 \rangle}{M^2(0, 0)} - \frac{2 \langle m^2 \rangle}{M^2(0, 0)} \right] \quad (3.51)$$

results in the expression

$$\left[\frac{M(T, H)}{M(0, 0)} \right]^2 = 1 - \left(\frac{T}{T_C} \right)^{4/3} \left[1 - \frac{\pi}{2q_c} \left(\frac{g \mu_B}{D} \right)^{1/2} \sqrt{H} \right]. \quad (3.52)$$

Considering that $M(0, H) \sim M(0, 0)$, Eq.(3.52) clearly demonstrates that the spin fluctuation model correctly predicts the \sqrt{H} dependence of $A'(H)$. Using the typical values $q_c \sim 1 \text{ \AA}^{-1}$, $g \sim 2$ and $D \sim 100 \text{ meV \AA}^2$, the coefficient of the \sqrt{H} term turns out to be $\sim 5 \times 10^{-4}$. This estimate is of the same order of magnitude as the observed values. If for a moment q_c , ($\sim 1 \text{ \AA}^{-1}$) is taken to be independent of composition and the observed values of stiffness coefficient D and splitting factor g (-2.07 ± 0.02 , value determined from **FMR** measurements) are inserted into Eq.(3.52), the coefficient B' of the \sqrt{H} term possesses the values 9.6×10^{-4} and 8.1×10^{-4} for the alloys with $x = 0$ and 6, respectively, as against the observed values 13.0×10^{-4} and 6.6×10^{-4} . From this comparison, one may be tempted to conclude that the spin fluctuation model predicts a much slower decrease of the coefficient B' with x than the observed one. But when it is realized that both the quantities c_ν (the coefficient of the gradient term in the Ginzburg-Landau expansion) and γ' , appearing in the expression, Eq.(3.49), of q_c , decrease rapidly with x because these alloys become more and more homogeneous magnetically and $N(\mathbf{E}_F)$ falls steeply as the Co concentration in them is increased, a much closer agreement between the theoretical and experimental variation of B' with x is expected. For a quantitative comparison between theory and experiment, values of c_ν and γ'_ν for different compositions are needed. Such data are not available at present.

3.3. Conclusions

Based on an elaborate analysis of highly accurate magnetization data taken over a wide range of temperatures and external magnetic fields on amorphous $\text{Fe}_{90+y}\text{Zr}_{10-y}$ ($y = 0, 1$) and $\text{Fe}_{90-x}\text{Co}_x\text{Zr}_{10}$ ($x = 0, 1, 2, 4, 6, 8, 10$ and 90) alloys and a detailed discussion of the results, following conclusions can be drawn.

- (i) Magnetization at 5 K does not saturate even for fields as high as 70 kOe for the alloys with $y = 0, 1$ and $x \sim 6$. The high-field differential susceptibility, $\chi_{hf}(0)$, is extremely large in the alloys with $y = 0, 1$ and $x = 0, 1$ and decreases rapidly with increasing x for $x \sim 4$ so that it possesses values typical of crystalline counterparts for $x > 6$. Large $\chi_{hf}(0)$ strongly indicate presence of *competing* interactions in the alloys with $y = 0, 1$ and $x \sim 6$.
- (ii) While spin-wave excitations are mainly responsible for thermal demagnetization at low temperatures ($T \sim 0.37c$), enhanced fluctuations in the local magnetization give a dominant contribution to $M(T, 0)$ over a wide range of intermediate temperatures ($0.47b \sim T \sim 0.87b$) and for temperatures close to T_C ($0.87b \sim T \sim 0.957b$) in all the alloys except for the one with $z = 90$. In this alloy, dominant spin-wave contribution to both $M(T, 0)$ and $M(T, H)$ at low temperatures ($T \sim 0.17b$) is followed by an overwhelming contribution from Stoner single-particle excitations at higher temperatures, implying thereby that the particle-hole pair excitations are very *weakly correlated* in this case.
- (iii) The **spin-wave** stiffness coefficient D is *independent* of the external field for all the compositions while the D/Tc ratio possesses a value ~ 0.14 in the alloys with $y = 0, 1$ and $x < 6$ which is *characteristic* of amorphous **ferromagnets** with *competing* interactions. In these alloys, competing interactions confine the direct exchange interactions to the nearest-neighbours only. The range of direct exchange interactions extends beyond the first nearest-neighbour distance in the alloys with $x > 6$.
- (iv) The observed temperature renormalization of D augurs well with the temperature variation predicted by the itinerant-electron model and asserts that the **magnon** - single-particle interactions are more important in these systems than the magnon-magnon interactions.
- (v) For compositions $y = 0, 1$ and $x \sim 6$, the value of D directly measured by inelastic neutron scattering (INS) experiments, D_N , is expected to greatly exceed that deduced from the magnetic measurements, D_M . This is so because in these alloys, "diffusons" (longitudinal spin fluctuations) contribute to the $T^{3/2}$ decrease of magnetization as significantly as the transverse spin fluctuations (spin waves) do but they (diffusons) show up as an elastic peak in the INS spectra.
- (vi) The infinite three-dimensional ferromagnetic (FM) matrix plus finite FM clusters model offers a straightforward explanation not only for the absence of spin-wave peaks in the INS

spectra taken in the wavevector transfer **range** of $0.05\text{\AA}^{-1} < q < 0.12\text{\AA}^{-1}$ but also for the **composition dependence** of $D(0)$, T_C , $M(0,0)$ and $\chi_{AF}(0)$.

- (vii) In accordance with the predictions of the spin fluctuation model, spin fluctuations get strongly suppressed by Co concentration and external magnetic field. This model provides a consistent theoretical basis for the observed temperature dependence of spontaneous and 'in-field' magnetization over the entire temperature range $0 \sim T \sim T_C$.
- (viii) The Stoner criterion $IN(E_F) > 1$ for the occurrence of **ferromagnetism** is satisfied. All the alloys studied in this work are *weak* itinerant **ferromagnets**.

Before concluding this section, certain issues relating to the application of the spin fluctuation (SF) model to the type of spin systems under consideration need to be addressed. From a puristic point of view, this model is strictly valid for *nearly* ferromagnetic metals or ferromagnetic metals with **unsaturated** moments only. Therefore, a direct application of the SF model to a concentrated system with 90 at.% or more 3d transition metal content would seem to be far fetched unless due consideration is given to the fact that the ferromagnetic ground state in $a - Fe_{100-p}Zr_p$ alloys becomes **unstable** when $p = p_c \sim 7$ at.% [36,46] and the alloys with $y = 0, 1$ and $x = 0, 1$, in particular, have a composition close to p_c where the ferromagnetic instability occurs. Considering that the SF model adequately describes the magnetic behaviour of the alloy systems in question, it is not immediately obvious as to why some of its predictions such as the field dependence of D and the **Curie-Weiss** behaviour of magnetic susceptibility for $T > T_c$ (chapter 4) are not borne out by the present results. One way to reconcile with this situation is to invoke the possibility that the field dependence of D in the investigated alloys is so small as to escape detection in the measurements that cover a relatively narrow field range ($0 \sim H \sim 15$ kOe). Magnetic measurements over a much wider field range (e.g., $0 \sim H \sim 150$ kOe) should help in clarifying this issue. The deviation from the Curie-Weiss behaviour in the present case is due to giant FM clusters which exist even at temperatures well above T_c and interact with one another through individual spins, as inferred previously from magnetization [17,33], Mossbauer [18,47], ac susceptibility [33,48], ferromagnetic resonance [8-10,22,49] and small-angle neutron scattering [50] studies. The spin fluctuation model, however, fails completely in the critical region because this theory is nothing more than the first fluctuation correction to Landau theory. Therefore, the SF theory represents a first step towards a crossover theory between the Landau region and the critical region. A correct description of the magnetic and **thermodynamic** behaviour in the critical region is provided by the **renormalization** group calculations, as is evident from the data presented in the following chapter. For this reason, one full chapter (Chapter 4) is devoted to the critical behaviour of the alloy systems of interest in this work.

B.: $a-(\text{Fe}_p\text{Ni}_{1-p})_{80}(\text{B},\text{Si})_{20}$ and $a-(\text{Fe}_p\text{Ni}_{1-p})_{80}\text{P}_{14}\text{B}_6$ alloys

3.4. Results and Analysis

Fig. 3.20 shows the magnetic phase diagrams for $a-(\text{Fe}_p\text{Ni}_{1-p})_{80}(\text{B},\text{Si})_{20}$ (series I) and $a-(\text{Fe}_p\text{Ni}_{1-p})_{80}\text{P}_{14}\text{B}_6$ (series II) alloys constructed using the values of T_C (Curie temperature), T_{SG} (spin glass freezing temperature) and T_{RE} (the reentrant transition temperature), accurately determined from ac susceptibility, electrical resistivity and bulk magnetization measurements [19,23,31,32,51-56]. Figure 3.20 indicates that the critical concentration $p = p_c$, at which the ferromagnetic (FM)-paramagnetic (PM), PM-spin glass (SG) and FM-reentrant (RE) phase transition lines meet, is different for the two series; $p_c \sim 0.03$ for series I and $\tilde{p}_c \sim 0.10$ for series II. Since the low-lying magnetic excitations in the compositions exhibiting ferromagnetism are of main interest in this chapter, henceforth attention is focussed on the FM phase only.

The magnetization, $M(T, H)$ data taken in the temperature range from 4.2 K to 300 K (or T_C , which over is lower) at an external magnetic field of $H = 9$ KOe on $a-(\text{Fe}_p\text{Ni}_{1-p})_{80}\text{B}_{19}\text{Si}_1$ ($0.0625 < p < 0.20$), $a-(\text{Fe}_p\text{Ni}_{1-p})_{80}\text{B}_{20}$ ($0.25 < p < 1.0$) and $a-(\text{Fe}_p\text{Ni}_{1-p})_{80}\text{P}_{14}\text{B}_6$ ($0.1125 < p < 1.0$) alloys using the Faraday technique were analyzed in the same way as in the case of $a-\text{Fe}_{90-x}\text{Co}_x\text{Zr}_{10}$ alloys. In order to identify the temperature ranges over which the functional dependence of $M(T, H)$ on T is governed by a dominant contribution arising from one or more types of low-lying magnetic excitations such as spin waves, single-particle excitations and local spin-density fluctuations, the reduced magnetization, $M(T, H)/M(0, H)$, is plotted against $T^{3/2}$ and T^2 whereas the reduced magnetization squared, $[M(T, H)/M(0, H)]^2$, is plotted against T^2 and $T^{4/3}$. Such plots for $a-\text{Fe}_{80}\text{B}_{20}$, shown in Figs. 3.21(a) and 3.21(b), also serve as an illustration of the behaviour observed in the remaining compositions. These figures indicate that for the $a-\text{Fe}_{80}\text{B}_{20}$ alloy, the $M(T, H = 9 \text{ KOe})$ data are better described by a $T^{3/2}$ law for $T \sim 140 \text{ K}$ and by a T^2 law for $140 < T < 300 \text{ K}$ while the other power laws (Fig. 3.21(b)) do not fit the data in any temperature range. Having completed such an exercise on the $M(T, H)$ data of all the compositions in both the alloy series, a detailed 'range-of-fit' analysis of the type described in Sec.3.1.1 has been carried out to ascertain the relative importance of different contributions to $\Delta m(T, H) = [M(0, H) - M(T, H)]/M(0, H)$. A representative example of the variation of various fitting parameters with the upper limit (T_{\max}) of the temperature range $T_{\min} < T < T_{\max}$ used for different types of fits is shown in figure 3.22. For the least-squares fits to $M(T, H)$ data based on Eqs.(3.1)-(3.3), use has been made of the values of demagnetizing factor N determined from low-field magnetization measurements and those of the splitting factor g as well as anisotropy field H_A reported in the literature [19,23,57,58]. Such an exhaustive analysis of the magnetization data taken on these alloys is necessitated by the fact that most of the previous determinations [19,23,24,26-28,53,59-78] of the spin wave stiffness, D , do not take into account either the single-particle contribution or the effect of external magnetic field or the temperature renormalization of D even though inelastic neutron scattering (INS) data [79-82] clearly demonstrate that an appreciable reduction

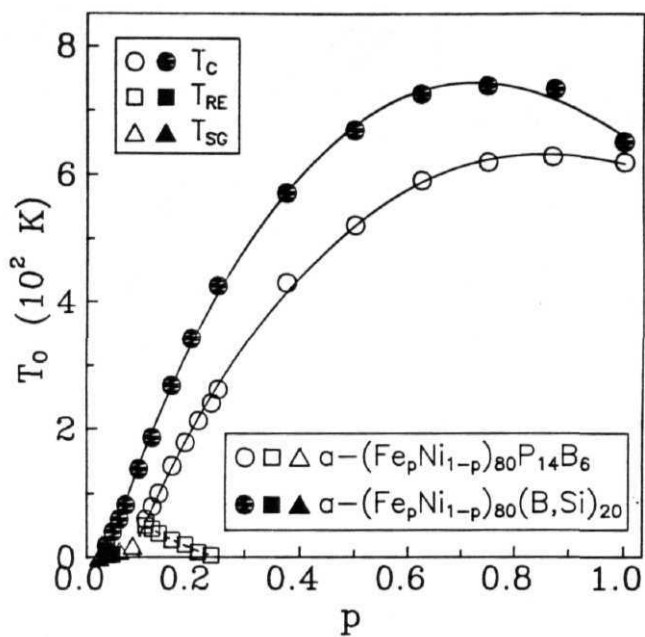


Fig. 3.20 Magnetic Phase diagrams for $\alpha-(Fe_pNi_{1-p})_{80}(B,Si)_{20}$ and $\alpha-(Fe_pNi_{1-p})_{80}P_{14}B_6$ alloys.

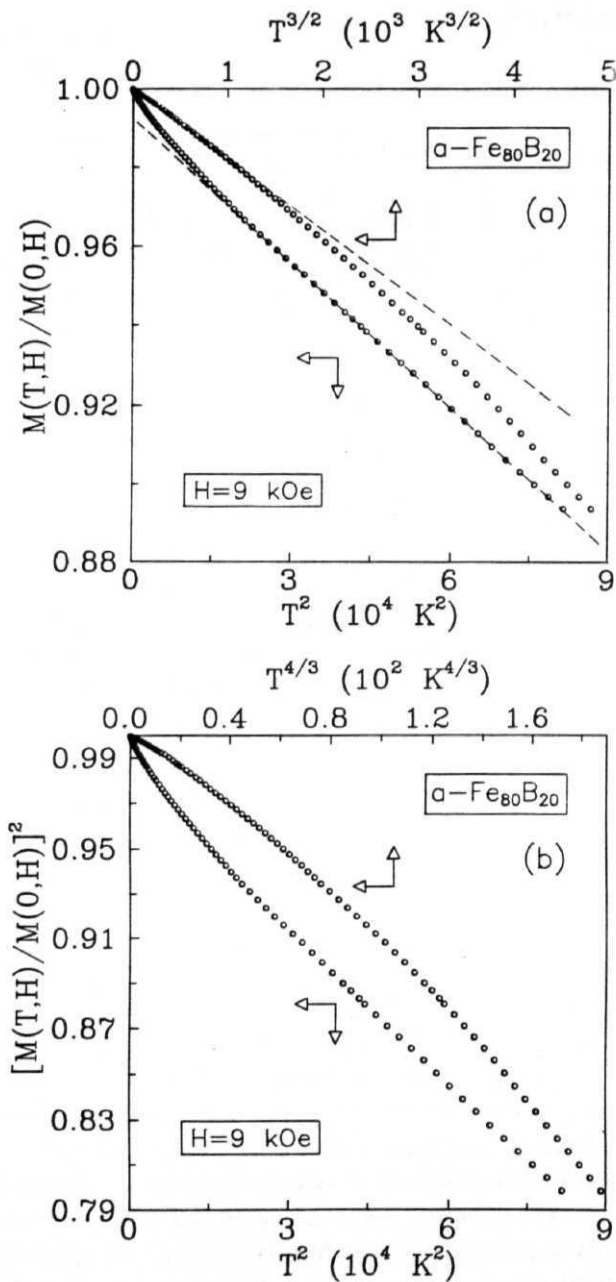


Fig. 3.21 (a) $M(T,H)/M(0,H)$ vs. $T^{3/2}$ and T^2 , and (b) $[M(T,H)/M(0,H)]^2$ vs. $T^{4/3}$ and T^2 plots for $a\text{-Fe}_{80}\text{B}_{20}$ at $H = 9 \text{ kOe}$. Dashed curves represent the LS fits to the data.

in D occurs with increasing temperature. The main observations based on the above analysis are as follows. (i) For temperatures $t(=T/T_C) < t^*(p)$, the best fit to $\Delta m(T, H)$ data is provided by Eq.(3.1a) with $\theta = 0$ and $D(T) = D(0)(1 - D_{5/2}T^{5/2})$ for the alloys with $p < 0.625$ and $D(T) = D(0)(1 - D_2T^2)$ for those with $p > 0.75$ in series I. For $t > t^*(p)$, the Stoner **single-particle** excitations of *weak-itinerant* (WI) type, i.e., Eq.(3.26), and local spin-density fluctuations (LSF), i.e., Eq.(3.30), are responsible for the thermal demagnetization for all the compositions in series I. In series II, the observed temperature variation of $\Delta m(T, H)$ is closely reproduced by the first spin-wave term in Eq.(3.1a) alone, i.e., by the expression represented by Eq.(3.1a) with $\theta = 0$ and $D(T) = D(0)(1 - D_{5/2}T^{5/2})$ for temperatures $t < 0.9$ ($T < 300$ K) and concentrations $p < 0.25$ ($0.375 < p < 0.625$). However, for the alloys with $p > 0.75$, the $T^{3/2}$ spin-wave term in Eq.(3.1a) with $D(T) = D(0)(1 - D_2T^2)$ plus the **single-particle** contribution of *strong-itinerant* (SI) type described by Eq.(3.2a) yield the best fit to the $\Delta m(T, H)$ data in the entire temperature range ($0 \sim T < 300$ K). (ii) In alloy series I, the **single-particle** contribution of WI type (Eq.(3.26)) as well as the LSF contribution (Eq.(3.30)), though present at all temperatures, are completely overshadowed by the **spin-wave** contribution for $t \sim t^*(p)$ but they completely account for the observed temperature dependence of $\Delta m(T, H)$ for $t > t^*(p)$. By comparison, single-particle excitations of the SI type (Eq.(3.2a)) contribute significantly, besides a dominant spin-wave contribution, to $\Delta m(T, H)$ in the entire temperature range $T < 300$ K only for *Fe* concentrations $p > 0.75$ in alloy series II whereas for $p < 0.625$ in this alloy series, the spin wave contribution is so large as to make a reliable estimation of $\Delta m_{SP}(T, H)$ and $\Delta m_{LSF}(T, H)$ actually impossible. The latter inference can be drawn from the fact that the addition of single-particle and LSF contributions of the form given by Eq.(3.26) or Eq.(3.30) to the spin-wave term *marginally* improves the quality of fit for $p < 0.625$ while the addition of **single-particle** contribution of the SI type, Eq.(3.2a), brings forth a *marked* improvement in the quality of fit for concentrations $p > 0.75$ compared to that when only the $T^{3/2}$ term is **present**. (iii) The quality of **LS** fits based on the theoretical expressions that set $D(T) = D(0)$ is much worse compared to the ones that allow $D(T)$ to vary as $D(T) \sim T^{5/2}$ or T^2 , indicating thereby that the temperature renormalization of D is **important**. (iv) The LS fits are able to clearly distinguish between the different functional dependences of $D(T)$ on T and they reveal that $D(T) \sim T^{5/2}$ for $p < 0.625$ whereas $D(T) \sim T^2$ for $p > 0.75$ in both the alloy series.

Figures 3.23 and 3.24 show the reduced magnetization data plotted against $T^{3/2}$ for series I and II, respectively. The continuous curves through the data points represent the best LS fits to the $\Delta m(T, H)$ data with the parameter values for series I and II given in Tables 3.5 and 3.6, respectively. The presently determined parameters, $M(0, 0)$, $D(0)$, T_C , $D_{5/2}$, D_2 and A are plotted as functions of *Fe* concentration for both the alloy series in figures 3.25 and 3.26 together with the values of these parameters for crystalline $(c-)\text{Fe}_x\text{Ni}_{100-x}$ alloys [83,84]. Note that in these figures, p , which denotes the *Fe* concentration in the alloy series I and II, has been changed to $x = 80p$ in order to facilitate a direct comparison between the present results and

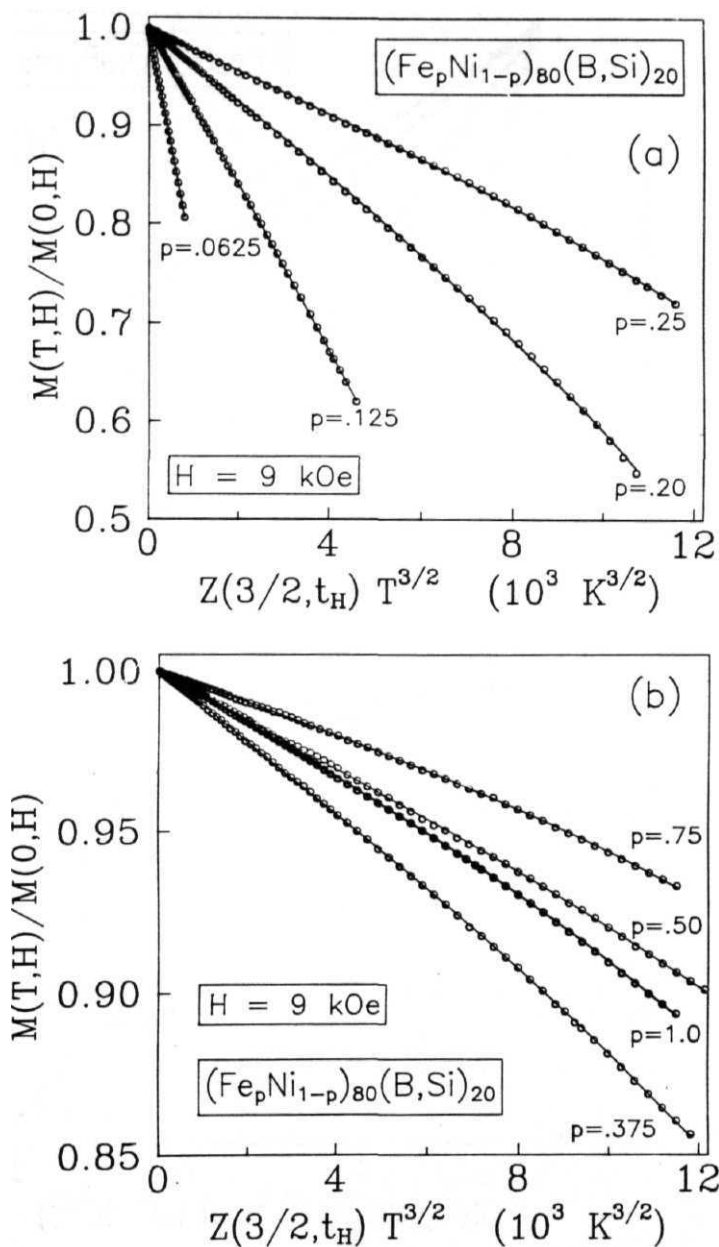


Fig. 3.23 Modified Bloch law behaviour of the $M(T, H)$ data taken at $H = 9 \text{ kOe}$ for a few representative compositions in the $a - (\text{Fe}_p \text{Ni}_{1-p})_{80} (\text{B}, \text{Si})_{20}$ alloy series. The continuous curves through the data points represent the LS fits to the data.

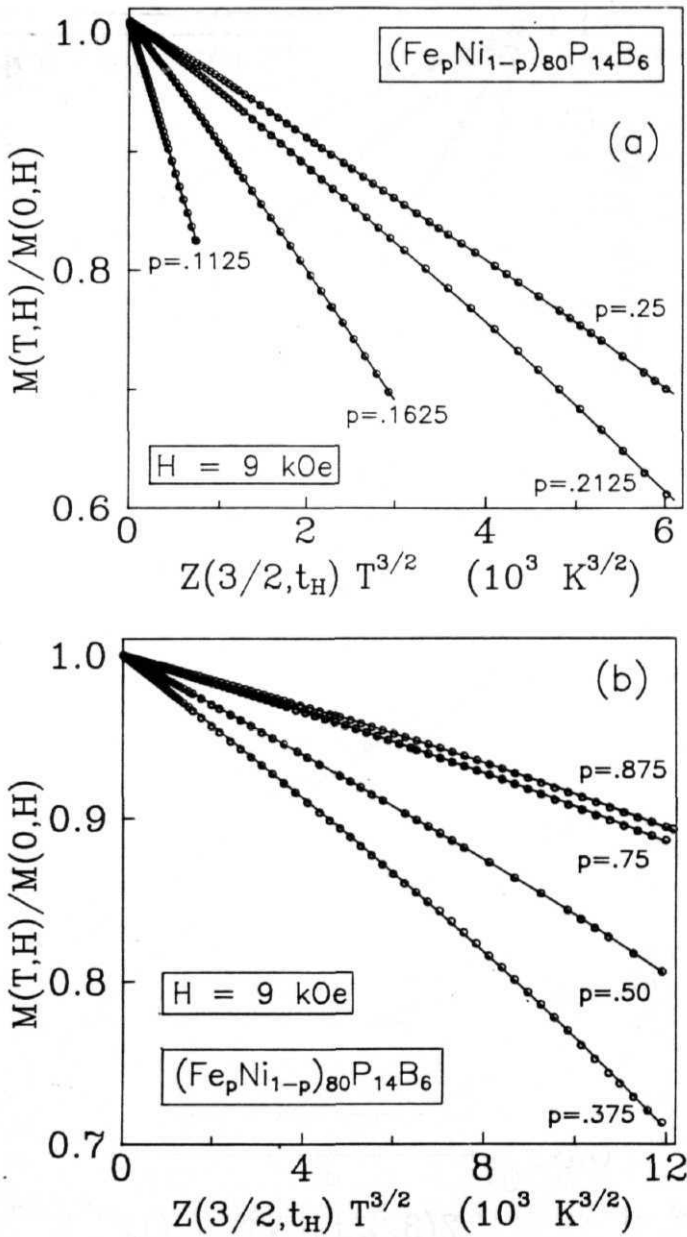


Fig. 3.24 Modified Bloch law behaviour of the $M(T, H)$ data taken at $H = 9 \text{ kOe}$ for a few representative compositions in the $(\text{Fe}_p \text{Ni}_{1-p})_{80} \text{P}_{14} \text{B}_6$ alloy series. The continuous curves through the data points represent the LS fits to the data.

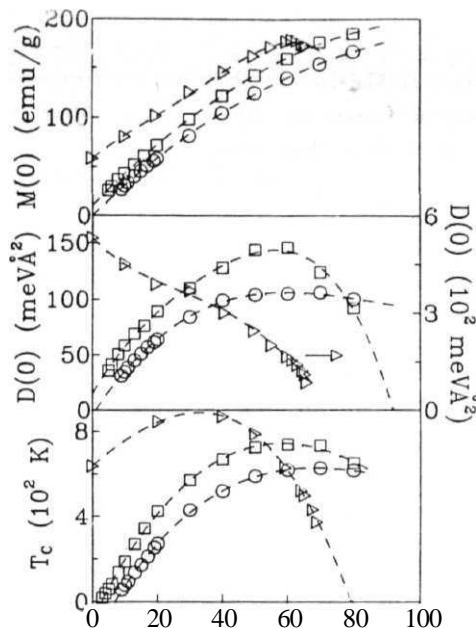


Fig. 3.25 (a) Variation of T_c , $D(0)$ and $M(0,0)$ with x in $a - \text{Fe}_x\text{Ni}_{80-x}(\text{B}, \text{Si})_{20}$ (open squares), $a - \text{Fe}_x\text{Ni}_{80-x}\text{P}_{14}\text{B}_6$ (open circles) and fcc $\text{Fe}_x\text{Ni}_{100-x}$ (open triangles), data taken from Ref.[83,84] alloys.

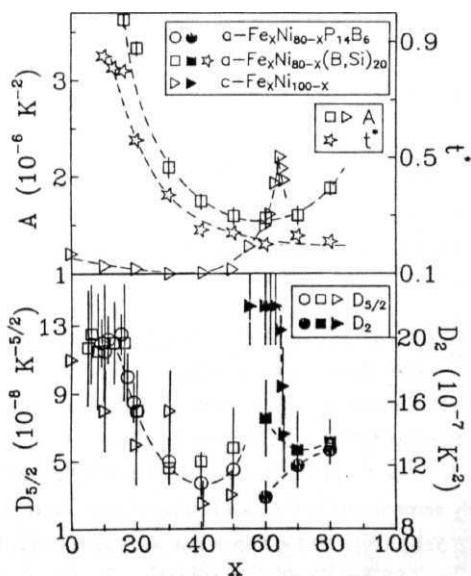


Fig. 3.26 The parameters A , D_2 , $D_{5/2}$ and t^* as function of x for $a - \text{Fe}_x\text{Ni}_{80-x}(\text{B}, \text{Si})_{20}$, $a - \text{Fe}_x\text{Ni}_{80-x}\text{P}_{14}\text{B}_6$ and fcc $\text{Fe}_x\text{Ni}_{100-x}$ (data taken from Ref. [83,84]) alloys.

those previously reported [83,84] for crystalline (c-) Fe_xNi_{100-x} alloys. In addition, the values of mean-square range of exchange interaction, $\langle r^2 \rangle$, for different compositions in series I and II, computed from the relations [19,23,53,85]

$$D_{5/2} = \pi \xi(5/2) \left(\frac{g\mu_B}{M(0,0)} \right) \left(\frac{k_B}{4\pi D(0)} \right)^{5/2} \langle r^2 \rangle \quad (3.53)$$

and

$$\frac{D(0)}{T_C} = \frac{(S/3) \int r^2 J(r) G(r) dr}{[2S(S+1)/3k_B] \int J(r) G(r) dr} = \frac{k_B}{2(S+1)} \langle r^2 \rangle \quad (3.54)$$

using the presently determined values of $M(0,0)$, $D(0)$, T_C and $D_{5/2}$ and by setting $S = 1$, are included in Tables 3.5 and 3.6 for comparison. The observations (i) - (iii) mentioned above assert that the temperature renormalization of D cannot be neglected for the alloys in question and the property D_N (stiffness value determined from inelastic neutron scattering data) $\gg D_M$ (stiffness deduced from the magnetization data) is inherent to Invar systems (e.g., $a - Fe_{80}B_{20}$ in Table 3.5). This result refutes the earlier claims [77,86] that the wide disparity between the values of D_M and D_N usually found in Fe-based amorphous (and crystalline) Invar alloys completely disappears when contribution to $\Delta m(T, H)$ arising from both spin-wave and single-particle excitations (of either WI type [77] or SI type [86]) are taken into account without considering the temperature renormalization of spin wave stiffness D .

3.5. Discussion

In order to facilitate a direct comparison between the present results and those reported on c- Fe_xNi_{100-x} alloys, the Fe concentration in the amorphous alloys in question will be referred to as x (=80p) instead of p in this section. Before proceeding with the discussion, the main findings of this work are summarized below.

(i) In $a - Fe_xNi_{80-x}(B, Si)_{20}$ alloys (series I), the spin wave excitations alone seem to account for the observed thermal demagnetization below a certain (reduced) temperature t' , which decreases with increasing x (Fig. 3.26), but the existence of single particle (SP) excitations of weak-itinerant (WI) type and local spin-density fluctuations (LSF) cannot be ruled out completely. For $t > t'$, SP excitations of WI type (Eq.(3.2b)) and LSF (Eqs.(3.30) and (3.43)) completely account for the decrease of magnetization with increasing temperature. As in $a - Fe_xNi_{80-x}(B, Si)_{20}$ alloys for $t < t'$, the spin-wave (SW) contribution completely masks the WI-type SP plus the LSF contributions in the temperature range $0 \sim T \sim 0.97t$ ($0 \sim T < 300$ K) for Fe concentrations $x < 20$ ($30 < x < 50$) in the $a - Fe_xNi_{80-x}P_{14}B_6$ alloy series (series II); however, SP excitations of strong-itinerant (SI) type (Eq.(3.2a)) contribute significantly

Table 3.5: Splitting factor g , density ρ , spin-wave and other relevant magnetic parameters, and mean-square range of the exchange interaction $\langle r^2 \rangle$ for α -(Fe₂Ni_{1-x})₂(B,Si)₂ alloys. Numbers in parentheses denote the estimated uncertainty in the least significant figure while those within the square brackets are the values of $\langle r^2 \rangle$ expressed in terms of the average nearest-neighbor distance $a \approx 2.55 \text{ \AA}$.

P	g	ρ (g/cm ³)	$M(0,0)$ (emu/g)	T_C (K)	$D(0)$ (meV \AA^2)	D_{ex} (10 ⁻⁷ K ^{-1/2})	D_2 (10 ⁻⁴ K ⁻¹)	A (10 ⁻⁶ K ⁻²)	$D(0)/T_C$ (meV $\text{\AA}^2/\text{K}$)	$\langle r^2 \rangle$ (\AA^2) Eq. (17)	$\langle r^2 \rangle$ (\AA^2) Eq. (18)
0.0375		8.11		19.00(5)							
0.0500		8.10		40.00(5)							
0.0625	2.06(2)	8.09	25.78(12)	60.00(5)	35.7(3)		1.17(30)		0.595(5)	0.6(2)	27.6(2)
0.0750	2.06(2)	8.08	29.71(13)	82.50(5)	41.2(3)		1.25(25)		0.500(5)	[0.09]	[4.24]
0.1000	2.06(2)	8.06	36.64(15)	137.50(5)	50.6(3)		1.15(30)			1.0(2)	23.2(2)
0.1250	2.07(2)	8.04	42.93(10)	186.50(5)	58.5(5)		1.20(30)		0.368(5)	[0.15]	[3.57]
0.1625	2.07(2)	8.01	51.82(8)	268.50(5)	69.0(5)		1.20(20)		0.314(5)	[0.31]	[2.63]
0.2000	2.07(2)	7.98	60.71(9)	342.00(10)	76.0(5)		1.20(30)	3.60(1)	0.257(3)	[0.54]	[2.25]
0.2500	2.06(2)	7.94	71.80(5)	425.00(10)	89.0(5)		0.80(20)		0.222(3)	[1.83]	11.9(1)
0.3750	2.07(2)	7.83	98.15(5)	571.00(10)	111.0(5)		0.46(2)	3.20(1)	0.209(2)	[0.97]	10.3(1)
0.5000	2.08(2)	7.49	122.00(5)	669.00(20)	128.0(10)		0.50(2)			[1.45]	[1.58]
0.6250	2.08(2)	7.38	142.41(5)	725.00(30)	144.0(10)		0.58(20)		0.193(2)	11.0(30)	9.7(1)
0.7500	2.07(2)	7.28	159.29(5)	738.00(40)	146.0(10)			1.50(5)	0.191(2)	[1.69]	[1.49]
0.8750	2.09(2)	7.17	176.36(5)	733.00(50)	124.0(15)			1.02(2)		[2.21]	[1.38]
1.0000	2.10(2)	7.08	185.09(5)	651.00(30)	92.0(20)			0.81(3)	0.199(2)	[4.15]	[1.37]
					170.0(250)*					[7.43]	48.3(185)
							1.50(20)		0.197(2)		[1.41]
							1.30(20)	0.78(6)	0.169(2)		9.2(1)
							1.35(10)	0.82(4)			7.9(1)
								1.21(1)	0.141(3)		[1.21]
											6.6(1)
											[1.01]

*Value of $D(0)$ determined by Brillouin scattering (Ref.[60]).

Table 3.6: Splitting factor g , density ρ , spin-wave and other relevant magnetic parameters, and mean-square range of the exchange interaction $\langle r^2 \rangle$ for $a(\text{Fe}, \text{Ni})_{1-x}\text{P}_{2x}\text{B}_{2x}\text{As}_{2x}$ alloys. Numbers in parentheses denote the estimated uncertainty in the least significant figure while those within the square brackets are the values of $\langle r^2 \rangle$ expressed in terms of the average nearest-neighbor distance $a \approx 2.55 \text{ \AA}$.

P	g	ρ (g/cm^3)	$M(0,0)$ (emu/g)	T_C (K)	$D(0)$ (meV \AA^2)	$D_{1/2}$ ($10^{-3} \text{ K}^{-1/2}$)	D_2 (10^{-6} K^{-1})	A' (10^{-6} K^{-1})	Δ/k_B (K)	$D(0)/T_C$ (meV $\text{\AA}^2/\text{K}$)	$\langle r^2 \rangle$ (\AA^2) [\AA] [\AA]	$\langle r^2 \rangle$ (\AA^2) [\AA] [\AA]
0.1125	2.09(2)	7.84	26.70(10)	56.00(5)	31.0(5)	1.20(10)				0.554(10)	0.4(1) [0.06]	25.7(5) [3.95]
0.1250	2.08(2)	7.83	30.60(10)	77.00(5)	34.5(5)	1.15(10)				0.448(7)	0.6(1) [0.09]	20.8(3) [3.20]
0.1375	2.07(2)	7.82	33.90(10)	94.00(5)	38.5(5)	1.22(10)				0.410(5)	1.0(1) [0.15]	19.0(2) [2.92]
0.1625	2.09(2)	7.80	40.00(5)	136.00(5)	45.0(5)	1.20(8)				0.331(4)	1.6(2) [0.25]	15.4(2) [2.37]
0.1875	2.06(2)	7.78	45.45(5)	171.00(5)	51.0(5)	1.25(8)				0.298(3)	2.6(2) [0.40]	13.8(1) [2.12]
0.2125	2.07(2)	7.76	50.90(5)	210.00(5)	57.0(5)	1.00(10)				0.271(2)	3.1(4) [0.48]	12.6(1) [1.94]
0.2375	2.09(2)	7.74	55.84(6)	252.00(5)	61.5(5)	0.85(8)				0.244(2)	3.5(4) [0.54]	11.3(1) [1.74]
0.2500	2.09(2)	7.73	58.36(4)	271.00(10)	64.0(5)	0.80(10)				0.236(2)	3.8(5) [0.58]	11.0(1) [1.69]
0.3750	2.11(2)	7.63	81.35(5)	430.00(10)	84.0(10)	0.50(10)				0.195(3)	6.3(15) [0.97]	9.1(1) [1.40]
0.5000	2.12(2)	7.52	104.67(5)	520.00(10)	99.0(10)	0.37(5)				0.190(2)	8.9(15) [1.37]	8.8(1) [1.35]
0.6250	2.12(2)	7.43	124.87(5)	590.00(20)	112.0(10)* 104.0(10)	0.60(5)* 0.45(8)				0.176(2)	14.4(30) [2.21]	8.2(1) [1.26]
0.7500	2.10(2)	7.33	139.67(5)	619.00(30)	105.0(10)		1.00(6)	1.2(2)	116(12)	0.170(2)		7.9(1) [1.21]
0.8750	2.11(2)	7.23	153.89(5)	628.00(50)	106.0(10)		1.20(5)	1.2(2)	157(35)	0.169(2)		7.9(1) [1.21]
1.0000	2.12(2)	7.14	166.50(5)	617.00(50)	100.0(20)		1.30(5)	1.2(2)	151(30)	0.162(3)		7.5(1) [1.15]

*Value of $D(0)$ and $D_{1/2}$ evaluated from the Fig. 5 of Ref. [103].

to the thermal demagnetization, in addition to the dominant SW contribution, in the entire temperature range $0 \sim T \sim 300$ K only for $x \sim 60$ at % in series II. In $c - Fe_xNi_{100-x}$ alloys, a SP contribution of WI type accompanies a dominant SW contribution throughout the temperature range covered in the experiments (note that the SP and SW contributions become comparable only for $x \sim 60$ at.%) as is also the case with $a - (Fe_xNi_{1-p})_{80}(Si)_{20}$ alloys in the entire composition range and $a - Fe_xNi_{80-x}P_{14}B_6$ alloys for $x < 50$ at.%. The only difference between the crystalline and amorphous alloys is that in the former case, the SP contribution (i.e., coefficient A in Fig. 3.26) could be estimated because of its larger magnitude whereas in the amorphous case, such an estimation is only possible for all the concentrations in series I at $t > t'$. (ii) In both the amorphous alloy series, D varies with temperature as $D(T) \sim T^{5/2}$ for $x < 50$ at.%, in accordance with the expression (Eq.(3.1c)) predicted by the localized-electron (Heisenberg) model, whereas consistent with the behaviour of $D(T)$ (Eq.(3.1b)) predicted by the itinerant-electron model it, renormalizes with temperature as $D(T) \sim T^2$ for Fe concentrations in the range $60 < x < 80$. A crossover from the $T^{5/2}$ to T^2 dependence of spin wave stiffness at $x \sim 60$ at.% in the presently studied amorphous alloys has also been previously observed [83,84] in $c - Fe_xNi_{100-x}$ alloys (Fig. 3.26). The concentration dependence of the coefficient $D_{5/2}$ of the $T^{5/2}$ term in Eq.(3.1r) for the amorphous alloys investigated is similar to that observed in $c - Fe_xNi_{100-x}$ alloys. (iii) The values of $\langle r^2 \rangle$ for different compositions in series I and II computed from Eq.(3.53) (Tables 3.5 and 3.6) suggest that the range of exchange interaction increases rapidly with x whereas Eq.(3.54) predicts that $\langle r^2 \rangle$ decreases with increasing x . (iv) The spontaneous magnetization, $M(T = 0, x)$, versus x curves in the range $0 < x < 60$ for series I and II are systematically shifted down by ~ 20 and ~ 40 emu/g, respectively, with respect to that for $c - Fe_xNi_{100-x}$ alloys (Fig. 3.25). However, a sudden drop in $M(0, x)$ for $x > 60$ at.% in the $c - Fe_xNi_{100-x}$ series is not observed in the investigated amorphous alloys for which $M(0, x)$ continues to increase with x but with a progressively slower rate (Fig. 3.25). (v) The spin-wave stiffness at 0 K, $D(T = 0, x)$ and Curie temperature, $T_c(x)$, as functions of x go through a broad peak at $x \sim 60$ at.% ($x \sim 70$ at.%) for $a - Fe_xNi_{80-x}(B, Si)$ ($a - Fe_xNi_{80-x}P_{14}B_6$) alloys (Fig. 3.25). As x is increased beyond $x \sim 60$ at.%, both $D(0, x)$ and $T_c(x)$ decrease at rate which is very steep in $c - Fe_xNi_{100-x}$ alloys but slows down considerably in the amorphous alloys studied so much so that the drop in these quantities is barely discernible in $a - Fe_xNi_{80-x}P_{14}B_6$ alloys.

Within the framework of the band model, the effect of increasing the Fe concentration x is to increase the exchange splitting of spin-up (\uparrow) and spin-down (\downarrow) d subbands (since T_C increases with x , Figs. 3.20 and 3.25) and to shift the Fermi level E_F to higher energies (as the spontaneous magnetization $Af(0, x)$ increases with x , Fig. 3.25). The observation (i) mentioned above implies that E_F lies within the d_{\uparrow} and d_{\downarrow} subbands in the entire composition range for the alloy series I (weak itinerant ferromagnetism) whereas E_F in series II shifts up with x to such an extent that it lies just above the top of d_{\uparrow} subband at $x \sim 60$ at.%, where a transition from

weak ($x < 60$ at.%) to strong ($x > 60$ at.%) itinerant **ferromagnetism** occurs. This deduction is consistent with the results of spontaneous resistivity anisotropy [87,88], **high-field** susceptibility [88], **spin-polarized** photoemission [89] and **compton** scattering [90] experiments on the same or similar *Fe — Ni* amorphous alloys as the present ones. In addition, the observation that t'' decreases with x is consistent with the result [91] that the temperature range over which $T^{3/2}$ variation of spontaneous magnetization in crystalline Fe dominates is confined to temperatures $T < 0.157c$ or simply to $t^* < 0.15$ only. In view of the arguments presented in subsection 3.2.3., one expects a significant reduction in the magnitude of coefficient A of the T^2 term in **Eq.(3.2b)** or **Eq.(3.5b)** in the presence of an external magnetic field as large as 9 kOe compared to its value in zero field because of the suppression of LSF by external field. Nevertheless, if we ignore this reduction in A for the moment, i.e., set $A(H) = A(0)$, and calculate T_C^* from the relation $T_C^* = [2A(0)]^{-1/2}$ using the present A values, the numerical estimates of T_C^* , so obtained, consistently *exceed* the actual T_C values by about 10 % for a - $Fe_xNi_{80-x}(LSi)_{20}$ alloys. Since $A(0)$ is actually larger than $A(H)$, the values of T_C^* should be very close to those of T_C . Considering that the Stoner theory overestimates T_C by at least an order of magnitude, this result strongly suggests that local spin-density fluctuations dominantly contribute to thermal demagnetization in these alloys.

The observation (ii) that a transition from $T^{5/2}$ variation of $D(T)$ to T^2 occurs at $x \sim 60$ at.% should not be interpreted as a transition from localized- to itinerant-electron behaviour but as an indication of the fact that the magnon-magnon interactions, within the framework of itinerant-electron model (Eq.(1.21), Chapter 1), weaken with increasing x so much so that the **magnon-SP** interactions show up with ease for $x > 60$ at.%. It is now well-known [19,23,53,92] that the nearest-neighbour (NN) configuration of atoms (short-range order) in the *Fe — Ni* amorphous alloys in question is similar to that found in their crystalline counterparts. In view of this result, the finding that the concentration dependence of $D_{5/2}$ is the same (within the error limits) regardless of whether Fe - Ni alloys are in the crystalline state or in the amorphous state and irrespective of whether the metalloids are present or not suggests that the observed functional dependence of $D_{5/2}$ on x (and hence the magnon-magnon interactions) is primarily dictated by the alteration in NN coordination (both type and number) brought about by the change in *Fe* concentration. Considering that even the slight change in NN coordination has a marked **influence** on the creation or annihilation of short-wavelength magnons, the magnon-magnon interactions involving the short-wavelength magnons play a decisive role in the temperature renormalization of spin-wave energies. In view of this argument and the observation that $M(0,0)$ and $D(0)$ have much lower values in the amorphous state compared to those in the crystalline state, it is not surprising that the values of $\langle r^2 \rangle$ calculated from Eq.(3.53) (Tables 3.5 and 3.6) underestimate the range of exchange interactions and hence tend to give the misleading impression that such interactions for the glassy alloys with x in the range $0 < x < 60$ at.% are confined to the nearest neighbours only. By contrast, the values of $\langle r^2 \rangle$ computed

from the $D(0)/T_C$ ratio using Eq.(3.54) (Tables 3.5 and 3.6) provide a better handle on the range of exchange interactions since both $D(0)$ and T_C are directly related to the χ change integral through the expression given by the numerator and denominator in Eq.(3.54), respectively.

A downward shift in the $M(T=0, x)$ vs. x curves (Fig. 3.25) for amorphous alloys in question, i.e., observation (iv) stated above, can be understood [52] in terms of the simple but crude rigid band model by assuming that P donates roughly twice as many electrons per atom to the transition metal d bands as B does. The sharp drop in $M(T=0, x)$, $D(T=0, x)$ and $T_C(x)$ for $x > 60$ at.% in c - Fe_xNi_{100-x} alloys is a manifestation of the Invar effect, i.e., the coexistence of antiferromagnetically coupled (low-spin state) and ferromagnetically coupled (high-spin state) spin pairs. Alternatively, the antiferromagnetic (AF) interactions build up at the expense of the ferromagnetic (FM) interactions in these alloys as x is increased beyond 60 at.% resulting in a sharp drop in these quantities. In view of these arguments, progressive slowing down of the rate of increase in $M(T=0, x)$ and drop in $D(T=0, x)$, $T_C(x)$ for $x > 60$ at.% in the presently studied alloys indicate that the competing (AF+FM) interactions, more pronounced in a — $Fe_{80}B_{20}$ than in a — $Fe_{80}P_{14}B_{6}$ are present in the alloys with x in the range $60 \sim x < 80$. This inference is consistent not only with the finding that the ratio $D(0)/T_C$ for a — $Fe_{80}B_{20}$ possesses a value ($= 0.14 \text{ meV } \text{\AA}^2/K$, Table 3.5) characteristic [9,10,17,26] of amorphous ferromagnets with competing interactions but also with the fact that a — $Fe_{80}B_{20}$ does exhibit [93] Invar behaviour. Competing interactions, in turn, give rise to canted spin arrangement in such ferromagnets. Mossbauer [94] and spin-polarized neutron scattering [95] experiments performed on amorphous Fe-rich (Fe-Ni)-metalloid and/or Fe-metalloid alloys do support the existence of non-collinear (canted) spin structure in the alloys with Fe concentration greater than 60 at.%.

As already mentioned earlier, the present results unambiguously demonstrate that $D_N \gg D_M$ is a characteristic property of the amorphous ferromagnets with competing interactions and/or of amorphous ferromagnetic alloys that exhibit Invar effect (e.g., a — $Fe_{80}B_{20}$ in Table 3.5). Several arguments [13,79-82,85,96-98] have been put forward to explain this discrepancy between D_M and D_N in amorphous ferromagnetic alloys. According to Continentino and Rivier [13], the diffusive modes (“diffusons”) originating from the longitudinal spin fluctuations, contribute as significantly to the $T^{3/2}$ decrease of magnetization in amorphous canted ferromagnets (i.e., the glassy ferromagnets with a noncollinear ground-state) as the transverse spin fluctuations (magnons) do, but these diffusons do not give rise to any propagating features in the constant- q INS intensity versus energy scans. The recent triple axis polarized INS data [99] on a — $Fe_{86}B_{14}$ (Invar system) and a — $Fe_{40}Ni_{40}P_{14}B_6$ (non-Invar system) alloys provide strong evidence for the existence of longitudinal spin fluctuations, which, far from being nonpropagating modes (as envisaged by Continentino and Rivier [13]), appear as propagating excitations at energies close to the spin wave peaks in constant- q scans for temperatures well below T_C in both the alloy systems studied. Moreover, these longitudinal propagating excitations, like

magnons, follow the dispersion relation $E(T) = D(T)q^2$ and hence give rise to an additional $T^{3/2}$ contribution to thermal **demagnetization** while leaving D_N unaltered from its 'spin-wave-only' value. The possibility of a coupling between transverse (spin-wave) and longitudinal spin fluctuations that leads to propagating longitudinal excitations which peak at spin-wave energies was earlier suggested by various workers [100-102]. Another important observation made by Lynn et al. [99], based on the triple-axis polarized INS experiments mentioned above, is that the intensity of the longitudinal mode peaks is very weak in a - $Fe_{40}Ni_{40}P_{14}B_6$ compared to that in a - $Fe_{86}B_{14}$. This result is in agreement with the present work (Tables 3.5 and 3.6) that the discrepancy between D_M and D_N is *more pronounced* for a — $Fe_{80}B_{20}$ (D_N/D_M 1.85(32)) than for a - $Fe_{40}Ni_{40}P_{14}B_6$ (D_N/D_M 1.13(2)). However, none of the theoretical models proposed hitherto [13,100-102] explains why the peaks in the INS spectra belonging to the longitudinal spin fluctuations are *more intense* in Invar alloys than in non-Invar systems. These results find a simple interpretation in light of the infinite three-dimensional (3D) ferromagnetic (FM) matrix plus finite FM spin clusters model [17,18,31,32,51] proposed earlier for amorphous ferromagnetic alloys and already described in detail in section 3.2.2. In this model, wild fluctuations in the NN distance within the frustration zones surrounding the finite clusters around the critical distance (r_c) at which the exchange integral changes sign in the Bethe-Slater curve gives rise to competing interactions, which, in turn, result in noncollinear arrangement of spins within the infinite 3D FM matrix in amorphous alloys. In Invar systems, an *additional* contribution to competing interactions arises from strong **magnetostrictive** coupling between the local 'quenched-in' stresses and spins in the buffer zones surrounding the finite spin clusters. Thus, the longitudinal spin fluctuations are *more pronounced* in Invar systems than in non-Invar ones. As the concentration of the moment bearing (Fe) atoms in the amorphous alloys under investigation increases, the total density decreases (Tables 3.5 and 3.6) such that the average NN distance (r_{NN}) between spins in both the FM matrix and the finite spin clusters increases progressively beyond r_c for $x < 60$ at.%, whereas for $x > 60$ at.% the finite spin clusters grow at the expense of the bulk with the result that r_{NN} between spins in the finite clusters is much larger than r_c but r_{NN} is lowered towards r_c for spins in the FM matrix. This process leads to an increase in the average NN (positive) exchange coupling, J_{NN} , between spins in the FM matrix (and hence in $D(T - 0, x)$ and $T_c(x)$) for x up to 60 at.% but as x is increased beyond 60 at.%, J_{NN} decreases and so do $D(T = 0, x)$ and $T_c(x)$.

3.6. Conclusions

From the detailed analysis and discussion of highly precise magnetization data taken on amorphous $(a-)(Fe_pNi_{1-p})_{80}(B,Si)_{20}$ (series I) and $(Fe_pNi_{1-p})_{80}P_{14}B_6$ (series II) alloys, the following conclusions can be drawn.

- (i) In **series I**, the spin wave **contribution** to thermal demagnetization completely dominates **over** that due to single-particle (SP) excitations of the '**weak-itinerant-type**' plus **local** spin-density fluctuations (LSF) in the temperature range $0 \sim t (= T/T_c) \sim t^*(p)$ for all p but the *reverse* is *true* for all the compositions at temperatures $t > t^*(p)$. By contrast, in **series II**, the SW contribution masks the feeble contribution from SP excitations of '**weak-itinerant-type**' and LSF in the range of temperatures $3.8 \text{ K} < T < 0.97t_c$ ($3.8 \text{ K} < T < 300 \text{ K}$) for $p < 0.25$ ($0.375 < p < 0.625$), but for $p \sim 0.75$ and $T < 300 \text{ K}$, a significant contribution from SP excitations of **strong-itinerant type** accompanies a dominant spin-wave contribution. This result indicates that all the compositions in the $a - (Fe_pNi_{1-p})_{80}(Si)_{20}$ alloy series behave as *weak* itinerant ferromagnets while a *transition* from *weak-itinerant* to *strong-itinerant* ferromagnetism occurs at a concentration $p \sim 0.75$ in the $a - (Fe_pNi_{1-p})_{80}P_{14}B_{6}$ alloy series.
- (ii) In both the alloy series, the spin-wave stiffness coefficient renormalizes with T as $D(T) \sim T^{5/2}$ for Fe concentrations up to $p \sim 0.625$ whereas $D(T) \sim T^2$ for $0.75 < p < 1.0$. Such a crossover in the temperature dependence of D from $T^{5/2}$ to T^2 at $p \sim 0.75$ is also observed in $c - Fe_xNi_{100-x}$ ($x = 80p$) alloys. Within the framework of the itinerant-electron model, this observation implies that the magnon-magnon interactions (especially the ones involving short-wavelength magnons) weaken with increasing p so much so that magnon-SP interactions show up with ease for $p \sim 0.75$.
- (iii) The present results unambiguously demonstrate that D_N (the value of D determined from either inelastic neutron scattering (INS) or Brillouin scattering experiments) $> D_M$ (the value of D deduced from the magnetization measurements) is a *characteristic* property of the amorphous ferromagnets with competing interactions and/or of amorphous ferromagnetic alloys that exhibit Invar effect. Based on the observed *Fe* concentration dependence of $M(T = 0, p)$, $D(T = 0, p)$ and $T_c(p)$ in the investigated amorphous alloys, it is argued that the competing interactions present in the alloys with p in the range $0.75 \sim p \sim 1.0$ give rise to noncollinear (canted) arrangement of spins in the ground state. This canted spin structure for $p \sim 0.75$, in turn, gives rise to longitudinal spin fluctuations which contribute as significantly **to** the $T^{3/2}$ decrease of magnetization as the transverse spin fluctuations (spin waves) do but leave D_N unaltered from its 'spin-wave-only' value. This explains as to why $D_N \gg D_M$ for the alloys with $p \sim 0.75$.
- (iv) The direct exchange interactions extend beyond the second nearest-neighbor distance for compositions close to, but above, the critical concentration for the appearance of long-range ferromagnetic order whereas the competing interactions in the amorphous alloys with $p > 0.75$ confine the direct d-d exchange interactions to the nearest neighbors only.
- (v) The concentration dependence of D and T_c observed in the present work as well as the recent finding that the peaks in the INS spectra due to the longitudinal spin fluctuations are

more intense in Invar alloys than in non Invar systems find a straightforward explanation in terms of the infinite 3D **ferromagnetic** matrix (FM) plus finite FM spin clusters model.

References

- [1] F. **Keffler**, Encyclopedia of Physics, edited by H.P.J. Wijn (**Springer-Verlag**, Berlin, 1966) Vol. XVIII part 2 p.1.
- [2] T. **Izuyama** and R. **Kubo**, *J. Appl. Phys.* **35**, 1674 (1964).
- [3] J. Mathon and E.P. Wohlfarth, *Proc. Roy. Soc. A* **302**, 409 (1968).
- [4] D.M. Edwards and E.P. Wohlfarth, *Proc. Roy. Soc. A* **303**, 127 (1968).
- [5] G.G. Lonzarich and L. **Taillefer**, *J. Phys. C* **18**, 4339 (1985); G.G. Lonzarich, *J. Magn. Magn. Mater.* **54-57**, 612 (1986).
- [6] J. Takeuchi and Y. **Masuda**, *J. Phys. Soc. Japan* **46**, 468 (1979).
- [7] T. Moriya, *J. Magn. Magn. Mater* **31-34**, 10 (1984); *ibid* **14**, 1 (1979); in *Spin Fluctuations in Itinerant Electron Magnetism* (Springer Verlag, Berlin, 1985).
- [8] S.N. **Kaul** and V. Siruguri, *J. Phys.: Condens. Matter* **4**, 505 (1992).
- [9] V. Siruguri and S.N. Kaul, *Phys. Rev. B* (communicated).
- [10] V. Siruguri, Ph.D thesis, University of Hyderabad (1993), unpublished.
- [11] P. Mohn and G. Hilscher, *Phys. Rev. B* **40**, 9126 (1989).
- [12] P.F. De Chatel and F.R. De Boer, *Physica (Utrecht)* **48**, 331 (1970); E.P. Wohlfarth and P.F. De Chatel, *Physica (Utrecht)* **48**, 477 (1970).
- [13] M.A. Continentino and N. Rivier, *J. Phys. F* **9**, L145 (1979); N. Rivier and M.A. Continentino, *J. Magn. Magn. Mater* **15-18**, 1419 (1980).
- [14] P. Mohn and E.P. Wohlfarth, *J. Magn. Magn. Mater.* **68**, L283 (1987); *J. Phys. F* **17**, 2421 (1987).
- [15] R. Krishnan, K.V. Rao and H.H. **Liebermann**, *J. Appl. Phys.* **55**, 1823 (1984).
- [16] W. Beck and H. **Kronmüller**, *Phys. Stat. Sol. b* **132**, 449 (1985).
- [17] S.N. Kaul, *J. Phys.: Condens. Matter* **3**, 4027 (1991).
- [18] S.N. Kaul, V. Siruguri and G. Chandra, *Phys. Rev. B* **45**, 12343 (1992).
- [19] S.N. Kaul, *Phys. Rev. B* **27**, 6923 (1983).
- [20] H. Hiroyoshi and K. **Fukamichi**, *J. Appl. Phys.* **53**, 2226 (1982).

- [21] P. Deppe, K. **Fukamichi**, F.S. Li, **M.** Rosenberg and M. **Sostarich**, IEEE Trans. Magn. **MAG-20**, 1367(1984).
- [22] S.N. **Kaul** and P.D. Babu, J. Phys.: Condens. Matter 4, 6429 (1992).
- [23] S.N. Kaul, Phys. Rev. B 27, 5761 (1983)
- [24] S. Dey, U. Gorres, H.J.V. Nielsen, M. Rosenberg and M. Sostarich, J. Phys. (Paris) 41, C8-678 (1980); S. Dey, P. Deppe, M. Rosenberg, F.E. Luborsky and J.L. Walter, J. **Appl.** Phys. 52, 1805(1981).
- [25] T. **Soumura**, K. Takeda, T. **Wakano**, K. Terasawa and T. Maeda, J. Magn. Magn. Mater. 58, 202 (1986).
- [26] S.N Kaul and T.V.S.M. Mohan Babu, J. Phys.: Condens. Matter 1, 8509 (1989).
- [27] R.J. Birgeneau, J.A. Tarvin, G. Shirane, E.M. Gyorgy, R.C.Sherwood, H.S. Chen and C.L. Chien, Phys. Rev. B 18, 2192 (1978).
- [28] G. Hilscher, R. **Haferl**, H. **Kirchmayr**, M. Müller and H.J. Giintherodt, J. Phys. F **11**, 2429 (1981).
- [29] A. Katsuki and E.P. Wohlfarth, *Proc. Roy. Soc. London A* **295**, 182 (1966); A. Katsuki, *Brit. J. Appl. Phys.* 18, 199 (1967); E.P. Wohlfarth, in *Quantum Theory of Atoms, Molecules, and the Solid State*, edited by P. Lowdin (Academic press, New York, 1966), p.485.
- [30] G.E. Fish and J.J. Rhyne, J. Appl. Phys. 61, 454 (1987).
- [31] S.N. Kaul, IEEE Trans. Magn. **MAG-20**, 1290 (1984).
- [32] S.N. Kaul, J. Magn. Magn. Mater. 53, 5 (1985)
- [33] S.N. Kaul, J. Phys. F 18, 2089 (1988).
- [34] K. Shirakawa, S. **Ohnuma**, M. Nose and T. **Masumoto**, IEEE Trans. Magn. **MAG-16**, 910 (1980).
- [35] J.A. Fernandez-Baca, J.W. Lynn, J.J. Rhyne and G.E. Fish, J. Appl. Phys. 61, 3406 (1987).
- [36] D.H. Ryan, J.M.D. Coey, E. Batalla, Z. Altounian and J.O. **Ström-Olsen**, Phys. Rev. B 35, 8630 (1987).
- [37] A.Singh and Z. Tesanovic, Phys. Rev. B 39, 7284 (1989).
- [38] V.A. Singh and L.M. Roth, J. Appl. Phys. 49, 1642 (1978); T. Kaneyoshi, J. Phys. Soc. Jpn. 45, 1835 (1978).

- [39] R.S. Iskhakov, Fiz. Tverd. **Tela** (Leningrad) 19, 3 (1977); [Sov. Phys. Solid State 19, 1 (1977)].
- [40] M. Rosenberg, U. **Hardebusch**, A. Schone - Warnefeld, R. Wernhardt and K. Fukamichi, J. Phys. F: Met. Phys. **118**, 2259 (1988).
- [41] S. Kanemaki, O. Takehira, **K.** Fukamichi and U. Mizutani, J. Phys.: Condens. Matter 1, 5903 (1989).
- [42] J. **Takeuchi** and Y. Masuda, J. Phys. Soc. Jpn. 46, 468 (1979).
- [43] J.E. Hirsch, Phys. Rev. B **44**, 675 (1991).
- [44] D. Wagner and E.P. Wohlfarth, Phys. Lett. A **118**, 29 (1986).
- [45] S.N. **Kaul**, unpublished.
- [46] N. Saito, **H.** Hiroyoshi, K. Fukamichi and Y. Nakagawa, J. Phys. F 16, 911 (1986).
- [47] M. Ghafari, N. Chmielek, W. Keune and C.P. **Foley**, Physica B **161**, 222 (1989).
- [48] S.N. Kaul, J. **Appl.** Phys. 61, 451 (1987).
- [49] S.N. Kaul and Ch.V. Mohan, J. Appl. Phys. **71**, 6090, (1992); *ibid* **71**, 6103 (1992).
- [50] J.J. Rhyne, R.W. Erwin, J.A. Fernandez-Baca and G.E. Fish, J. Appl. Phys. 63, 4080 (1988).
- [51] S.N. Kaul, Solid State **Commun.** 36, 279 (1980).
- [52] S.N. Kaul, IEEE Trans. Magn. **MAG-17**, 1208 (1981).
- [53] S.N. Kaul, Phys. Rev. B 24, 6550 (1981).
- [54] S.N. Kaul, Phys. Rev. B 38, 9178 (1988).
- [55] S.N. Kaul and M. Sambasiva Rao, Phys. Rev. B 43, 11240 (1991); J. Phys.: Condens. Matter 6, 7403 (1994).
- [56] M. Sambasiva Rao and S.N. Kaul, J. Magn. Magn. Mater. **147**, 149 (1995).
- [57] S.M. Bhagat, D.J. Webb and M.A. **Manheimer**, J. Magn. Magn. Mater. 53, 209 (1985); D.J. Webb and S.M. Bhagat, J. Magn. Magn. Mater 42, 109 (1984).
- [58] Z. Frait and D. Fraitova, Phys. Stat. Sol. (b) **154**, 363 (1989); Z. Frait and D. Fraitova, in *Spin Waves and Magnetic Excitations*, edited by A.S. **Borovik-Romanov** and S.K. Sinha (Elsevier, Amsterdam, 1988) Vol.2, **p.1**.
- [59] J.A. Tarvin, G. Shirane, R.J. Birgeneau and H.S. Chen, Phys. Rev. B **17**, 241 (1978).

- [60] H. Grinsditch, A. Malozemoff and A. Brunsch, Phys. Rev. Lett. **43**, 711 (1979).
- [61] Y. Ishikawa, K. Yamada, K. Tajima and K. Fukamichi, J. Phys. Soc. Jpn. **50**, 1958 (1981).
- [62] Z. Xianyu, Y. Ishikawa and S. Onodera, J. Phys. Soc. Jpn. **51**, 1799 (1982).
- [63] W. Minor, B. Lebech, K. Clausen and W. Dmowski, in *Rapidly Quenched metals*, edited by S. Steeb and H. Warlimont (Elsevier, Amsterdam, 1985), p.1149.
- [64] J.A. Fernandez-Baca, J.J. Rhyne, G.E. Fish, M. Hennion and B. Hennion, J. Appl. Phys. **67**, 5223 (1990); S.C. Yu, J.W. Lynn and G.E. Fish, Jpn. J. Appl. Phys. **32**, 67 (1993).
- [65] R.W. Cochrane and G.S. Cargill III, Phys. Rev. Lett. **32**, 476 (1974).
- [66] C.C. Tsuei and H. Lilienthal, Phys. Rev. B **13**, 4899 (1976).
- [67] T. Mizoguchi, in *Magnetic and Magnetic Materials - 1976* Proceedings of first Joint MMM-Intermag Conf. edited by J.J. Becker and G.H. Lander, AIP Conf. Proc. No. 34, (AIP, New York, 1976), p.286.
- [68] C.L. Chien and R. Hasegawa, Phys. Rev. B **16**, 2115 (1977); *ibid.* **16**, 3024 (1977).
- [69] N.S. Kazama, M. Mitera and T. Masumoto, in *Proceedings of the third International Conference on Rapidly Quenched Metals, Brighton, 1978*, edited by B. Cantor (The Metals Society, London, 1978), p.164.
- [70] S.M. Bhagat, M.L. Spano and K.V. Rao, J. Appl. Phys. **50**, 1580 (1979); S. Hatta and T. Egami, *ibid.* **50**, 1589 (1979).
- [71] R. Hasegawa and R. Ray, Phys. Rev. B **20**, 211 (1979).
- [72] C.L. Chien, D. Musser, E.M. Gyorgy, R.C. Sherwood, H.S. Chen, F.E. Luborsky and J.L. Walter, Phys. Rev. B **20**, 283 (1979).
- [73] M. Sostarich, S. Dey, P. Deppe, M. Rosenberg, G. Czjzek, V. Oestreich, H. Schmidt and F.E. Luborsky, IEEE Trans. Magn. **MAG-17**, 2612 (1981).
- [74] G. Bayreuther, G. Enders, H. Hoffmann, U. Korndorfer, W. Oestreicher, K. Roll and M. Takahashi, J. Magn. Magn. Mater. **31-34**, 1535 (1983).
- [75] A.K. Majumdar, V. Oestreich, D. Weschenfelder and F.E. Luborsky, Phys. Rev. B **27**, 5618 (1983).
- [76] K. Hiiller and G. Dietz, J. Magn. Magn. Mater **50**, 250 (1985); K. Hiiller, J. Magn. Magn. Mater. **61**, 347 (1986).
- [77] O. Yamada, M. Mimura, H. Maruyama, I. Nakai, S. Ishio and M. Takahashi, J. Magn. Magn. Mater **54-57**, 250 (1986).

- [78] I. Nakai, **O. Yamada**, M. Mimura, S. Ishio and M. Takahashi, J. Phys. Soc. Jpn. **66**, 4056 (1987).
- [79] J.D. Axe, L. Passel and C.C. Tsuei, in *Magnetic and Magnetic Materials - 1974* (San Francisco), Proceedings of the 20th Annual Conference on Magnetism and Magnetic Materials, edited by C.D. Graham, Jr., G.H. Lander, and J.J. Rhyne (AIP, New York, 1975), p.119; H.A. Mook, N. Wakabayashi and D. Pan, Phys. Rev. Lett. **34**, 1029 (1975).
- [80] J.W. Lynn, G. Shirane, R.J. Birgeneau and H.S. Chen, in *Magnetism and Magnetic Materials - 1976* (Ref 67), p.313.
- [81] J.D. Axe, G. Shirane, T. Mizoguchi and K. Yamauchi, Phys. Rev. B **15**, 2763 (1977); H.A. Mook and C.C. Tsuei, Phys. Rev. B **16**, 2184 (1977).
- [82] J.A. Fernandez-Baca, J.W. Lynn, J.J. Rhyne and G.E. Fish, Phys. Rev. B **36**, 8497 (1987).
- [83] I. Nakai, J. Phys. Soc. Jpn. **52**, 1781 (1983); I. Nakai, F. Ono and O. Yamada, J. Phys. Soc. Jpn. **52**, 1791 (1983).
- [84] J. Crangle and G.C. Hallam, Proc.Roy.Soc. (London) A **272** 119 (1963).
- [85] S.N. Kaul, Solid State Commun. **52**, 1015 (1984); T. Egami, Rep. Prog. Phys. **47**, 1601 (1984).
- [86] E. Babic, Z. Marohnic and E.P. Wohlfarth, Phys. Lett. **95A**, 335 (1983).
- [87] S.N. Kaul, Phys. Stat. Sol. (b) **116**, K99 (1983).
- [88] S.N. Kaul and M. Rosenberg, Phys. Rev. B **27**, 5698 (1983).
- [89] H. Hopster, R. Kurzawa, R. Raue, W. Schmidt, G. Güntherodt, K.H. Walker and H.J. Güntherodt, J. Phys. F **15**, L11 (1985).
- [90] A. Anderjczuk, L. Dobrzynski, E. Zukowski, M.J. Cooper, S. Hamouda and J. Latuszkiewicz, J. Phys.: Condens. Matter **4**, 2735 (1992).
- [91] B.E. Argyle, S.H. Charap and E.W. Pugh, Phys. Rev. **132**, 2051 (1963).
- [92] V. Dose, in *Rapidly Quenched Metals - 1985*, (Ref 63), p. 963.
- [93] F. Fukamichi, T. Masumoto and M. Kikuchi, IEEE Trans. Magn. **MAG-15**, 1404 (1979).
- [94] S.J. Harker and R.J. Pollard, J. Phys.: Condens. Matter **1**, 8269 (1989).
- [95] R.A. Cowley, C. Patterson, N. Cowlam, P.K. Ivison, J. Martinez and L.D. Cussen, J. Phys.: Condens. Matter **3**, 9521 (1991).

- [96] H. Mano, J. Phys. **Soc. Jpn.** 51, 3157 (1982).
- [97] E.P. **Wohlfarth**, J. Magn. Magn. Mater. 10, 120 (1979).
- [98] S.N. **Kaul** and M. Rosenberg, Phys. Rev. B 25, 5863 (1982).
- [99] J.W. Lynn, N. Rosov and G.E. Fish, J. **Appl.** Phys. 73, 5369 (1993).
- [100] V.G. **Vaks**, A.I. Larkin and S.A. Pikin, Zh. Eksp. Teor. Fiz 53, 1089 (1967) [Sov. Phys. - JETP **26**, 647 (1968)].
- [101] R. Raghavan and D.L. Huber, Phys. Rev. B 14, 1185 (1976).
- [102] J.K. Bhattacharjee, Phys. Rev. B 27, 3058 (1983).
- [103] H.A. Mook and J.W. Lynn, Phys. Rev. B 29, 4056 (1984).

CHAPTER 4

THERMAL AND PERCOLATION CRITICAL BEHAVIOUR

This chapter is divided into two parts. The first part describes the bulk magnetization (BM) and ferromagnetic resonance (FMR) study of the thermal critical behaviour near the ferromagnetic (FM) - paramagnetic (PM) phase transition at the Curie temperature, T_C , in $a - Fe_{90+y}Zr_{10-y}$ and $a - Fe_{90-x}Co_xZr_{10}$ alloys whereas the second part deals with the percolation critical phenomena associated with the critical concentration (percolation threshold) for ferromagnetism in $a - (Fe, Ni)$ -metalloid alloys.

A. THERMAL CRITICAL BEHAVIOUR

4.1. Results and analysis

Several methods of analysis have been used in the literature [1] to extract the critical exponents from bulk magnetization data. The critical exponents that some of these methods yield are the *effective* exponents which **depend** on the temperature range used in the analysis (even within the asymptotic critical region) and can be significantly different in magnitude from the 'true' *asymptotic* exponents that are of interest in the theory. The values of these effective exponents approach those of the asymptotic exponents only in the immediate vicinity of T_C (i.e., in the limit $T \rightarrow T_C$). On the other hand, the method that includes the 'correction-to-scaling' (CTS) terms in the analysis yields the true asymptotic values of the exponents. Some of these methods described below are used to analyze the magnetization data of $a - Fe_{90+y}Zr_{10-y}/y = 0, 1$ and $a - Fe_{90-x}Co_xZr_{10}/x = 0, 1, 2, 4$ and 6 alloys.

4.1.1. Arrott equation-of-state

This method employs the Arrott-Noakes equation-of-state [1,2] (cf. Eq.(1.32) of Chapter 1) given by

$$(H/M)^{1/\gamma} = a' + b' M^{1/\beta} \quad (4.1a)$$

where β and γ are the spontaneous magnetization and initial susceptibility critical exponents, respectively, and the temperature-independent coefficients a' and b' are related to the critical amplitudes m_o, T and D defined by Eqs.(1.29a), (1.296) and (1.306) of Chapter 1 as

$$\Gamma = (m_o/h_o) = (a')^{-\gamma}, \quad D = (b')^{\gamma} \quad \text{and} \quad m_o = (a'/b')^{\beta} \quad (4.16)$$

According to this method, the raw M vs. H isotherms taken at different temperatures in the critical region are used to construct the $M^{1/\beta}$ vs. $(H/M)^{1/\gamma}$ plot, popularly known as the modified Arrott plot (MAP). The values of critical exponents β and γ are varied so as to make the $M^{1/\beta}$ vs. $(H/M)^{1/\gamma}$ isotherms in a narrow temperature range around T_c nothing but a set of parallel straight lines (with the critical isotherm at T_c passing through the origin) over as wide a range of H/M values as possible. The critical exponents obtained in this way are still effective exponents. However, exponent values very close to the asymptotic ones can be obtained if during the course of this analysis, the temperature range around T_c is narrowed down to such an extent as to approach T_c as closely as possible [3,4]. The modified Arrott plots so constructed for a — $Fe_{90+y}Zr_{10-y}$ ($y = 0, 1$) and a — $Fe_{90-x}Co_xZr_{10}$ ($x = 0, 1, 2, 4$ and 6) alloys are displayed in Fig. 4.1(a)-(f). In these figures, only the isotherms at a few selected temperatures in the critical region are included for the sake of clarity. It is evident from these figures that the $M(T, H)$ data significantly deviate from the linear MAP isotherms at low fields for temperatures away from T_c and such deviations become more pronounced as $|T - T_c|$ increases. In order to determine the 'zero-field' quantities such as spontaneous magnetization, $M(T, 0)$, and initial susceptibility, $\chi_o(T)$, the high-field linear portions of the MAP isotherms are extrapolated to $H/M = 0$ to yield intercepts $[M(T, 0)]^{1/\beta}$ and $[\chi_o^{-1}(T)]^{1/\gamma}$ on the ordinate ($T < T_c$) and abscissa ($T > T_c$), respectively. The $M(T, 0)$ and $\chi_o^{-1}(T)$ data, computed from these intercepts, are plotted against $\epsilon = (T - T_c)/T_c$ in Fig. 4.2(a) and 4.2(b), respectively. The $M(T, 0)$ and $\chi_o^{-1}(T)$ data, so obtained, are analyzed using the methods described below.

4.1.2. Single-power-law (SPL) analysis

The spontaneous magnetization and initial susceptibility data in the critical region have been directly fitted to single power law expressions (cf. Eqs.(1.29a) and (1.29b); Chapter 1) given by [1,3-5]

$$M(T, 0) = m_o^{\epsilon_{eff}} (-\epsilon)^{\beta_{eff}} \quad \epsilon < 0 \quad (4.2)$$

and

$$\chi_o(T) = \Gamma_{eff} \epsilon^{-\gamma_{eff}} \quad \epsilon > 0 \quad (4.3)$$

where β_{eff} and γ_{eff} are the effective exponents, and $m_o^{\epsilon_{eff}}$ and $\Gamma_{eff} = (m_o/h_o)^{\epsilon_{eff}}$ are the effective critical amplitudes. A detailed range-of-fit analysis of $M(T, 0)$ and $\chi_o(T)$ data based on the above expressions indicate that the values of critical exponents and amplitudes depend on the temperature range chosen for the analysis. The dashed curves in Figs. 4.2(a) and 4.2(b), respectively, represent the best theoretical fits based on Eqs.(4.2) and (4.3) over the temperature range $|\epsilon| < 0.02$ with the choice of the parameters given in Table 4.1.

Table 4.1. Results of the Kouvel-Fisher (KF) and Single Power Law (SPL) analysis of the $M(T, 0)$ and $\chi_o(T)$ data taken on the $a - Fe_{90+y}Zr_{10-y}$ and $a - Fe_{90-x}Co_xZr_{10}$ alloys.

Alloy conc.	analysis	fit range ($10^3 t $)	(K)	ffl	(G)	$\overline{T_C^F}$	γ_{eff}	$(m_o/h_o)^{eff}$ (10^{-3})
y=1	KF	1.0-10	209.69(10)	0.382(15)	870(30)	209.63(10)	1.400(20)	4.95(5)
	KF	1.0-20	209.72(10)	0.392(15)	905(30)	209.62(10)	1.415(20)	4.65(5)
	KF	1.0-40	209.81(10)	0.406(15)	950(30)	209.60(10)	1.431(20)	4.35(5)
	SPL	1.0-10	209.76(10)	0.386(18)	850(40)	209.60(10)	1.402(20)	4.90(10)
	SPL	1.0-20	209.80(10)	0.398(18)	935(40)	209.60(10)	1.420(20)	4.60(10)
y=0;	KF	1.0-10	225.00(10)	0.382(15)	870(35)	224.98(10)	1.405(20)	3.50(10)
	KF	1.0-20	225.04(10)	0.392(15)	905(35)	224.96(10)	1.435(20)	3.05(10)
	KF	1.0-40	225.11(10)	0.406(15)	950(35)	224.87(10)	1.473(20)	2.80(10)
	SPL	1.0-10	225.00(10)	0.370(15)	840(50)	224.94(10)	1.409(20)	3.50(15)
	SPL	1.0-20	225.05(10)	0.400(15)	950(50)	224.92(10)	1.440(20)	3.10(15)
x=0	KF	1.0-10	256.75(12)	0.384(15)	925(35)	256.62(10)	1.416(25)	2.45(10)
	KF	1.0-20	256.76(12)	0.400(15)	995(35)	256.64(10)	1.439(25)	2.25(10)
	KF	1.0-40	256.75(12)	0.411(15)	1060(35)	256.66(10)	1.473(25)	1.90(10)
	SPL	1.0-10	256.73(20)	0.390(20)	940(50)	256.67(15)	1.413(20)	2.30(12)
	SPL	1.0-20	256.80(20)	0.410(20)	1035(50)	256.65(15)	1.440(20)	2.20(12)
x=1	KF	1.0-10	281.60(10)	0.381(15)	915(35)	281.63(10)	1.388(20)	2.05(8)
	KF	0.9-20	281.61(10)	0.384(15)	935(35)	281.58(10)	1.431(20)	1.75(8)
	KF	0.9-40	281.67(10)	0.392(15)	950(35)	281.54(10)	1.491(20)	1.35(8)
	SPL	0.9-10	281.54(12)	0.370(15)	875(50)	281.63(12)	1.390(20)	1.95(10)
	SPL	0.9-20	281.57(12)	0.383(15)	950(40)	281.61(12)	1.420(20)	1.80(10)
x=2	KF	0.9-10	281.60(10)	0.381(15)	915(35)	281.63(10)	1.388(20)	2.05(8)
	KF	0.9-20	281.61(10)	0.384(15)	935(35)	281.58(10)	1.431(20)	1.75(8)
	KF	0.9-40	281.67(10)	0.392(15)	950(35)	281.54(10)	1.491(20)	1.35(8)
	SPL	0.9-10	281.54(12)	0.370(15)	875(50)	281.63(12)	1.390(20)	1.95(10)
	SPL	0.9-20	281.57(12)	0.383(15)	950(40)	281.61(12)	1.420(20)	1.80(10)
x=4	KF	1.0-10	327.95(10)	0.386(15)	1130(35)	327.99(10)	1.407(20)	1.60(8)
	KF	1.0-20	327.99(10)	0.404(15)	1195(35)	327.98(10)	1.428(20)	1.40(8)
	KF	1.0-40	328.10(10)	0.416(15)	1260(35)	327.91(10)	1.479(20)	1.15(8)
	SPL	1.0-10	327.95(10)	0.382(15)	1150(50)	327.99(12)	1.399(25)	1.55(15)
	SPL	1.0-20	327.94(10)	0.400(15)	1170(50)	327.98(12)	1.425(25)	1.40(15)
x=6	KF	0.8-10	374.77(10)	0.390(15)	1095(35)	374.79(10)	1.402(20)	1.36(6)
	KF	0.8-20	374.81(10)	0.402(15)	1130(35)	374.80(10)	1.423(20)	1.20(6)
	KF	0.8-40	374.93(10)	0.416(15)	1190(35)	374.81(10)	1.466(20)	0.98(6)
	SPL	0.8-10	374.79(15)	0.382(20)	1090(50)	374.74(15)	1.400(25)	1.40(12)
	SPL	0.8-20	374.80(15)	0.395(20)	1105(50)	374.72(15)	1.430(25)	1.25(12)

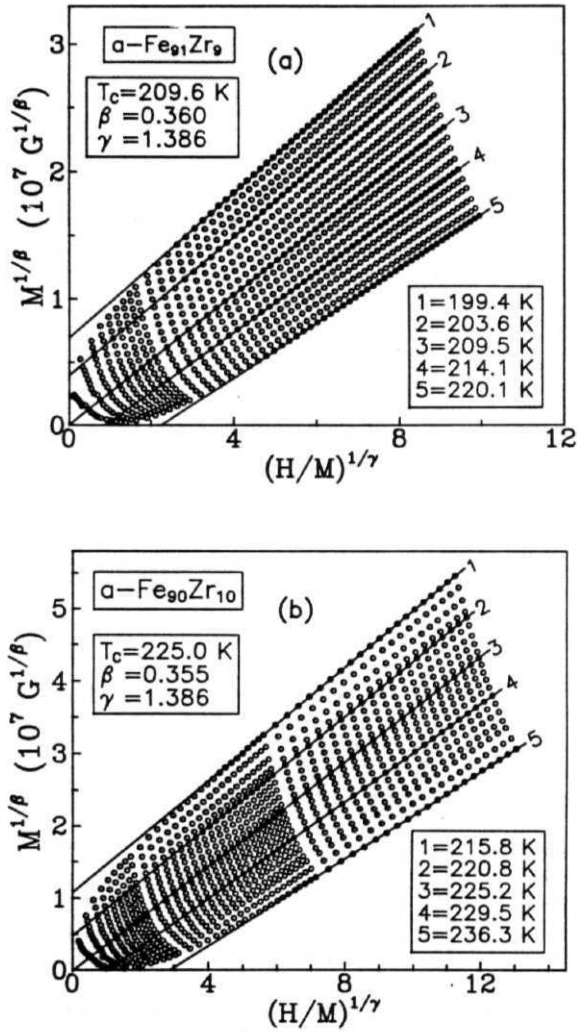


Fig. 4.1 $M^{1/\beta}$ vs. $(H/M)^{1/\gamma}$ plot for (a) $a\text{-Fe}_{91}\text{Zr}_9$ and (b) $a\text{-Fe}_{90}\text{Zr}_{10}$ at a few selected temperatures in the critical region.

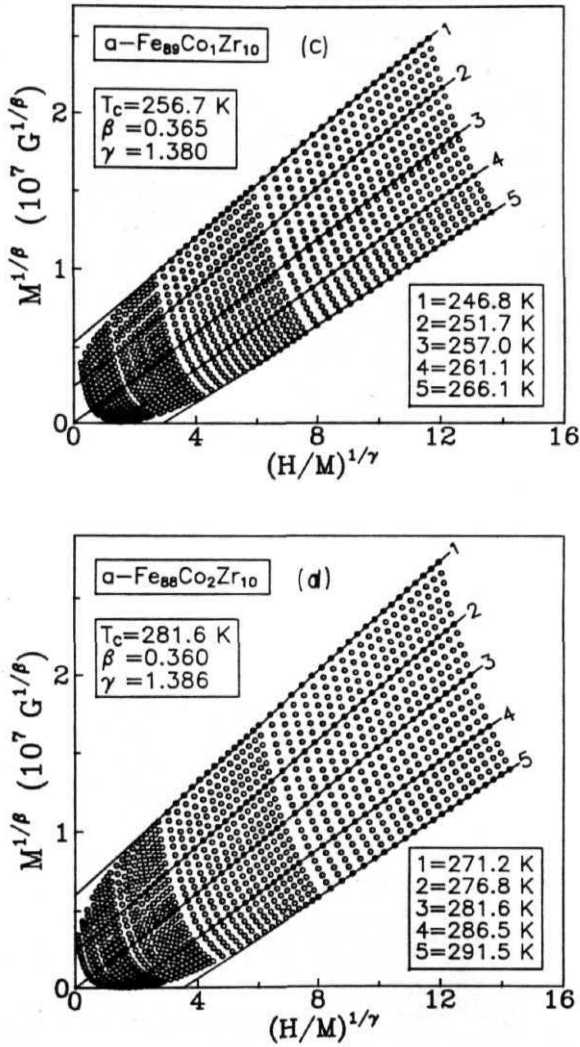


Fig. 4.1 Modified Arrott plot for (c) $a\text{-Fe}_{89}\text{Co}_1\text{Zr}_{10}$ and (d) $a\text{-Fe}_{88}\text{Co}_2\text{Zr}_{10}$ in the critical

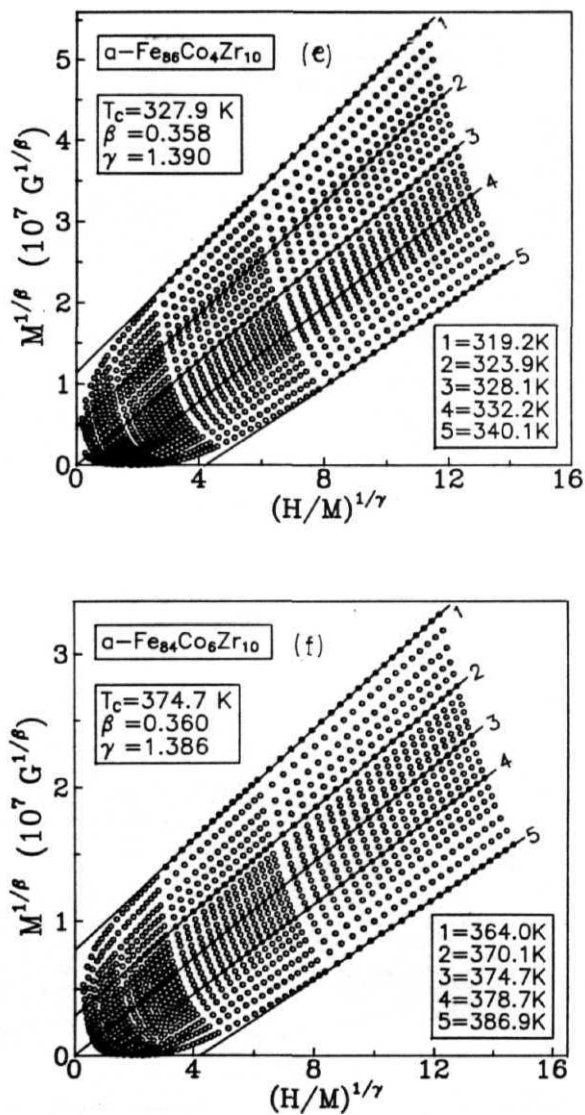


Fig. 4.1 Modified Arrott plot for (e) $\alpha\text{-Fe}_{86}\text{Co}_4\text{Zr}_{10}$ and (f) $\alpha\text{-Fe}_{84}\text{Co}_6\text{Zr}_{10}$ in the critical region.

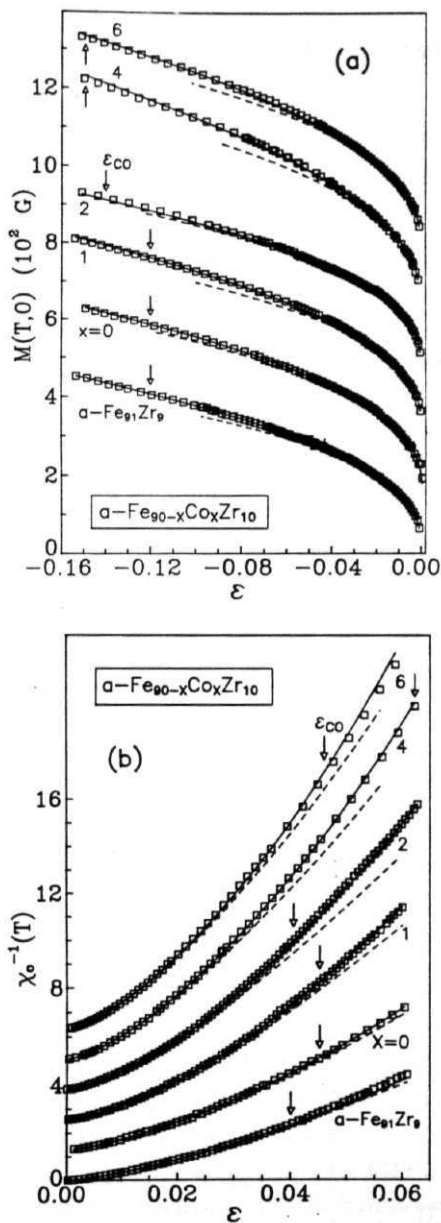


Fig. 4.2 (a) $M(T, 0)$ vs. $e = (T - T_C)/T_C$ and (b) χ_0^{-1} vs. ϵ in the critical region. Note that $M(T, 0)$ and χ_0^{-1} data for $x = 0, 1, 2, 4, 6$ are shifted by the amount 0.155 G, 0.31 G, 0.465 G, 0.62 G, 0.775 G, and 1.27, 2.54, 3.81, 5.08, 6.35 with respect to that for $a\text{-Fe}_{91}\text{Zr}_9$ in (a) and (b), respectively.

4.1.3. Kouvel-Fisher (KF) Method

Kouvel-Fisher (KF) method [6] is based on the single power laws, Eqs.(4.2) and (4.3), and determines critical exponents through analytical means by rewriting the Eqs.(4.2) and (4.3) in the form

$$Y(T) = M(T, 0)[dM(T, 0)/dT]^{-1} = (T - T_C)/\beta_{eff} \quad (4.4a)$$

and

$$X(T) = \chi_o^{-1}(T) [d\chi_o^{-1}(T)/dT]^{-1} = (T - T_C)/\gamma_{eff} \quad (4.46)$$

These equations indicate that in the temperature range (asymptotic critical region) over which Eqs.(4.2) and (4.3) and hence **Eqs.(4.4a)** and (4.46) are valid, the plots of $Y(T)$ vs. T and $X(T)$ vs. T should be straight lines with slopes $(1/\beta_{eff})$ and $(1/\gamma_{eff})$ and the intercepts on the T-axes equal to T_C^- and T_C^+ , respectively [3,4,6]. The $Y(T)$ and $X(T)$ data plotted against $\epsilon = (T - T_C)/T_C$ in Fig. 4.3(a) and 4.3(b) demonstrate the validity of the KF approach for the presently investigated alloys. In these figures, $Y(T)$ and $X(T)$ have been displayed as functions of reduced temperature, ϵ , instead of T so as to accommodate such plots for compositions with widely different T_C values in a single graph. The straight lines through the data points represent the linear fits, based on Eq.(4.4a) or (4.46), over the ϵ range indicated by the upward arrows. Accurate values for β_{eff} , γ_{eff} and T_C in different temperature ranges for the alloys in question obtained by using the KF procedure are listed in Table 4.1. The entries in this table clearly show that the results of the KF analysis are in very good agreement with those of the single-power-law analysis and that the *effective* exponents and amplitudes *depend* on the temperature range used for the fit.

4.1.4. Scaling equation-of-state (SES) analysis

This type of analysis assumes the validity of scaling and makes use of a particular form of the scaling equation-of-state (SES) to extract two critical exponents (θ and γ or β and δ) at a time from the 'in-field' magnetization data. This method completely avoids the problems associated with the extrapolation and facilitates analysis of **FMR** data as shown below. At any given temperature, FMR spectrum yields only a single value of saturation magnetization corresponding to the resonance field, H_{res} , as against a complete M vs. H isotherm obtained in bulk magnetization measurements. Consequently, neither FMR data can be used to construct the modified Arrott plot nor the extrapolation methods can be employed to deduce $M(T, 0)$ and $X_o(T)$ from such data. However, the SES analysis of FMR data, which yields reliable values

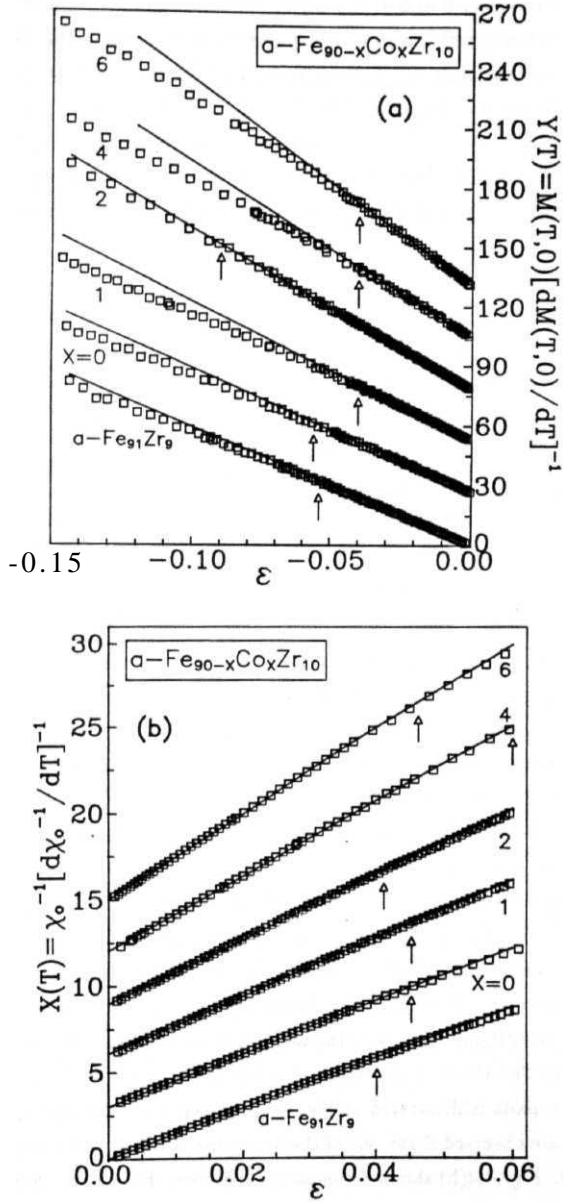


Fig. 4.3 (a) $Y(T)$ vs. ϵ and (b) $X(T)$ vs. t in the critical region. The zero on the ordinate scale for $x = 0, 1, 2, 4$ and 6 should read as 26.25, 52.5, 78.75, 105.0, 131.25 and 3.0, 6.0, 9.0, 12.0, 15.0 in (a) and (b), respectively.

for the critical exponents 0 and 7, is possible. At this stage, it should be noted that the 'zero-field' **FMAR** (ferromagnetic antiresonance) transmission technique has been successfully used [7] in the past to determine spontaneous magnetization and hence the critical exponent β for crystalline **ferromagnets**. That the SES analysis of FMR and BM data in the critical region yield identical results (within the uncertainty limits) can be noticed from the analysis presented below. Two types of SES methods, referred to as **SES-I** and **SES-II** in the literature [1], have been used to analyze the magnetization as well as FMR data, as described below.

This approach is based on the SES form

$$m = f_{\pm}(h) \quad (4.5a)$$

where plus and minus signs refer to temperatures above and below T_c and $m = M/|\epsilon|^{\beta}$ and $h = H/|\epsilon|^{\beta+\gamma}$ (with $\epsilon = (T - T_c)/T_c$) are the scaled magnetization and scaled field, respectively. According to **Eq.(4.5a)**, the M vs. H isotherms in the critical region are made to fall onto two universal curves (f_- for $\epsilon < 0$ and f_+ for $\epsilon > 0$) with a proper choice of the parameters T_c , β and γ [1,4,8-10]. However, this choice is by no means unique in the sense that nearly the same quality of data collapse onto two universal curves can be achieved for a wide range of parameter values (typically, $\pm 2\%$ for T_c and $\pm 10\%$ for β and γ) particularly when the data outside the asymptotic critical region are also included in the analysis. This problem is effectively tackled by employing the range-of-fit SES analysis [10] in which more and more of data taken at temperatures away from T_c are excluded from the m vs. h plot so that the exponents β and γ become increasingly sensitive to the choice of T_c and the data exhibit strong departures from the curves $f_-(h)$ and $f_+(h)$ if the choice of the parameters differs even slightly from the correct one. This procedure, therefore, goes on refining the values of the critical exponents until they approach the asymptotic values. Evidently, such an analysis can be carried out successfully only when sufficient data are available in the asymptotic critical region. FMR data taken on $a - Fe_{90-x}Co_xZr_{10}$ alloys with $x = 0, 1, 2, 4, 6$ and 8 have been analyzed in this way by identifying H_{res} with the ordering field conjugate to M ($\equiv M_S$, the saturation magnetization). The effect of the variation in the value of T_c on the quality of data collapse in $\ln m$ vs. $\ln h$ plots is illustrated in Fig. 4.4(a) using the FMR data of $a - Fe_{90}Zr_{10}$ alloy. Similar effects are observed if any one of the exponents is varied while keeping T_c and the other exponent fixed. Fig. 4.4(b) shows a comparison between the $\ln m$ vs. $\ln h$ scaling plots for the alloy with $x = 0$ constructed using the BM data and three sets of FMR data (taken in different experimental runs) on the same sample. A perfect agreement between different sets of FMR data and between the results of FMR and BM measurements is evident from this figure. At this stage, it is important to note that in the present work, two sets of BM data have been taken on

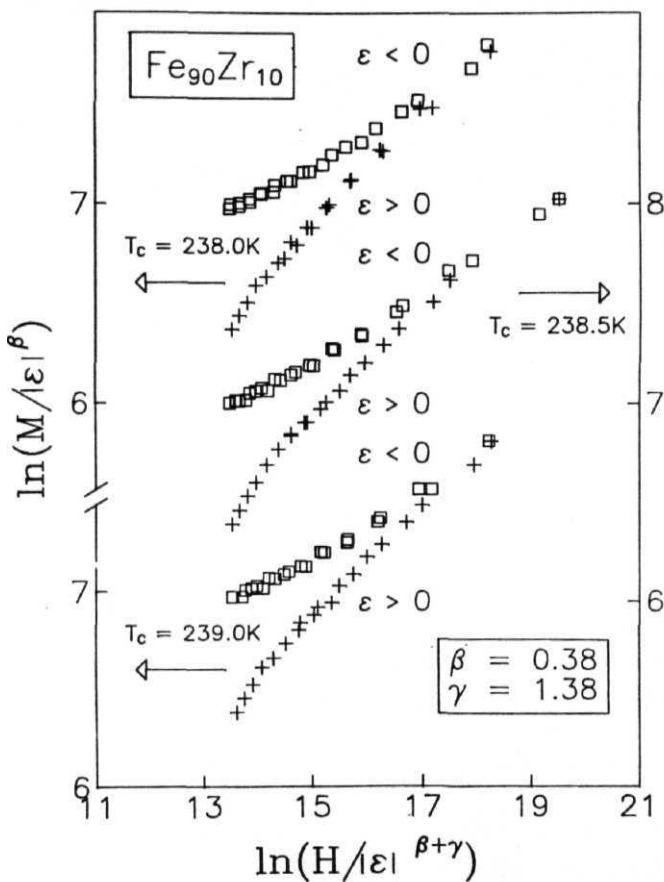


Fig. 4.4 (a) $\ln(M/|\epsilon|^\beta)$ vs. $\ln(H/|\epsilon|^{\beta+\gamma})$ plots for different values of T_c constructed from FMR data taken on the sample B1 (see text) of a $\text{Fe}_{90}\text{Zr}_{10}$.

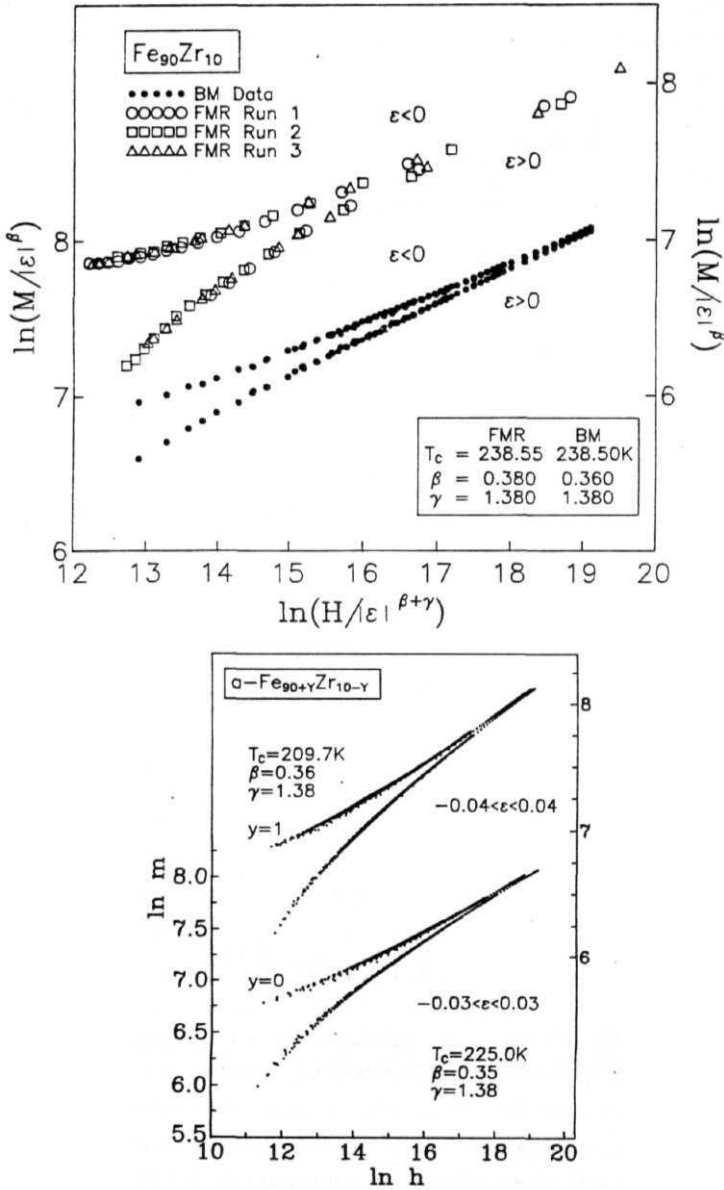


Fig. 4.4 (b) $\ln(M/|\epsilon|^\beta)$ vs. $\ln(H/|\epsilon|^{\beta+\gamma})$ plots constructed from the FMR and BM data taken on sample B1 of a - $\text{Fe}_{90}\text{Zr}_{10}$ (c) Scaling plots constructed from the BM data taken on the samples B2 (see text) of a - $\text{Fe}_{90+y}\text{Zr}_{10-y}$ ($y = 0, 1$) alloys.

the alloy samples having the same nominal composition $Fe_{90}Zr_{10}$ but coming from *two* different batches. These samples will henceforth be referred to as **B1** and B2. The **FMR** and one set of **BM** data, taken on the sample **B1** with $T_c = 238.5$ K in the critical region only, are presented in this section alone with the sole purpose of comparing FMR and BM results on the same sample. On the other hand, the **BM** data on the B2 sample of the same nominal composition $x = 0$ but with a different value of $T_c = 225$ K have been taken in a much wider temperature range 70 K $< T \sim 1.3T_c$, which embraces the critical region. Thus, the **BM** data taken on sample B2 figure not only in this chapter but also in other relevant chapters of this thesis. Moreover, for all other compositions in the amorphous alloy series $a - Fe_{90-x}Co_xZr_{10}$ FMR and **BM** data have been taken on samples coming from two *different* batches. The $\ln m$ vs. $\ln h$ scaling plots for $a - Fe_{91}Zr_9$ and sample B2 of $a - Fe_{90}Zr_{10}$, depicted in Fig. 4.4(c), when compared with the plots shown in Fig.4.4(b) clearly demonstrate that such plots for both the samples B1 and B2 are essentially the same even though the two samples have different T_c values.

(b) SES-II:

An alternative form of SES given by [1]

$$m^2 = \mp a_{\pm} + b_{\pm} (h/m) \quad (4.56)$$

(where the plus and minus signs have the same meaning as mentioned earlier and the constants a_{\pm} and b_{\pm} are related to the critical amplitudes as $m_o = \sqrt{a_{\pm}}$ and $h_o/m_o = a_{\pm}/b_{\pm}$) has also been used in the literature [1,11-14] to determine the exponents 0 and 7. In this case too, the M vs. H isotherms (and hence $M_S(T, H)$ data of FMR) in the critical region are made to fall onto two universal curves, one below T_c and the other above T_c , in a m^2 vs. h/m plot through a proper choice of T_c , 0 and 7. This form of SES has the distinction of providing a more rigorous means of determining T_c , 0 and 7 since even the slight deviations of the data from the universal curves, which do not show up clearly in a $\ln m$ vs. $\ln h$ plot because of the insensitive nature of the **double-logarithmic** scale, become easily discernible [11-13] in the m^2 vs. h/m plot. Another advantage of SES-II (Eq.4.56) is that it allows estimation of the critical amplitudes (m_o and h_o/m_o) from the intercepts made by the universal curves on the m^2 and h/m axes. The m^2 vs. h/m plots constructed using the FMR and **BM** data taken on sample B1 with the choice of parameters T_c , 0 and 7 given in Table 4.2 are shown in Fig. 4.5(a) and 4.5(b). Consistency among different sets of data is now all the more obvious from these figures, particularly when FMR and **BM** data are plotted on a more sensitive scale and only those **BM** data that are taken at fields comparable in strength to H_{res} values of the FMR data are included in Fig. 4.5(a). The critical amplitudes are then computed from the intercepts made by the smooth curves drawn through the data points (Fig. 4.5) on the m^2 ($T < T_c$) and h/m ($T > T_c$) axes. This is clearly brought out by the insets in which data near the origin are plotted on a more sensitive

Table 4.2. Values of the critical exponents and amplitudes obtained from the scaling equation-of-state analysis of the FMR and BM data. Note that μ_0 values used here are the ones determined from BM data in chapter 3. Numbers in the parentheses denote the uncertainty in the least significant figure and the numbers 1, 2 and 3 denote the first, second and third experimental runs on the same sample. Abbreviations: BM - Bulk magnetization; FMR - ferromagnetic resonance. *Samples belonging to the alloy batch B2 (see text).

conc. (y/x)	Method	T_C (K)	β_{eff}	γ_{eff}	m_0^{eff} (G)	h_0^{eff}/m_0^{eff}	h_0^{eff} (10^5 G)	μ_0 (μ_B)	$\mu_0 h_0^{eff}/k_B T_C$	μ_{eff} (μ_B)	ϵ (%)
y=1	BM*	209.66(10)	0.360(10)	1.38(2)	750(35)	155(50)	1.1(4)	1.34(2)	0.049(20)	44(17)	3(1)
x=0; y=0	FMR 1	238.55(15)	0.380(30)	1.40(6)	870(30)	500(50)	4.4(6)	1.44(2)	0.172(17)	12.7(16)	11(1)
	FMR 2	238.50(15)	0.370(30)	1.39(6)	870(30)	525(50)	4.6(6)	1.44(2)	0.180(20)	12.2(17)	11(1)
	FMR 3	238.55(15)	0.380(30)	1.38(6)	865(30)	500(50)	4.3(6)	1.44(2)	0.168(17)	13.0(15)	11(1)
	BM	238.50(10)	0.360(20)	1.38(3)	870(25)	500(50)	4.4(6)	1.44(2)	0.172(16)	12.7(16)	11(1)
	BM*	225.00(10)	0.350(15)	1.39(3)	800(30)	175(50)	1.4(4)	1.44(2)	0.060(20)	38(14)	4(1)
x=1	FMR 1	254.50(20)	0.380(30)	1.38(6)	1030(35)	500(75)	5.1(9)	1.52(2)	0.187(35)	11.7(18)	13(2)
	FMR 2	254.80(20)	0.380(30)	1.38(6)	1045(25)	430(50)	4.5(7)	1.52(2)	0.165(22)	13.3(15)	11(1)
	BM*	256.70(10)	0.370(10)	1.38(2)	840(30)	200(50)	1.7(5)	1.52(2)	0.067(20)	36(11)	5(1)
x=2	FMR 1	284.00(25)	0.375(25)	1.38(5)	1070(25)	400(60)	4.3(8)	1.62(2)	0.164(30)	11.3(10)	11(2)
	FMR 2	284.50(25)	0.385(25)	1.38(5)	1065(25)	450(50)	4.8(6)	1.62(2)	0.182(22)	13.9(15)	12(1)
	BM*	281.60(10)	0.360(10)	1.39(2)	800(30)	250(50)	2.0(5)	1.62(2)	0.077(22)	33(8)	5(1)
x=4	FMR 1	336.00(10)	0.386(20)	1.38(5)	1075(20)	650(50)	7.0(6)	1.79(2)	0.235(16)	11.3(10)	15(1)
	FMR 2	335.85(10)	0.380(20)	1.39(6)	1075(20)	650(50)	7.0(6)	1.79(2)	0.235(16)	11.3(10)	15(1)
	BM*	328.00(10)	0.350(15)	1.39(3)	900(30)	350(48)	3.2(5)	1.79(2)	0.116(22)	25(4)	7(1)
x=6	FMR 1	377.04(10)	0.375(25)	1.38(5)	1160(30)	950(50)	11.0(9)	1.81(2)	0.333(25)	8.0(6)	22(2)
	FMR 2	377.10(10)	0.385(25)	1.39(6)	1165(30)	950(50)	11.0(8)	1.81(2)	0.333(25)	8.0(6)	21(2)
	BM*	374.80(10)	0.355(10)	1.39(2)	950(30)	500(50)	4.8(6)	1.81(2)	0.154(22)	19(3)	10(1)
x=8	FMR 1	419.50(10)	0.384(20)	1.38(6)	1215(35)	1200(50)	14.6(7)	1.84(2)	0.397(18)	6.8(5)	25(2)
	FMR 2	419.55(10)	0.382(20)	1.38(6)	1215(35)	1200(50)	14.6(7)	1.84(2)	0.397(18)	6.8(5)	25(2)

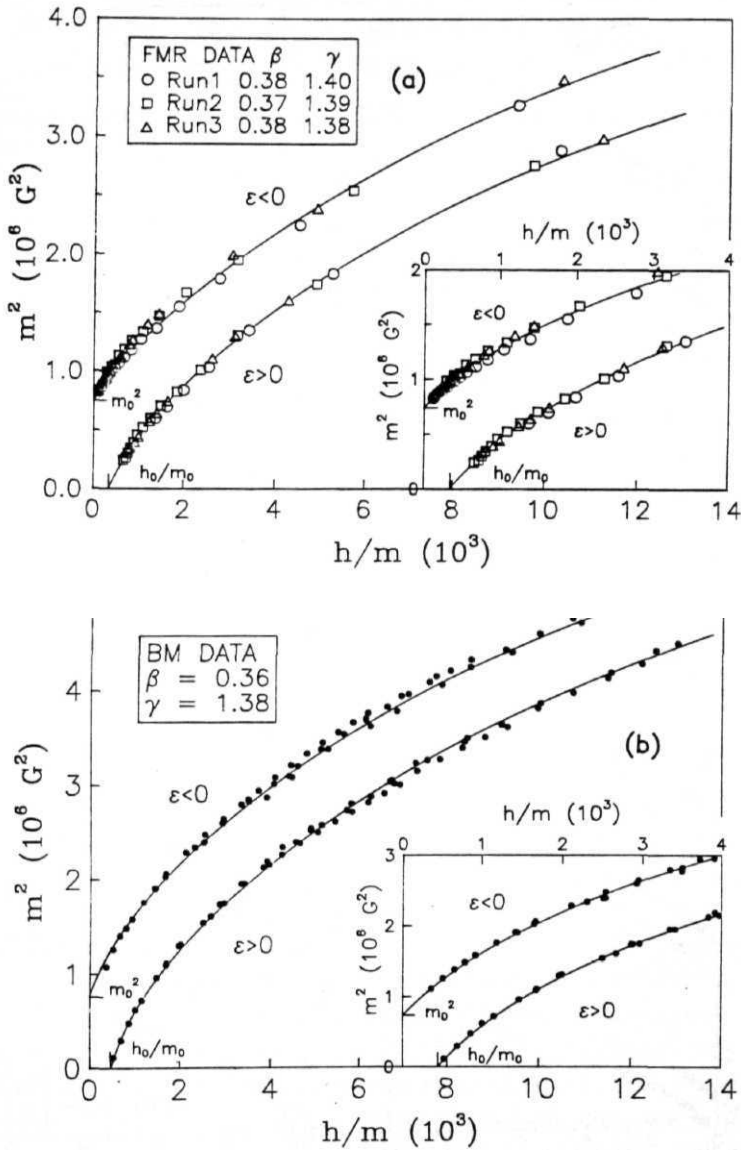
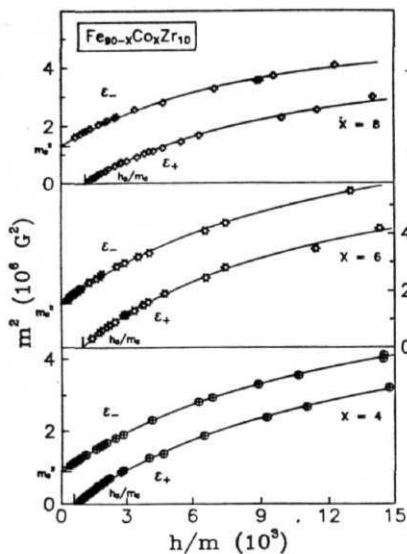
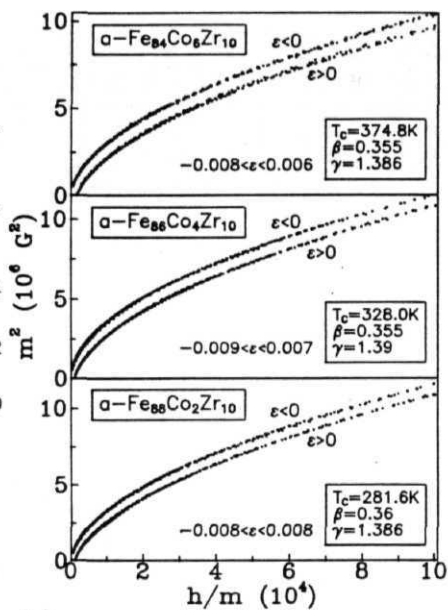
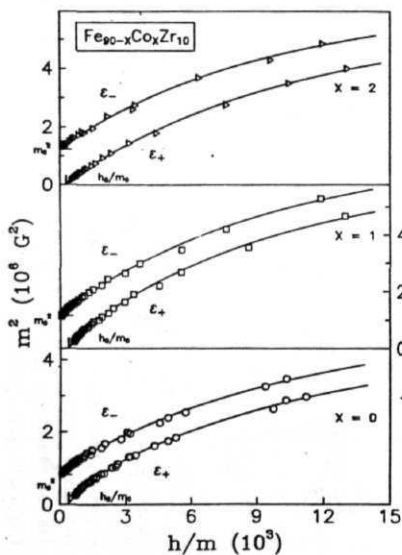


Fig. 4.5 m^2 vs. h/m scaling plots constructed from the (a) FMR and (b) BM data taken on the sample B1 of $a - \text{Fe}_{90}\text{Zr}_{10}$.



(a)



(b)

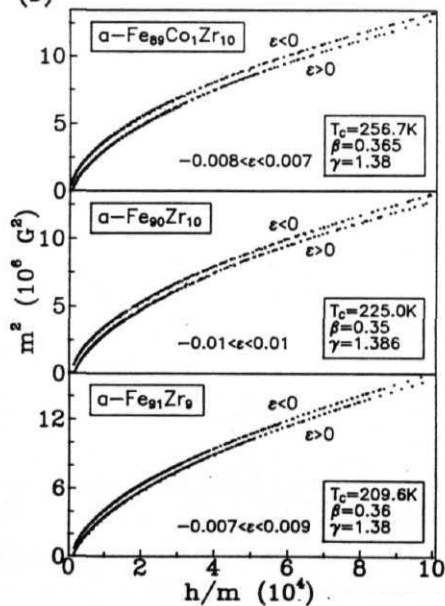


Fig. 4.6 m^2 vs. h/m plots constructed from the (a) FMR data taken on a — $Fe_{90-x}Co_xZr_{10}$ alloys and (b) BM data taken on a — $Fe_{90+y}Zr_{10-y}$ and a — $Fe_{90-x}Co_xZr_{10}$ alloys.

scale. The critical exponent and amplitude values obtained in this way are listed in Table 4.2. It is noted from the values displayed in this table that both FMR and BM data yield similar results in the critical region and that FMR is a powerful tool to study the critical behaviour.

The FMR and BM data for the remaining compositions have also been analyzed by using both the SES forms and the results of the **SES-II** analysis are listed in Table 4.2. Since the **SES-I** and **SES-II** analyses yield identical values for critical exponents, the exponent values obtained by the **SES-I** method are not listed separately in this table. Fig. 4.6(a) and 4.6(b) depict the m^2 vs. h/m plots, constructed out of the FMR and BM data, respectively, for all the alloys in question. The values of T_C for different Co concentrations extracted from the FMR data do not match those yielded by the BM data (Table 4.2) partly because the alloy ribbons used in the FMR and BM measurements could differ slightly in composition as they belong to different batches and partly due to the extreme sensitivity of the Curie temperature of a given amorphous alloy to the preparation conditions. Like T_C , the critical amplitudes obtained from the FMR and BM data are also different, but this disparity is mainly due to the fact that these *effective* amplitude values are obtained from data taken in different temperature ranges, i.e., $|\epsilon| < 0.05$ and $|g| < 0.01$ in case of FMR and BM data, respectively. But for these minor differences in the absolute values of certain quantities, the present work clearly demonstrates that both FMR and BM data yield similar results (when analyzed in the same way) as far as the critical behaviour in these alloys is concerned. Before undertaking further analysis of BM data by a different method, it is imperative to examine the behaviour of FMR linewidths in the critical region.

4.1.5. FMR linewidth

The temperature dependence of 'peak-to-peak' FMR linewidth, $\Delta H_{pp}(T)$, in the critical region for horizontal-parallel (\parallel^h) sample geometry is displayed in Fig. 4.7(a). Since the values of $\Delta H_{pp}(T)$ in the critical region are the same (within error limits) for both \parallel^h and \parallel^v sample configurations, Fig. 4.7(a) reproduces all the features of the $\Delta H_{pp}(T)$ data in \parallel^v configuration even to the minutest detail. The slope change (not pronounced) in the $\Delta H_{pp}(T)$ data (Fig. 4.7(a)) noticed at $T \sim T_C$ is an indication of a well-defined phase transition at T_C . Frequency-dependent FMR studies on a large number of amorphous ferromagnets [15-17] have revealed that ΔH_{pp} consists of a *frequency-independent* part, ΔH_I , and a *frequency-dependent* Landau-Lifshitz-Gilbert (LLG) part, ΔH_{LLG} . While ΔH_I probably originates from the **two- or multi-magnon** scattering from spatially localized magnetic inhomogeneities [18,19], $\Delta H_{LLG} = 1.45 (\lambda \omega / \gamma_s^2 M_s)$ (where $\omega = 2\pi\nu$) has a linear dependence on microwave frequency ν and results from the LLG relaxation mechanism [20]. In the above definition of ΔH_{LLG} the quantities A , γ_g and M_s , respectively, are the Gilbert damping parameter, gyromagnetic ratio and saturation magnetization (cf. section 2.4., Chapter 2). We find that in the critical region

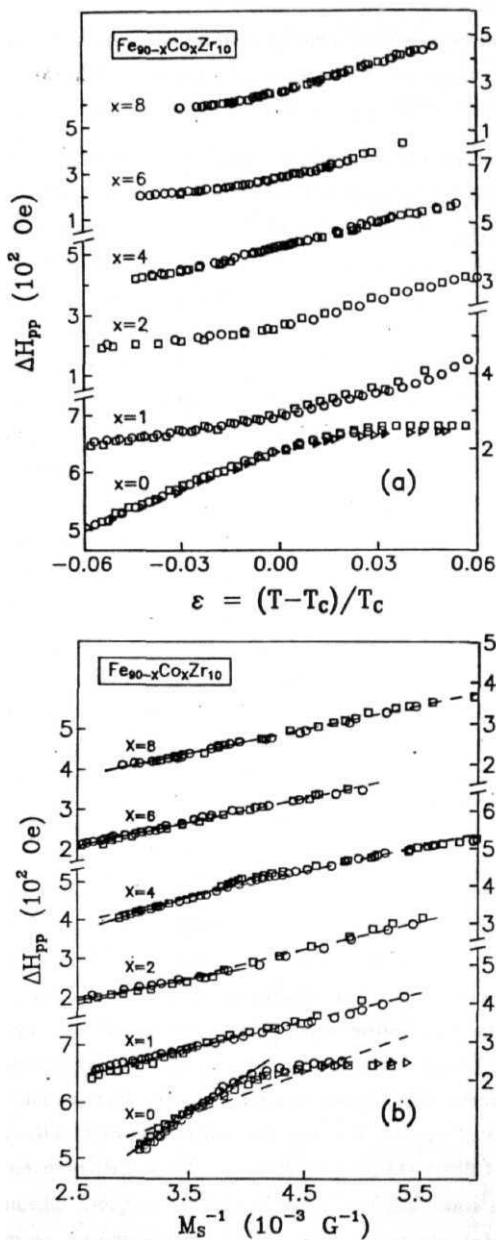


Fig. 4.7 (a) Variation of ΔH_{pp} with the (a) reduced temperature, ϵ and (b) inverse saturation magnetization, M_s^{-1} for different Co concentrations. While the dashed curves in (b) represent the LS fits in the range $-0.05 < \epsilon < 0.05$, the solid lines denote fits in the range $-0.05 < \epsilon < 0$.

($-0.05 \sim \epsilon \sim 0.05$), $\Delta H_{pp}(T)$ for all the alloys in question except for those with $x = 0$ and 4 can be very well described (dashed lines) by the empirical relation

$$\Delta H_{pp}(T) = \Delta H(0) + [A/M_S(T)] \quad . \quad (4.6)$$

That a linear relation between ΔH_{pp} and M_S^{-1} of the type given by Eq.(4.6) holds is clearly brought out when $\Delta H_{pp}(T)$ is plotted against $M_S^{-1}(T)$ (Fig. 4.7(b)). For the alloys with $x = 0$ and 4, best fit to the $\Delta H_{pp}(T)$ data is obtained only for temperatures below T_C in the range $-0.05 \sim \epsilon \sim 0$. The terms $\Delta H(0)$ and $[A/M_S(T)]$ in Eq.(4.6) can be identified with ΔH_I and ΔH_{LLG} respectively, and hence the coefficient $A = 1.45 \lambda \omega / \gamma_g^2$, determined by the least-squares (LS) fits (Fig. 4.7(b)) based on Eq.(4.6) for different compositions, permits a calculation of the damping parameter A . The values of A so obtained lie in the range $2 \times 10^8 - 3 \times 10^8 \text{ sec}^{-1}$ and exhibit a weak decreasing trend with Co concentration (x). By contrast, the values of $\Delta H(0)$ do not show any systematic trend with x ; $\Delta H(0)$ has a minimum value of $\Delta H(0) \sim 20 \text{ Oe}$ for $x = 2$ and a maximum value of $\Delta H(0) \sim 140 \text{ Oe}$ for $x = 4$. Moreover, the quality of LS fits based on Eq.(4.6) improves considerably when such fits are attempted only for temperatures below T_C in the range $-0.05 \sim \epsilon \sim 0$ but the parameters $\Delta H(0)$ and A (hence λ) undergo only slight changes when the fit range is increased to $-0.05 \sim \epsilon \sim 0.05$. However, for the alloys with $x = 0$ and 4, drastic changes in the parameter values occur when the temperature range $-0.05 \sim \epsilon \sim 0.05$ is narrowed down to $-0.05 \sim \epsilon \sim 0$, e.g., $\Delta H(0)$ decreases by a factor of 1.5 while A (and hence λ) increases by the same factor. The appearance of secondary resonance (cf. Chapter 2) at $T \sim T_C$ for $x = 0$ and 4 alloys and at a temperature well above T_C for the remaining alloys could be the reason for the distinctly different behaviour of $\Delta H_{pp}(T)$ for the alloys with $x = 0$ and 4. That the parameter A is temperature independent in the critical region for the alloys in question is also observed in many crystalline ferromagnets [21-23].

4.1.6. Analysis with 'correction-to-scaling' (CTS) terms

So far the $M(T,0)$ and $X_o(T)$ data have been analyzed in terms of single power laws which are strictly valid in the asymptotic limit of $T \rightarrow T_C$. However, in practice, T_C cannot be approached so closely as to warrant use of single power laws and frequently **single-power-law** fits are attempted on data taken at temperatures not very close to T_C . Such fits, therefore, invariably yield *effective* critical exponents and amplitudes which depend on the fit range chosen. In view of the fact that all the methods of analysis considered so far are based on single power laws and yet, with the exception of the MAP method, they have been used to analyze data taken at temperatures not too close T_C , the values of exponents and amplitudes so determined are nothing but the *effective* values. In order to determine the true *asymptotic* values of the critical exponents and amplitudes, the expressions for spontaneous magnetization and initial susceptibility (and of

course, for other 'zero-field' **thermodynamic** quantities) valid in the asymptotic critical region should include the '**correction-to-scaling**' (CTS) **terms** arising from nonlinear irrelevant scaling fields, as predicted by the **renormalization group** (**RG**) theories [24-31]. The expressions that are valid for amorphous ferromagnets and retain only the leading CTS terms have the form [25-29] (cf. **Eqs.(1.33b)** and (1.33c); Chapter 1)

$$M(T, 0) = m_o |\epsilon|^\beta \left[1 + a_{M1} |\epsilon|^{\Delta_1} + a_{M2} |\epsilon|^{\Delta_2} \right] \quad \epsilon < 0 \quad (4.7a)$$

and

$$\chi_o(T) = \Gamma |\epsilon|^{-\gamma} \left[1 + a_{\chi1} |\epsilon|^{\Delta_1} + a_{\chi2} |\epsilon|^{\Delta_2} \right] \quad \epsilon > 0 \quad (4.76)$$

where Δ_1, Δ_2 and $(a_{M1}, a_{M2}), (a_{\chi1}, a_{\chi2})$ are the leading CTS critical exponents and amplitudes, respectively and $T - (h_o/m_o)$ while the remaining quantities have the same meaning as stated earlier. By virtue of the fact that $\Delta_1 \ll \Delta_2$ [25-27,29,31], the CTS term involving **exponent** Δ_1 in Eq.(4.7) is significant only for temperatures close to T_c whereas the second CTS term dominates for temperatures in the asymptotic critical region but away from T_C . In order to accurately determine these correction terms, the following procedure has been adopted. At first, the amplitudes a_{M2} and $a_{\chi2}$ are set equal to zero and a detailed 'range-of-fit' analysis of the $M(T, 0) [\chi_o(T)]$ data, based on the modified version of Eq.(4.7a) [**Eq.(4.7b)**] is carried out with the help of a nonlinear least-squares (LS)-fit computer program which treats $m_o, \beta, T_C^-,$ and $a_{M1} [\Gamma, \gamma, T_C^+,$ and $a_{\chi1}]$ as free fitting parameters and keeps the CTS exponent Δ_1 fixed at the theoretically predicted [31-33] value of $\Delta_1 = 0.11$. In the 'range-of-fit' analysis, the lower bound $|\epsilon_{\min}|$ of the temperature range $|\epsilon_{\min}| < |\epsilon| < |\epsilon_{\max}|$ is fixed at $|\epsilon_{\min}| \approx 0$ while the upper bound $|\epsilon_{\max}|$ is increased so as to include more and more data points for temperatures away from T_C . Such an exercise reveals that over a certain temperature range close to T_C , the values of all the parameters including the coefficient a_{M1} or $a_{\chi1}$ are essentially unaffected by the variation in $|\epsilon_{\max}|$. Next, the coefficient of first CTS term $a_{M1} [a_{\chi1}]$ is fixed at this value and the 'range-of-fit' analysis of $M(T, 0) [\chi_o(T)]$ data is carried out by using **Eq.(4.7a)** [**Eq.(4.7b)**] with both the correction terms included and treating m_o, T_C^-, β and $a_{M2} [\Gamma, T_C^+, \gamma$ and $a_{\chi2}]$ as free fitting parameters while keeping Δ_1 and Δ_2 fixed at $\Delta_1 = 0.11$ and $\Delta_2 = 0.55$ [32-36]. The quality of LS fits obtained in this way (henceforth referred to as the CTS analysis) is much superior to that of the single-power-law fits in the same temperature range, as inferred from the lower sum of deviation squares, χ_r^2 , and from the deviation plots. Fig. 4.8 shows the deviation plots for a - $Fe_{91}Zr_9$ and a - $Fe_{90}Zr_{10}$ alloys in which the percentage deviation of the $M(T, 0)$ or $\chi_o^{-1}(T)$ data from the corresponding theoretical values deduced from the best LS fit, i.e., $100 \times [M(exp) - M(fit)]/M(exp)$ or $100 \times [\chi_o^{-1}(exp) - \chi_o^{-1}(fit)]/\chi_o^{-1}(exp)$, plotted against ϵ . This figure clearly demonstrates the superiority of the CTS fits over the KF (or SPL) fits in the asymptotic critical region in that the former type of fits closely reproduce the observed variation of $M(T, 0)$ and $\chi_o(T)$ with T over a wider temperature range (especially so for temperatures in the immediate vicinity of T_c) whereas the latter type fits present *systematic*

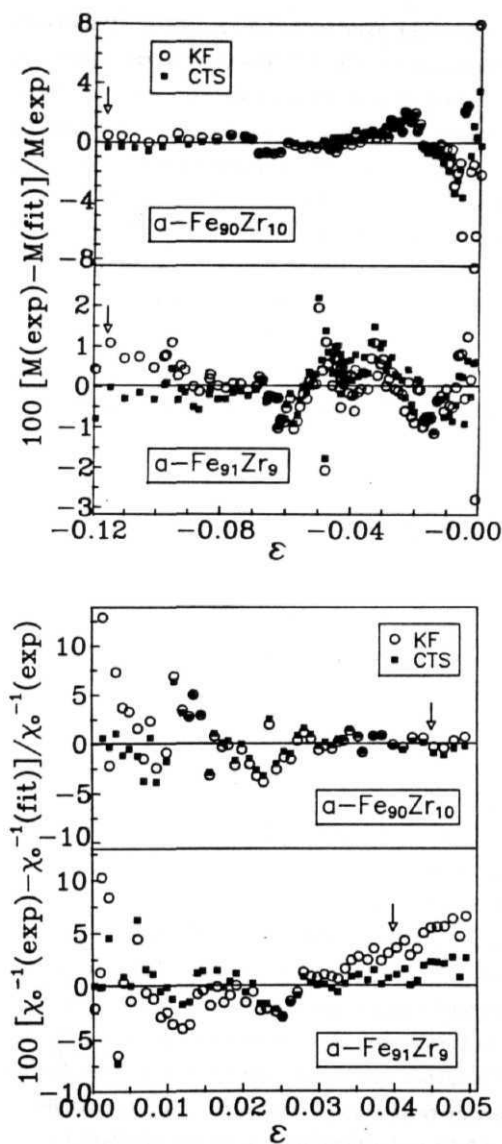


Fig. 4.8 Percentage deviation of the $M(T,0)$ and $\chi_o^{-1}(T)$ data from the theoretical values corresponding to the LS fits obtained from the Kouvel-Fisher (KF) and 'correction-to-scaling' (CTS) data analysis for $T < T_C$ and $T > T_C$, respectively.

deviations. The deviation plots for $\chi_o^{-1}(T)$ as well as $M(T, 0)$ data for all the remaining alloys are similar to those shown in Fig. 4.8. The CTS analysis, apart from yielding accurate values for the asymptotic critical exponents and amplitudes, reveals that the exponents and amplitudes are temperature-independent (within the error limits) over a wide temperature range which spans the asymptotic critical region (ACR). The maximum value of $|\epsilon_{\max}|$ upto which the CTS fits yield stable values for all the parameters marks the crossover temperature ϵ_{co}^- ($\epsilon < 0$) and ϵ_{co}^+ ($\epsilon > 0$) for $M(T, 0)$ and $\chi_o(T)$, respectively, while $\epsilon_{co}^- < \epsilon < \epsilon_{co}^+$ gives the extent of the ACR. The theoretical fits, based on Eqs.(4.7a) and (4.76), in the ACR with the values of parameters given in Table 4.3, are shown as continuous curves in Figs. 4.2(a) and 4.2(b). In these figures, the crossover temperatures ϵ_{co}^\pm are indicated by upward arrows. It is noticed from Table 4.3 that the values of T_C^- and T_C^+ are in good agreement with one another within the uncertainty limits and the asymptotic critical exponents are *composition-independent*. These results are discussed in section 4.2.

4.1.7. Critical isotherm

The critical exponent δ characterizing the $M(T, H)$ versus H isotherm at $T = T_c$ (the critical isotherm) is obtained by analyzing the M vs. H isotherms in the immediate vicinity of T_C using the relation [1,3-5]

$$M = A_o H^{1/\delta} \text{ or } H = D M^\delta \quad \text{at } \epsilon = 0 \quad (4.8)$$

where $D = A_o^{-\delta}$. It is evident from Eq.(4.8) that the plot of $\ln M$ vs. $\ln H$ at $T = T_C$ should be a straight line with slope δ^{-1} and intercept on the ordinate equal to $\ln A_o$. Such $\ln M$ vs. $\ln H$ plots, constructed using the M vs. H isotherms in the immediate vicinity of T_C for the presently investigated alloys (Fig. 4.9), clearly demonstrate that the isotherm at T_C is indeed a straight line and the isotherms on either side of T_C exhibit a concave-upward curvature and concave-downward curvature for $T < T_C$ and $T > T_C$, respectively. The curvature becomes more pronounced as the temperature increasingly deviates from T_C . Fig. 4.9 (in which isotherms at a few selected temperatures only are used for the sake of clarity) brings out these features clearly, which are characteristic of many amorphous as well as crystalline ferromagnets [35-39]. The solid line in Fig. 4.9 for each composition is the straight line fit to the critical isotherm at T_C . The exponent δ and amplitude A_o or D are computed from the slope and intercept of this straight line on the ordinate. The values of T_C, δ and D so obtained are listed in Table 4.4. The values of T_C for all the alloy compositions determined by this method are in excellent agreement with those extracted using methods described earlier.

Table 4.3(a). Results of the CTS analysis of the $M(T,0)$ data.

Alloy conc.	fit range ($10^3 \mid \epsilon \mid$)	T_C^- (K)	β	m_o (G)		
y=1	1.0-115	209.68(3)	0.366(4)	795(15)	-0.03(1)	0.52(8)
x=y=0	1.0-115	225.02(4)	0.360(5)	830(25)	-0.05(1)	0.85(15)
x=1	1.0-120	256.69(5)	0.368(6)	840(25)	-0.04(2)	0.80(10)
x=2	0.9-137	281.57(5)	0.363(5)	870(25)	-0.02(1)	0.25(10)
x=4	1.0-137	327.90(6)	0.365(6)	1000(20)	-0.06(2)	0.90(10)
x=6	0.8-151	374.75(5)	0.370(5)	950(25)	-0.05(2)	0.70(8)

Table 4.3(b). Results of the CTS analysis of the $Xo(T)$ data.

Alloy conc.	fit range ($10^3 \mid \epsilon \mid$)	T_C^+ (K)	7	m_o/h_o (10^{-3})	a_{x1}	a_{x2}
y=1	1.0-41	209.63(3)	1.383(4)	5.7(3)	-0.03(1)	-0.5(1)
x=y=0	1.0-45	224.97(4)	1.390(5)	4.3(2)	-0.05(1)	-0.8(1)
x=1	1.0-45	256.66(5)	1.385(5)	3.2(2)	-0.05(2)	-1.0(2)
x=2	0.9-41	281.61(5)	1.389(6)	2.2(1)	-0.05(2)	-1.0(3)
x=4	1.0-62	327.98(6)	1.383(7)	1.9(1)	-0.05(2)	-1.1(3)
x=6	0.8-46	374.72(5)	1.386(6)	1.6(1)	-0.05(2)	-1.0(2)

Table 4.4. Parameter values for the critical isotherm.

Alloy conc.	T_c (K)	δ	D ($10^{-9} \text{ Oe}^{1-\delta}$)
y=1	209.6(1)	4.75(5)	3.04(10)
x=y=0	225.0(1)	4.83(4)	2.00(6)
x=1	256.7(1)	4.80(4)	3.20(10)
x=2	281.6(1)	4.81(5)	3.76(10)
x=4	328.0(1)	4.85(5)	1.98(7)
x=6	374.8(1)	4.84(5)	3.08(12)

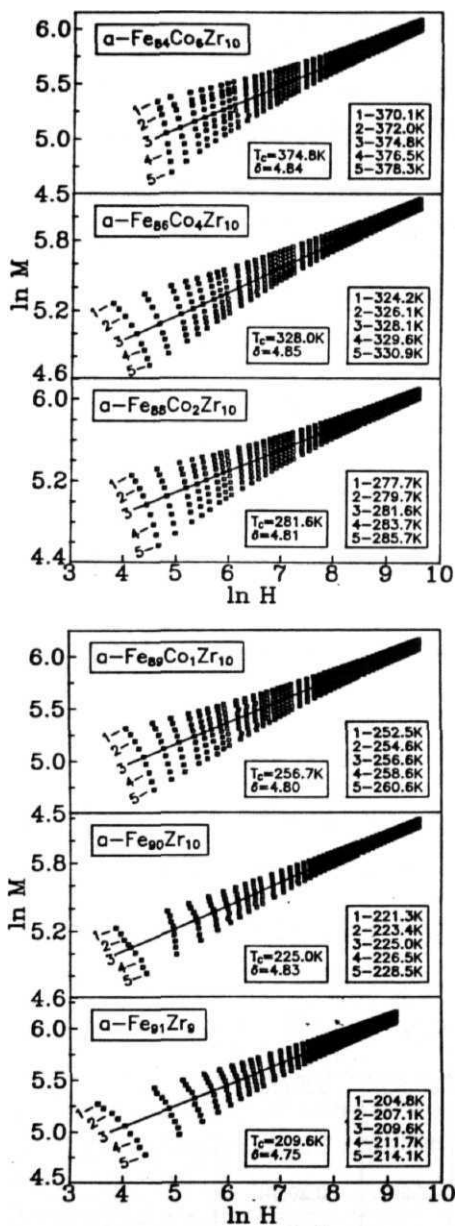


Fig. 4.9 $\ln M$ vs. $\ln H$ isotherms at a few selected temperatures around T_C for $a\text{-Fe}_{x}\text{Co}_{y}\text{Zr}_{10-y}$ and $a\text{-Fe}_{90-x}\text{Co}_x\text{Zr}_{10}$ alloys.

4.1.8. Analysis using nonlinear variables

All the methods of analysis employed till now are based on the expressions that involve the linear variables ϵ and H only. Such expressions, e.g., Eqs.(4.7a) and (4.76), provide the best theoretical fits to the spontaneous magnetization and initial susceptibility data in the ACR only. However, the quality of these fits deteriorates considerably for temperatures outside the ACR. Such a behaviour has been previously observed [1,3,4,6,10,33-39] in many crystalline and amorphous **ferromagnets**. However, nearly a decade ago, Souletie and Tholence [40] have found that $\chi_o(T)$ data of crystalline *Ni* are described by a power law of the form $\chi_o(T) = A_x T^{-1} \tilde{\epsilon}^{-\gamma} + B_x$, in the nonlinear variable $\tilde{\epsilon} = (T - T_c)/T$ (generally referred to as the modified Curie-Weiss law) over an incredibly large temperature range of T_c to $3T_c$. A theoretical treatment (the so-called nonlinear scaling theory) [41] that, besides making use of the renormalization group ideas and nonlinear variables $\tilde{\epsilon} = t - 1$ and $h = H/t$ (with $t = T/T_c$), takes into account both nonlinear irrelevant as well as nonlinear relevant scaling fields has provided a firm basis for this power law. Now that the recent investigations [35,41,42] of the critical behaviour of certain ferromagnetic systems over a very wide temperature range vindicate the nonlinear scaling approach [41], a detailed analysis of $M(T, 0)$ and $\chi_o(T)$ data has been carried out based on the expressions, predicted by this theory, that either include the leading **nonanalytic corrections**, arising from **nonlinear irrelevant** scaling fields, i.e.,

$$M(T, 0) = m_o \mid \tilde{\epsilon} \mid^{\beta} \left[1 + \bar{a}_{M1} \mid \tilde{\epsilon} \mid^{\Delta_1} + \bar{a}_{M2} \mid \tilde{\epsilon} \mid^{\Delta_2} \right] \quad \tilde{\epsilon} < 0, \quad (4.9a)$$

$$\chi_o(T) = \Gamma t^{-1} \mid \tilde{\epsilon} \mid^{-\gamma} \left[1 + \bar{a}_{\chi 1} \mid \tilde{\epsilon} \mid^{\Delta_1} + \bar{a}_{\chi 2} \mid \tilde{\epsilon} \mid^{\Delta_2} \right] \quad \tilde{\epsilon} > 0 \quad (4.9b)$$

or **analytic corrections**, originating from **nonlinear relevant** scaling fields, i.e.,

$$M(T, 0) = B_M \mid \tilde{\epsilon} \mid^{\beta} [1 + \bar{a}_M \tilde{\epsilon}] \quad \tilde{\epsilon} < 0, \quad (4.10a)$$

$$\chi_o(T) = A_x t^{-1} \mid \tilde{\epsilon} \mid^{-\gamma} [1 + \bar{a}_x \tilde{\epsilon}] \quad \tilde{\epsilon} > 0. \quad (4.10b)$$

The $M(T, 0)$ and $\chi_o(T)$ data have been extracted in the same way as described in section 4.1.1 from the MAP isotherms constructed in a temperature range as wide as $0.37c \sim T \sim 1.57c$ using the values of exponents β and γ obtained in the critical region (Fig. 4.1(a)-(f)). One such modified Arrott plot (MAP) for a - **Fe₉₁Zr₉**, constructed out of a few selected M vs. H isotherms taken in the range 68 K to 300 K, is shown in Fig. 4.10(a) and 4.10(b) for $T < T_c$ and $T > T_c$, respectively. This figure captures all the essential features of the modified Arrott plots for the remaining compositions. Detailed analysis of the $M(T, 0)$ and $\chi_o(T)$ data (Figs. 4.11 and 4.12) based on Eqs.(4.9) and (4.10) reveals that in the ACR, the Eqs.(4.9a) and (4.9b), reproduce the $M(T, 0)$ and $\chi_o(T)$ data to far greater an accuracy than the expressions given by Eqs.(4.10a) and (4.10b). Note that in the theoretical fits based on Eq.(4.9), the CTS exponents **are** kept fixed at their theoretical values $\Delta_1 = 0.11$ and $\Delta_2 = 0.55$ as was the case with the

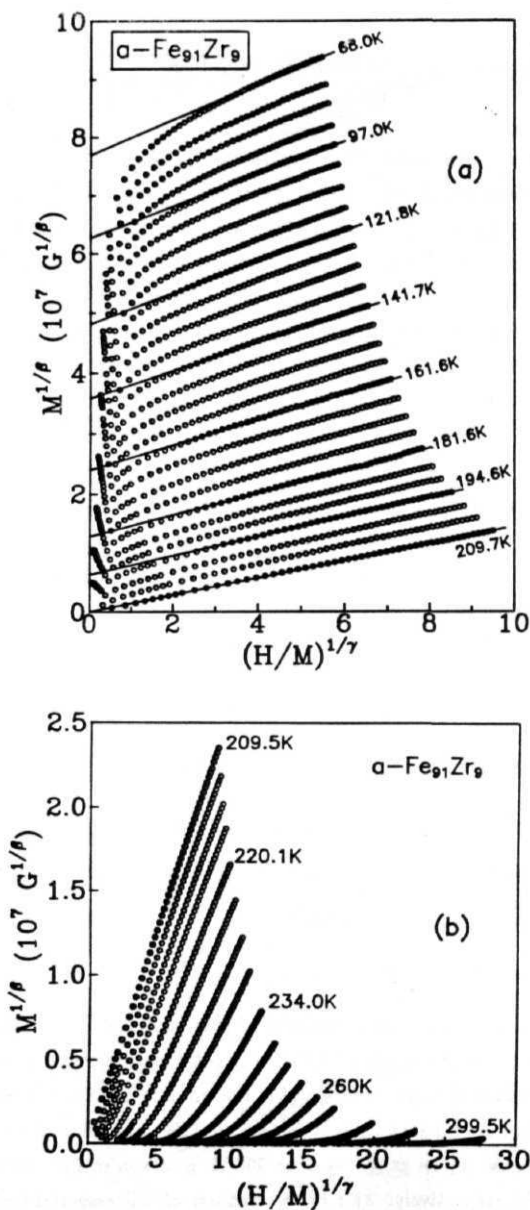


Fig. 4.1 Modified Arrott plot for $a\text{-Fe}_{91}\text{Zr}_9$ over a wide temperature range for (a) $T < T_r$ and (b) $T > T_r$.

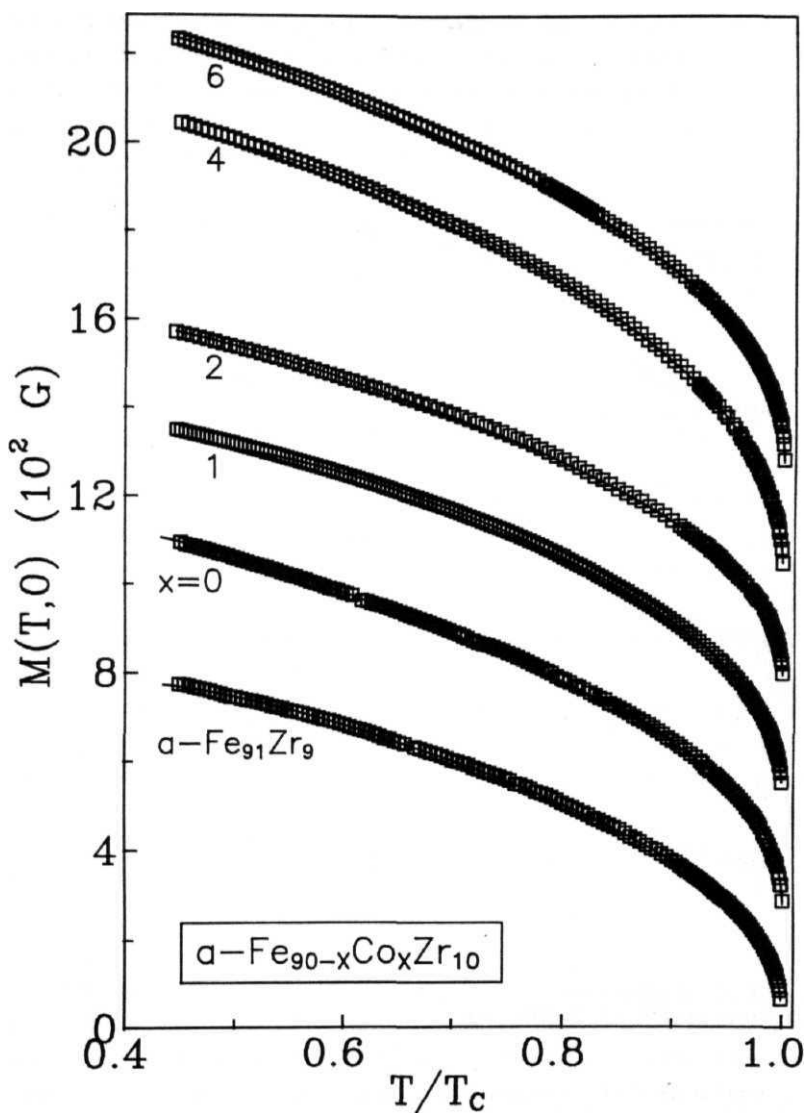


Fig. 4.11 Variation of $M(T, 0)$ with reduced temperature, T/T_c over a wide temperature range for $T < T_c$. Note that the zero on the ordinate scale for $x = 0, 1, 2, 4$ and 6 should read as $2.5, 5.0, 7.5, 10.0$ and 12.5 , respectively, and the solid curves represent the LS fits based on Eq.(4.10a).

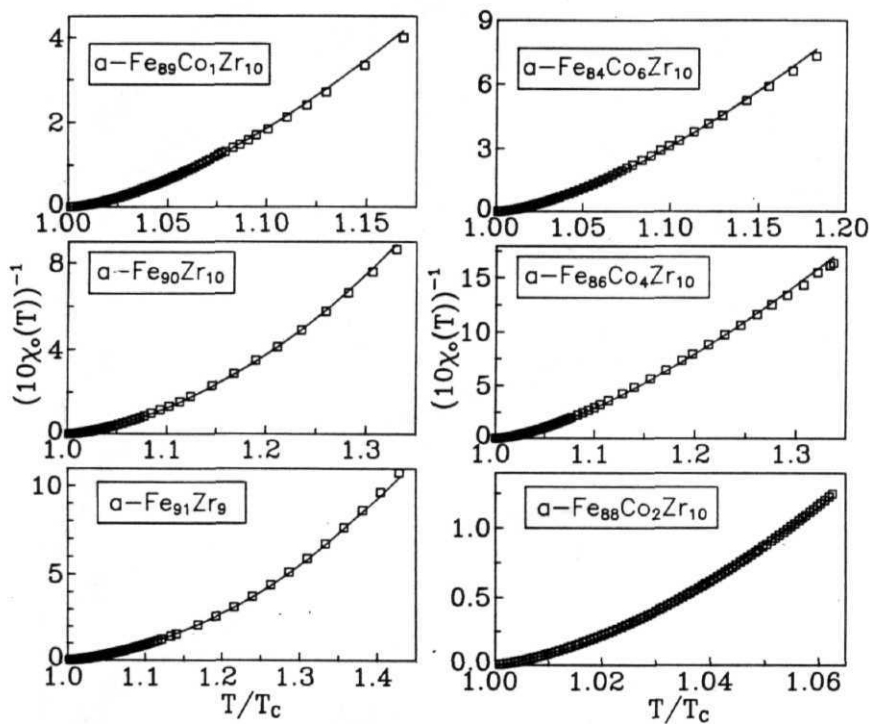


Fig. 4.12 χ_0^{-1} as a function of temperature over a wide temperature range for $T > T_c$. The continuous curves through the data points denote the LS fits based on Eq.(4.106).

CTS analysis involving linear variables ϵ and H earlier. In the ACR, the CTS analysis, based on the expression that includes the non-analytic correction terms alone, yields the same results regardless of whether these correction terms are expressed in linear variables, Eq.(4.7), or in nonlinear variables, Eq.(4.9). On the other hand, Eqs.(4.10a) and (4.10b), which include a single leading analytic correction term, provide very good overall fits in temperature ranges as wide as $0.45 T_b \sim T \sim T_C$ for $M(T,0)$ and $T_C \sim T \sim 1.37 T_b$ for $\chi_o(T)$ for all the alloys in question with the values of fit parameters and fit ranges given in Table 4.5. These fits are represented by continuous curves in Figs. 4.11 and 4.12. In view of the claim [40] that for crystalline Ni the empirical relation

$$\chi_o(T) = A_\chi t^{-1} |\bar{\epsilon}|^{-\gamma} + B_\chi \quad \bar{\epsilon} > 0 \quad (4.10c)$$

with the background correction term B_χ describes very well the observed variation of χ_o with T from T_C to 37b, Eq.(4.10c) has been used to analyze the $\chi_o(T)$ data over the entire temperature range. This exercise shows that even though Eq.(4.10c) with $B_\chi \neq 0$ provides a slightly better fit than when $B_\chi = 0$ in Eq.(4.10c), it does not reproduce the observed temperature variation of χ_o as closely as Eq.(4.10b) does. The deviation plot shown in Fig. 4.13 for $a\text{-Fe}_{90+y}\text{Zr}_{10-y}$ ($y = 0, 1$) alloys testifies to the correctness of this inference in that the percentage deviation for the fits based on Eq.(4.10b) is considerably smaller than that for the fits based on Eq.(4.10c) in the entire temperature range (even for temperatures close to T_C). However, none of these expressions (i.e., Eqs.(4.10b) and (4.10c)) correctly describes the actual functional form of $\chi_o(T)$ in the ACR, as inferred from large systematic deviations of the theoretical values from the observed ones in the ACR (Fig. 4.13). By comparison, the expression that includes the nonanalytic correction terms either in linear variables, Eq.(4.76), or in nonlinear variables, Eq.(4.9b), provides a much better description of $\chi_o(T)$ in the ACR (Fig. 4.8).

Slopes and intercepts of MAP isotherms :

A cursory glance at the modified Arrott plots depicted in Figs. 4.1(a)-(f) and 4.10 suffices to reveal that the slope of modified-Arrott-plot (MAP) isotherms decreases continuously with increasing temperature. This feature of MAP is characteristic [1,3,4,10,12-14,35-38,41,42] of both crystalline and amorphous ferromagnets. The Arrott-Noakes equation of state in linear variables ϵ and H (i.e., Eq.(4.1a)) cannot account for this variation in the slope of MAP isotherms since the coefficients a' and $6'$ in Eq.(4.1a) are temperature-independent. By contrast, the magnetic equation-of-state in nonlinear variables ϵ and h of the form

$$M^{1/\beta} = a(-\bar{\epsilon}) + b t^{-1/\gamma} (H/M)^{1/\gamma}, \quad (4.11)$$

with

Table 4.5(a). Parameter values for the LS fits, based on Eq.(4.10a) of the text, to the $M(T, 0)$ data over a wide temperature range.

Alloy conc.	fit range (T/T_C)	(K)		B_M (G)	
y=1	0.45-1.0	209.68(8)	0.380(10)	885(30)	-0.15(3)
x=y=0	0.45-1.0	225.10(10)	0.390(15)	970(30)	-0.20(3)
x=1	0.50-1.0	256.72(8)	0.395(10)	1000(30)	-0.22(3)
x=2	0.45-1.0	281.59(10)	0.380(10)	1030(30)	-0.14(3)
x=4	0.50-1.0	327.95(10)	0.395(15)	1230(30)	-0.20(4)
x=6	0.45-1.0	374.70(10)	0.385(10)	1100(30)	-0.13(3)

Table 4.5(b). Parameter values for the LS fits, based on Eq.(4.106) of the text, to $\chi_o^{-1}(T)$ data over a wide temperature range .

Alloy conc.	fit range (T/T_C)	(K)	γ	A_x (10^{-3})	a_x	\mathfrak{C} (μ_B)	q_s (MB)	$9c/9s$
y=1	1.0-1.43	209.60(8)	1.39(2)	4.5(3)	-2.0(4)	6.67(24)	1.34(2)	4.98(25)
x=y=0	1.0-1.33	224.96(8)	1.39(2)	3.7(2)	-1.8(3)	6.25(22)	1.44(2)	4.34(20)
x=1	1.0-1.17	256.67(10)	1.40(2)	2.9(2)	-2.5(4)	5.85(25)	1.52(2)	3.85(20)
x=2	1.0-1.07	281.61(10)	1.39(2)	2.1(2)	-3.6(4)	5.13(30)	1.62(2)	3.17(20)
x=4	1.0-1.35	327.98(10)	1.41(3)	1.5(2)	-1.5(4)	4.61(30)	1.79(2)	2.58(20)
x=6	0.8-1.20	374.70(10)	1.42(3)	1.0(2)	-1.0(3)	3.92(30)	1.81(2)	2.17(20)

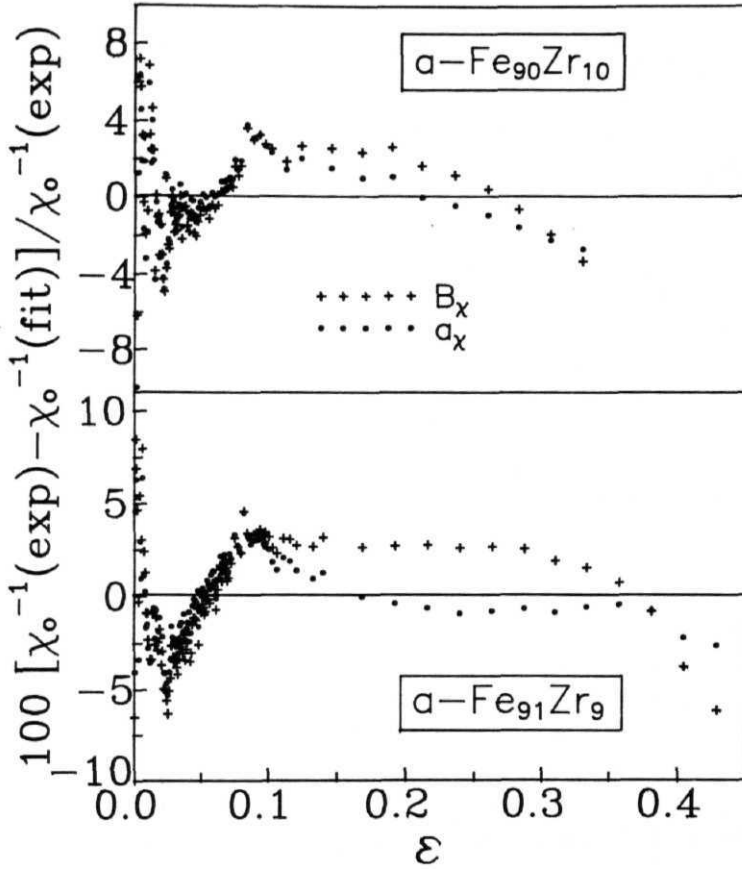


Fig. 4.13 Percentage deviation of the $\chi_o^{-1}(T)$ data from the theoretical values corresponding to the LS fits based on Eqs.(4.106) (circles) and (4.10c) (+).

$$a \sim \tilde{A}_M [1 + \tilde{a}_M] \in |\Delta_1 + a_{M2}| \in |\Delta_2| \quad (4.12a)$$

and

$$6 \sim \tilde{A} [1 + \tilde{a}_1 | \tilde{\epsilon}^{|\Delta_1|} + \tilde{a}_2 | \tilde{\epsilon}^{|\Delta_2|}] \quad (4.126)$$

or

$$a = [B'_M (1 + a_M \tilde{\epsilon})]^{1/\beta} \sim A_M [1 + a_M \tilde{\epsilon}] \quad (4.13a)$$

and

$$6 = [B_M (1 + \tilde{a}_M \tilde{\epsilon})]^{1/\beta} [A_x (1 + a_x \tilde{\epsilon})]^{1/\gamma} \sim A [1 + a \tilde{\epsilon}] \quad (4.136)$$

yielded by the nonlinear (NL) scaling theory [41], predicts the temperature dependence of the MAP intercept [= $a(-\tilde{\epsilon})$] and slope [= $bt^{-1/\gamma}$] of the type given by Eq.(4.12a) or Eq.(4.13a) and Eq.(4.12b) or Eq.(4.136), respectively. Note that Eq.(4.12) [Eq.(4.13)] contains nonanalytic [analytic] correction terms alone but the NL theory predicts the expressions that combine both the types of corrections. However, to facilitate comparison with experiment, it is convenient to separate correction terms that become important in different temperature ranges. Encouraged by the accurate predictions that the nonlinear scaling theory makes about the temperature dependence of $M(T, 0)$ and $\chi_o(T)$ over a wide temperature range, which embraces the critical region, a detailed analysis of the observed temperature variation of the MAP intercept and slope in terms of Eqs.(4.11)-(4.13) was undertaken. The main outcome of this exercise is that the observed temperature variation of slope and intercept (on the MAP ordinate) is closely reproduced by the relations, slope(T) = $bt^{-1/\gamma}$ and intercept(T) [= $M^{1/\beta}(T, 0)$] = $a(-\tilde{\epsilon})$, respectively, for temperatures in the immediate vicinity of T_C (over a much wider temperature range) with the expressions for the coefficients a and 6 given by Eq.(4.12) (Eq.(4.13)). This implies that the nonanalytic correction terms dominate over the analytic ones for temperatures close to T_c whereas the reverse is true for temperatures away from T_C . This result is consistent with the similar observation made above in the case of $M(T, 0)$ and $\chi_o(T)$. Furthermore, when the intercept data for $T < T_C$ only are used in the analysis, the term $a(-\tilde{\epsilon})$ with the coefficient a given by either Eq.(4.12a) or Eq.(4.13a) provides the best fit with the choice of parameters and temperature range that is exactly the same as that for the fit to $M(T, 0)$ data based on Eq.(4.9a) or Eq.(4.10a). This results is not surprising when it is realized that the intercepts for $T < T_C$ are nothing but $M(T, 0)$ expressed as $[M(T, 0)]^{1/\beta}$. Fig. 4.14 shows the observed temperature variations of slope and intercept for a — $Fe_{90+y}Zr_{10-y}$ alloys. In these figures, the continuous curves through the data points represent the best LS fits based on the versions of the expressions for the coefficients a and 6 given by Eq.(4.13) while the dashed curves correspond to the LS fits based on the expressions for a and 6 given by Eq.(4.12). Such an agreement between the theory and experiment is symptomatic of the remaining samples as well.

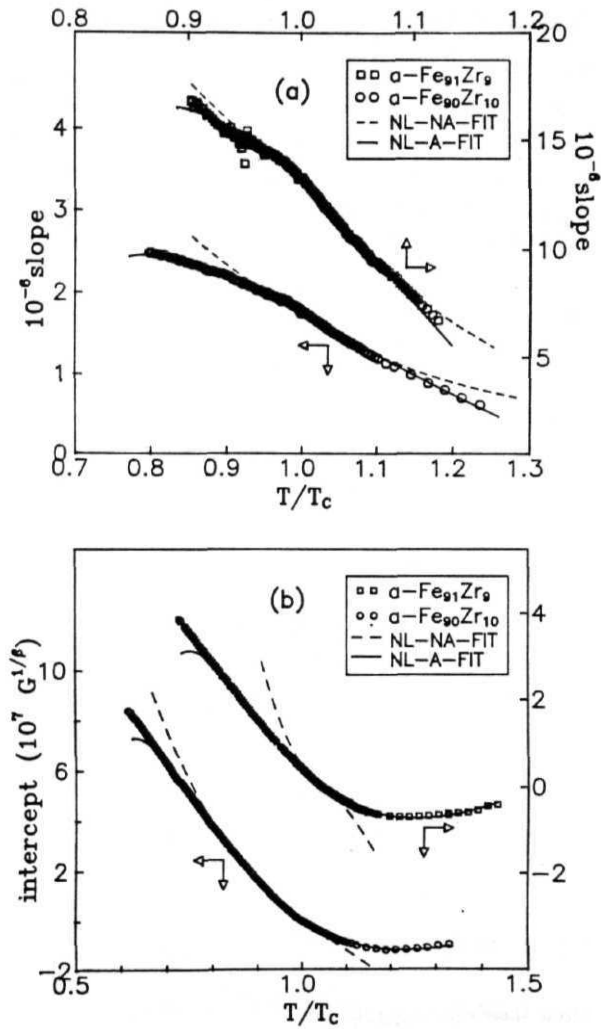


Fig. 4.14 Variation of (a) slope and (b) intercept (on the ordinate) of the linear modified Arrott plot isotherms over a wide temperature range around T_c . Dashed and continuous curves represent the LS fits to the data based on Eqs.(4.12) and (4.13), respectively.

4.2. Discussion

4.2.1. Asymptotic and effective critical exponents and amplitudes

The present results demonstrate that the CTS analysis that includes the nonanalytic correction terms, arising from nonlinear irrelevant scaling fields, yields accurate values for the *asymptotic* critical exponents and amplitudes that are *independent* of temperature over a temperature range which spans the asymptotic critical region (ACR). On the other hand, the *effective* critical exponents and amplitudes obtained by using **KF** and **SPL** methods *depend* on the temperature range used and denote the *average* values over this temperature range. This observation is clearly brought out by the results presented in Table 4.1. It is also noticed from this table that the results of KF and SPL analyses conform well with one another. Such an agreement is expected since both the methods are based on the same pure-power-law expressions (Eqs.(4.2) and (4.3)) for $M(T,0)$ and $\chi_o(T)$. The effective exponents β_{eff} and γ_{eff} as functions of temperature can be obtained from the **Kouvel-Fisher** relations Eqs.(4.4a) and (4.46) rewritten in the form [1,6]

$$\beta_{eff}(T) = \frac{(T - T_C)}{Y(T)} = \frac{T_C}{Y(T)} \epsilon \quad \text{and} \quad \gamma_{eff}(T) = \frac{(T - T_C)}{X(T)} = \frac{T_C}{X(T)} \epsilon . \quad (4.14)$$

The values of β_{eff} and γ_{eff} at different temperatures, so obtained, are plotted as a function of ϵ in Figs. 4.15 and 4.16, respectively, within the ACR. The asymptotic and effective critical exponents for temperatures not too far from T_C are related in accordance with the expressions [24,33-36,42]

$$\beta_{eff} = \beta + a_{M1} \Delta_1 |\epsilon|^{\Delta_1} + a_{M2} \Delta_2 |\epsilon|^{\Delta_2} , \quad (4.15)$$

and

$$\gamma_{eff} = \gamma - a_{\chi 1} \Delta_1 |\epsilon|^{\Delta_1} - a_{\chi 2} \Delta_2 |\epsilon|^{\Delta_2} . \quad (4.16)$$

It is evident from these equations that over a finite temperature range around T_C , where the correction terms are significant, the effective exponents can appreciably differ from the asymptotic ones and that $\beta_{eff}(\epsilon)$ and $\gamma_{eff}(\epsilon)$ coincide with β and γ only in the limit $\epsilon \rightarrow 0$. This observation is clearly brought out by the data presented in figures 4.15 and 4.16 for the alloys in question. The continuous curves through the data points in these figures represent the theoretical fits to the $\beta_{eff}[\gamma_{eff}]$ data based on Eq.(4.15) [Eq.(4.16)] obtained by keeping the CTS exponents (T_C) fixed at their theoretical values $\Delta_1 = 0.11$ and $\Delta_2 = 0.55$ (at the KF value obtained in the range $|\epsilon| \sim 0.01$) and treating β , a_{M1} and $a_{M2}[\gamma, a_{\chi 1}$ and $a_{\chi 2}]$ as free fitting parameters. The

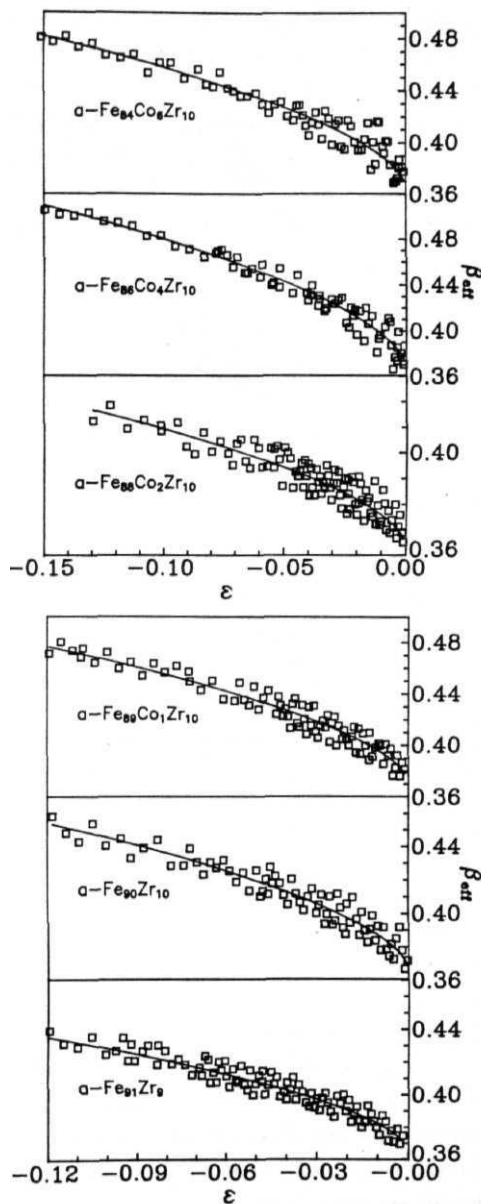


Fig. 4.15 β_{eff} vs. ϵ in the asymptotic critical region. The continuous curves denote the LS fits based on Eq.(4.15).

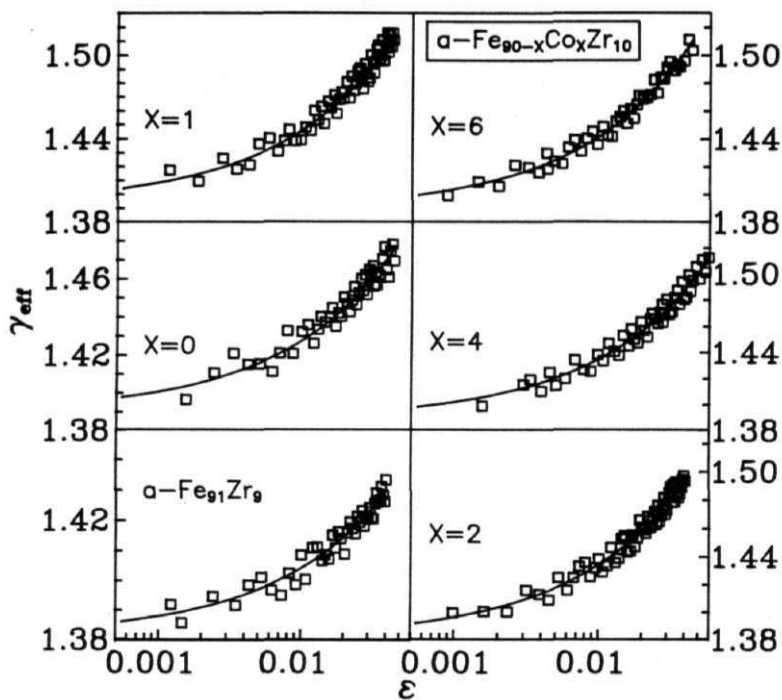


Fig. 4.16 γ_{eff} vs. ϵ in the asymptotic critical region. The continuous curves represent the LS fits based on Eq.(4.16).

values of these parameters determined in this way serve as a cross-check for those deduced from the CTS analysis of $M(T, 0)$ and $χ(T)$ data (Table 4.3) in the ACR because the above analysis involves *three* fitting parameters as against *five* in the CTS analysis. Therefore, it is gratifying to note that both the analyses yield the same parameter values. Moreover, the necessity of including the (non-analytic) confluent singularity corrections in the analysis is evident from the functional dependences of $β_{eff}$ and $γ_{eff}$ on $ε$ depicted in figures 4.15 and 4.16 when it is recognized that the exponents $β_{eff}$ and $γ_{eff}$ should be *independent* of temperature if such correction terms are not important. Another interesting feature presented by the data shown in Figs. 4.15 and 4.16 is that both $β_{eff}$ and $γ_{eff}$ *increase* with increasing $|ε|$ for the presently investigated alloys as contrasted with a monotonous decreasing trend with increasing $|ε|$ exhibited by these effective exponents in the ACR in many amorphous 3d transition metal-metalloid ferromagnetic alloys as well as crystalline elemental ferromagnets [6,33,35,36,42]. Consistent with this variation of $β_{eff}(ε)$ and $γ_{eff}(ε)$, the sign of the CTS amplitudes (*positive* for a_{M2} and *negative* for a_{M1} , a_{x1} and a_{x2} ; Table 4.3) in the present case is exactly opposite of that previously found in the ferromagnetic systems mentioned above. However, the overall behaviour of $γ_{eff}(ε)$ in a larger temperature range, i.e., from T_c to T_{max} (the maximum temperature covered in the present experiments), shown in Figs. 4.17(a) and 4.17(b), for the present alloys is similar to that observed earlier in a number of disordered systems [1,3,10,35-38]. The continuous curves in Figs. 4.17(a) and 4.17(b) represent the CTS fits to the $γ_{eff}(ε)$ data based on Eq.(4.16) in the ACR, as described above. It is evident from these figures that for temperatures outside the asymptotic critical region, i.e., for $ε > ε_{co}^+$, $γ_{eff}$ increases rapidly and goes through a peak (peak value $γ_{eff}^p$) at $ε_p$ and as the Co concentration is increased, $ε_{co}^+$ ($ε_p$) shifts to slightly higher (lower) temperatures while $γ_{eff}^p$ slowly diminishes in value.

Table 4.6. tests the validity of the **Widom** scaling relation, $β S = β + 7$, for the investigated alloys besides comparing the experimentally determined values of asymptotic exponents 0.7 and 6 with the corresponding theoretical estimates yielded by three-dimensional (3D) Heisenberg, Ising and XY models for ordered spin systems [1,31,32]. The values for the amplitude ratios $D m_o^δ / h_o m_o / M(0, 0)$ and $μ_o h_o / k_B T_c$ (the values of $μ_o$, the magnetic moment per alloy atom at 0 K, and $M(0, 0)$ have already been determined in Chapter 3; Table 3.2) calculated using the presently determined values of asymptotic critical amplitudes are listed in Table 4.7 along with the corresponding theoretical estimates. Note that the theoretical values for these amplitude ratios have been taken from references [1,36,43] which are, in turn, computed from the data given in references [44-48]. The main observations, based on the data presented in Tables 4.6 and 4.7, are: (i) the CTS values for the asymptotic critical exponents and the universal amplitude ratios $D m_o^δ / h_o$ and a_{M2} / a_{x2} (as well as a_{M1} / a_{x1}) are *composition-independent* (within the error limits) and conform very well with the theoretical estimates for the pure (ordered) spin system with d (lattice dimensionality) - n (order-parameter dimensionality) = 3, (ii) the Widom scaling relation is satisfied to a far greater accuracy by the asymptotic critical exponents than

Table 4.6. Asymptotic and effective critical exponents, validity of the Widom scaling equality. Comparison between theory and experiment. Abbreviations: CTS - correction-to-scaling; HM - Heisenberg Model; **IM** - **I**sing Model; KF - Kouvel-Fisher; MFT - Mean Field Theory. ^aRef.[1,32,36].

Alloy conc.	Analysis	θ	γ	b	$\beta+\gamma$	
y=1	CTS	0.366(4)	1.383(4)	4.75(5)	1.749(8)	1.739(38)
	KF	0.382(15)	1.400(20)		1.782(35)	1.807(90)
x=y=0	CTS	0.360(5)	1.390(5)	4.83(4)	1.750(10)	1.739(39)
	KF	0.382(15)	1.405(20)		1.787(35)	1.845(88)
x=1	CTS	0.368(6)	1.385(5)	4.80(4)	1.753(11)	1.766(43)
	KF	0.384(15)	1.416(25)		1.800(40)	1.836(87)
x=2	CTS	0.363(5)	1.389(6)	4.81(5)	1.752(11)	1.746(42)
	KF	0.381(15)	1.388(20)		1.769(35)	1.825(90)
x=4	CTS	0.365(6)	1.383(7)	4.85(5)	1.748(13)	1.770(48)
	KF	0.386(15)	1.407(20)		1.793(35)	1.872(92)
x=6	CTS	0.370(5)	1.386(6)	4.84(5)	1.756(11)	1.791(43)
	KF	0.390(15)	1.402(20)		1.792(35)	1.888(93)
3D-HM^a		0.365(3)	1.386(4)	4.80(4)	1.751(7)	1.752(30)
3D XY^a		0.325(2)	1.241(2)	4.82(3)	1.566(4)	1.567(20)
3D IM^a		0.345(2)	1.316(3)	4.81(3)	1.661(5)	1.660(20)
MFT		0.500	1.000	3.00	1.500	1.500

Table 4.7. Amplitude ratios: comparison between theory and experiment. Abbreviations have the same meaning as mentioned in Table 4.6. ^aRef.[1,36,43], ^bRef.[43].

conc. (y/x)	h_o (10 ⁵ Oe)	Dm^5/h_o	a_{M1}/a_{X1}	a_{M2}/a_{X2}	$M(0,0)$ (G)	$\mu_o/M(0,0)$	$\mu_o h_o/k_B T_C$	μ_{eff} (μ_B)	c (%)
y=1	1.4(1)	1.30(60)	1.0(10)	1.0(4)	965(25)	0.82(4)	0.060(5)	35.2(25)	4(1)
x=y=0	1.9(2)	1.32(65)	1.0(10)	1.1(4)	1041(30)	0.79(5)	0.082(7)	27.7(22)	5(1)
x=1	2.6(2)	1.34(65)	0.8(7)	0.8(3)	1100(35)	0.76(4)	0.104(11)	23.0(21)	7(1)
x=2	4.0(3)	1.30(65)	0.4(4)	0.3(2)	1170(25)	0.75(4)	0.154(14)	16.7(13)	10(1)
x=4	5.3(4)	1.33(85)	1.2(15)	0.8(3)	1296(20)	0.77(4)	0.194(26)	14.7(18)	12(1)
x=6	6.0(5)	1.33(95)	1.0(14)	0.7(3)	1305(30)	0.83(4)	0.195(31)	14.8(23)	12(1)
3D-IM ^a		1.33(1)				1.37(7)	1.58		
3D-IM ^a		1.81		0.9(21) ^b		1.49	1.52		
MFT ^a		1.00				1.73	1.73		

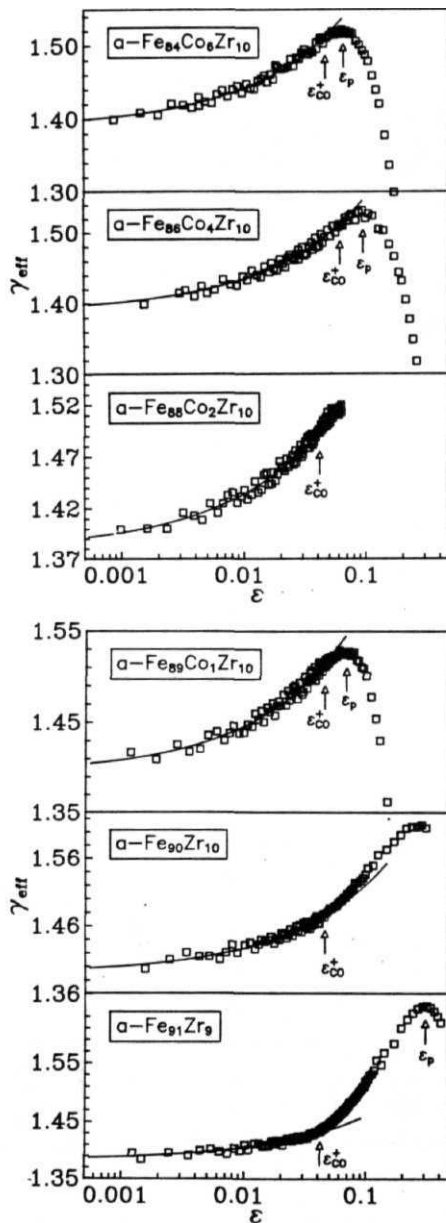


Fig. 4.17 Variation of γ_{eff} with ϵ over a wide temperature range for $T > T_C$. The solid curves though the data points denote the LS fits, obtained in the ACR, based on Eq.(4.16)

by the effective ones, (iii) the agreement between theory and experiment is much better for the asymptotic exponents than for the effective counterparts, and (iv) while the discrepancy between experimental and theoretical values of the ratio $m_o/M(0,0)$ is small, the ratio $\mu_o h_o/k_B T_C$ is at least one order of magnitude lower than the theoretical estimate of 1.58 for a 3D Heisenberg ferromagnet.

The result that the values of asymptotic critical exponents for the $a - Fe_{90+y}Zr_{10-y}$ and $a - Fe_{90-x}Co_xZr_{10}$ alloys are the same as those of an isotropic 3D Heisenberg ferromagnet refutes the earlier claims [49,50], based on the single power law analysis, that for the same alloys critical exponents β and γ have anomalously large values. The results of the present investigation make it clear that such unphysically large exponent values are an artifact of the analysis carried out on the bulk magnetization data taken outside the critical region since even in the ACR, $\gamma_{eff}(\epsilon)$ depends on temperature (Fig. 4.16) and possesses much larger values for $\epsilon > \epsilon_{co}^+$ (Fig. 4.17). The finding that the values of asymptotic critical exponents and universal amplitude ratios for the investigated amorphous alloys exactly coincide with the 3D Heisenberg values (observation (i)) vindicates the Harris criterion [51] which states that the critical behaviour of an ordered $n - d = 3$ spin system remains unaltered in the presence of short-ranged quenched disorder if the specific heat critical exponent α_p of the pure (ordered) system is *negative* (i.e., $\alpha_p < 0$). Validity of the Widom scaling relation for the alloys in question (observation (ii)) demands that the $M(T,H)$ data taken in the critical region must satisfy the scaling equation of state for a second-order phase transition, i.e., SES-I (Eq.(4.5a)) or even SES-II (Eq.(4.56)). That this is indeed the case for the glassy alloys under consideration is evident from Figs. 4.4-4.6. The critical exponents β and γ determined from the BM as well as FMR data in a narrow temperature range around T_C , using both the forms of SES (Eqs.(4.5a) and (4.56)), are in very good agreement (within the error limits) with the asymptotic exponents obtained from the CTS analysis. The values for the ratio $\mu_o h_o/k_B T_C$, obtained from the FMR and BM data using the SES analysis (Table 4.2), are of similar order as those listed in Table 4.7. The physical implication of the significantly lower values of the ratio $\mu_o h_o/k_B T_C$ than that expected for a 3D nearest-neighbour Heisenberg ferromagnet is as follows. Since h_o is presumably an *effective* exchange interaction field, the product of h_o and an *average effective* elementary moment (μ_{eff}) involved in the FM-PM phase transition, i.e., the effective exchange energy $\mu_{eff} h_o$, is expected to equal the thermal energy $k_B T_C$ at T_C . Evidently, this is not the case for the alloys in question unless μ_{eff} takes on values that are much larger than μ_o . Now that the critical exponents possess the 3D Heisenberg values for the presently investigated alloys, the ratio $\mu_{eff} h_o/k_B T_C$ is also expected to equal the 3D Heisenberg estimate of 1.58. This is possible only when μ_{eff} assumes values given in Tables 4.2 and 4.7. Moreover, if the concentration of such effective moments is $c = \mu_o/\mu_{eff}$. The values of c calculated in this way, included in Tables 4.2 and 4.7, indicate that only a small fraction of moments actually participates in the FM-PM phase transition and this fraction increases with increasing Co concentration (x).

These results find a straightforward but qualitative explanation [1,3,35,36] in terms of the infinite ferromagnetic matrix plus finite FM spin clusters model [1,3,4,20,52,53], described in detail in section 3.2.1. of Chapter 3. Within the framework of this model, even at low temperatures ($T \ll T_C$), the ferromagnetic coupling between the spins that constitute the finite clusters is much *stronger* than that between the spins of FM matrix. As the temperature is increased towards T_C , the exchange interaction between the spins in the FM matrix weakens whereas the FM coupling between the spins within the finite clusters is still relatively strong so that the spins of finite clusters increasingly polarize the FM matrix spins and hence these clusters grow in size at the expense of FM matrix. Consequently, number of spins in the FM matrix decreases rapidly as $T \rightarrow T_C$ so much so that only a small fraction of spins participates in the FM-PM phase transition at T_C . As explained already in section 3.2.2 of Chapter 3, the effect of increasing Co concentration in the a— $Fe_{90-x}Co_xZr_{10}$ alloy series is to (i) decrease the size as well as number of finite spin clusters, (ii) increase the number of spins in the infinite FM matrix and (iii) make the ferromagnetic coupling between the spins in the FM matrix stronger (hence increase T_C). This implies that higher the Co concentration, larger is the number of spins available in the FM matrix to start with at low temperatures and greater is the number of spins left behind at T_C by the temperature-induced growth of finite spin clusters. In other words, consistent with the present observation, the fraction of spins, c , participating in the FM-PM transition at T_C increases with Co concentration. Moreover, since the spin-spin correlation length, $\xi(T)$, diverges at T_C , the presence of finite clusters is not felt at all for temperatures close to T_C and as such amorphous and crystalline **ferromagnets** exhibit the same critical behaviour in the ACR. As the temperature is increased beyond T_C , $\xi(T)$ decreases and a temperature ϵ_{co}^+ is reached at which $\xi(T)$ equals the caliper dimension of the largest spin cluster. The magnetic inhomogeneity in the spin system is now no longer averaged out and γ_{eff} begins to increase and attains a peak value γ_{eff}^p at ϵ_p when $\xi(T)$ is comparable to the linear dimension of the smallest cluster. For $\epsilon > \epsilon_p$, the clusters shrink in size at a much faster rate than that at which $\xi(T)$ decreases with increasing temperature and hence γ_{eff} decreases towards the mean field value. Furthermore, as the Co concentration is increased, cluster size as well as their number decreases and hence $\xi(T)$ becomes comparable to the size of the largest (smallest) cluster at larger value of the temperature ϵ_{co}^+ (ϵ_p) whereas γ_{eff}^p decreases because of the lower average size and narrower size distribution of the spin clusters for higher Co concentrations.

4.2.2. Nonlinear scaling behaviour

Elaborate analysis of the $M(T, 0)$ and $\chi_o(T)$ data in terms of the expressions predicted by the nonlinear scaling theory [41] reveals that the *nonanalytic* 'correction-to-scaling' (CTS) terras are of paramount importance for temperatures close to T_C and that in the ACR, nonlinear scaling theory yields exactly the same results as the linear counterpart whereas the *analytic*

corrections become important for temperatures outside the **ACR**. Furthermore, the magnetic equation-of-state in nonlinear variables (Eq.(4.11)) correctly predicts the temperature variation of slope and intercept (on the ordinate) of the modified Arrott plot isotherms over a wide temperature range around T_C . Since the expression that includes a single leading analytic correction term in nonlinear variable ϵ , i.e., Eq.(4.106), adequately describes the $\chi_o(T)$ data over a wide temperature range above T_C for the investigated alloys and thereby permits an unambiguous determination of the paramagnetic moment q_c (magnetic moment per alloy atom in the paramagnetic state), Eq.(4.106) may be termed as the generalized Curie-Weiss law [41]. The Curie constant $C = A_X T_C$ is related to the effective paramagnetic moment (p_{eff}) as $p_{eff} = 2.828 \sqrt{C A / \rho}$ where A and ρ are the atomic weight and density, respectively. p_{eff} , in turn, is related to q_c as $p_{eff}^2 = q_c(q_c + 2)$. The values of q_c , computed from these relations using the A_X and T_C values listed in Table 4.5(b), and those of the ratio q_c/q_s , where $q_s (\equiv \mu_o)$ is the magnetic moment per alloy atom at 0 K, are included in Table 4.5(b). For all the amorphous alloys in question, the ratio $q_c/q_s > 1$ and its values for different compositions when plotted against T_C^{-1} or $T_C^{-2/3}$ fall on a straight line as shown in Fig. 4.18. According to the criteria proposed by Rhodes and Wohlfarth [54] and by Moriya [54] for weak itinerant ferromagnetism, the observations $q_c/q_s \gg 1$ and $q_c/q_s \propto T_C^{-1}$ or $q_c/q_s \propto T_C^{-2/3}$ imply that the presently investigated amorphous alloys are *weak* itinerant ferromagnets.

Based on the finding [40] that $\chi_o(T)$ data of crystalline *Ni* can be described by a single power law in nonlinear variables, i.e., $\chi_o(T) \sim (1/T) \tilde{\epsilon}^{-\gamma}$ (Eq.(4.10c)), over the temperature range T_C to $3T_C$, Fahnle and Souletie (FS) [55] introduced the effective exponent

$$\gamma_{eff}^{FS} = \gamma_{eff}^{KF} t - \epsilon \quad , \quad (4.17)$$

where γ_{eff}^{KF} is $T_C \chi_o(T) [d\chi_o^{-1}(T)/dT] \epsilon$ is the usual KF effective exponent, and using the series expansion method [55], calculated its temperature dependence over an extremely wide temperature range, $0 < \epsilon < 1$ for 3D Ising and Heisenberg spin systems in which spins of arbitrary magnitude are localized at the sites of a simple cubic (sc) or body-centered cubic (bcc) or face-centered cubic (fcc) lattice. Since in the present work, Eq.(4.106), which includes the leading analytic correction term in nonlinear variables, but not the single power law (i.e., the first term in Eq.(4.106) alone) provides a very good overall fit to the $\chi_o(T)$ data, a direct comparison with the theoretically predicted [55] temperature variation of γ_{eff}^{FS} is not possible unless Eq.(4.106) is reduced to a single power law by subtracting the correction term ($= A_X a_X t \tilde{\epsilon}^{1-\gamma}$) from both the sides of this equation. In other words, the measured $\chi_o(T)$ data are corrected for this correction term by using the presently determined values of T_C^+ , A_X and a_X and the $\chi_o(T)$ data **so corrected** are used to calculate $\gamma_{eff}^{KF}(T)$ which, in turn, is employed to compute $\gamma_{eff}^{FS}(T)$ from Eq.(4.17). The values of γ_{eff} at different temperatures obtained in this way are plotted against ϵ in Figs. 4.19(a) and 4.19(b) for all the compositions and compared with the corresponding theoretical values [55] (continuous and dashed curves). A close examination of these figures

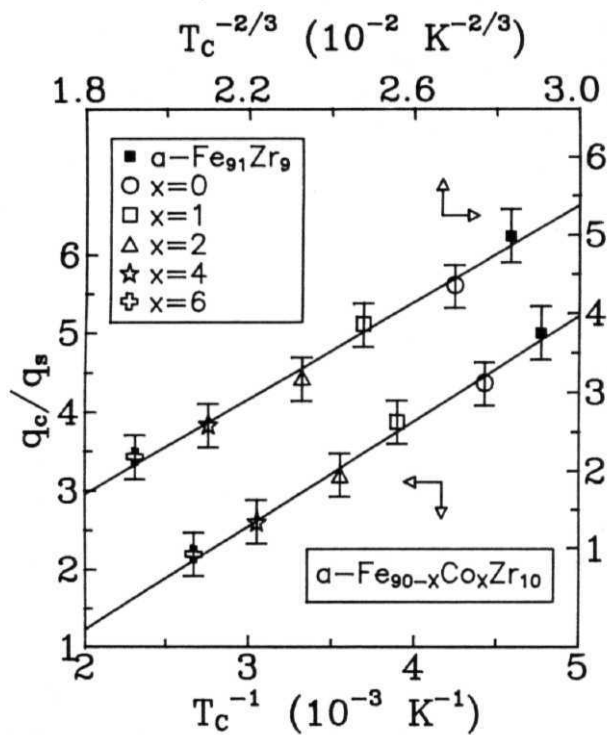


Fig. 4.18 q_c/q_s vs. T_c^{-1} and q_c/q_s vs. $T_c^{-2/3}$ plots. The solid line denotes the straight line fit to the data.

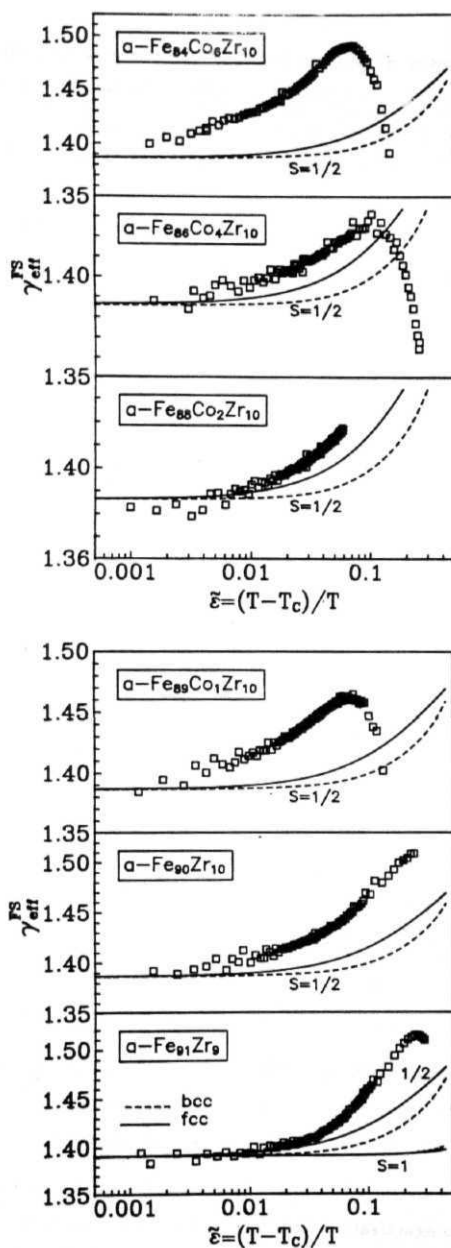


Fig. 4.19 γ_{eff}^{FS} vs. $\tilde{\epsilon}$ plots for $a\text{-Fe}_{91}\text{Zr}_9$ and $a\text{-Fe}_{90-x}\text{Co}_x\text{Zr}_{10}$ alloys. The continuous and dashed curves denote the theoretical variation predicted by the series expansion method [55]

reveals that (a) compared to $\gamma_{eff}^{KF}(T)$ in Fig. 4.17, the temperature variation of γ_{eff}^{FS} has slowed down while the peak value has decreased; but for these changes, the overall variation of $\gamma_{eff}^{FS}(T)$ remains the same as that of $\gamma_{eff}^{KF}(T)$ and hence the $\gamma_{eff}^{FS}(T)$ finds same qualitative interpretation in terms of the infinite 3D FM matrix plus finite spin FM clusters model as $\gamma_{eff}^{KF}(T)$ does, and (b) out of the theoretical curves shown in Fig. 4.19(a), only the one for $S = 1/2$ spins on the fee lattice has a form which mimics the observed variation of γ_{eff}^{FS} with temperature over a large temperature range but the agreement between theory and experiment is satisfactory only in the ACR.

4.3. Conclusions

The main conclusions regarding the thermal critical behaviour of $a - Fe_{90-y}Zr_{10-y}$ and $a - Fe_{90-x}Co_xZr_{10}$ alloys that can be drawn from the results of the bulk magnetization measurements on these systems over a wide temperature range, which embraces the critical region, are as follows.

- (i) The asymptotic critical exponents and the universal amplitude ratios Dm_o^δ/h_o and $a_{M2}/a_{\chi2}$, are in very good agreement with the corresponding theoretical estimates for the pure (ordered) spin system with $d = n = 3$. Such an agreement vindicates the famous Harris criterion.
- (ii) Consistent with the result that Widom scaling equality is satisfied to a very high degree of accuracy, the magnetization data obey the scaling equation of state valid for the second-order phase transition. Both BM and FMR data in the critical region yield identical results and assert that FMR is a powerful technique to study the critical behaviour of ferromagnetic systems.
- (iii) The fraction of spins that actually participates in the FM-PM phase transition in the amorphous alloys in question is small and increases with increasing Co concentration.
- (iv) Nonanalytic correction terms, arising from nonlinear irrelevant scaling fields, dominate over the analytic ones, originating from nonlinear relevant scaling fields, in the asymptotic critical region but the reverse is true for temperatures outside the ACR.
- (v) The magnetic equation of state in linear variables, valid for second-order phase transition, describes the magnetization data for temperatures close to T_C whereas its counterpart in nonlinear variables properly accounts for the observed $M(T, H)$ behaviour in a much wider temperature range around T_C .
- (vi) $\chi_o(T)$ follows the generalized Curie-Weiss law, Eq.(4.106), from T_C to $\sim 1.5 T_C$ and thereby makes an unambiguous determination of the paramagnetic moment possible.

- (vii) All the investigated amorphous alloys are *weak* itinerant **ferromagnets**.
- (viii) The infinite 3D FM matrix plus finite FM spin **clusters** model provides a simple but qualitative explanation for all the diverse aspects of the present results including the temperature variations of γ_{eff}^{KF} and γ_{eff}^{FS} .

B. PERCOLATION CRITICAL BEHAVIOUR

This part of the chapter is devoted to a detailed study of the percolation critical behaviour of the **a** - $(Fe_pNi_{1-p})_{80}(Si)_{20}$ (series I) and **a** - $(Fe_pNi_{1-p})_{80}P_{14}B_6$ (series II) alloys near the percolation critical point $Q(p = p_c, T = 0)$. Using the results of the preceeding chapter (Chapter 3), the **thermal-to-percolation** crossover exponent ϕ ($= \nu_p / \nu_T \nu_p$ and ν_T are the critical exponents for the percolation connectedness length and thermal correlation length, respectively) as well as the percolation critical exponents for spin wave stiffness, θ_p , and spontaneous magnetization, β_p , defined as [56-58] (cf. section 1.8, Chapter 1)

$$T_c(p) = t_p (p - p_c)^\phi \quad P > p_c \quad (4.18)$$

$$D(T = 0, p) = d_p (p - p_c)^{\theta_p} \quad P > p_c, \quad (4.19)$$

and

$$M(T = 0, p) = m_p (p - p_c)^{\beta_p} \quad P > p_c, \quad (4.20)$$

are determined from the $T_c(p)$, $D(T = 0, p)$ and $M(T = 0, p)$ data. Above definitions, Eq.(4.18), on the one hand, and Eqs.(4.19) and (4.20), on the other, pertain to the cases in which the critical point $Q(p = p_c, T = 0)$ is approached either along the ferromagnetic (FM)-paramagnetic (PM) phase transition line in the magnetic phase diagram or along the path $p \rightarrow p_c$ at $T = 0$. The values for different exponents, obtained in this way, are compared with the estimates given by the existing percolation theories mentioned in Chapter 1 and the validity of various scaling relations is tested.

4.4. Results and analysis

4.4.1. Magnetic Phase diagram

The magnetic phase diagrams **for the** **a** - $(Fe_pNi_{1-p})_{80}(B, Si)_{20}$ (series I) and **a** -

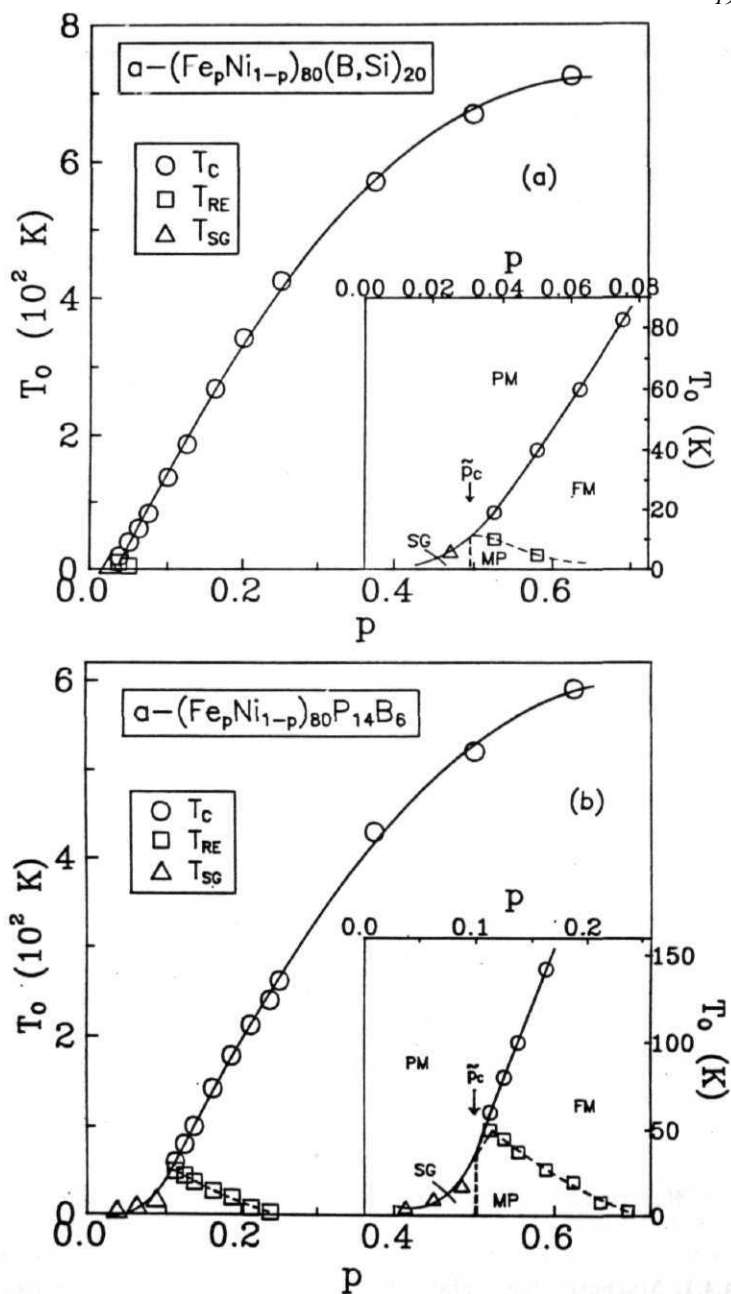


Fig. 4.20 Magnetic phase diagrams on the Fe-poor side for (a) $a-(\text{Fe}_p\text{Ni}_{1-p})_{80}(\text{BSi})_{20}$ and (b) $a-(\text{Fe}_p\text{Ni}_{1-p})_{80}\text{P}_{14}\text{B}_6$ alloys. The uncertainty limits lie well within the size of the symbols.

(Fe_pNi_{1-p})₈₀ $P_{14}B_6$ (series II) alloys in the Fe concentration range $0 \sim p \sim 0.625$, displayed in Fig. 4.20(a) and 4.20(b), respectively, are constructed using the values of T_C , T_{RE} and T_{SG} accurately determined [1,3,13,33,34,36,59-62] from χ susceptibility, electrical resistivity and bulk magnetization measurements. In these diagrams, T_C and T_{SG} denote the temperature at which ferromagnetic (FM)-paramagnetic (PM) and spin glass (SG)-PM phase transitions occur while T_{RE} ($\ll T_C$) marks the onset of strong irreversibility in the low-field ($H \sim 100$ Oe) magnetization. In other words, $T_{RE}(H)$ represents the temperature at and below which the zero-field-cooled (ZFC) and field-cooled (FC) magnetization curves bifurcate (ZFC magnetization starts decreasing while FC magnetization remains essentially constant as T is lowered below T_{RE}) from each other for a given field value and $T_{RE} = \lim_{H \rightarrow 0} T_{RE}(H)$. It is evident from these figures that the Fe concentration at which FM, PM, RE and SG phases coexist is $p_c \sim 0.03$ for series I and $p_c \sim 0.10$ for series II. As the temperature is lowered below T_C , the alloys with $p \sim p_c$ enter into the reentrant (RE) state at T_{RE} . The observations that the spontaneous magnetization does not drop to zero but instead remains finite as T is lowered through T_{RE} and this non-zero spontaneous magnetization in the RE phase is accompanied by the thermomagnetic and thermoremanent effects, which are normally associated with SG order, strongly suggest that the reentrant phase is a mixed phase in which long-range ferromagnetic order coexists with the cluster spin glass order. Moreover, there are strong indications that, unlike PM-FM and PM-SG phase transitions, the FM-RE transition (dashed curve through $T_{RE}(p)$ in Fig. 4.20) is not a true thermodynamic phase transition [53]. However, since the main concern of this part of the chapter (and of the thesis) is the percolation critical behaviour in these amorphous alloys, the exact nature of the reentrant phase or the transition at T_{RE} do not fall within the scope of this thesis.

4.4.2. Thermal-to-percolation crossover exponent (ϕ)

In order to accurately determine the thermal-to-percolation crossover exponent ϕ from the $T_C(p)$ data, Eq.(4.18) is rewritten in the following form

$$\left(\frac{T_C(p)}{p - p_c} \right) \left[\frac{dT_C(p)}{dp} \right]^{-1} = (p - p_c) / \phi \quad (4.21)$$

It is obvious from Eq.(4.21) that for concentrations in the close proximity to p_c (i.e., in the asymptotic critical region, ACR), the plot of t vs. p should be a straight line with slope $(1/\phi)$ and the intercept on the p -axis equal to p_c (this approach is identical to the Kouvel-Fisher (KF) analytic method described in section 4.1.3). The data presented in Fig. 4.21 testify to the validity of this approach for both the alloy series in question. The best least-squares (LS) fits to the $t(p)$ data based on Eq.(4.21) yield the values $\phi = 1.09(3)$ and $p_c = 0.026(2)$ [$\phi = 1.06(3)$ and $p_c = 0.070(2)$] in the concentration range $0.012 < (p - p_c) < 0.174$ [$0.043 < (p - p_c) < 0.168$] for

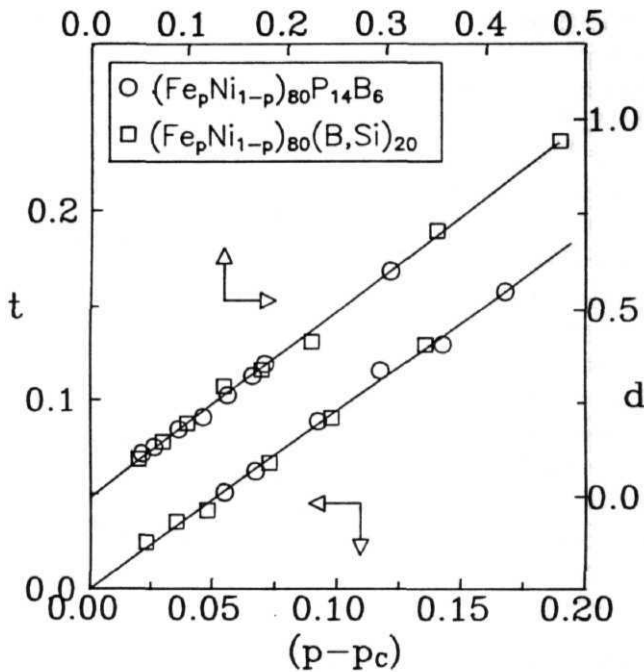


Fig. 4.21 Quantities $t = T_C(p)[dT_C(p)/dp]^{-1}$ and $d = D(T = 0, p)[dD(T = 0, p)/dp]^{-1}$ as functions of Fe concentration for $a - (\text{Fe}_p \text{Ni}_{1-p})_{80} (\text{B}, \text{Si})_{20}$ and $a - (\text{Fe}_p \text{Ni}_{1-p})_{80} \text{P}_{14} \text{B}_6$ alloys. The solid straight lines through the data points denote the least-square fits to the combined data. The size of the symbols denotes the uncertainty limits.

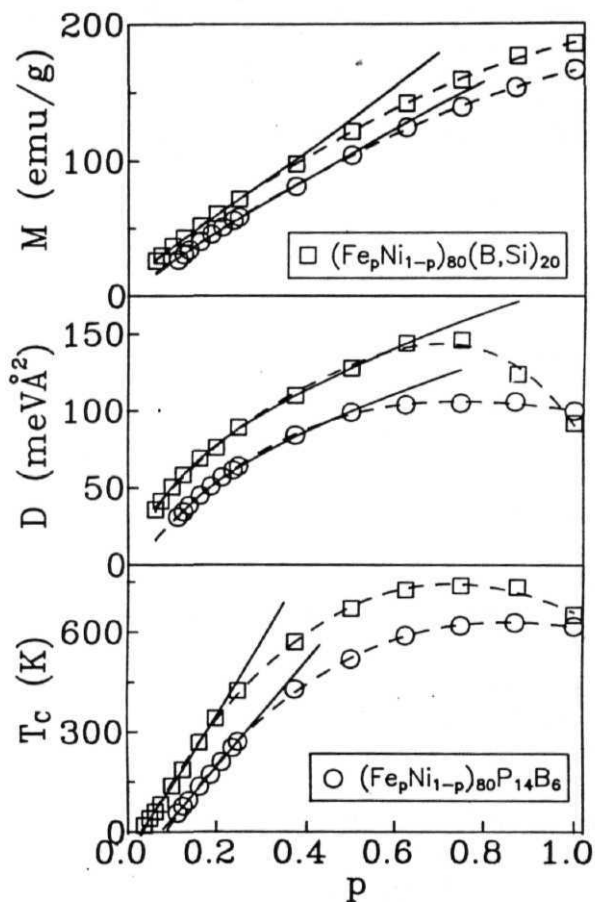


Fig. 4.22 Variation of $T_C(p)$, $D(T = 0, p)$ and $M(T = 0, p)$ with Fe concentration p . The continuous curves through the data points represent the LS fits to the data based on Eqs.(4.18), (4.19) and Eq.(4.23). The dashed curves serve to highlight the deviation of the data from the LS fits. The uncertainty limits lie well within the size of the symbols.

series I [series II]. The straight line fit in Fig. 4.21 represents the LS fit to the combined $t(p)$ data for both the alloy series with the choice of the ~~cross~~over exponent $\phi = 1.08(3)$, and p_c for series I and II the same as those mentioned above. The critical amplitude t_p is then computed using these values of ϕ and p_c in Eq.(4.18). The continuous curves through the $Tc(p)$ data points in Fig. 4.22 represent the fit obtained by using the presently determined values of t_p, p_c and ϕ in Eq.(4.18).

4.4.3. Percolation exponent for spin-wave stiffness at OK

Accurate values of the spin-wave stiffness at 0 K, $D(T = 0, p)$, plotted in Fig. 4.22 against p , have been determined accurately in Chapter 3 (section 3.1) through a detailed analysis of the $M(T, H)$ data. The percolation critical exponent θ_p is extracted from the $D(T = 0, p)$ data by employing the same procedure as described in section 4.4.2, i.e., at first, Eq.(4.19) is rewritten in the form

$$d = D(T = 0, p) [dD(T = 0, p)/dp]^{-1} = (p - p_c)/\theta_p \quad (4.22)$$

and then the quantity d is plotted against $(p - p_c)$, as shown in Fig. 4.21. This figure demonstrates that the above analytic approach is valid for the investigated glassy alloys. The best LS fits to the $d(p)$ data based on Eq.(4.22) yield the values $\theta_p = 0.505(5)$; $p_c = 0.025(2)$ [$\theta_p = 0.509(5)$; $p_c = 0.071(2)$] in the concentration range $0.038 < p < 0.6$ [$0.042 < p < 0.43$] for series I [II]. The solid straight line through the data points in Fig. 4.21 corresponds to the best LS fit to the combined $d(p)$ data with $\theta_p = 0.505(5)$ and p_c values for series I and II the same as those stated above. These values of θ_p and p_c are then inserted in Eq.(4.19) to obtain the values of the critical amplitude d_p for both the alloy series. The continuous curves through the $D(T = 0, p)$ data (denoted by open circles and squares) shown in Fig. 4.22 represent the theoretical variation arrived at using the presently determined values of d_p, p_c and θ_p in Eq.(4.19).

4.4.4. Percolation exponent for spontaneous magnetization

at 0 K

The M vs. H isotherm in fields up to 20 kOe has been recorded at $T = 1.6K$ for all the compositions in both the alloy series. Fig. 4.23 shows such M vs. H curves for a few representative compositions in series I. These curves present all the features characteristic of all compositions in the alloy series II as well. The spontaneous magnetization at 0 K for different compositions in a given alloy series, $M(T = 0, p)$, is obtained as an intercept on the ordinate

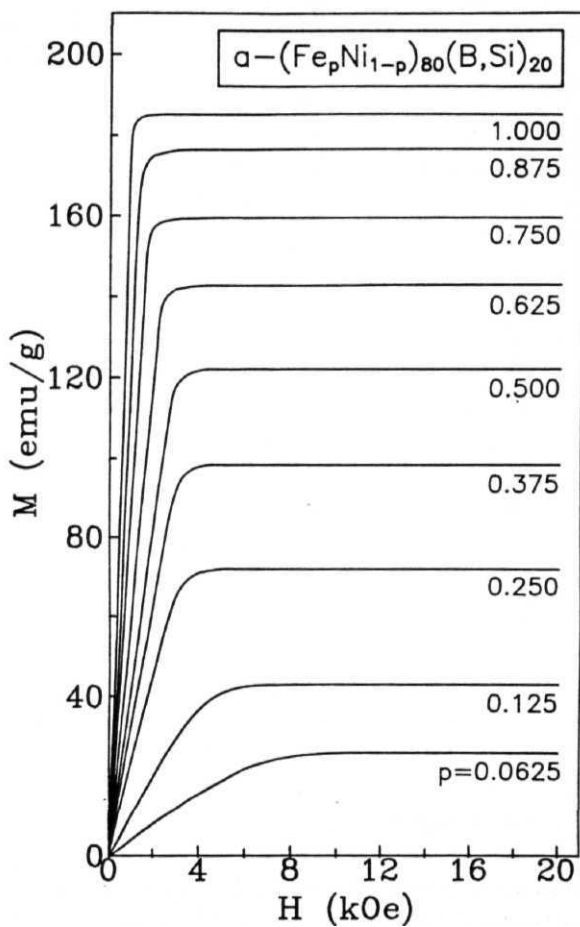


Fig. 4.23 M vs. H curves at $T = 1.6$ K for a few representative compositions in the amorphous $(\text{Fe}_p\text{Ni}_{1-p})_{80}(\text{B},\text{Si})_{20}$ alloy series.

when the linear high-field portion of the M vs. H isotherm taken at $T = 1.6$ K is extrapolated to $H = 0$. Note that no distinction between the values of spontaneous magnetization at 1.6 K and 0 K is made in this work. The M vs. H isotherm at 1.6 K presents a slight curvature in the high-field region that persists to fields as high as 20 kOe (the curvature is more pronounced in series II than in series I) and a large [63] high-field susceptibility ($\sim 5 \times 10^{15}$ emu/g Oe) particularly for the alloys with compositions just above p_c (i.e., for $p - p_c \sim 0.06$), presumably due to the frozen randomly oriented clusters (SG order) embedded in a (long-range) FM matrix. The curvature increases progressively as $p \rightarrow p_c$. Such a curvature gives rise to undesirably large uncertainty in $M(T = 0, p)$ values for $(p - p_c) \sim 0.06$ if the above-mentioned extrapolation technique is used. This problem is overcome by making the modified Arrott plot $[M^{1/\beta} \text{ vs. } (H/M)^{1/\gamma}]$ isotherm, constructed out of the $M(T, H)$ data taken at $T = 1.6$ K, linear, particularly in the high-field region, through a proper choice of the thermal critical exponents β and γ . $M(T = 0, p)$ is then computed from the intercept on the ordinate obtained by extrapolating the high-field linear portion of the MAP isotherm to $(H/M)^{1/\gamma} = 0$. The concentration dependence of $M(T = 0, p)$, so obtained, for both the alloy series is shown in Fig. 4.22. In the ACR, percolation theories [56-58] predict a variation of $M(T = 0, p)$ with p of the form given by Eq.(4.20). At first an attempt has been made to extract the exponent β_p from the

$$m(p) = M(T = 0, p) [dM(T = 0, p)/dp]^{-1}$$

data using the analytic method employed earlier for the $t(p)$ and $d(p)$ data. However, such an attempt did not succeed, primarily because the plot of m vs. p exhibits a marked curvature and hence β_p and p_c depend on the range of p used for the fit. A curvature in the m vs. p plot evidently implies that the ACR for $M(T = 0, p)$ is extremely narrow compared to that for $T_c(p)$ and $D(T = 0, p)$ and that the correction-to-scaling (CTS) terms contribute significantly for concentrations not too close to p_c . In order to verify this assertion, the expression

$$M(T = 0, p) = m_p (p - p_c)^{\beta_p} [1 + a(p - p_c)^{\Delta_1}] \quad (4.23)$$

which includes the CTS term with exponent Δ_1 and coefficient 'a', is fitted to the $M(T = 0, p)$ data over different concentration ranges by the LS method. The range-of-fit analysis, in which the variation of the fitting parameters m_p, p_c, β_p, a and Δ_1 , if any, is monitored as more and more data points taken at p values far away from p_c are excluded from the fit, yields the best LS fits (continuous curves through the $M(T = 0, p)$ data in Fig. 4.22) corresponding to the choice of the parameters values $m_p = 90(3)$ [109(2)] emu/g, $p_c = 0.026(2)$ [0.070(2)], $\beta_p = 0.41(2)$ [0.43(2)], $a = 1.95(5)$ [0.95(5)] and $\Delta_1 = 1.00(1)$ [1.00(1)] in the concentration range $0.037 < (p - p_c) < 0.22$ [$0.043 < (p - p_c) < 0.43$] for series I [II].

Note that the values of $T_c(p)$, $D(T = 0, p)$ and $M(T = 0, p)$ for a - $(Fe_p Ni_{1-p})_{80} (B, Si)_{20}$ (series I) and $a - (Fe_p Ni_{1-p})_{80} P_{14} B_{6}$ (series II) alloys are listed in Tables 3.5 and 3.6 of Chapter 3.

4.5. Discussion

In order to demonstrate that the values of the percolation exponents ϕ , θ_p and β_p as well as the amplitudes t_p , d_p and m_p determined by the methods described in the previous section are true asymptotic values and to bring out clearly the importance of the CTS term in case of $M(T = 0, p)$, the quantities $[T_C(p)/t_p]^{1/\phi} D(T = 0, p)/d_p]^{1/\theta_p}$ and $[M(T = 0, p)/m_p]^{1/\beta_p}$ are plotted against $(p - p_c)$ in Fig. 4.24. In this figure, the continuous straight lines/curves represent the best LS fits described earlier whereas the dashed curves serve as a guide to the eye. The main observations are: (i) the $T_C(p)$, $D(T = 0, p)$ and $M(T = 0, p)$ data yield the same value for p_c (within the uncertainty limits) for a given alloy series, (ii) p_c is nearly three times smaller in series I than in series II, (iii) the asymptotic critical region (where Eqs.(4.18)-(4.20) hold) is very wide for $T_C(p)$ and $D(T = 0, p)$ data but extremely narrow for $M(T = 0, p)$, and (iv) the CTS term has to be included in Eq.(4.23) in order to arrive at the true asymptotic values of ϕ , θ_p and m_p from $M(T = 0, p)$ data taken at p values not too close to p_c . The present values of p_c ($= 0.026(2)$ for series I and $0.070(2)$ for series II) lie well below the critical concentrations for bond and site percolation [58] for nearest-neighbour (NN) exchange interactions on the **fcc** lattice (note that the presently investigated amorphous alloy systems possess **fcc-like** short-range atomic order [13,61]) $p_c^b = 0.119$ and $p_c^s = 0.195$, but compare favourably with the critical concentration for site percolation on the **fcc** lattice when the exchange interactions involve first (1), second (2) and third (3) nearest neighbours [58], i.e., with $p_c^s(1,2,3) = 0.061$. This implies that the range of exchange interactions in series II nearly equals the third NN distance whereas the exchange interactions in series I extend well beyond the third NN distance.

To understand most of the properties of random systems such as dilute magnets, random resistor **networks**, microemulsions and gels, a complete knowledge about the structure of **percolating** cluster at and above the percolation threshold is necessary. Of all the model descriptions [56-58, 64-66] of the structure of the percolating cluster proposed so far, the node-link model [66] due to **Skal** and Shklovskii, and de Gennes (SSG) is by far the simplest one. In the node-link picture, the backbone of the infinite cluster is considered to be made up of a superlattice of **small** clusters (nodes) which are connected by one-dimensional random paths or links (for details see Chapter 1). According to this model, the exponents ϕ , θ_p and σ , the percolation critical exponent for macroscopic conductivity ($\Sigma(p) \sim (p - p_c)^\sigma$) are related to the critical exponents ν_p and ζ for the average distance between the nodes (the percolation correlation or connectedness length, $\xi(T = 0, p) \sim (p - p_c)^{-\nu_p}$) and the average length L of the one-dimensional random paths between adjacent nodes ($L \sim (p - p_c)^{-\zeta}$) through the exponent equalities [56-58,64-67]

$$\phi = \zeta = \nu_p/\nu_T, \quad \theta_p = 2(\zeta - \nu_p) \quad \text{and} \quad \sigma = (d - 2)\nu_p \zeta. \quad (4.24)$$

The values of the percolation exponents $\nu_p = \phi - (\theta_p/2)$ and σ computed from Eq.(4.24) using

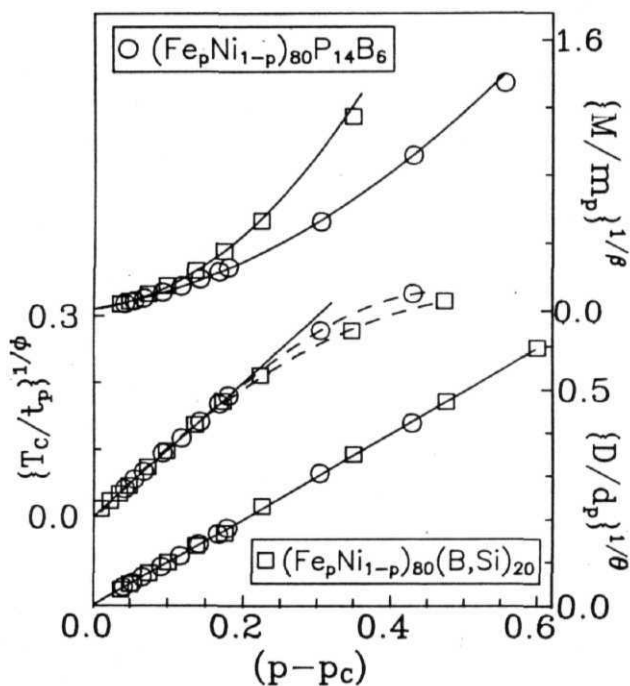


Fig. 4.24 Quantities $[T_c(p)/t_p]^{1/\phi}$, $[D(T = 0, p)/d_p]^{1/\theta}$ and $M(T = 0, p)/m_p]^{1/\beta}$ as functions of Fe concentration p . The Solid lines and curves through the data points denote the best LS fits to the data based Eqs.(4.18), (4.19) and (4.23) of the text, while the dashed curves serve to highlight the deviation from the LS fits. The size of the symbols denotes the uncertainty limits.

Table 4.8. Comparison between experiment and theory. ^aRef.[64,68-72], ^bRef.[73], ^cRef.[68,70,71,74,75], ^eRef.[75,80], ^eRef.[78].

parameter	series I	series II (K)	combined data	Theory d = 3
	1.09(3)	1.06(3)	1.08(3)	1.10(2) ^a
	0.505(5)	0.509(5)	0.505(5)	
β_p	0.41(2)	0.43(2)		0.41(3) ^a
A,	1.00(1)	1.00(1)		1.10(20) ^a
ν_p	0.84(3)	0.81(3)	0.83(3)	0.87(7) ^a
a	1.93(6)	1.87(6)	1.91(6)	2.00(5) ^{a,b}
β_p/ν_p	0.488(42)	0.531(45)	0.506(55)	0.471(16) ^c
	2.30(15)	2.31(16)	2.30(16)	2.31(6) ^c
d	2.51(4)	2.47(5)	2.49(5)	2.50(2) ^d
\bar{d}	1.32(13)	1.31(13)	1.31(14)	4/3 ^e

the presently determined values of ϕ and θ_p for the alloy series I and II as well as for the combined data are listed in Table 4.8 along with the corresponding theoretical estimates [64,68-72]. A close examination of the data presented in Table 4.8 reveals that the presently determined exponent values are in excellent agreement with the recently reported [64,68-72] theoretical estimates for site or bond percolation on $d = 3$ lattices. The value of σ obtained in this work is not only in perfect agreement with the corresponding theoretical value but also with the experimental value [73] $\sigma = 1.94(6)$ for **water-in-oil** microemulsion. Like the exponent values, the values of the exponent ratios σ/ν_p and f_{li}/ν_p for series I and II, and the combined data conform very well with the corresponding theoretical estimates obtained by finite-size scaling [71], series expansion [68,70], and Monte Carlo simulations [74,75]. Moreover, the conductivity critical exponent σ for the alloys in question satisfies the Golden inequality [76] $\sigma < 2$ for $d = 3$, derived by assuming that the conducting backbone near p_c has a hierarchical node-link-blob structure [65] (cf. Chapter 1).

Within the framework of a model which is based on the assumption that the finite cluster at p_c has a self-similar fractal structure [77] and makes use of the scaling arguments, the fractal dimension d and the spectral (fracton) dimensionality d of the percolating cluster at threshold can be expressed in terms of the Euclidean dimension d and percolation critical exponents β_p , ν_p and σ as [78,79]

$$3 = d - (\beta_p/\nu_p) \quad \text{and} \quad 3 = 2(d\nu_p - \beta_p)/(\sigma - \beta_p + 2\nu_p). \quad (4.25)$$

Alexander and Orbach [78] have conjectured that for percolation on the infinite cluster

$$3 = 4/3 \quad (4.26)$$

independent of d . The values of d , computed by substituting the exponent values determined in the present work and setting $d = 3$ in Eq.(4.25) for both the alloy series and the combined data, (included in Table 4.8) are in good agreement with the Monte Carlo [75] and series expansion [80] results while the present estimates of d (Table 4.8) are consistent with the **Alexander-Orbach** conjecture (Eq.(4.26)). Combining Eqs.(4.25) and (4.26) and solving for σ , one arrives at the expression

$$\sigma = [(3d - 4)\nu_p - \beta_p]/2. \quad (4.27)$$

For $d = 3$, Eq.(4.27) reduces to $\sigma = (5\nu_p - \beta_p)/2$ and the presently determined values of ν_p and β_p , when substituted in this relation, give the values $\sigma = 1.90(8)$ and $1.81(8)$ for series I and II, which are same (within the error limits) as those obtained from Eq.(4.24) and predicted by SSG node-link model [66]. Note that the expression for σ in Eq.(4.24) reduces to Eq.(4.27) if $\zeta m d \nu_p/2$. This condition is also satisfied in the present case.

The above observations demonstrate that the SSG node-link, **hierarchical** node-link-blob and self-similar fractal models are mutually consistent, **eventhough**, they differ widely in microscopic details and hence form completely different descriptions of the structure of the infinite cluster at p_c . This is not surprising in view of the fact that the structural details at length scales less than the correlation or connectedness length, $\xi(T = 0, p)$, are of no consequence so long as $\xi(T = 0, p)$ diverges at p_c . Thus, Eqs.(4.24) and (4.27) have a universal character in that they are of more general validity than what an oversimplified underlying model would normally suggest. Other important points worth noting are: (i) a close agreement between the experimental values of the percolation critical exponents for *amorphous* site-diluted ferromagnets determined in this work and those theoretically predicted for site- or bond- percolation on three-dimensional *crystalline* lattices asserts that the critical behaviour of percolation on a *regular* $d = 3$ lattice remains unaltered in the presence of *quenched randomness* if the **specific** heat critical exponent of the *regular* system is negative [56-58], and (ii) the finding that the range of exchange interactions is widely different in the two alloy series and yet both the alloy series possess the same values for the percolation critical exponents vindicates the universality hypothesis. The inference same as the observation (i) made above has also been drawn recently based on the results of Monte Carlo simulations [81] of bond (site) percolation on random two-dimensional (three-dimensional) systems. Furthermore, consistent with the above observation (i), the results of electrical resistivity [34,36,82], bulk magnetization [1,3,36,38] and 'zero-field' susceptibility [33,36,39,83] measurements (performed in the asymptotic critical region on the same and/or similar *(Fe — Ni)-metalloid* alloy systems as the present ones) have proved beyond any doubt the validity of the Harris criterion even for *extreme* disorder by unambiguously demonstrating that, even for compositions extremely close to (just above) p_c , T_C is sharply defined ($\Delta T_C/T_C \sim 10^{-4}$) and the asymptotic values of the *thermal* critical exponents for specific heat, spontaneous magnetization and initial susceptibility are *composition-independent* and the *same* as those theoretically predicted for an ordered three-dimensional ($d = 3$) **Heisenberg** spin system.

Considering the fact that the critical concentration has not been approached sufficiently closely in the present experiments, a close agreement between experiment and theory may seem to be fortuitous, but the following observations do not support such an inference. These observations are : (a) three different types of data namely, $T_C(p)$, $M(T = 0, p)$ and $D(T = 0, p)$, yield the *same* value for p_c for a given alloy series, (b) eventhough p_c is widely different in the two alloy series, both the alloy series yield identical values for the percolation critical exponents, and (c) within roughly the same concentration range, the need to include the 'correction-to-scaling' (CTS) term is felt only in the case of $M(T = 0, p)$ but not for $T_C(p)$ and $D(T = 0, p)$. The main difficulty in approaching p_c sufficiently closely in this work arises from the breakdown of long-range ferromagnetic order at \tilde{p}_c (the concentration at which the present alloys enter into a spin-glass state when the concentration p is lowered through p_c , see Figs. 4.20(a) and 4.20(b)

which lies above p_c . At this juncture, one has to admit that the actual behaviour of the investigated alloy systems is much more complicated than a simple dilution picture would normally suggest. This is so because the spin glass phase exists for $p < p_c$ (and hence the SG order is present even for concentrations $p_c \sim p \sim \tilde{p}_c$) and long-range ferromagnetic order breaks down before the percolation threshold, p_c , is reached. As a consequence, the magnetic atoms have a power-law (fractal) correlation near the percolation threshold if only the nearest-neighbour interaction is assumed. The Harris criterion is replaced by the Weinrib-Halperin criterion [28] which predicts new exponents even if $\alpha < 0$ in the pure system. Thus, a crossover to a new fixed point (critical behaviour) is expected. The presence of spin interactions beyond the first neighbour in the systems under consideration should make the crossover spread out and new critical behaviour hard to detect. This might offer a simple explanation for a seemingly wide critical region for $T_c(p)$ and $D(T = 0, p)$ but certainly not for the necessity to include the CTS term only for $M(T = 0, p)$. Moreover, there is no *a priori* reason to believe that one should obtain the *pure* values for the exponents in the crossover region. Furthermore, if the Weinrib-Halperin criterion [28] is applicable to the amorphous alloy systems studied in the present work, the *thermal* critical exponents are also expected to possess values widely different from the pure ones for p close to p_c . However, the detailed studies [33,34,36,38,39,82,83] of the thermal critical behaviour in the alloys with p close to p_c , in which T_C has been approached sufficiently closely, reveal that the *thermal* critical exponents do possess *pure* values. These contradictions can be laid to rest only when the type of measurements described in this work are performed on amorphous magnetic systems in which the formation of the spin glass state at low concentrations can be completely avoided and long-range ferromagnetic order breaks down at p_c . However, such a *metallic* alloy system is hard to realize in practice.

4.6. Conclusions

Through an elaborate data analysis, accurate values for the *crossover* exponent $<p$ and percolation exponents for spin-wave stiffness θ_p and magnetization β_p have been determined from the $T_C(p)$, $D(T = 0, p)$ and $M(T = 0, p)$ data taken on amorphous $(Fe_pNi_{1-p})_{80}(B, Si)_{20}$ $(Fe_pNi_{1-p})_{80}P_{14}B_6$ alloys over a wide range of Fe concentration $0.025 \sim p \sim 0.625$. The exponent values, so obtained, are used to compute the percolation critical exponents ν_p and σ for percolation correlation length and the conductivity, respectively, with the help of the exponent equalities. A detailed comparison between experiment and theory then permits us to draw the following conclusions regarding the percolation critical behaviour of the amorphous alloys in question.

- (i) An excellent agreement between the experimentally determined values of crossover and

percolation critical exponents (ϕ , β_p , δ , ν_p and σ) and the corresponding theoretical estimates predicted for site- or bond-percolation on $d = 3$ *crystalline* lattice **assure** that the critical behaviour of percolation on a *regular* $d = 3$ *lattice* remains *unaltered* in the presence of *quenched randomness* if the specific heat exponent of the *regular* system is *negative*.

- (ii) The asymptotic critical region, where the single power-law behaviour (i.e., Eqs.(3.18)-(3.20)) is valid, is wide for $T_C(p)$ and $D(T = 0, p)$ but extremely narrow for $M(T = 0, p)$; in the latter case, the correction-to-scaling term had to be included in order to arrive at the true **asymptotic** value of the critical exponent β_p and amplitude m_p from $M(T = 0, p)$ data taken at concentrations not too close to p_c .
- (iii) Consistent with the Alexander-Orbach *conjecture*, the fracton dimensionality d of the percolating cluster at threshold turns out to be $d \sim 4/3$ and the conductivity exponent σ obeys the Golden *inequality* $a < 2$.
- (iv) The observation that the range of exchange interactions is widely different in the two glassy alloy series and yet the percolation critical exponents have the **same** values for both of them vindicates the universality hypothesis.

References

- [1] S.N. Kaul, **J. Magn. Magn. Mater.** 53, 5 (1985).
- [2] A. Arrott and J.E. Noakes, *Phys. Rev. Lett.* **19**, 786 (1967).
- [3] S.N. Kaul, *IEEE Trans. Magn.* MAG-20, 1290 (1984).
- [4] S.N. Kaul, *J. Phys. F* 18, 2089 (1988).
- [5] H.F. Stanley, *Introduction to Phase Transitions and Critical Phenomena* (Clarendon press. Oxford, 1971); S.K. Ma, *Modern Theory of Critical Phenomena* (Benjamin **Inc.**, 1976).
- [6] J.S. Kouvel and M.E. Fisher, *Phys. Rev. A* 136, 1626 (1964).
- [7] J.D. Cohen and T.R. Carver, *Phys. Rev. B* 15, 5350 (1977); J. H. Abeles, T.R. Carver and G.C. Alexandrakis, *J. Appl. Phys.* **53**, 7935 (1982).
- [8] S.N. Kaul, *Phys. Rev. B* 22, 278 (1980).
- [9] Y. Yeshurun, M.B. Salamon, K.V. Rao and H.S. Chen, *Phys. Rev. B* 24, 1536 (1981).
- [10] M. Fahnle, W.U. Kellner and H. Kronmüller, *Phys. Rev. B* 35, 3640 (1987); W.U. Kellner, M. Fahnle, H. Kronmüller and S.N. Kaul, *Phys. Stat. Sol.(b)* **144**, 397 (1987).
- [11] J.S. Kouvel and J.B. Comley, *Phys. Rev. Lett.* 20, 1237 (1967).
- [12] S.J. Poon and J. Durand, *Phys. Rev. B* **16**, 316 (1977).
- [13] S.N. Kaul, *Phys. Rev. B* **23**, 1205 (1981); *Phys. Rev. B* 24, 6550 (1981).
- [14] S.N. Kaul and M. Rosenberg, *Phil. Mag. B* 44, 357 (1981); *Solid State Commun.* 41, 857 (1982).
- [15] M.L. Spano and S.M. Bhagat, *J. Magn. Magn. Mater.* 24, 143 (1981).
- [16] B. Heinrich, J.M. Rudd, K. Ugruhart, K. Myrtle, J.F. Cochran and R. Hasegawa, *J. Appl. Phys.* 55, 1814 (1984).
- [17] S.M. Bhagat, D.J. Webb and M.A. Manheimer, *J. Magn. Magn. Mater.* 53, 209 (1985).
- [18] S.M. Bhagat, S. Haraldson and O. Beckman, *J. Phys. Chem. Solids* 38, 593 (1977).
- [19] B. Heinrich, J.F. Cochran and R. Hasegawa, *J. Appl. Phys.* 57, 3690 (1985); J.F. Cochran, **R.W.** Qiao and B. Heinrich, *Phys. Rev. B* 39, 4399 (1989).
- [20] S.N. Kaul and V. Siruguri, *J. Phys.: Condens. Matter* 4, 505 (1992); *J. Phys.:F* 17, L255 (1987).

- [21] D.S. **Rodbell**, *Phys. Rev. Lett.* **13**, 471 (1964); *Physica* **1**, 279 (1965).
- [22] S.M. Bhagat and H.O. Stevens, *J. Appl. Phys.* **39**, 1067 (1968).
- [23] S. **Haraldson** and L. Petterson, *J. Phys. Chem. Solids* **42**, 681 (1981).
- [24] A. Aharony and G.Ahlers, *Phys. Rev. Lett.* **44**, 782 (1980).
- [25] T.C. Lubensky, *Phys. Rev. B* **11**, 3573 (1975).
- [26] D.E. Khmelnitzki, *Sov. Phys. JETP* **41**, 981 (1975).
- [27] G. Grinstein and A. Luther, *Phys. Rev. B* **13**, 1329 (1976).
- [28] A. Weinrib and B.I. Halperin, *Phys. Rev. B* **27**, 413 (1983).
- [29] G. Jug, *Phys. Rev. B* **27**, 609 (1983).
- [30] A. Aharony and M.E. Fisher, *Phys. Rev. B* **27**, 4394 (1983).
- [31] A. Aharony, in *Phase Transitions and Critical Phenomena*, edited by C. **Domb** and M.S. Green (Academic, New York, 1976) vol.6, p.357.
- [32] J.C. Le Guillou and J. Zinn-Justin, *Phys. Rev. B* **21**, 3976 (1980); S.G. Gorishny, S.A. Larin and F.V. Tkachov, *Phys. Lett. A* **101**, 120 (1984).
- [33] S.N. **Kaul**, *Phys. Rev. B* **38**, 9178 (1988).
- [34] S.N. Kaul and M. **Sambasiva Rao**, *Phys. Rev. B* **43**, 11240 (1991).
- [35] S.N. Kaul and Ch.V. Mohan, *Phys. Rev. B* **50**, 6160 (1994).
- [36] S.N. Kaul and M. Sambasiva Rao, *J.Phys.: Condens. Matter* **6**, 7403 (1994); M. Sambasiva Rao and S. N. Kaul, *J. Magn. Magn. Mater.* **147**, 149 (1995); M. Sambasiva Rao, Ph.D thesis 1995 (unpublished).
- [37] S.N. Kaul, W.-U. Kellner and H. **Kronmüller**, *Key. Engg. Mater* **13-15**, 669 (1987).
- [38] R. Reisser, M. **Fähnle** and H. **Kronmüller**, *J. Magn. Magn. Mater.* **97**, 83 (1991).
- [39] P. Hargraves and R.A. Dunlap, *J. Phys. F* **18**, 533 (1988); *J. Magn. Magn. Mater.* **75**, 378 (1988).
- [40] J. Souletie and J.L Tholence, *Solid State Commun.* **48**, 407 (1983).
- [41] S.N. **Kaul**, *Phase Transitions* **47**, 23 (1994).
- [42] M. Seeger, S.N. Kaul, H. **Kronmüller** and R. Reisser, *Phys. Rev. B* **51**, 12585 (1995).

- [43] V. Privman, P.C. Hohenberg and A. Aharony, in *Phase Transitions and Critical Phenomena*, edited by C. Domb and J.L. Lebowitz (Academic press, New York, **1991**) Vol.14, p.1; C. Bagnuls, C. Breviller, D.I. Meiron and B.C. Nickel, **Phys. Rev. B** 35 3585 (1987).
- [44] S. Milosevic and H.E. Stanley, *Phys. Rev. B* 6, **986**, 1002 (1972).
- [45] R. Krasnow and H.E. Stanley, *Phys. Rev. B* 8, 332 (1973).
- [46] M. Barmatz, P.C. Hohenberg and A. Kornblit, *Phys. Rev. B* **12**, 1947 (1975).
- [47] P.C. Hohenberg, A. Aharony, B.I. Halperin and E.D. Siggia, *Phys. Rev. B* 13, 2986 (1976).
- [48] A. Aharony and P.C. Hohenberg, *Phys. Rev. B* 13, 3081 (1976).
- [49] H. Yamauchi, H. Onodera and H. Yamamoto, *J. Phys. Soc. Jpn.* 53, 747 (1984).
- [50] K. Winschuh and M. Rosenberg, *J. Appl. Phys.* 61, 4401 (1987).
- [51] A.B. Harris, *J. Phys. C* **7**, 1671 (1974).
- [52] S.N. Kaul, *J. Phys.: Condens. Matter* 3, 4027 (1991).
- [53] S.N. Kaul, V. Siruguri and G. Chandra, *Phys. Rev. B* 45, 12343 (1992).
- [54] E.P. Wohlfarth, *J. Magn. Magn. Mater.* 7, 113 (1978).
- [55] M. Fahnle and J. Souletie, *J. Phys.:C* 17, L469 (1984); *Phys. Stat. Sol.(b)* **138**, 181 (1986).
- [56] D. Stauffer, *Phys. Rep.* 54, 1 (1979); J.W. Essam, *Rep. Prog. Phys.* 43, 833 (1980).
- [57] D. Stauffer and A. Aharony, *Introduction to Percolation Theory* (Taylor & Francis, Bristol, 1991).
- [58] R.B. Stinchcombe, in *Phase Transitions and Critical Phenomena*, edited by C. Domb and M.S. Green (Academic, New York, 1983) Vol.7, p.151.
- [59] S.N. Kaul, *Solid State Commun.* **36**, 279 (1980).
- [60] S.N.Kaul, *IEEE Trans. Magn.* **MAG-17**, 1208 (1981).
- [61] S.N. Kaul, *Phys. Rev. B* **27**, 5761 (1983); *Phys. Rev. B* 27, 6923 (1983).
- [62] P.D. Babu, M. Sambasiva Rao and S.N. Kaul, *Proceedings of Solid State Physics Symposium (India)*, **37c**, 134 (1994).
- [63] S.N. Kaul and M. Rosenberg, *Phys. Rev. B* 27, 5698 (1983).

- [64] L.J. de Jongh, in *Magnetic Phase Transitions*, edited by M. Ausloos and R.J. Elliott (Springer-Verlag, Berlin, 1983), p.172; A.Coniglio, *ibid*, p.195; Phys. Rev. Lett. **4**, 250 (1981).
- [65] H.E. Stanley, J. Phys. A 10, L211 (1977); A. Coniglio, J. Phys. A 15, 3829 (1982).
- [66] A.S. Skål and B.I. Shklovskii, Fiz. Tekh. Poluprovodn. 8, 1582 (1974) [Sov. Phys.-Semicond. 8, 1029 (1975)]; P.G. de Gennes, J. Phys. (Paris) Lett. 37, L1 (1976).
- [67] T.A.L. Ziman, J. Phys. C 12, 2645 (1979).
- [68] J. Adler, Y. Meir, A. Aharony and A.B. Harris, Phys. Rev. B 41, 9183 (1990) and references cited therein; T.C. Lubensky and J. Wang, Phys. Rev. B 33, 4998 (1986).
- [69] D.J. Bergman, E. Duering and M. Murat, J. Stat. Phys. 58, 1 (1990).
- [70] J. Adler, Y. Meir, A. Aharony, A.B. Harris and L. Klein, J. Stat. Phys. 58, 511 (1990).
- [71] D.B. Gingold and C.J. Lobb, Phys. Rev. B 42, 8220 (1990).
- [72] E. Duering and H.E. Roman, J. Stat. Phys. 64, 851 (1991).
- [73] C. Cametti, P. Codastefano, P Tartaglia, J. Rouch and S.H Chen, Phys. Rev. Lett. 64, 1461 (1990).
- [74] H.E. Roman, J. Stat. Phys. 58, 375 (1990).
- [75] R.M. Ziff and G. Stell (private communication).
- [76] K. Golden, Phys. Rev. Lett. 65, 2923 (1990).
- [77] B. Mandelbrot, in *Fractals: Form, Chance and Dimension* (Freeman, San Francisco, 1977).
- [78] S. Alexander and R. Orbach, J.Phys.(Paris) Lett. 43, L625 (1982).
- [79] R. Rammal and G. Toulouse, J. Phys. (Paris) Lett. 44, L13 (1983).
- [80] A.U. Neumann and S. Havlin, J. Stat. Phys. 52, 203 (1988).
- [81] D.Y. Kim, H.J. Herrmann and D.P. Landau, Phys. Rev. B 35, 3661 (1987); I. Balberg, Phys. Rev. B 37, 2391 (1988).
- [82] Z. Marohnic and E. Babic, in *Rapidly Quenched Metals*, edited by S. Steeb and H. Warlimont (Elsevier, Amsterdam, 1985), p. 1063.
- [83] D. Drobac and Z. Marohnic, in *Rapidly Quenched Metals* (ref.81), p. 1133.

CHAPTER 5

ELECTRICAL RESISTIVITY OF (Fe,Co)-Zr AMORPHOUS ALLOYS

In this chapter, the electrical resistivity data taken over a wide temperature range on amorphous $Fe_{90+y}Zr_{10-y}$ ($y = 0, 1$) and $Fe_{90-x}Co_xZr_{10}$ ($x = 0, 1, 2, 4, 6, 8$ and 10) alloys have been analyzed with a view to identify the scattering processes that dominantly contribute to the total resistivity in different temperature ranges and the results are discussed in light of the existing theoretical models which have already been briefly introduced in chapter 1.

5.1. Results and data analysis

Electrical resistivity ($\rho(T)$) of $a - Fe_{90+y}Zr_{10-y}$ ($y = 0, 1$) alloys has been measured as a function of temperature in the ranges 4.2 - 600 K at the University of Cantabria (UC), Spain and 77 - 350 K at the University of Hyderabad (UH), India. One more set of $\rho(T)$ data for the alloys with $y = 0$ has been taken in the range 2 - 300 K at the Ruhr Universität Bochum (RUB), Germany. The above-mentioned sets of data taken on samples coming from different batches of the alloys with nominal composition $y = 0$ and 1, whose details have already been given in Chapter 2, will henceforth be referred to as the UC, UH and RUB $\rho(T)$ data. Figs. 5.1(a) and 5.1(b) compare different sets of $\rho(T)$ data for the alloys with $y = 0$ and 1 by plotting them in the form of the normalized resistivity, $r(T) = \rho(T)/\rho(T = 273.15A)$, versus T plots. Similarly, Fig. 5.1(c) shows the temperature dependence of $r(T)$ in the range from 77 K to 350 K for different Co concentrations in the $a - Fe_{90-x}Co_xZr_{10}$ alloy series. Note that very high density of data points gives rise to the continuous $r(T)$ curves in these figures (for that matter, in most of the figures of this chapter) and the different sets of data belonging to different concentrations of either Fe in $a - Fe_{90+y}Zr_{10}$ or Co in $a - Fe_{90-x}Co_xZr_{10}$ alloy series are shifted with respect to one another for the sake of clarity; the exact shift in the ordinate scale for different sets of data for the same or different concentrations is indicated in the figure captions. The main observations based on the data presented in these figures are: (i) for all the amorphous alloys in question, resistivity as a function of temperature goes through a broad minimum at a temperature as high as ($T_{min} \sim 250$ K); T_{min} lies fairly close to, but above, the Curie temperature T_C (T_C and T_{min} are indicated by downward arrows in Fig. 5.1, (ii) like T_C , T_{min} shifts to higher temperatures and the difference ($T_{min} - T_C$) progressively decreases as the Co concentration is increased, (iii) specifically for the alloys with $y = 0$ and 1, T_{min} almost coincides with the Debye temperature Θ_D ($\Theta_D = 249$ K and 251 K [1] for $y = 1$ and 0, respectively), (iv) temperature coefficient of resistivity (TCR)

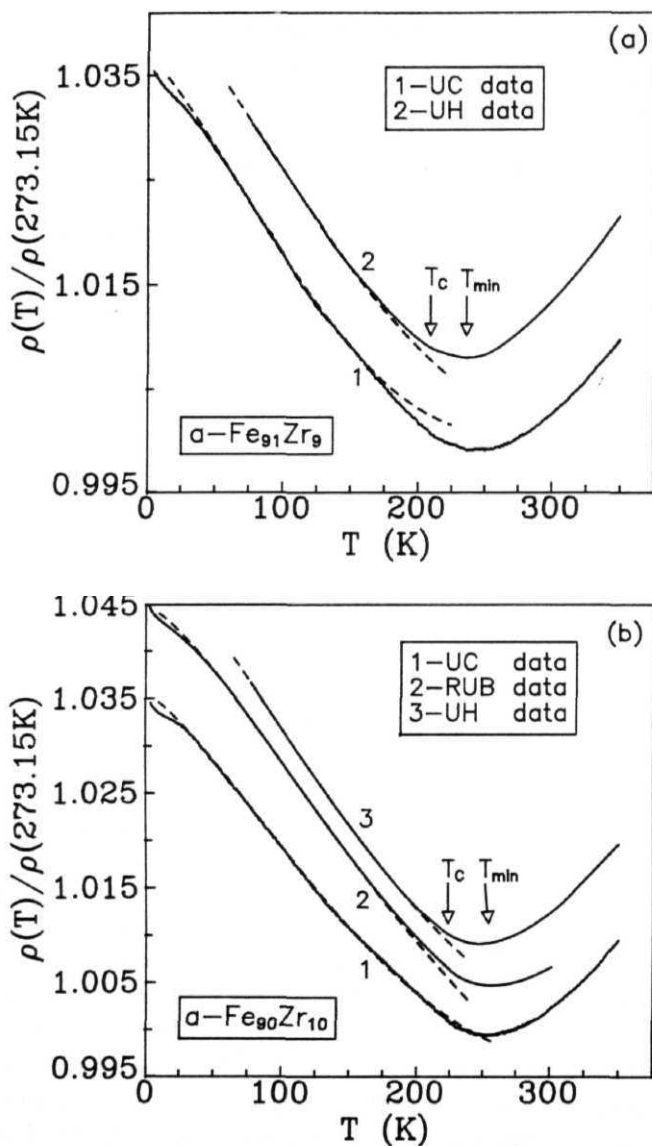


Fig. 5.1 $\rho(T)/\rho(273.15K)$ vs. T for different sets of data taken on the $a\text{-Fe}_{90+y}\text{Zr}_{10-y}$ alloys. The origin on the ordinate scale for curve 2 in (a) should read as 0.985, while for curves 2 and 3 in (b) it should be read as 0.985 and 0.975. Dashed curves are the LS fits to the data based on Eq.(5.3).

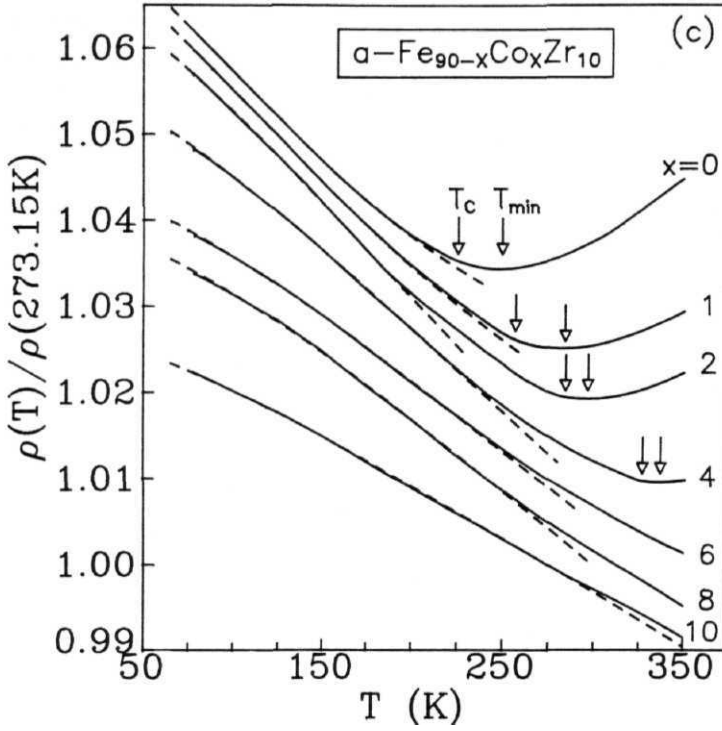


Fig. 5.1 (c) Normalized resistivity as a function of temperature for the UH sets of data on $\alpha\text{-Fe}_{90}\text{Co}_x\text{Zr}_{10}$ alloys. The dashed curves are the LS fits based on Eq.(5.2). The origin on the ordinate scale for $x = 0, 1, 2, 4, 6$ and 8 should read as $0.955, 0.965, 0.970, 0.975, 0.980$ and 0.985 , respectively.

is *negative (positive)* for $T < T_{\min}$ ($T' > T_{\min}$); *negative* TCR decreases **in magnitude** as the Co concentration increases and (iv) $\rho(T)$ exhibits another weak **minimum** at very low **temperatures** ($T \sim 10$ K) in the alloys with $y = 0$ and 1; for the alloys with $x = 6, 8$ and 10, the minimum in $\rho(T)$ presumably occurs at a temperature which lies well above the maximum temperature ($T_{\max} = 350$ K) covered in the present experiments. In the absence of a theory that takes into account all the possible scattering mechanisms for a correct description of electrical resistivity in amorphous magnetic alloys over an extremely wide range of temperatures, Matthiessen's rule is assumed to be valid in the present case. The $\rho(T)$ data in different temperature ranges have been analyzed in terms of the expressions, predicted by the existing theoretical models already mentioned in Chapter 1, which represent the scattering mechanisms that dominantly contribute to total resistivity in a given temperature range. The present analysis gives due consideration to the contributions to $\rho(T)$ arising from electron-electron interaction (EEI), quantum interference (QI) or weak localization (WL) effects, Kondo spin-flip scattering, structural-disorder scattering, electron-magnon scattering and the scattering of conduction electrons from spin fluctuations.

In order to find out the functional dependence of resistivity on temperature at very low **temperatures**, different sets of $\rho(T)$ data in this range have been plotted against $\ln T$ and \sqrt{T} for the alloys with $y = 0$ and 1 in Figs. 5.2(a)-(c). It is evident from these figures that both UC and RUB data for $y = 0$ and UC data for $y = 1$ exhibit a logarithmic dependence on T for $T \sim 10$ K and a \sqrt{T} variation in the range $\sim 10 - 25$ K. Thus, a detailed range-of-fit analysis of $\rho(T)$ data based on the expressions

$$\rho(T) = \rho(0) - \hat{a} \ln T \quad (5.1)$$

and

$$\rho(T) = \rho(0) - \bar{b} \sqrt{T} \quad (5.2)$$

has been carried out in order to ascertain the relative importance of $\ln T$ and \sqrt{T} terms and to identify the exact temperature ranges in which these terms dominate. The range-of-fit analysis, as already described in previous chapters, consists of narrowing down the temperature range of the fit either by fixing the lower limit of the range at a certain value and lowering the upper limit so as to exclude more and more high-temperature data points or by keeping the upper limit of the range fixed at a certain value and raising the lower limit. During both these **processes**, the reduced chi square (χ_r^2) (defined as the sum of deviation squares (x^2) divided by number of points (N) minus number of free fitting parameters (N_{para}), i.e., $\chi_r^2 = \chi^2 / (N - N_{para})$) and the stability of the fitting parameters are continuously monitored. The best least-squares (LS) fits, based on Eqs.(5.1) and (5.2), obtained in this way are depicted by the solid straight lines through the data points in Figs. 5.2(a)-(c), while the corresponding values of the fitting parameters and the temperature ranges of the fits are displayed in Table 5.1.

Table 5.1: Parameter values for the fits, based on Eqs.(5.1) and (5.2), to the UC and RUB sets of $r(T)$ data on $a - \text{Fe}_{90+y}\text{Zr}_{10-y}$ alloys. The numbers within the parenthesis denote errors in the least significant figure.

conc. v	data	lit to $r(T) = r(0) - a \ln T$			fit to $T(T) = r(0) - b\sqrt{T}$			
		fit range (K)	$r(0)$	a (10^{-3})	fit range (K)	$r(0)$	b ($10^{-4} \text{ K}^{-1/2}$)	D (cm^2/sec)
1	UC	4 - 10	1.0348(2)	1.35(3)	10 - 24	1.0352(2)	11.0(2)	0.10(1)
0	UC	4 - 10	1.0338(2)	1.10(2)	10- 25	1.0333(2)	6.5(3)	0.29(2)
	RUB	2 - 10	1.0411(1)	1.12(2)	10 - 20	1.0413(2)	8.4(3)	0.18(2)

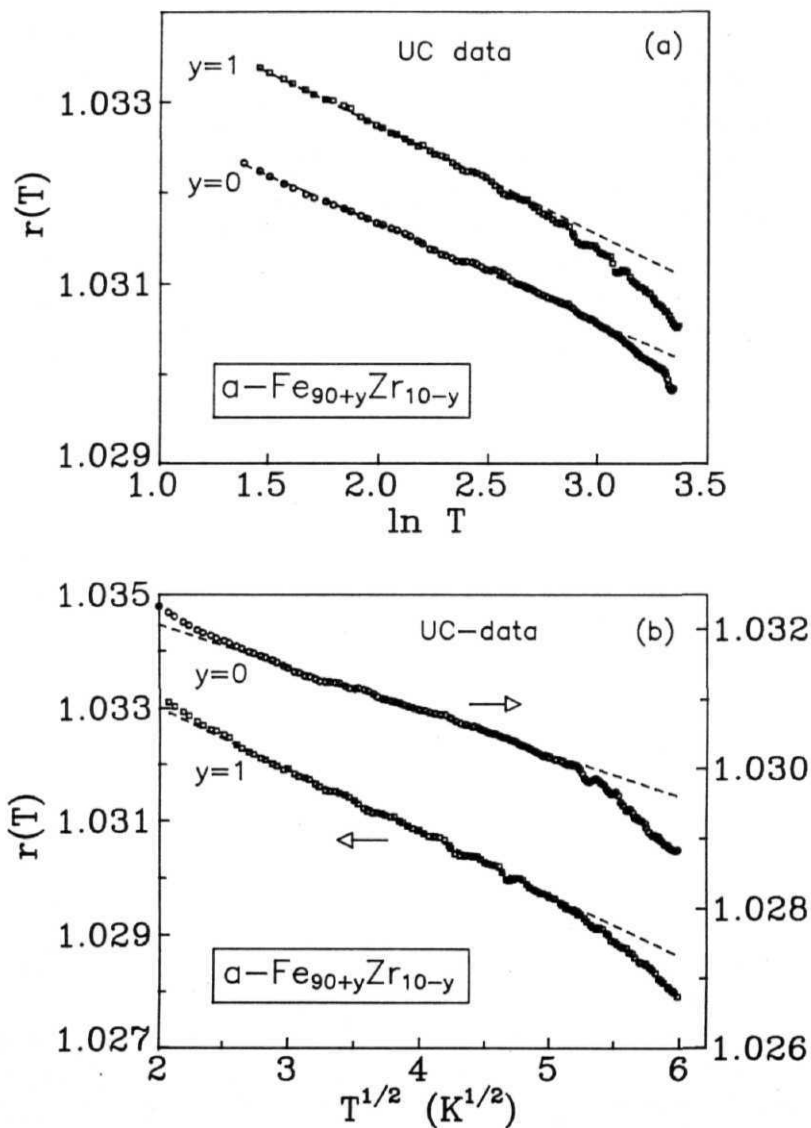


Fig. 5.2 $r(T)$ vs. (a) $\ln T$ and (b) \sqrt{T} for the UC set of data on $a\text{-Fe}_{90+y}\text{Zr}_{10-y}$ alloys. The dashed lines are the LS straight line fits to the data. The origin on the ordinate scale for the data corresponding to $y = 1$ in (a) should read as 1.027.

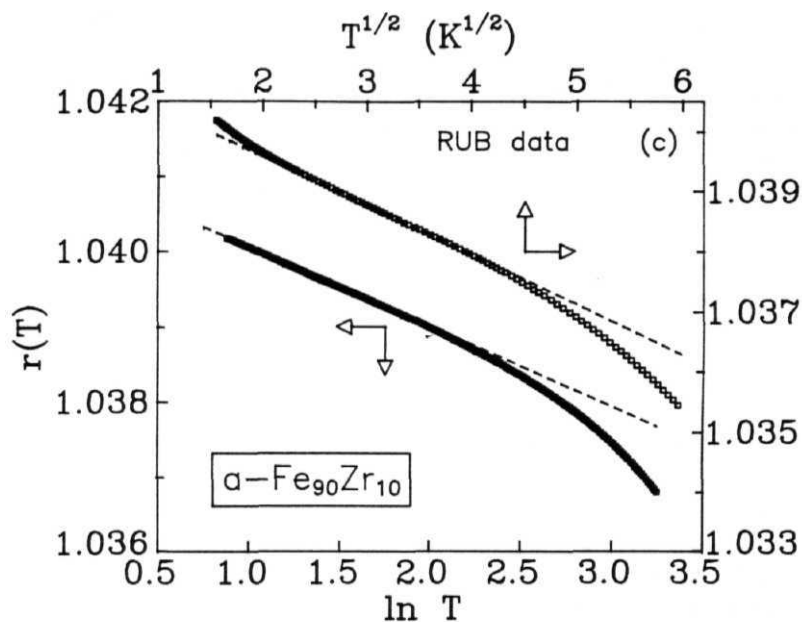


Fig. 5.2 (c) $r(T)$ vs. (a) $\ln T$ and (b) \sqrt{T} for the RUB set of data on $a\text{-Fe}_{90+y}\text{Zr}_{10-y}$ alloys. The dashed lines are the LS straight line fits to the data.

The resistivity data for temperatures $T > 25$ K have been analyzed in terms of the expressions that exhaust all possible combinations of the contributions to electrical resistivity originating from different scattering mechanisms (including those of structural and magnetic origin). Moreover, this type of analysis has been carried out in different temperature ranges since not only the contributions due to electron-phonon scattering and weak localization have different temperature dependences for $T < T_C$ and for $T > T_C$ but the temperature variation of magnetic contribution is also different for $T < T_C$ and $T > T_C$. In view of the experimental observation that the density remains nearly constant [2] in the concentration range ($0 < x < 10$) and that the reported [3] values of Θ_D for Co concentrations $x = 0$ ($\Theta_D = 251$ K) and $x = 90$ ($\Theta_D = 279$ K) are not significantly different, Θ_D in $\text{Fe}_{90-x}\text{Co}_x\text{Zr}_{10}$ alloys is expected to hardly vary with x in the concentration range just mentioned. Out of all the LS fits attempted, the one based on the expression

$$r(T) = r(0) - aT^{3/2} + bT^2 \quad (5.3)$$

provides the best fit to the resistivity data for temperatures $T < \Theta_D$ in the range $T' < T < T''$. Note that the exact temperature ranges over which the above expression describes the $r(T)$ data and the values of fitting parameters, listed in Table 5.2(a), are obtained using a detailed range-of-fit analysis of the data, based on Eq.(5.3), as described above. This table also includes the values of T_C and T_{\min} for the alloys in question. The LS fits obtained in this way are represented by dashed curves in figures 5.1(a)-(c) and 5.3. Similarly, for temperatures close to, but below, T_C the best fit to the $r(T)$ data is provided by the expression

$$r(T) = r'(0) - a'T^{3/2} + b'T^{5/3} \quad (5.4)$$

in the range $T' < T < T''$ with the choice of the parameters given in Table 5.2(b). Such fits (dashed curves) are displayed in Figs. 5.4(a) and 5.4(b) for all the investigated alloys. For temperatures $T > T_C$, the $r(T)$ data of the alloys with $y = 1$ and $x < 2$ (for which T_C and T_{\min} lie well below T_{\max}) are reproduced with far greater precision by the expression

$$r(T) = r''(0) - a''T + b''T^{5/3} \quad (5.5)$$

than by Eq.(5.4) in the temperature range $T' < T < T''$. For the remaining compositions in the $\text{Fe}_{90-x}\text{Co}_x\text{Zr}_{10}$ alloy series, i.e., $4 < x < 10$ ($x = 4$), validity of Eq.(5.5) could not be tested for want of (sufficient) data for $T > T_C$. These LS fits for $T > T_C$, based on Eq.(5.5), are depicted as dashed curves in figure 5.5 while the corresponding parameter values and fit ranges are given in Table 5.2(b). An important observation that merits attention at this stage is that the expressions for $r(T)$ given by Eqs.(5.4) and (5.5) both fail to correctly describe the functional dependence of resistivity on temperature in the critical region, i.e., $|T - T_C| \sim 0.05$, $\Theta = (T - T_C)/T_C$,

Table 5.2(a): Fit parameters and the temperature ranges of the LS fits, based on Eq.(5.3), to the UC, RUB and UH sets of $\tau(T)$ data on $a - Fe_{90+y}Zr_{10-y}$ and $a - Fe_{90-x}Co_xZr_{10}$ alloys. The numbers within the parenthesis denote the uncertainty in the least significant figure.

conc. x/y	T_C (K)	T_{min} (K)	data	$t^* - t^{**}$ $t = T/T_C$	$r(0)$	a ($10^{-5} \text{ K}^{-3/2}$)	b (10^{-6} K^{-2})	τ_{ic} ($10^{-8} \text{ s K}^3 T^{-3}$)
$y=1$	209.66	237	UC	0.24 - 0.72	1.036(1)	3.45(15)	1.55(10)	1.3(2)
			UC	0.37 - 0.72	1.038(1)	3.90(20)	1.95(15)	1.0(2)
			UH	0.37 - 0.72	1.033(1)	3.25(15)	1.45(10)	1.4(2)
$y=0$; $x=0$	225.00	254	UC	0.22 - 0.73	1.035(1)	2.85(15)	1.15(10)	1.8(3)
			UC	0.35 - 0.73	1.036(1)	3.00(15)	1.30(15)	1.7(2)
	255	255	RUB	0.22 - 0.73	1.040(1)	2.75(15)	1.00(10)	2.0(3)
			RUB	0.35 - 0.73	1.041(1)	2.85(15)	1.05(10)	1.9(3)
$x=1$	256.66	284	UH	0.35 - 0.73	1.041(1)	3.05(15)	1.22(10)	1.6(2)
			UH	0.30 - 0.74	1.048(1)	2.70(15)	0.95(10)	2.2(3)
			UH	0.27 - 0.71	1.048(1)	2.10(15)	0.60(10)	3.9(7)
$x=2$	281.63	297	UH	0.24 - 0.69	1.042(1)	1.55(20)	0.37(10)	7.6(12)
			UH	0.21 - 0.65	1.035(1)	1.22(15)	0.27(10)	12.6(35)
$x=4$	327.95	337	UH	0.19 - 0.63	1.035(1)	1.10(20)	0.22(10)	15.7(67)
			UH	0.17 - 0.60	1.027(1)	0.90(15)	0.19(10)	26.3(95)

Table 5.2(b): Results of the theoretical fits, based on **Eq.(5.4)** and (5.5), for $T \sim T_c$ and $T \sim T_c$, respectively. The quantities within the square brackets correspond to temperatures $T \sim T_c$. Errors in the least significant figure are indicated in the parenthesis.

conc.	data	$t^{**} - i^{***}$ [$t > -t''$] $t = T/T_c$	$r'(0)$ [$r''(0)$]	a' ($10^{-5} \text{ K}^{-\frac{3}{2}}$)	$[a'']$ (10^{-4} K^{-1})	$6'$ [b''] ($10^{-5} \text{ K}^{-\frac{5}{3}}$)
$y = 0;$ $x = 0$	UC	0.72 - 0.95 [1.05 - 1.33]	1.038(2) [1.091(5)]	7.5(5)		2.5(2) [1.4(1)]
	UH	0.72 - 0.95 [1.05 - 1.29]	1.035(2) [1.115(5)]	7.5(5)	[9.4(6)] [12.4(11)]	2.6(3) [2.0(1)]
	UC	0.73 - 0.98 [1.05 - 1.24]	1.032(2) [1.113(5)]	6.8(10)	[11.5(13)]	2.3(7) [1.7(2)]
	RUB	0.73 - 0.96 [1.05 - 1.18]	1.044(1) [1.109(5)]	7.5(5)	[10.6(7)]	2.5(5) [1.6(1)]
	UH	0.73 - 0.96 [1.05 - 1.18]	1.045(3) [1.120(5)]	8.7(13)	[12.1(12)]	3.0(5) [1.8(2)]
	UH	0.74 - 0.97 [1.05 - 1.23]	1.052(2) [1.115(5)]	7.6(5)	[10.2(6)]	2.5(3) [1.4(1)]
	UH	0.71 - 0.94 [1.05 - 1.24]	1.047(1) [1.100(10)]	6.0(5)	[8.6(9)]	1.9(2) [1.2(1)]
	UH	0.69 - 0.95	1.042(1)	7.0(10)		2.3(4)
	UH	0.65 - 0.93	1.035(1)	5.0(5)		1.5(2)
	UH	0.63 - 0.83	1.035(1)	3.5(5)		1.0(3)
$x=10$	UH	0.60 - 0.76	1.030(2)	2.4(6)		0.6(3)

Table 5.3: Parameter values for the LS fits to the UC sets of $r(T)$ data based on Eq.(5.6) at high temperatures for a - $Fe_{90+y}Zr_{10-y}$ alloys.

conc.	data	$t^{\dagger} - t^{\dagger\dagger}$ $t = T/T_c$	$r(0)$	3	b (10^{-4} K^{-1})
$y=1$	UC	1.50-2.45	1.038(3)	9.5(5)	4.0(5)
$y=0$	UC	1.48 - 2.42	1.035(4)	10.0(10)	4.4(6)

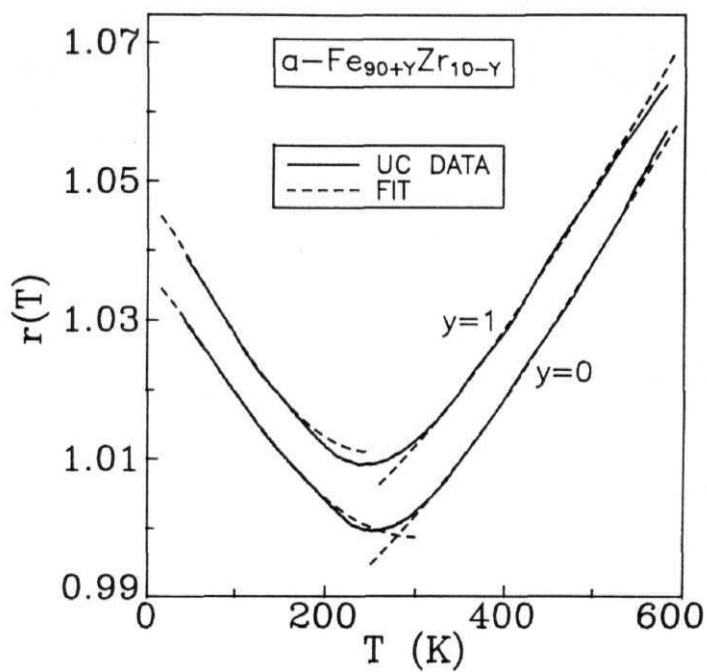


Fig. 5.3 $r(T)$ as a function of T over a wide temperature range. The data for $y = 1$ is shifted up by 0.01. The dashed curves represent the LS fits to the data based on Eqs.(5.3) and (5.6).

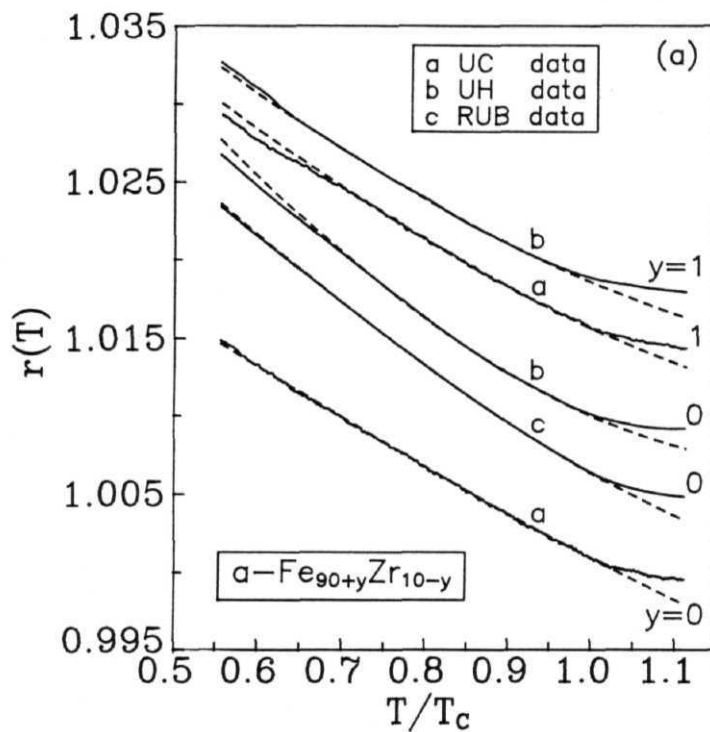


Fig. 5.4 (a) Variation of $r(T)$ with T/T_c for different sets of data taken on $a - Fe_{90+y}Zr_{10-y}$ alloys. The dashed curves denote the LS fits based on Eq.(5.4). Note that the origin on the ordinate scale for the curves c, b of $y = 0$ and a, b of $y = 1$ should read as 0.99, 0.985 and 0.98, 0.975, respectively.

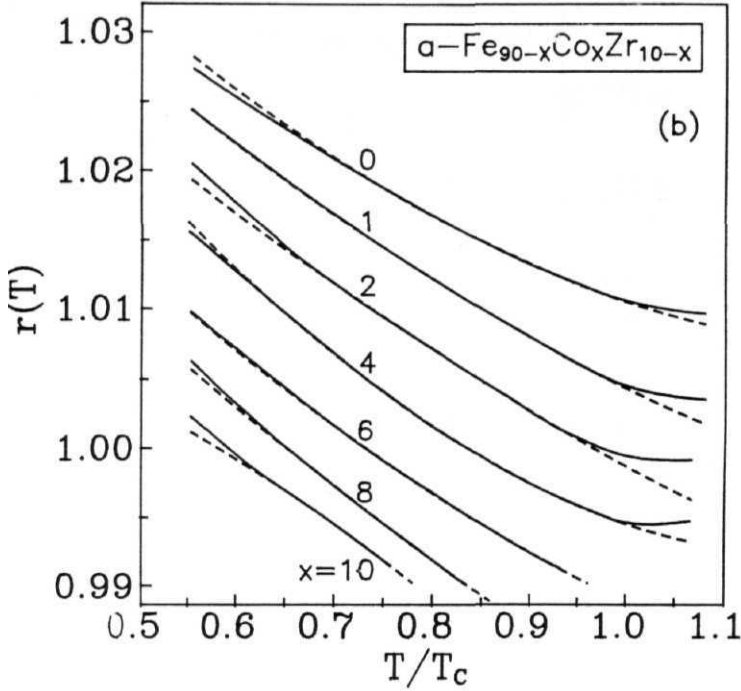


Fig. 5.4 (b) $r(T)$ VS. T/T_c for the UH set of data taken on $a - Fe_{90}Co_xZr_{10}$ alloys. The origin on the ordinate scale for $x = 0$ and 1 should read as 0.9795 and 0.9865 (there is no shift in the remaining compositions). The dashed curves represent the LS fits based on Eq.(5.4).

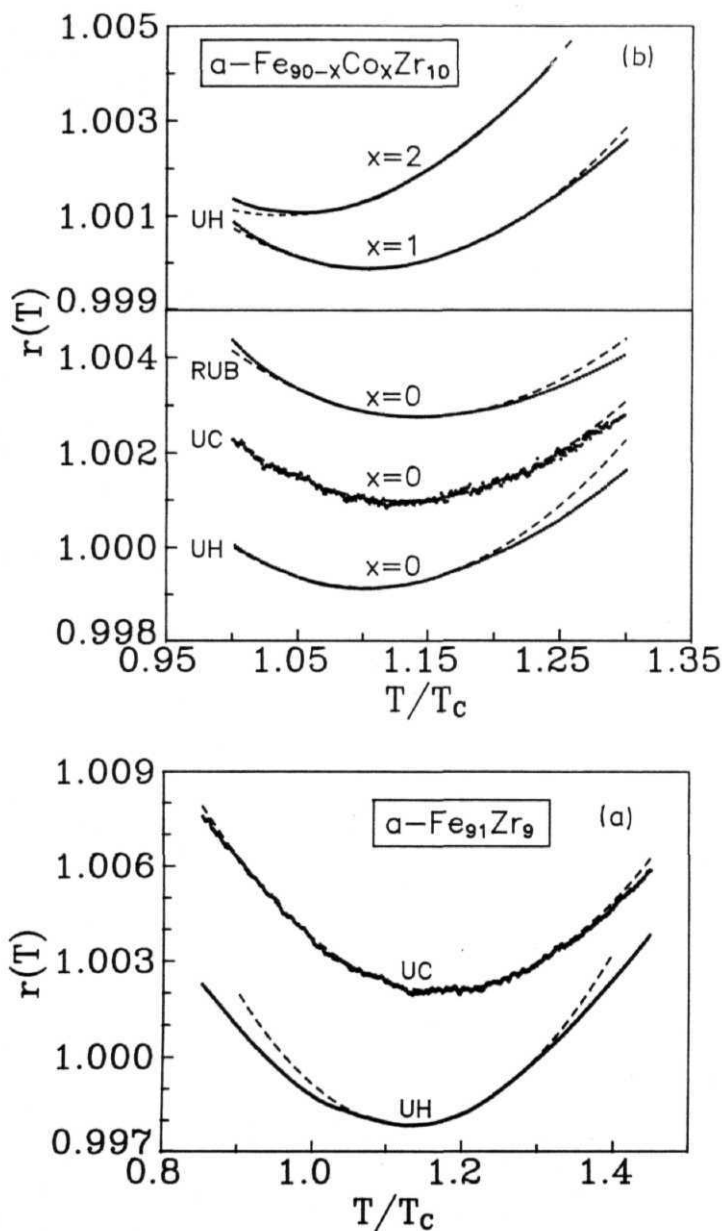


Fig. 5.5 Plot of $r(T)$ against T/T_c for different sets of data. The zero on the ordinate scale for the UC data of $y = 1$ in (a) should read as 0.994, while for the UC, RUB data on $x = 0$ and UH data on $x = 2$ alloy in (b) it should read as 0.9956, 0.995 and 0.985, respectively. The dashed curves are the LS fits based on Eq.(5.5)

presumably due to an additional contribution to the resistivity arising from the scattering of conduction electrons from critical fluctuations of magnetization. Since this contribution is known to manifest itself as a singularity in the temperature derivative of resistivity at $T = T_C$, $dr(T)/dT$ is plotted against T/T_C in figure 5.6. using the values of T_C determined from the magnetization data (Chapter 4). In order that such plots for compositions with widely different T_C values can be accommodated in a single graph, $dr(T)/dT$ data are not plotted against T but against the reduced temperature T/T_C . However, for the presently investigated alloys, neither a clear-cut slope change in the T/T curves (Fig. 5.1) nor a pronounced anomaly in the $dr(T)/dT$ vs. T curve (Fig. 5.6) is noticed at T_C . At the first sight, the result that a structure identifiable with the critical anomaly at T_C is not discernible from the $dr(T)/dT$ vs. T curves would seem to contradict our earlier findings about the critical behaviour of these systems based on the magnetization data. This apparent contradiction is resolved in the next section where a plausible explanation is provided for the mysterious absence of a cusp-like singularity in dr/dT at $T = T_C$.

The sets of resistivity data labelled as UC and taken on $a - Fe_{90+y}Zr_{10-y}$ alloys with $y = 0$ and 1 over a wide temperature range extending from 4.2 K to 600 K permit a close examination of the temperature dependence of $r(T)$ for temperatures $T > \Theta_D$ in these alloys. A detailed analysis of the $r(T)$ in this temperature range reveals that the expression

$$r(T) = r(0) - a\sqrt{T} + \sim bT \quad (5.6)$$

reproduces the resistivity data of the alloys with $y = 0$ and 1 with greatest accuracy in the temperature range $T^\dagger < T < T^{\dagger\dagger}$ (Table 5.3) with the choice of parameters given in Table 5.3. These LS fits are denoted by dashed curves in figure 5.3. For the concentrations $x > 0$ in the $a - Fe_{90-x}Co_xZr_{10}$ alloy series, the maximum temperature ($T_{\max} = 350$ K) up to which the present measurements (the UH data sets) extend does not lie well above Θ_D . Consequently, the validity of Eq.(5.6) for these alloy systems could not be tested in the present work.

5.2. Discussion

Before proceeding on with the discussion, the main results are summarized as follows. (i) For the alloys with $y = 0$ and 1, resistivity varies with temperature as $\ln T$ (Eq.(5.1)) and \sqrt{T} (Eq.(5.2)) in the temperature ranges $2 \sim T < 10$ K and $10 \text{ K} < T < 25$ K, respectively. (ii) In the temperature range extending from 77 K (50 K for $y = 0$ and 1) to T^\dagger , Eq.(5.3) completely accounts for the observed temperature variation of resistivity in all the investigated amorphous alloys. (iii) For temperatures close to, but below, T_C , $r(T)$ is best described by the relation $r(T) = r'(0) - a'T^{3/2} + b'T^{5/3}$ (Eq.(5.4)) in the range $T^{**} < T \lesssim 0.95T_C$ [$T^{**} < T < T_{\max}$]

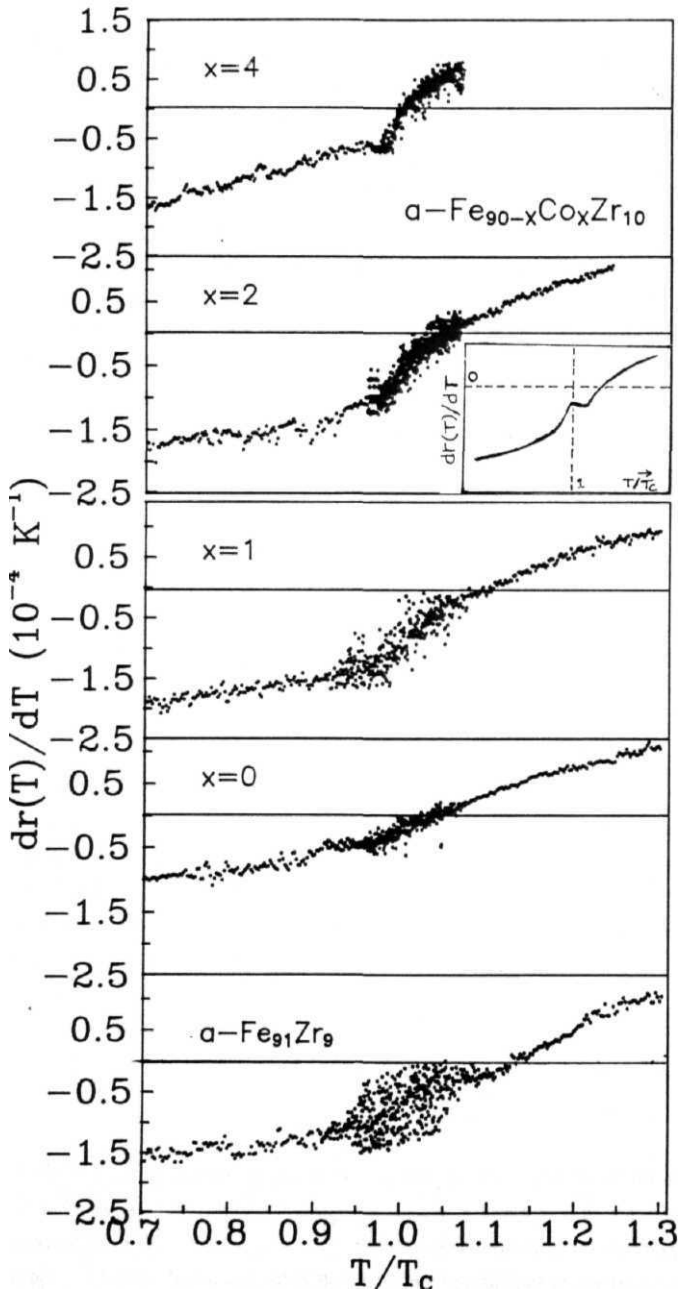


Fig. 5.6 $dr(T)/dT$ vs. T/T_c in the critical region. Inset shows the expected behaviour of $dr(T)/dT$ in the critical region if the contribution due to the scattering from critical fluctuations is of reasonable order of magnitude.

for the concentrations $y = 0, 1$, $x < 4$ [$x > 4$]. (iv) For temperatures above T_C and in the range $V < T < T''$, the expression $r(T) = r''(0) - a''T + b''T^{5/3}$ (Eq.(5.5)) provides the best fit to the $T(T)$ data for the alloys with $y = 0, 1$ and $x < 2$. (v) Electrical resistivity follows closely the temperature variation dictated by the relation $r(T) = r(0) - a\sqrt{T} + bT$ (Eq.5.6) for temperatures ($T > \Theta_D$) in the range $320 \sim T \sim 540$ K for the alloys with $y = 0$ and 1 . (vi) The coefficients (a, b) , (a', b') and (a'', b'') appearing in Eqs.(5.3), (5.4) and (5.5), all decrease in magnitude with increasing Co concentration, as shown in figures 5.7(a) and 5.7(b). (vii) For a given concentration, the coefficient of the $T^{5/3}$ term is *larger* in magnitude for $T < T_C$ than for $T > T_C$ (cf. the values of the coefficients b' and b'' , appearing in Eqs.(5.4) and (5.5), in Table 5.2(b)). (viii) Neither a clear-cut slope change in $r(T)$ nor a well-defined anomaly in the temperature derivative of resistivity ($dr(T)/dT$) at T_C is discernible for the alloys with $y = 0, 1$ and $x < 4$ whose T_C values fall well within the temperature range covered in the present experiments.

The logarithmic temperature dependence of resistivity observed at very low temperatures ($T < 10$ K) can normally be attributed to any one of the three possible scattering mechanisms, viz., Kondo spin-flip scattering [4], scattering from two-level tunneling states (TLS) [5] and scattering of conduction electrons from ("diffusons") longitudinal spin fluctuations [6], all of which give rise to a $\ln T$ variation of resistivity at low temperatures. The Kondo spin-flip scattering (which is essentially the scattering of the conduction electrons of a non-magnetic host from the (local) moment of an isolated magnetic (impurity) solute atom) dictates the behaviour of resistivity at low temperatures only in dilute magnetic alloys and is therefore an unlikely candidate for the $\ln T$ behaviour in concentrated systems such as $a - Fe_{90+y}Zr_{10-y}$ ($y = 0, 1$) alloys even though in the past, the Kondo mechanism has been held responsible for the $\ln T$ behaviour of $\rho(T)$ found previously in a large number of magnetically concentrated metallic glasses [7,8]. The experimental observation [5,9] that the resistivity minimum is insensitive to even strong applied magnetic fields has led Cochrane and coworkers [5] to propose a two-level tunneling model in which $\ln T$ variation is of structural origin. However, the main difficulty [6] of this model is that if electrons have to distinguish two possible configurations of tunneling states, their scattering time should be less than the tunneling time but the reverse should be true for the flips to give rise to the resistance minimum. Moreover, the TLS contribution to $r(T)$ has been calculated to be an order of magnitude smaller than the experimental contribution [10]. According to Continentino and Rivier [6], scattering of conduction electrons by the diffusive modes associated with the longitudinal spin fluctuations ("diffusons") gives rise to a $\ln T$ variation in resistivity at low temperatures. Since our magnetization results strongly indicate that the amorphous alloys with $y = 0, 1$ and $x \sim 4$ have a **non-collinear** spin arrangement in the ground state, the longitudinal displacements of magnetization from the local equilibrium value are of the same order of magnitude as the transverse displacements, which give rise to spin waves. Moreover, large values of the residual resistivity in amorphous alloys ($\rho(0) \approx 125 \mu\Omega\text{-cm}$ in the present case) reflect short

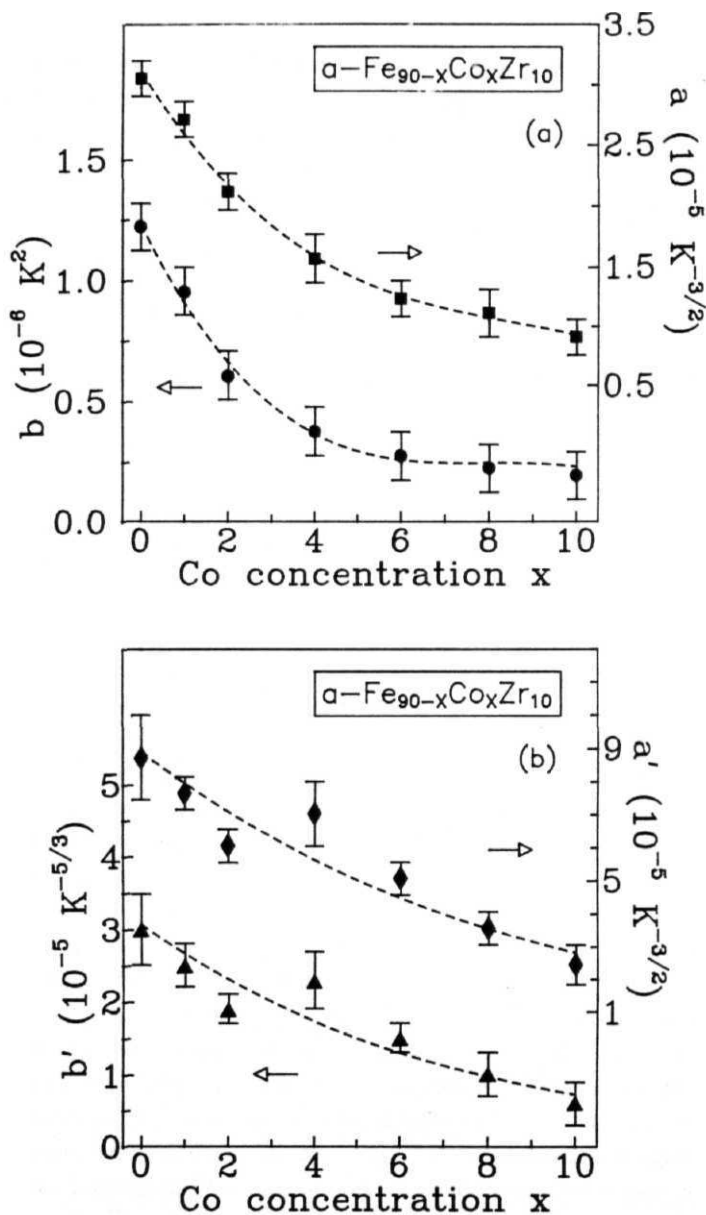


Fig. 5.7 (a) Concentration dependence of the coefficients a and b appearing in Eq.(5.3). (b) Variation of the coefficients a' and b' appearing in Eq.(5.4) with Co concentration.

mean free paths of conduction electrons and since the collisions with diffusons do not involve momentum conservation, electron-diffuson scattering becomes the fundamental scattering process at very low temperatures [6]. In addition, the results of bulk magnetization described in Chapter 3 of this thesis clearly indicate that longitudinal spin fluctuation do contribute to thermal demagnetization at very low temperatures. Therefore, the logarithmic temperature dependence of resistivity observed at very low temperatures in the alloys with $y = 0$ and 1 (observation (i) stated above) can be attributed to the scattering of conduction electrons from the diffusive modes associated with the longitudinal spin fluctuations.

Conduction electrons undergo more frequent collisions in amorphous (disordered) systems with high resistivity than in crystalline (ordered) solids. Increased scattering makes electronic screening less effective and thereby leads to a substantial enhancement in the electron-electron interactions (EEI) [8,11-13]. Therefore, at very low temperatures, the quantum corrections to conductivity, arising from the EEI effects in amorphous alloys, cannot be ignored. The EEI contribution to resistivity due to the particle-hole diffusion mechanism is given by [11-13] (cf. Eq.(1.68) of chapter 1)

$$r(T) = r(0) \left[1 - \rho(0) \frac{1.294}{\sqrt{T}} \left(\frac{4}{3} - \frac{3}{2} \bar{F}_\sigma \right) \left(\frac{\epsilon^2}{4\pi^2 \hbar} \right) \left(\frac{k_B T}{\hbar D} \right)^{1/2} \right]$$

where D is the diffusion constant and \bar{F}_σ , defined by Eq.(1.67b) of Chapter 1, is the screening factor for the coulomb interaction. Note that the EEI contribution to resistivity arising from the particle-particle Cooper mechanism is negligibly small in metallic (non-superconducting) systems with very high Fermi temperature. Eq.(5.7) clearly demonstrates that the \sqrt{T} dependence of $r(T)$ observed over the temperature range 10K - 25 K in the present work (observation (ii)) arises from the electron-electron interaction (EEI) effects. The values of diffusion constant D for the alloys with $y = 0$ and 1 have been calculated by replacing [14] the screening factor \bar{F}_σ in Eq.(5.7) with $\bar{F}_\sigma - X$ (where A , the electron-phonon mass enhancement factor, has a value of 0.3 [15] for $a - Fe_{90+y}Zr_{10-y}$ alloys) and using the estimate $\bar{F}_\sigma - X \sim 0$ (because the values of \bar{F}_σ in the range 0.3 - 0.4 have been reported [16,17] for similar alloy systems such as CoZr and CuTi) as well as the presently determined values of $r(0)$, $\rho(0)$ and the coefficient 6 of the \sqrt{T} term in Eq.(5.7). The values of D so obtained and listed in Table 5.2 are not only in reasonable agreement with the estimates $0.16(1) \text{ cm}^2 \text{ sec}^{-1}$ and $0.17(1) \text{ cm}^2 \text{ sec}^{-1}$ for concentrations $y = 1$ and 0 deduced from the Einstein relation $D = [\rho(0) e^2 N(E_F)]^{-1}$ when the $N(E_F)$ values given in Table 3.3 of Chapter 3 are used but also with those previously reported [16-21] for a number of 3d transition metal (TM) - 4d TM and 3d TM - metalloid amorphous alloys.

In disordered systems, electrons experience intense scattering owing to the random potential and hence their mean free path is of the order of interatomic distance. Due to the elastic nature of collisions at low temperatures, electron wavefunctions retain their phase over long distances. Therefore, there exists a finite probability for two partial waves starting from the same point

(origin) and undergoing scattering in a time-reversed sequence with respect to each other to return to their origin and interfere constructively. Alternatively, multiple elastic scattering leads to a phase coherence between partial waves scattered from nearby ions and hence enhances the probability for an electron to (get localized) return to its origin. Such weak-localization (WL) or quantum interference (QI) effects set in if the disorder is not strong enough to give rise to completely localized states. A number of processes such as inelastic (ie) electron-phonon scattering, spin-orbit (SO) scattering, Zeeman splitting of spin sub-bands, electron-magnon scattering and scattering from spin fluctuations, apart from the external magnetic field, tend to destroy the phase coherence and hence progressively (delocalize electrons) reduce the additional resistivity (due to weak localization). The last three scattering mechanisms occur in magnetic systems only. As the temperature is raised from very low temperatures, quantum corrections to conductivity (or resistivity) arising from EEI and WL or QI effects become *less* effective with the consequence that the classical Boltzmann behaviour of conductivity is progressively *restored*. With these considerations, the expression for total resistivity takes the form [12.13.22-26]

$$\begin{aligned} r(T) = r(0) & \left[1 - \rho(0) \left\{ \left(\frac{\epsilon^2}{2\pi^2\hbar} \right) \left(\frac{\epsilon}{c\hbar} \right)^{1/2} (3\sqrt{B_2} - \sqrt{B_\phi}) \right. \right. \\ & \left. \left. - \left(\frac{\epsilon^2}{3\pi^2\hbar} \right)^2 (k_F l_e)^2 k_F^2 (\rho_{ep}(T) + \rho_{em}(T) + \rho_{LSF}(T)) \right\} \right] \end{aligned} \quad (5.8)$$

where

$$B_2 = B_{ie} + \frac{4}{3} B_{SO} + \frac{2}{3} B_S, \quad B_\phi = B_{ie} + 2 B_S, \quad B_j = \frac{c\hbar}{4\epsilon D\tau_j} \quad (5.9)$$

the index j stands for *it* (inelastic electron-phonon scattering), *SO* (spin-orbit scattering), *S* (scattering from either a single impurity spin or collective excitations of a spin system) whereas ρ_{ep} , ρ_{em} and ρ_{LSF} denote the Boltzmann contributions to resistivity arising from the electron-phonon (ep) scattering, electron-magnon (em) scattering and scattering from local spin-density fluctuations (LSF), respectively. In Eq.(5.8), the contribution due to the EEI effects. Eq.(5.7), (which is significant at very low temperatures only) has been dropped, the first term represents the zero-temperature quantum-corrected resistivity due to localization, the second term is the correction to temperature-dependent resistivity arising from the weak localization and the third term is the classical Boltzmann contribution to resistivity due to the thermal excitation of various inelastic scattering processes. While the second term tends to decrease resistivity, the third term increases resistivity as the temperature is increased. Hence, a minimum in $r(T)$ is produced at a certain temperature T_{\min} . For the magnetic glassy alloys under consideration, the most appropriate expressions for $\rho_{ep}(T)$, $\rho_{em}(T)$ and $\rho_{LSF}(T)$ are the ones predicted by the diffraction model [27-28], spin-disorder model [29] and spin fluctuation model [30], respectively. Thus, the relevant expressions for these contributions are

$$\rho_{ep}(T) = \frac{60 \pi^3 \hbar}{(\epsilon k_F^2)^2 \Omega_c} \sin^2[\eta_2(E_F)] \left\{ 1 + [S_o(2k_F) - 1] \exp \left[-8W(0) \left(\frac{T}{\Theta_D} \right)^2 \int_0^{\Theta_D/T} \frac{z dz}{e^z - 1} \right] \right\} \quad (5.10)$$

$$\begin{aligned} \rho_{em}(T) &= \rho_{mag}(0) \left[1 + \frac{1}{J_S(2k_F)} \frac{\pi^2}{3S} \left(\frac{k_B T}{D(0)} \right)^2 \right], \quad T < T_C \\ &= \left(\frac{\pi \hbar}{8 \epsilon^2 Z} \right) \left(\frac{k_F^2}{E_F} \right) \Omega_c N(E_F) J_{sd}^2 S(S+1), \quad T \gg T_C \end{aligned} \quad (5.11)$$

with

$$\rho_{mag}(0) = \frac{3 \pi \hbar \Omega_c S^2}{16 \epsilon^2 k_F^2} \left(\frac{J_{sd}}{E_F} \right)^2 J_S(2k_F)$$

and

$$\left. \begin{aligned} \rho_{LSF}(T) &= A T^2, & T &\ll T_C \\ &= A' T^{5/3}, & T &\lesssim T_C \\ &= A'' T^{5/3}, & T &\gtrsim T_C \\ &= A''' T, & T &\gg T_C \end{aligned} \right\} \quad (5.12)$$

The meaning of various symbols appearing in Eqs.(5.10) and (5.11) as well as the details about the above-mentioned models are given in Chapter 1. In the event that $B_{SO} \ll B_s \ll B_{ie}$ (i.e., spin-orbit scattering time, $\tau_{SO} >$ spin-flip scattering time, $\tau_S >$ inelastic scattering time, τ_{ie}), Eqs.(5.8)-(5.12) assert that at temperatures *well below* T_C and Θ_D , $r(T)$ is given by

$$r(T) = r(0) - \rho(0) r(0) \left(\frac{\epsilon^2}{2 \pi^2 \hbar} \right) \sqrt{\frac{1}{D \tau_{ie}}} + C T^2 \quad (5.13)$$

where the constant C is the sum of the coefficients of the T^2 terms in $\rho_{ep}(T)$, $\rho_{em}(T)$ and $\rho_{LSF}(T)$ since all the three contributions vary as T^2 in this temperature range. For dominant inelastic electron-phonon scattering, different theoretical treatments [13,31] predict a temperature dependence of τ_{ie} of the form $\tau_{ie} \sim T^{-p}$ for $T < \Theta_D$ with the exponent p assuming a value 2, 3 or 4 depending upon the temperature range. If in a certain temperature range $p = 3$, Eq.(5.13) has the *same* form as Eq.(5.3). A close similarity between the two expressions for $r(T)$ strongly indicates that the origin of the second term in Eq.(5.3) lies in the *destruction* of phase coherence by the electron-phonon scattering, which is the *dominant* inelastic scattering mechanism in the present case, whereas the third term is the sum of the contributions to $r(T)$ arising from the electron-phonon, electron-magnon and electron-spin fluctuation scattering processes. Out of the three scattering processes, the inelastic electron-phonon scattering dominantly contributes to

the T^2 term in Eq.(5.3) since the remaining two contributions are expected to be smaller by at least an order of magnitude [28] in amorphous magnetic alloys. At this stage, it should be pointed out that, at the first sight, the above interpretation seems to be contradictory. To elucidate this point further, it is not immediately clear as to why τ_{ie} varies as T^{-3} and T^{-2} for the second and third terms in Eq.(5.3) in the same temperature range when the inelastic electron-phonon scattering mechanism is the common cause of the both the terms. However, the theoretical prediction [31] that the inelastic electron-phonon collision rate, i.e., τ_{ie}^{-1} , varies as T^3 and T^2 for longitudinal and transverse phonons, respectively, at moderately high temperatures ($T < \Theta_D$) provides a simple explanation for this puzzle in that the longitudinal phonons offer a more effective dephasing mechanism than their transverse counterparts whereas the transverse phonons basically dictate the behaviour of Boltzmann conductivity. A temperature dependence of τ_{ie} of the type $\tau_{ie} \sim T^{-p}$ with $p = 3.5 \pm 0.5$ has also been observed previously [32-35] at temperatures in the range 10 K \sim $T \sim$ 50 K in a large number of three-dimensional non-magnetic/weakly magnetic amorphous alloys that include Zr-rich Zr - M ($M = Ni, Co, Fe$) glassy alloys. A power-law variation of τ_{ie} with T of the form $\tau_{ie} \sim T^{-3}$ has been found in two-dimensional thin Cv films [36] as well. Thus, the inelastic electron-phonon scattering time seems to have a universal temperature dependence over a fairly large temperature range.

The physical basis for the expressions for $r(T)$ in different temperature ranges, i.e., Eqs.(5.4)-(5.6), becomes clear when due consideration is given to the following cases. Case I: for temperatures close to, but below, T_C and $T < \Theta_D$, τ_{ie} continues to vary as T^{-3} while $\rho_{ep}(T)$, $\rho_{em}(T)$ and $\rho_{LSF}(T)$ exhibit a crossover from the T^2 dependence to T , T and $T^{5/3}$ dependences (however, the crossover is complete only in the case of $\rho_{LSF}(T)$). Case II: for temperatures just above T_C but close to Θ_D , the rate at which τ_{ie}^{-1} increases with temperature slows down from T^3 to T^2 while $\rho_{ep}(T)$, $\rho_{em}(T)$ and $\rho_{LSF}(T)$ exhibit the same temperature variations as in the previous case. Case III: for temperatures well above T_C and Θ_D , $\tau_{ie} \sim T^{-1}$, $\rho_{em}(T) = \text{constant}$ whereas both $\rho_{ep}(T)$ and $\rho_{LSF}(T)$ increase linearly with temperature. Taking cognizance of the above temperature variations of the quantities in question and the fact that the second term in Eq.(5.8) reduces to the second term in Eq.(5.13), i.e., to a term proportional to $\tau_{ie}^{-1/2}$, in all the above cases, it is obvious that the second terms in Eqs.(5.4)-(5.6) are manifestations of the dephasing action of the electron-phonon scattering while the third terms in these expressions reflect the dominance of the structural (electron-phonon) and spin fluctuation contributions to $T(T)$ for temperatures $T \sim T_C$ ($T < \Theta_D$), $T \sim T_C$ ($T \approx \Theta_D$) and $T > T_C$ ($T > \Theta_D$). Consistent with the above identification of the scattering processes that contribute to $r(T)$ in different temperature ranges and the theoretical prediction [30] that the coefficient $A'' < A'$ in Eq.(5.12), we indeed find that for a given composition, the coefficient $6' > 6''$ (Table 5.2(b)) in Eqs.(5.4) and (5.5), i.e., the observation (vii) mentioned at the beginning of this section.

Considering that the atomic density does not vary with composition [2] for the amorphous alloys studied, the diffusion constant D is expected to remain essentially unaltered when the

composition is varied in the present range. In view of this argument and the structure of the second term in Eq.(5.13), reduction in the **magnitude of the coefficients a , a' and a'' [a], appearing in Eqs.(5.3)-(5.5) [Eq.(5.6)]. with increasing Co concentration x in $a - Fe_{90-x}Co_xZr_{10}$ alloys (Fig. 5.7) [increasing Fe concentration in $a - Fe_{90+y}Zr_{10-y}$ alloys] is a consequence of the fact that the increase in τ_{ie} with J more than offsets the increase in $\rho(0)$. Keeping D constant at its value for $x = 0$ and using the values of $\rho(0)$ presently determined for $a - Fe_{90+y}Zr_{10-y}$ alloys and previously reported [37] for $a - Fe_{90-x}Co_xZr_{10}$ alloys, the values of τ_{ie} for different Co concentrations have been computed from the second term in Eq.(5.13) and are listed in Table 5.2(a). These estimates of τ_{ie} , when modified so as to be valid in the temperature ranges covered in previous experiments [32-35], are in close **agreement** with the values obtained earlier [32-35] for a wide variety of amorphous alloys. A monotonous decrease in the coefficients b , b' and b'' (appearing in Eqs.(5.3)-(5.5)) with increasing x reflects a progressive weakening of all the three contributions $r_{ep}(T)$, $r_{em}(T)$ and $r_{LSF}(T)$ at a given temperature as the Co concentration is increased. According to Eqs.(5.8), (5.10)-(5.12), r_{ep} , r_{em} and r_{LSF} constantly fall in strength when x increases, respectively, due to the fact that the elastic scattering mean free path, l_e , decreases as the impurity (Co in the present case) concentration increases, the spin-wave stiffness $D(0)$ increases with x (Fig. 3.12) and spin fluctuations get *suppressed* with Co substitution (Chapter 3).**

Finally, the absence of a pronounced anomaly in $d\rho(T)/dT$ vs. T curve at T_C despite a well-defined ferromagnetic (FM) to paramagnetic (PM) phase transition at this temperature revealed by magnetization measurements finds the following straightforward explanation. For the presently investigated amorphous alloys, a detailed analysis of the magnetization data taken in the critical region, described in the previous chapter, clearly demonstrates that the fraction of spins actually participating in the *FM - PM* phase transition is as small as 5% for the alloy with $x = 0$ and increases to 12% at $x = 6$. This result implies that the magnetic entropy released at T_C is also correspondingly very small. Therefore, the singular contribution to resistivity due to the scattering of conduction electrons from critical **fluctuations** of magnetization is at least one order of magnitude smaller than the case in which all the spins are involved in the magnetic order-disorder phase transition. The problem of detecting such a weak critical resistivity contribution in total resistivity, $\rho(T)$, measurements is compounded by an overwhelmingly large non-singular background arising mainly from the scattering of conduction electrons from the disordered structure (the so-called 'lattice' contribution). Such a problem is, however, not encountered in magnetization or 'zero-field' (ac) susceptibility, $\chi_{ac}(T)$, measurements because the magnetic response of the system is directly probed in such experiments and hence even a small magnetic entropy release at T_C cannot go undetected in these measurements [38-40].

5.3. Conclusions

An elaborate analysis of high-precision electrical resistivity data taken over a wide temperature range on amorphous $Fe_{90+y}Zr_{10-y}$ ($y = 0, 1$) and $Fe_{90-x}Co_xZr_{10}$ ($x = 0, 1, 2, 4, 6, 8$ and 10) alloys and a detailed discussion of the results so obtained, permit us to draw the following conclusions.

- (i) In the alloys with $y = 0$ and 1 , diffusons associated with the longitudinal fluctuations of magnetization are mainly responsible for the observed $\ln T$ variation of electrical resistivity at very low temperatures ($T < 10$ K) while the electron-electron interaction effects account for the \sqrt{T} behaviour of $\rho(T)$ in the temperature range 10 K to 25 K.
- (ii) In the presently investigated amorphous alloys, weak-localization or quantum interference effects, electron-phonon scattering, electron-magnon scattering and scattering of conduction electrons from spin fluctuations are the main mechanisms that contribute to total resistivity for temperatures $T > 25$ K.
- (iii) Spin fluctuations make their presence felt through contributions to resistivity varying as T^2 and $T^{5/3}$ in the intermediate temperature range and for temperatures close to T_C , respectively. The temperature ranges over which spin fluctuation contribution is significant coincide with the corresponding ranges in the magnetization data (Chapter 3).
- (iv) The coefficients of spin fluctuation terms, i.e., the T^2 and $T^{5/3}$ terms, gradually decrease with increasing Co concentration as is also the case with the coefficients of the T^2 and $T^{4/3}$ terms (which reflect the spin fluctuation contribution to magnetization). The decay of these coefficients with x is a consequence of the suppression of spin fluctuations by Co substitution.
- (v) Consistent with the prediction of the spin fluctuation model, the coefficient of the $T^{5/3}$ term is larger for $T \sim T_C$ than for $T \sim T_C$.
- (vi) Out of the inelastic scattering processes such as electron-phonon scattering, spin-orbit scattering, spin-flip scattering, that destroy phase coherence, electron-phonon scattering is the most effective dephasing mechanism.
- (vii) Dephasing due to inelastic electron-phonon scattering mechanism persists to temperatures well above T_C and Θ_D .
- (viii) Absence of a pronounced anomaly in the temperature derivative of resistivity asserts that only a small amount of magnetic entropy is released at T_C which goes undetected in a

measurement of total resistivity which, besides this singular (magnetic) contribution, contains an overwhelmingly large non-singular contribution arising mainly from **the** scattering of conduction electrons from the disordered structure.

REFERENCES

- [1] V. Obi, L.C. Wang, R. Motsay, D.G. Onn and M. Nose, J. Appl. Phys. **53**, 2304 (1982).
- [2] T. Masumoto, S. Ohnuma, K. Shirakawa, M. Nose and K. Kobayashi, J. de Phys. (Paris) **41**, C8-686 (1980).
- [3] S. Kanemaki, O. Takehira, K. Fukamichi and U. Mizutani, J. Phys.: Condens. Matter **1** 5903(1989).
- [4] J. Kondo, *Solid State Physics* Vol. 23, edited by F. Seitz, D. Turnbull and H. Ehrenreich (Academic press, New York, 1969), p. 184; D.R. Hamann, Phys. Rev. **158**, 570 (1967).
- [5] R.W. Cochrane, R. Harris, J.O. Strom-Olsen and M.J. Zuckerman, Phys. Rev. Lett. **35**, 676 (1975).
- [6] M.A. Continentino and N. Rivier, J. Phys. F **8**, 1187 (1978) .
- [7] K.V. Rao, in *Amorphous Magnetic Alloys*, edited by F.E. Lubrosky (Butterworths, London, 1983) p.401; R. Harris and J.O. Strom-Olsen, in *Glassy Metals II*, edited by H.-J. Giintherodt and H. Beck (Springer-Verlag, Berlin, 1983), p.325.
- [8] M.A. Howson and B.L. Gallagher, Phys. Rep. **170**, 265 (1988); J.S. Dugdale, Contemp. Phys. **28**, 547 (1987);
- [9] R.W. Cochrane and J.O. Strom-Olsen, Physica **86-88** B 779 (1977) .
- [10] J.L. Black and B.L. Gyorffy, Phil. Mag. B **40**, 331 (1979) .
- [11] B.L. Altshuler and A.G. Aronov, in *Electron-Electron Interactions in Disordered Systems*, edited by F.L. Efros and M. Pollak (Elsevier, New York, 1985) p.1.
- [12] P.A. Lee and T.V. Ramakrishnan, Rev. Mod. Phys. **57**, 287 (1985).
- [13] G. Bergmann, Phys. Rep. **107**, 1 (1984).
- [14] B.G. Hickery, D. Greig and M.A. Howson, J. Phys. F **16**, L13 (1986) .
- [15] M. Matsuura, U. Mizutani and K. Fukamichi, *Proc. of 5th Int. Conference on Rapidly Quenched Metals*, edited by S. Steeb and H. Warlimont, 1019 (1985); U. Mizutani, M. Matsuura and K. Fukamichi, J. Phys. F **14**, 731 (1984) ; D.G. Onn, L.C. Wang and K. Fukamichi, Solid State Commun. **47**, 479 (1983).
- [16] S.J. Poon, E.J. Cotts and K.M. Wong, Solid Sate Commun. **52**, 519 (1984).
- [17] M.A. Howson and D. Greig, J. Phys. F **16**, 989 (1986) .

- [18] M. Oliver, J.O. Strom-Olsen, Z. Altounian, R.V.V. Cochrane and M. Trudeau, Phys. Rev. B 33, 2799 (1986) .
- [19] M. Olivier, J.O. Strom-Olsen and Z. Altounian. Phys. Rev. B 35. 333 (1987) .
- [20] G. Thummes, J. Kotzler, R. Ranganathan and R. Krishnan, Z. Phys. B - Condens. Matter **69**, 489 (1988).
- [21] A. Das and A.K. Majumdar, Phys. Rev. B 43, 6042 (1991) .
- [22] H. Fukuyama and K. Hoshino, J. Phys. Soc. (Japan) 50, 2131 (1981).
- [23] M. Kaveh and N.F. Mott, J. Phys. C 15, L707 (1982) .
- [24] M.A. Howson, J. Phys. F 14, L25 (1984) .
- [25] C.C. Tsuei. Phys. Rev. Lett. 57, 1943 (1986).
- [26] S.N. Kaul, unpublished.
- [27] S.R. Nagel, Phys. Rev. B 16, 1694 (1977) ; P.J. Cote and L.V. Meisel, Phys. Rev. Lett. **39**, 102 (1977); L.V. Meisel and P.J. Cote. Phys. Rev. B 16. 2978 (1977) .
- [28] S.N. Kaul, W. Kettler and M. Rosenberg, Phys. Rev. B 33, 4987 (1986) ; Phys. Rev. B 35, 7153(1987) .
- [29] R. Richter, M. Wolf and F. Goedsche, Phys. Stat. Sol. (b) 95. 473 (1979).
- [30] K. Ueda and T. Moriya, J. Phys. Soc. (Japan) 39, 605 (1975).
- [31] S. Chakravarty and A. Schmid, Phys. Rep. **140**, 193 (1986).
- [32] R. Richter. D.V. Baxter and J. O. Strom-Olsen, Phys. Rev. B **38**, 10 421 (1988) .
- [33] A. Sahnoune and J.O. Strom-Olsen, Phys. Rev. B 39, 7561 (1989) .
- [34] M. L. Trudeau and R.W. Cochrane, Phys. Rev. B **41**, 10 535 (1990) .
- [35] P. Lindqvist, J. Phys.: Condens. Matter 4, 177 (1992).
- [36] C. Van Haesendonk, J. Vranken and Y. Bruynseraede, Phys. Rev. Lett. 58, 1968 (1987).
- [37] K. Shirakawa, K. Fukamichi, T. Kaneko and T. Masumoto, J. Phys. F **14**, 1491 (1984) .
- [38] S.N. Kaul, J. Magn. Magn. Mater. **53**, 5 (1985).
- [39] S.N. Kaul, A. Hofmann and H. Kronmüller, J. Phys. F 16, 365 (1986) ; N. Saito, H. Hiroyoshi, K. Fukamichi and Y. Nakagawa, J. Phys. F 16, 911 (1986) .
- [40] S.N. Kaul, J. Appl. Phys. **61**, 451 (1987).

SUMMARY

High-precision bulk magnetization (BM) measurements on amorphous (a —) $Fe_{90+y}Zr_{10-y}$ ($y = 0, 1$), $Fe_{90-x}Co_xZr_{10}$ ($0 < x < 10$; $r = 90$), $(Fe_pNi_{1-p})_{80}(B, S)(0.0625 < p < 1.0)$ and $(Fe_pNi_{1-p})_{80}P_{14}B_6$ ($0.1125 < p < 1.0$) alloys over a wide range of temperatures ($4 \text{ K} < T < 300 \text{ K}$ or $70 \text{ K} < T < 400 \text{ K}$) and fields ($0 < H < 15 \text{ kOe}$), ferromagnetic resonance (FMR) measurements on $a - Fe_{90+y}Zr_{10-y}$ ($y = 0, 1$) and $a - Fe_{90-x}Co_xZr_{10}$ ($0 < x < 8$) alloys in the critical region, and electrical resistivity ($\rho(T)$) measurements on $a - Fe_{90-x}Co_xZr_{10}$ ($0 < x < 10$) [$a - Fe_{90+y}Zr_{10-y}$ ($y = 0, 1$)] alloys in the temperature range $77 \text{ K} < T < 350 \text{ K}$ [$4 \text{ K} < T < 600 \text{ K}$] have been performed with the following objectives in mind.

- (i) To make an in-depth study of low-lying magnetic excitations in all the above-mentioned alloy systems.
- (ii) To investigate the asymptotic critical behaviour of $a - Fe_{90+y}Zr_{10-y}$ and $a - Fe_{90-x}Co_xZr_{10}$ alloys near the ferromagnetic (FM)-paramagnetic (PM) phase transition.
- (iii) To study the effect of quenched randomness on the percolation critical behaviour of three-dimensional site-diluted ferromagnets.
- (iv) To identify the scattering mechanisms responsible for $\rho(T)$ in $a - Fe_{90+y}Zr_{10-y}$ and $a - Fe_{90-x}Co_xZr_{10}$ alloys and to determine their relative strengths in different temperature ranges.

A brief summary of the most important findings, based on elaborate data analyses and a detailed discussion of the results in terms of the existing theoretical models, is given below.

In $a - Fe_{90+y}Zr_{10-y}$ and $a - Fe_{90-x}Co_xZr_{10}$ alloys, magnetization (M) does not saturate even for external magnetic fields (H) as high as 70 kOe at 5 K for the alloys with $y = 0, 1$ and $x \sim 6$. The high-field differential susceptibility, $\chi_{hf}(0)$, determined from the M vs. H isotherm taken at 5 K is extremely large in the alloys with $y = 0, 1$ and $x = 0, 1$ but decreases rapidly with increasing x for $x \sim 4$ so that it possesses values typical of crystalline counterparts for $x > 6$. Large values $\chi_{hf}(0)$ have been observed previously in the alloys with $p \sim 0.75$ in the series $a - (Fe_pNi_{1-p})_{80}B_{20}$ and $a - (Fe_pNi_{1-p})_{80}P_{14}B_6$ well. Large $\chi_{hf}(0)$ is a strong indication of the presence of *competing* interactions in the alloys mentioned above. Competing interactions progressively *pick up* in strength as $x \rightarrow 0$, $y \rightarrow 1$ and $p \rightarrow 1$ in the corresponding alloy systems. This inference is further corroborated by the observations that (a) spontaneous magnetization as well as Curie temperature (T_c) fall steeply as these limiting concentration values (i.e., $x = 0$, $y = 1$ and $p = 1$) are approached, and (b) the spin-wave stiffness coefficient (D) to T_c ratio (i.e., D/T_c ratio) possesses a value ~ 0.14 that is *characteristic* of amorphous ferromagnets with

competing interactions. Competing interactions confine the direct exchange interactions to the nearest neighbours only and are primarily responsible for a non-collinear arrangement of spins in the ground state. **Non-collinearity** in the spin structure in a way ensures that the diffusons (diffusive modes associated with the longitudinal component of magnetization) contribute to the $T^{3/2}$ decrease of magnetization as significantly as the transverse spin fluctuations (spin waves) do. However, longitudinal spin fluctuations (diffusons) do not alter the 'spin-wave-only' value, D_N , of the spin wave stiffness because their coupling with the transverse spin fluctuations leads to propagating longitudinal excitations which peak at spin-wave energies in the inelastic neutron scattering (INS) spectra. Consequently, for the alloys with $x < 6$, $y = 0, 1$ and $p > 0.75$, D_M (the value of D deduced from the magnetization measurements) $\ll D_N$ (the value of D determined from INS experiments). Significantly large longitudinal spin fluctuation contribution also gives rise to a $\ln T$ temperature dependence of resistivity at low temperatures ($T < 10$ K) in a $-Fe_{90+y}Zr_{10-y}$ ($y = 0, 1$) alloys.

Dominant contribution to the thermal demagnetization of spontaneous magnetization, $M(T, 0)$ in all the alloys in the series $a - Fe_{90+y}Zr_{10-y}$ and $a - Fe_{90-x}Co_xZr_{10-x}$ except for the one with $x = 90$, is due to spin-wave excitations at temperatures $T \sim 0.3T_C$ (at these temperatures, diffusons also give a contribution whose strength depends on composition) and enhanced fluctuations in the local magnetization over a wide temperature range extending from $\sim 0.4T_C$ to $\sim 0.95T_C$. In $a - Co_{90}Zr_{10}$ alloy, a dominant spin-wave contribution to both $M(T, 0)$ and $M(T, H)$ at low temperatures ($T \sim 0.17T_C$) is followed by an overwhelming contribution from Stoner single-particle excitations of weak-itinerant type at higher temperatures, implying thereby that the particle-hole pair excitations are very *weakly correlated* in this case. Notwithstanding the temperature ranges, which depend on composition, spin waves and local spin-density fluctuations do contribute to the thermal demagnetization in all the alloys in the series $a - (Fe_pNi_{1-p})_{80}(Si)_{20}$ and $a - (Fe_pNi_{1-p})_{80}P_{14}B_{66}$ with the exception of those with $p \sim 0.75$ in the latter series, in exactly the same way as in the alloys with $y = 0, 1$ and $T < 10$. For the compositions $p \sim 0.75$ in the alloy series $a - (Fe_pNi_{1-p})_{80}P_{14}B_6$, a significant contribution from the Stoner single-particle excitations of strong-itinerant type accompanies a dominant spin-wave contribution at temperatures < 300 K. The above finding asserts that all the alloys in the series $a - Fe_{90+y}Zr_{10-y}$, $a - Fe_{90-x}Co_xZr_{10-x}$ and $a - (Fe_pNi_{1-p})_{80}(B, Si)_{20}$ are *weak itinerant* ferromagnets while a *transition* from *weak-itinerant* to *strong-itinerant* ferromagnetism occurs at a concentration $p \sim 0.75$ in the $a - (Fe_pNi_{1-p})_{80}P_{14}B_{66}$ alloy series. Despite an overwhelmingly large electron-phonon scattering (structural disorder scattering) contribution, spin wave excitations and local spin-density fluctuations make their presence felt through their contributions to resistivity in the temperature ranges similar to those observed in the $M(T, 0)$ data for the alloys with $y = 0, 1$ and $x < 10$. Contrasted with the *suppression* of spin fluctuations by the external magnetic field (H) and/or Co substitution in $a - Fe_{90-x}Co_xZr_{10}$ alloys, spin-wave stiffness does not depend on H and spin-wave modes *stiffen* with increasing Co concentration

(i.e., $D(0)$ increases with x). Sensitivity of spin fluctuations to field and Co **concentration** finds a straight forward explanation in terms of the spin fluctuation model.

Accurate values of the asymptotic critical exponents and universal amplitude ratios that characterize the FM-PM phase transition at T_C , determined from the magnetization data taken in the critical region on a - $Fe_{90+y}Zr_{10-y}$ ($y = 0.1$) and a - $Fe_{90-x}Co_xZr_{10}$ ($x = 0, 1, 2, 4, 6$) alloys, are **composition-independent** and conform very well with the corresponding theoretical estimates for an ordered (pure) isotropic spin system with $d - n = 3$. This result vindicates the famous Harris criterion which states that the critical behaviour of a three-dimensional (3D) ordered spin system does not get altered in the presence of short-ranged quenched disorder if the specific heat critical exponent of the pure system is *negative*. Consistent with the result that the presently determined asymptotic critical exponents satisfy the Widom scaling equality to a very high degree of accuracy, the magnetization data obey the scaling equation of state (SF.S) valid for the second-order phase transition. SES analysis of the BM and FMR data taken in the critical region yields identical values for the effective critical exponents and amplitudes. This result, for the first time, projects the FMR technique as a powerful experimental tool to study critical behaviour of ferromagnetic systems. In accordance with the theoretical expectations, the present results demonstrate that the nonanalytic confluent corrections, arising from nonlinear irrelevant scaling fields, dominate over the analytic ones, originating from nonlinear relevant scaling fields, in the asymptotic critical region (ACR) but the reverse is true for temperatures outside the ACR. Another important finding is that the magnetic equation of state in linear variables forms an adequate description of the magnetization data for temperatures close to T_C whereas its counterpart in nonlinear variables properly accounts for the observed $M(T, H)$ behaviour in a much wider temperature range around T_C . Instead of exhibiting a Curie-Weiss-like behaviour, the initial susceptibility follows the generalized Curie-Weiss law for temperatures in the range T_C to $\sim 1.5T_C$. This permits an unambiguous determination of the atomic moment in the paramagnetic state, q_c . Consistent with the conclusions drawn from the $M(T, H)$ data taken at temperatures below T_C regarding the nature of magnetism in these alloys, the observations that the q_c/q_s ratio is > 1 and scales with T_C^{-1} or $T_C^{-1/3}$ assert that the alloys with $y = 0, 1$ and $x < 6$ are *weak itinerant ferromagnets*. An order of magnitude smaller value of the ratio $\mu_0 h_c / k_B T_C$ in the above-mentioned alloys than that theoretically predicted for a 3D Heisenberg ferromagnet is shown to imply that the fraction of spins actually participating in the FM-PM phase transition is as small as 5% for the alloy with $x = 0$ and increases to 12% at $x = 6$. This inference is in consonance with the absence of a pronounced anomaly in the temperature derivative of resistivity at T_C because it is impossible to detect a small amount of magnetic entropy released at T_C in the measurement of total resistivity which, besides this singular (magnetic) contribution, contains an overwhelmingly large non-singular contribution arising mainly from the scattering of conduction electrons from the disordered structure. The infinite ferromagnetic matrix plus finite (ferromagnetic) spin clusters model provides a simple but qualitative **interpretation** for all

the diverse aspects of the results mentioned so far.

The $T_C(p)$, $M(T=0, p)$ and $D(T=0, p)$ data, obtained from the bulk magnetization measurements performed on a $-(Fe_pNi_{1-p})_{80}(B, Si)_{20}$ and $-(Fe_pNi_{1-p})_{80}P_{14}B_{86}$ alloys, when analyzed with caution, yield accurate values for the 'percolation-to-thermal' crossover exponent, ϕ , for Curie temperature and the percolation critical exponents, θ_p , for spin wave stiffness at 0 K, and β_p for spontaneous magnetization at 0 K. It is observed that the asymptotic critical region, where single power laws are valid, is wide for $T_C(p)$ and $D(T=0, p)$ but extremely narrow for $M(T=0, p)$; in the latter case, the leading 'correction-to-scaling' term had to be included in the expression for $M(T=0, p)$ in order to arrive at the true asymptotic values of the critical exponent β_p and amplitude m_p . Other percolation critical exponents such as ν_p for the correlation (connectedness) length and σ for macroscopic conductivity are calculated from the exponent equalities using the presently determined values of the exponents β_p , θ_p and ϕ . Making use of the values of β_p , ν_p and σ in the relations predicted by the self-similar fractal model for the structure of the percolating cluster at threshold (p_c), the fractal dimension d and the fracton (spectral) dimensionality d of the percolating cluster at p_c are calculated. A close agreement between the percolation critical exponents for amorphous site-diluted ferromagnets, so determined, and those theoretically predicted for site- or bond-percolation on three-dimensional *crystalline* lattices asserts that the critical behaviour of percolation on a *regular* $d = 3$ lattice remains unaltered in the presence of *quenched randomness* if the specific heat critical exponent of the *regular* system is *negative*. In other words, the Harris criterion is valid for the percolation critical behaviour, as is the case for the thermal critical behaviour also. In accordance with the Alexander-Orbach *conjecture*, the fracton dimensionality d has a value close to $4/3$. Moreover, the conductivity critical exponent c obeys the Golden *inequality* $c < 2$. From the values of the critical concentrations for site percolation in the glassy alloy series in question, it is inferred that, particularly for concentrations near p_c , the range of exchange interactions in $a - (Fe_pNi_{1-p})_{80}P_{14}B_{86}$ alloys nearly equals the third nearest-neighbour (NN) distance whereas the exchange interactions in $a - (Fe_pNi_{1-p})_{80}(B, Si)_{20}$ alloys extend well beyond the third NN distance. The observation that the range of exchange interactions is widely different in the two series and yet the percolation critical exponents have the *same* values for both of them vindicates the universality hypothesis.

While the enhanced electron-electron interaction effects account for the \sqrt{T} behaviour of $\rho(T)$ in the temperature range 10 K to 25 K, the weak-localization or quantum interference effects, electron-phonon scattering, electron-magnon scattering and scattering of conduction electrons from the spin fluctuations are the main mechanisms that contribute to the total resistivity for temperatures $T > 25$ K. Unambiguous identification of the dominant scattering processes in different temperature ranges and the determination of their relative magnitudes permits us to calculate the values of the diffusion constant, D , and the dephasing time (inelastic scattering time) τ_{ic} . Consistent with the prediction of the spin fluctuation model, the coefficients of the

T^2 and $T^{5/3}$ terms (which reflect the spin fluctuation contribution to resistivity in different temperature ranges) decrease with increasing Co **concentration** and the coefficient of the $T^{5/3}$ term is *larger* for $T \sim T_C$ than for $T \sim T_C$. Out of the inelastic scattering processes such as electron-phonon scattering, spin-orbit scattering and **spin-flip scattering**, that destroy phase coherence, electron-phonon scattering is the most effective dephasing mechanism. Dephasing due to inelastic electron-phonon scattering mechanism persists to temperatures well above T_C and Θ_D for the alloys with $y = 0$ and 1.

FUTURE SCOPE

The study of magnetic and transport properties of ferromagnetic systems in the amorphous state, whose results this thesis embodies, besides doing full justice to its objectives, raises a number of fundamental questions which the future investigations should address themselves to. Some of these questions are listed below.

- (i) Do the diffusive modes of the longitudinal spin fluctuations, besides spin waves, contribute to the thermal demagnetization of spontaneous magnetization in all the amorphous alloys or do they contribute only in the case of amorphous systems with competing interactions ?
- (ii) Are diffusons non-propagating or propagating longitudinal excitations ? Alternatively, under what conditions do the longitudinal modes strongly couple to the transverse modes of spin fluctuations ?
- (iii) Is there a fundamental connection between competing interactions, Invar effect and the re-entrant behaviour ?
- (iv) What is the exact nature of the re-entrant state and the transition at T_{RE} in site-diluted amorphous systems such as $a-(Fe_pNi_{1-p})_{80}Si_{20}$ and $a-(Fe_pNi_{1-p})_{80}P_{14}B_6$ alloys ?
- (v) Does the $\ln T$ variation of $p(T)$, observed in $a-Fe_{90+y}Zr_{10-y}$ ($y = 0, 1$) and $a-Fe_{90-x}Co_xZr_{10}$ ($x = 0$) alloys at $T < 10$ K, persist when Fe is progressively replaced by Co in the latter alloys series ?

In order to find proper answers to the questions (i)-(iii) stated above, spin-polarized inelastic neutron scattering experiments and magnetic measurements need to be performed on amorphous spin systems with or without competing interactions which either do or do not exhibit Invar/re-entrant behaviour. Such a comparative study would clearly bring out the role of competing interactions so far as the nature of low-lying magnetic excitations in such systems is concerned and the fundamental connection, if any, between competing interactions, Invar effect and re-entrant behaviour. Systematic neutron depolarization studies in zero-field as well as in the presence of the external magnetic field on the systems in question should unambiguously answer the queries such as whether the re-entrant state is a *mixed* state in which long-range ferromagnetic order *coexists* with cluster spin glass order or whether the re-entrant state is a pure spin glass state and if the transition to the re-entrant state is a true *thermodynamic* phase transition. The present resistivity measurements on $a-Fe_{90-x}Co_xZr_{10}$ alloys need to be extended to as low temperatures as possible if the exact functional dependence of resistivity on temperature at low temperatures has to be ascertained. Detailed magnetoresistance measurements in the low temperature region ($1\text{ K} \sim T \sim 50\text{ K}$) should help in revealing the physical origin of $\ln T$, \sqrt{T} and other terms in the expression for $p(T)$.

LIST OF PUBLICATIONS

I. Publications in **refereed** journals:

1. "Ferromagnetic resonance study of magnetic order-disorder phase transition in amorphous $Fe_{90-x}Co_xZr_{10}$ alloys"
S.N. Kaul and P.D. Babu
Phys. Rev. B **5**, 295 (1992).
2. "Thermal demagnetization due to spin-wave and Stoner single-particle excitations in amorphous $Co_{90}Zr_{10}$ alloy"
S.N. Kaul and P.D. Babu
J. Phys.: Condens. Matter **4**, 6429 (1992).
3. "Electrical resistivity of Fe - Zr glasses from 4.2 to 1000 K"
L. Fernandez Barquin, **J.C. Gomez Sal**, P.D. Babu and S.N. Kaul
J. Magn. Magn. Mater **113**, 82 (1994).
4. "Detailed magnetization study of quenched random ferromagnets I. Low-lying magnetic excitations"
S.N. Kaul and P.D. Babu
Phys. Rev. B **50**, 9308 (1994).
5. "Detailed magnetization study of quenched random ferromagnets II. Site-dilution and percolation exponents"
S.N. Kaul and P.D. Babu
Phys. Rev. B **50**, 9323 (1994).
6. "Spin fluctuation effects in, and Quantum corrections to, the conductivity of $Fe_{90+x}Zr_{10-x}$ ($x = 0, 1$) metallic glasses"
P.D. Babu and S.N. Kaul, L. Fernandez Barquin and J.C. Gomez Sal
J. Magn. Magn. Mater. **140-144**, 295 (1995).
7. "Nonlinear scaling behaviour of magnetization in amorphous ferromagnets"
P.D. Babu and S.N. Kaul
J. Magn. Magn. Mater. **140-144**, 1561 (1995).
8. "Comment on Scaling analysis of amorphous $Fe_{90-x}Mn_xZr_{10}$ alloys near the paramagnetic-to-ferromagnetic transition"
P.D. Babu and S.N. Kaul
Phys. Rev. B (in press, to appear in October issue of 1995).

II. Papers presented at National/International Conferences/Symposia :

1. "Different scattering contributions to the electrical resistivity in amorphous $Fe_{90}Zr_{10}$ alloy"
Ch.V. Mohan, P.D. Babu, M. Sambasiva Rao, T. Lucinski and S.N. Kaul
 Presented at Solid State Physics Symposium held at I.I.T. Madras during Dec 19-22 (1989).
 Proc. of Solid State Symposium **32C**, 44 (1989).
2. "Ferromagnetic Resonance as a powerful tool to study critical phenomena in ferromagnets"
P.D. Babu and S.N. Kaul
 Presented at Int. Conf. on Disordered Materials held at Devi Ahilya Univ., Indore, during Feb 2-6 (1991).
 Proc. of Inter. Conf. INDIAS-91 (Indias publ., Allahabad) p.223.
3. "Electrical resistivity behaviour near the Curie point in an amorphous invar alloy"
Ch.V. Mohan, P.D. Babu, M. Sambasiva Rao, T. Lucinski and S.N. Kaul
 Presented at Int. Conf. on Disordered Materials held at Devi Ahilya Univ., Indore. during Feb 2-6 (1991).
 Proc. of Inter. Conf. INDIAS-91 (Indias publ., Allahabad) p.158.
4. "Low-Energy magnetic excitations in amorphous $Fe_{80-x}Ni_{10-x}P_{14}B_{16}$ alloys"
P.D. Babu and S.N. Kaul
 Presented at Solid State Physics Symposium held at B.H.U. Varanasi during Dec 21-24 (1991).
 Proc. of Solid State Symposium **34C**, 122 (1991).
5. "Weak itinerant ferromagnetism in amorphous $Co_{90}Zr_{10}$ alloy"
P.D. Babu and S.N. Kaul
 Presented at Solid State Physics Symposium held at B.H.U. Varanasi during Dec 21-24 (1991).
 Proc. of Solid State Symposium **34C**, 123 (1991).
6. "Scaling behaviour of magnetization in the critical region of a - $Fe_{90-x}Co_xZr_{10}$ alloys"
V. Siruguri, P.D. Babu and S.N. Kaul
 Presented at Indo-US workshop on Ordering Disorder Prospect and Retrospect in Condensed Matter Physics held at Univ. of Hyderabad, Hyderabad during Dec 29 1992 to Jan 5 1993.
 AIP Proc. No. 286, 309 (1994).
7. "Weak Localization and Spin-Fluctuation effects in the resistivity of **Fe-Rich Fe-Zr** and **Fe-Co-Zr** metallic glasses"
P.D. Babu and S.N. Kaul

Presented at SSP Symposium held at BARC, Bombay Dec 27-31 (1993). Proc. of Solid State Physics Symposium **36C**, 318 (1993).

8. "Asymptotic Critical Behaviour of Glassy $Fe_{91}Zr_9$, $Fe_{90}Zr_{10}$ and $Fe_{89}Co_1Zr_{10}$ alloys"

P.D. Babu and S.N. Kaul

Presented at SSP Symposium held at B.A.R.C., Bombay during Dec 27-31 (1993).
Proc. of Solid State Physics Symposium **36C**, 436 (1993).

9. "Spin fluctuation effects in, and Quantum corrections to, the conductivity of $Fe_{90+x}Zr_{10-x}$ ($x = 0, 1$) metallic glasses"

P.D. Babu and S.N. Kaul, L. Fernandez Barquin and J.C. Gomez Sal

Presented at Int. Conf. on Magnetism (ICM) held at Warsaw, Poland, from August 22-26, 1994.

10. "Nonlinear scaling behaviour of magnetization in amorphous ferromagnets"

P.D. Babu and S.N. Kaul

Presented at Int. Conf. on Magnetism (ICM) held at Warsaw, Poland, from August 22-26, 1994.

11. "Magnetic Phase diagrams for amorphous $(Fe_pNi_{1-p})_{80}P_{14}B_4$ and $(Fe_pNi_{1-p})_{80}(B,Si)_{20}$ alloys"

P.D. Babu, M. Sambasiva Rao and S.N. Kaul

Proc. of Solid State Physics Symposium **37C**, 134 (1994).

12. "Percolation Critical exponents for quenched random site-diluted three-dimensional Heisenberg ferromagnets"

P.D. Babu and S.N. Kaul

Proc. of Solid State Physics Symposium **37C**, 407 (1994).